Time-Reversal Based Hybrid Quantum State Transfer and the Interference of Two Interference Effects

by

Kevin J. Randles

A dissertation accepted and approved in partial fulfillment of the
requirements for the degree of
Doctor of Philosophy
in Physics

Dissertation Committee:
Daniel A. Steck, Chair
Steven J. van Enk, Advisor & Core Member
David T. C. Allcock, Core Member
Jeffrey A. Cina, Institutional Representative

University of Oregon
Spring 2025

DISSERTATION ABSTRACT

Kevin J. Randles

Doctor of Philosophy in Physics

Title: Time-Reversal Based Hybrid Quantum State Transfer and the Interference of Two Interference Effects

Much of quantum science is about developing and employing methods for controlling quantum systems to perform tasks that are either classically hard, interesting (e.g., novel or useful), or ideally both. In this dissertation, we analyze the essential role of controlling the modes photons occupy (e.g., their shape, polarization, and path taken) in performing quantum-information-processing tasks. This dissertation includes two disjoint but complementary research directions. The first and primary direction concerns the deterministic transfer of quantum information or entanglement between heterogeneous quantum systems using itinerant photons. We present a unitary transformation that time reverses, frequency translates, and stretches the photon wave packet emitted by one system to match the spectral properties of the receiving system. We show how the underlying input-output formalism is modified due to such manipulations, leading to a new interpretation, wherein the receiving system is effectively driven by a fictitious version of the emitter that evolves backwards in time at a new decay rate and frequency. The probability of interfacing successfully is determined by the temporal-spectral overlap of the actual photonic wave packet and an ideal shape. This allows us to analytically and numerically analyze how the probability of success is impacted by realistic errors and show the utility of our scheme in consonance with known error correction methods.

In the second direction, we analyze a linear-optical setup in which two kinds of standard interference effects—namely, Mach–Zehnder interference and Hong–Ou–Mandel interference—interfere with one another, partially canceling each other out. This new perspective, along with the overall pedagogical exposition of this work, illustrates how quantum effects can combine nontrivially, the importance of photon indistinguishability for interference, and, moreover, that quantum interference happens at measurement. This work can serve as a pedagogical bridge to more advanced quantum mechanical concepts, including photonic quantum computing, complementarity, and tests of quantum mechanics (e.g., Hardy's Paradox).

This dissertation contains previously published as well as unpublished co-authored materials.

CURRICULUM VITAE

NAME OF AUTHOR: Kevin J. Randles

GRADUATE AND UNDERGRADUATE SCHOOLS ATTENDED:

University of Oregon, Eugene, OR
Weber State University, Ogden, UT

DEGREES AWARDED:

Doctor of Philosophy, Physics, 2025, University of Oregon
Master of Science, Physics, 2023, University of Oregon
Bachelor of Science, Physics and Applied Mathematics, 2020, Weber State University

AREAS OF SPECIAL INTEREST:

Analytical and numerical modeling of quantum mechanical systems for applications in the quantum versions of computing, transduction, networking, communication, measurement, and open systems.

PROFESSIONAL EXPERIENCE:

Graduate Research Assistant, University of Oregon, 9/20–6/25

Graduate Teaching Assistant, University of Oregon, 9/20–6/25

Supplemental Instructor, Weber State University, 1/19–4/20

Math Grader, Weber State University, 8/19–4/20

Scientific Computing Lab Aide, Weber State University, 8/18–12/18

GRANTS, AWARDS AND HONORS:

Emanuel Optical, Molecular, and Quantum Sciences Scholarship, writing and defending PhD thesis, University of Oregon, 2025

Emanuel Optical, Molecular, and Quantum Sciences Scholarship, US QIS Summer School, University of Oregon, 2024

University of Oregon Professional Development Graduate Scholarship, APS DAMOP Meeting, University of Oregon, 2024

Oregon Center for Optical, Molecular, and Quantum Sciences Director's Fellowship, University of Oregon, 2020–2021

Outstanding Graduate of the Department of Physics, Weber State University, 2020

Outstanding Graduate of the Department of Mathematics, Weber State University, 2020

Presidential Scholarship, Weber State University, 2016–2020

Burkhart Physics Research Fellowship, Weber State University, 2018

Freshman Chemistry Award, Weber State University, 2017–2018

PUBLICATIONS:

K. J. Randles and S. J. van Enk. Interference of interference effects. *preprint arXiv:2501.03505*, 2025. A condensed version of this article has been accepted by the American Journal of Physics. After it is published, it will be found at https://doi.org/10.1119/5.0256745.

K. J. Randles and S. J. van Enk. Success probabilities in time-reversal-based hybrid quantum state transfer. *Physical Review A*, 110(1):012415, 2024.

K. J. Randles and S. J. van Enk. Quantum state transfer and input-output theory with time reversal. *Physical Review A*, 108(1):012421, 2023.

K. J. Randles, D. V. Schroeder, and B. R. Thomas. Quantum matrix diagonalization visualized. *American Journal of Physics*, 87(11):857–861, 2019.

ACKNOWLEDGEMENTS

I thank my advisor Steven J. van Enk for his continued insights into physics, support, good-humored presence, and for showing me the kind of theorist I aspire to be. Steven has helped me develop the skills necessary to pose interesting research questions, thoroughly investigate them, and persist after getting stuck. For their support, guidance, and feedback, I thank the UO quantum theory group (Steven, Sean Ericson, Dan Steck, and Peter Zheng), my graduate instructors (including Dan Steck, Brian Smith, and John Toner), my undergraduate research advisors (Dan Schroeder, Jean-Francois van Huele, and Manuel Berrondo), the OMQ staff (Jorjie Arden and Brandy Todd), and my dissertation committee. I am grateful for those who pioneered this field and established the viewpoint from which I have been able to explore it.

I thank my friends and family—especially my father, my sister, and Kylie—for their continued support and for helping me stay motivated while writing this dissertation, studying physics, and beyond. I wouldn't be where I am without you. Finally, if you are reading this, I thank you. Through this dissertation, I strive to present my work and related background in a cohesive fashion that is easy for me to understand and useful for me to reference. I hope that ease and utility extends to you.

In loving memory of my mom.

When reading, writing, and learning, a part of you is by my side.

Look in the distance, what do you see?

The sea, by a wave going at c.

The splish-splash of the ocean?

No – just the motion

Of photons that bounce off to me.

TABLE OF CONTENTS

LIST OF FIGURES

Figure Page

LIST OF TABLES

Table Page

CHAPTER I

INTRODUCTION

This dissertation presents theoretical work on controlling photons to achieve quantum-information-processing tasks. In particular, it focuses on controlling itinerant photons, their interactions with material quantum systems, and the systems themselves. This work explores both active photonic control through nonlinear optical transformations (wave packet engineering) and passive control via linear optical elements such as beamsplitters. A central goal is the development of a scheme for hybrid quantum state transfer, with additional covered topics including hybrid remote entanglement generation and a pedagogical exposition of photonic interference.

1.1 Dissertation outline

In this chapter, we will give an introductory overview of the quantum information concepts and background necessary for understanding the rest of this dissertation (with the level of technicality tending to increase progressively). This dissertation presents analyses of two separate research directions, both of which involve the common theme of controlling the shape and indistinguishability of photons for quantum-information-processing (QIP) tasks. The first direction concerns hybrid quantum state transfer [3, 4], which is introduced in §1.5, while the second concerns the interference of two photonic interference effects [5]. These three articles, Refs. 3, 4, and 5, were all written jointly by myself and S. J. van Enk.

In Ch. II, we present a more technical background to motivate the starting point of input-output theory, which is the formalism underlying the first direction. In Ch. III, we will explore and analyze a scheme for hybrid quantum state transfer. In

Ch. IV, we extend this analysis with a focus on characterizing the scheme's success and exploring its realizability when adorned with both standard errors and errors that are more particular to our setup. In Ch. V, our focus shifts to direction 2, which concerns a pedagogical analysis of a simple linear-optical network that exhibits a combination of Mach–Zehnder and Hong–Ou–Mandel interference that can be understood visually in terms of Feynman paths. Note that Ch. V is quite self-contained and one may reasonably opt to read it before Chs. II–IV, heeding that it is simpler. Lastly, in Ch. VI, we highlight the main conclusions of our analyses and discuss some unifying themes of our works and QIP more generally.

1.2 Why go quantum?

Before going on to model and analyze specific quantum mechanical systems of light, matter, and their interactions, it is worthwhile to zoom out and provide a broader context for why "going quantum" is an interesting and important pursuit. One answer is the physical one: nature is not classical and quantum mechanics is the best known framework we have for describing it (at least quite generically and certainly for the types of systems we will be considering here). Thus, if we want to understand nature, we better start with quantum mechanics. A different, more utilitarian, answer is that quantum mechanical systems not only exhibit novel physics but can be useful. These motivations are further cemented by the underlying epistemological intrigue of quantum mechanics as a topic that has continued to confound scientists as it clashes with our everyday experiences.

A century ago, in 1925, Heisenberg and Schrödinger began developing their matrix and wave mechanics formulations of quantum mechanics, respectively. These formulations and the breakthroughs they sparked, ushered in a new era of quantum

mechanics, and serve as the framework of modern quantum theory. This quantum revolution enabled immense progress in science, including the refinement of our understanding of the structure of systems such as atoms, molecules, and materials as well as our ability to predict their behaviors. These scientific strides were accompanied by technological progress, ranging from advancements in electronics and semiconductors driving the information age, to laser physics, material science, and imaging devices such as MRIs. With the ability to use quantum mechanics to understand, predict, and capitalize on natural systems continually being concretized, it has been natural to explore the limits of quantum's utility. In particular, rather than just using quantum mechanics as a lens through which to *explain* the world, there has been an ongoing pursuit to *engineer* quantum mechanical systems, which includes controlling their interactions as well as designing new ones unbeknownst to nature prior. The corresponding advancement of distinctly quantum technologies has been deemed the "second quantum revolution" [6]. We will highlight three pillars of quantum information science (QIS) and technology that underscore the success hitherto achieved by this pursuit through their demonstrable utility and potential: quantum sensing, quantum communication, and quantum computation (see Ref. 7 for a more technical introduction).

Quantum sensing leverages the intricacy of quantum systems for precise measurements, including of time, electromagnetic fields, and gravity [8]. For instance, atomic clocks are used for precision time keeping in GPS and telecommunication systems as well as for fundamental science applications. Meanwhile, squeezed quantum light can be used to increase the sensitivity of certain measurements, a prominent example being the gravitational-wave detector LIGO's leveraging of squeezed light to reduce noise, enabling them to detect weaker gravitational waves

[9]. Other, perhaps more practical, examples include quantum enhanced imaging, magnetometry, and accelerometry.

Quantum communication systems involve the sharing of quantum information and entanglement between multiple parties. This sharing of quantum resources enables cryptographic protocols that enhance the security of various communication and computing scenarios [10, 11]. A paramount example of this is quantum key distribution, which is quite mature and demonstrably useful (as evidenced by its being the first commercialized QIS task) in securely sending information in a manner that detects eavesdropping attempts and whose security is guaranteed by quantum mechanics. Meanwhile, quantum networks are an emerging application, to be discussed in §1.5.2.

Considerations of computation using quantum systems began stirring over four decades ago, including Hamiltonian models of computation by Paul Benioff, as well as the emerging notion that quantum physics could be harnessed to enable a new, potentially more powerful of kind of computation as proposed by Yuri Manin and soon after by Richard Feynman (see Ref. 12 for a more thorough account of this history and the ensuing developments). Since then, the field of quantum computation has been under rapid development with its potential solidified by Peter Shor's 1994 factoring algorithm [13]. Some pioneering early experiments include the 1995 realization of the controlled NOT quantum logic gate between two trapped ion qubits [14] and the 1998 demonstration of quantum algorithm solving Deutsch's problem on a two-qubit NMR quantum computer [15]. Subsequent developments in theory, algorithms, and experiment have beget significant progress in the field, now enabling the control of dozens of qubits (with the details very much depending on the underlying architecture). The tremendous progress in these pillars of QIS

demonstrates considerable promise (as well as an undercurrent of 'hype'), but the field is still emerging with much of its utility contingent on building much better quantum systems, e.g., quantum computers with significantly more, better quality qubits.

1.2.1 Challenges and routes to scaling

Quantum systems are hard to control: manipulating them requires precise, often strong interactions with carefully tuned drives (lasers, RF fields, voltages, etc.), yet they are inherently fragile (susceptible to environmental decoherence), so they must simultaneously be isolated from interactions with everything else. Accordingly, much of QIS is about enhancing specific interactions, while mitigating all others. One qualitative way of explaining this fragility is by contrasting the physical implementation of a classical bit and a quantum bit (qubit).

Classically, a bit is defined by some macroscopic true or false question, which is designed to be quite robust to errors (thermal noise, material imperfections, etc.). The prototypical realization of a bit is a transistor (or collection thereof) with either a high or low voltage, e.g., 5 Volts and 0 Volts are typical, corresponding to a '1' and '0', respectively. Thus, even if one has appreciable voltage errors, even as large as 0.1 Volts, the two states can easily be discerned. A qubit on the other hand is in a linear combination of two specifically chosen logical basis states (e.g., two energy states of a system), often denoted as $|0\rangle$ and $|1\rangle$ to mirror the classical 0 and 1 (see §1.3.2 for notes on notation).

We can contrast the number of microscopic states corresponding to a classical bit versus a qubit state. Transistors have a characteristic length of around 10 nm and are made of nearly pure silicon, which has a density of 2.3 g cm^{-3} and an

atomic mass of 28 amu. Hence a transistor contains approximately $N_{\text{atom}} \sim 10^4$–$10^5$ atoms. The thermodynamic entropy per atom at room temperature is of order Boltzmann's constant, $S_{\text{atom}} \sim k_B$,[1] so the total thermodynamic entropy is roughly $S = S_{\text{atom}} N_{\text{atom}} \sim 10^4 k_B$. Thus, the number of microstates corresponding to a classical '0' or '1' is $\Omega = \exp(S/k_B) \sim \exp(10^4) \sim 10^{4000}$. Meanwhile, a qubit is in a superposition of just two microscopic states. This enormous difference helps explain why qubits are inherently vulnerable to errors in a way that classical bits are not.

While a few (or perhaps a dozen) relatively good qubits can be engineered and controlled on many quantum computing architectures, one major challenge is scaling this number up to thousands, millions, etc., while still maintaining good control over all of them. The power of quantum computation relies on this scaling up of the number of high-quality qubits being used to, in a sense, access exponentially bigger Hilbert spaces. Thus, for n qubits, one not only needs to design algorithms that cleverly choreograph all 2^n quantum amplitudes to interfere in a interesting or useful way, they must be able to handle additional complications and interactions that come with having more qubits coupled together and more external drives to control them. Thus, a unifying theme of QIS is that to leverage the utility of quantum systems, we need to be able to control them. Improving fundamental primitives for quantum operations and mitigating errors to better control quantum systems are conceptually the simplest ways to scale up and improve quantum systems (though the details tend to not be so simple; see §1.3). Meanwhile, a complementary approach for scaling up quantum systems is quantum error correction, where one heeds that some

[1]This estimate follows from the fact that, at room temperature, phononic excitations dominate over electronic ones. Each atom in the crystalline solid contributes three vibrational degrees of freedom that are partially populated contributing on the order of k_B to the entropy. Moreover, such as argument is consistent with the standard molar entropy of silicon at room temperature and atmospheric pressure of 18.8 J $\text{K}^{-1}\text{mol}^{-1} = 2.27 k_B$/atom. All silicon parameter values were obtained from NIST reference data [16].

errors are unavoidable, yet, if they are sufficiently small, by leveraging some carefully constructed redundancy, they can be corrected [17]. That is, error correction makes it possible to maintain control even in the presence of errors (we will briefly consider a simple kind of error correction in Ch. IV, though it is an extensive modern research direction that is largely beyond the scope of this work).

1.3 Taming the zoo of degrees of freedom

For all but the simplest physical systems, a "full description" (such as the Hamiltonian for an entire setup), although perhaps more accurate and powerful in principle, is too unwieldy to be of any practical use. Thus, a large part of quantum science consists of determining what simplifications can be made to a physical description while retaining its key features. Fortunately, there are many approximations for distilling the key physics underlying quantum information protocols. We will start by giving some examples to indicate why QIS systems select certain dominant interactions that allow such simplifications to be made.

1.3.1 Controlling quantum systems

Nature has many degrees of freedom (DOFs) that can all potentially couple to one another and interact in a complicated way. One beauty of physics is that good experiments (or theory proposals) can be devised to effectively decouple the many undesired DOFs from the few of interest. This decoupling often leverages resonant interactions, where specific system DOFs only interact strongly with a small subset of external DOFs, e.g., those operating on certain energy and time scales. For instance, to single out and drive a particular transition in a quantum system, the drive properties (such as the frequency, bandwidth, and power of a laser) should be

designed to be compatible with just the transition of interest, so that other DOFs of the system are "frozen out," i.e., do not interact with the drive. This requires a careful choice of the pair of system DOFs and drive based on the dominant interactions that can be leveraged in a system, knowledge of the various allowed transitions in a system, and modern drive technology. Similarly, cavities have a tower of resonances, yet an atom placed inside can single out an individual frequency mode.

Thus, the phenomenological models we use in physics are the joint effort of theory, in finding such simplified effective descriptions of systems, and experiment, to tame the necessary DOFs. For instance, two-level atoms and single-mode cavities are extreme idealizations, yet are incredibly successful as simple, effective systems. This is not by luck or natural design, but because experimentalists go through a lot of effort to make it so, as facilitated by technological progress. A few example of resources used to hone in on the DOFs of interest are, (i) good (stable, high coherence, low bandwidth) lasers can be used to single out specific interactions, (ii) good (high-Q) cavities can be used the enhance interactions with light at certain frequencies, e.g., that of a relevant transition for an atom inside, while suppressing others, and (iii) good cryogenics can be used to isolate microwave systems from thermal noise.

We will soon discuss two common (often extremely good) approximations in QIS, the few-level (§1.3.4) and long-wavelength (§1.3.5) approximations. However, to preface our discussions of these approximations, we will first remark on the mathematical notation used in this dissertation (§1.3.2) and provide a brief overview of quantum dynamics itself (§1.3.3). Note that the taming of DOFs provided by these approximations may seem obvious (at least in retrospect), however, this is not always the case. An explicit, non-obvious demonstration of such a reduction of relevant DOFs is provided by Ref. 18 for strong laser light interacting with an atom, where,

in certain parameter regimes, the dipole-wave interaction is singled out, and the full three-dimensional calculation can be reduced to a quasi-one-dimensional (1D) one in terms of input-output theory.

1.3.2 Mathematical notation and conventions

We will tend to use notation that is common to the quantum information and atomic, molecular, and optical physics (AMO) literatures. This includes using Dirac notation, as briefly introduced in the following subsection, as well as the notational conventions described below. We will explicitly indicate if we are using a non-standard notation or one that differs from the below conventions. As is standard, (non-state) vectors are denoted using bold symbols, $\boldsymbol{f}$, with their magnitudes denoted by corresponding (nonbold) symbol, $f \equiv |\boldsymbol{f}|$, and the corresponding unit vectors denoted with a hat, $\hat{f} \equiv \boldsymbol{f}/f$. We use the partial derivative shorthand $\partial_f \equiv \partial/\partial f$. Time derivatives are often indicated using overdots: $\dot{f} \equiv \partial_t f = \partial f/\partial t$. Integrals without explicit bounds are taken over the full relevant space (as indicated by the integration measure).

One has freedom in defining where the necessary factors of 2π go in the Fourier transform. To be consistent with many of our primary references, we opt to work with the symmetric definition, where both the Fourier transform and its inverse are endowed with a $(2\pi)^{-1/2}$ factor (see App. C.1). We consider many quantum operators, which are often adorned with hats in other works to distinguish them from their corresponding classical alternatives. However, this distinction should be evident based on context here, so we opt to avoid the additional clutterment (and any potential confusion with unit vectors). Similarly, we will sometimes omit function arguments when they should be clear from context.

1.3.3 Quantum dynamics

Here we will briefly overview some of the fundamentals of quantum mechanics that will be used throughout this dissertation. Our goal here is to remind the reader of some key notions of quantum mechanics without getting too bogged down with technical details and caveats, e.g., regarding the standard axiomatic structure underlying quantum mechanics, which are best left to textbooks or specialized treatments [19, 20].

The state of a quantum system is represented by a vector in Hilbert space, $\mathcal{H}$, which is a complex vector space endowed with an inner product that has certain nice (but technical) properties (including being complete; see chapter 1 of Ref. 20). We use the standard Dirac notation, wherein this state vector is denoted by a "ket" $|\psi\rangle \in \mathcal{H}$ and linear forms (functionals) on $\mathcal{H}$ are denoted by a "bra" $\langle\phi|$. For simplicity we will focus on finite dimensional Hilbert spaces,[2] with the occasional remark about $L^2(\mathbb{R}, dx)$ [which is infinite but separable; see remark (ii)]. The inner product between two state vectors, $|\phi\rangle$ with $|\psi\rangle$, is then given by a corresponding form $\langle\phi|$ (as provided by the Riesz representation theorem for continuous linear maps) acting on $|\psi\rangle$, which yields a complex number, the "bracket" $\langle\phi|\psi\rangle \in \mathbb{C}$, that quantifies how similar (linearly dependent) the states are. In particular, $\langle\phi|\psi\rangle$ can be understood as the projection of $|\psi\rangle$ onto $|\phi\rangle$. These state vectors will be our main objects of study and our task will be to understand and develop methods for controlling how they evolve. Thus, we must study their dynamics, which are governed by the Schrödinger equation:

$$i\hbar\frac{d}{dt}|\psi(t)\rangle = H(t)|\psi(t)\rangle, \tag{1.1}$$

[2]This allows us to avoid subtleties with infinite-dimensional spaces, such as the differences between Hermitian and self-adjoint operators [21]. Moreover, the effective systems we end up working with, and certainly those modeled on a computer, are all finite dimensional.

where $H(t)$ is the Hamiltonian operator of the system(s) under consideration. Here we include the possibility that H may depend on time due to the system exchanging energy with external influences, though, for a closed system, it is a constant of the motion. In Ch. II we will rehearse well-established and standard approaches for understanding light-matter interaction to motivate a particular Hamiltonian that will serve as the starting point of Chs. III and IV.

More generally, any physical observable, $\mathcal{O}$, in quantum mechanics (of which the Hamiltonian is an important example) is represented by a linear, Hermitian ($\mathcal{O} = \mathcal{O}^\dagger$) operator on $\mathcal{H}$. As is standard, a superscript $\dagger$ denotes the Hermitian conjugate of an operator, defined via $\langle\phi|\mathcal{O}|\psi\rangle^* = \langle\psi|\mathcal{O}^\dagger|\phi\rangle$, with $*$ denoting the complex conjugate. In a finite dimensional space, the spectrum of $\mathcal{O}$ is a set of real eigenvalues, $\{o_n\}$, corresponding to the possible results when measuring said observable. Upon measurement of $\mathcal{O}$, the state immediately before measurement $|\psi\rangle$ *collapses* to one of $\mathcal{O}$'s eigenvectors $|o_n\rangle$ (i.e., $|\psi\rangle \to |o_n\rangle$), defined as $\mathcal{O}|o_n\rangle = o_n|o_n\rangle$, with the measurement outcome then being o_n. The probability of outcome n is given by the Born rule to be

$$P_n = \text{Prob}(o_n) = |\langle o_n|\psi\rangle|^2. \tag{1.2}$$

As something (namely, one of the outcomes) must occur, these probabilities must add up to one, $\sum_n P_n = 1$. Moreover, the eigenvectors of $\mathcal{O}$ form a complete, orthonormal basis that can be used to resolve the identity:

$$\sum_n |o_n\rangle\langle o_n| = \mathbb{1}. \tag{1.3}$$

Thus, both $\mathcal{O}$ and states $|\psi\rangle$ (taken to be normalized, $\langle\psi|\psi\rangle = 1$) can be expanded in terms of this eigenbasis, namely,

$$\mathcal{O} = \sum_n o_n \, |o_n\rangle\langle o_n| \tag{1.4}$$

and

$$|\psi\rangle = \sum_n c_n |o_n\rangle \tag{1.5}$$

with

$$c_n \equiv \langle o_n|\psi\rangle \in \mathbb{C} \tag{1.6}$$

the *amplitude* for $|\psi\rangle$ to be in basis state $|o_n\rangle$. The average or expected value of the random measurement outcome is thus given by

$$\langle\mathcal{O}\rangle = \sum_n P_n o_n = \langle\psi|\mathcal{O}|\psi\rangle \tag{1.7}$$

and higher order moments can be computed similarly (for bounded operators).

Remarks:

(i) In the style of Ref. 22, we will occasionally include notable but somewhat tangential lines of thought at the end of a subsection, denoted as "remarks."

(ii) When $\mathcal{H}$ has a finite or countably infinite, orthonormal basis (called $\mathcal{H}$ being separable), as is almost always the case in physics, its elements, kets $\{|\psi\rangle \in \mathcal{H}\}$, can be identified as column vectors represented in said basis. Similarly, bras can be identified as row vectors (equal to the conjugate transpose of their corresponding ket) and linear operators $\mathcal{O}$ on $\mathcal{H}$ then admit a matrix representation.

(iii) The spectral theorem guarantees the existence of an eigenbasis of $\mathcal{O}$, even for unbounded operators. However, for infinite-dimensional Hilbert spaces, $\mathcal{H}$, some of the vectors in the eigenbasis of $\mathcal{O}$ may lie outside $\mathcal{H}$ and are so-deemed generalized eigenvectors. For instance, the eigenvectors of the position operator $\hat{x}$ are not vectors in Hilbert space, $|x\rangle \notin \mathcal{H} = L^2(\mathbb{R})$, yet expansions like $|\psi\rangle = \int dx \psi(x)|x\rangle$ (and similarly for the momentum operator $\hat{p}$) can be formalized in the context of a rigged Hilbert space (via the Gelfand-Maurin theorem) [23].

(iv) Here we are working in the Schrödinger picture, where we focus on the dynamics of states $|\psi(t)\rangle$, see Eq. (1.1), with the operators $\mathcal{O}$ either not evolving or having their dynamics fixed, e.g., by external controls, $\mathcal{O} = \mathcal{O}_S(t)$. However, one can also view the observables as the dynamical objects of the theory, $\mathcal{O}(t)$, with the states not evolving—this is called the Heisenberg picture. Therein, the Heisenberg operators, $\mathcal{O}_H(t)$, governed by Hamiltonian H, evolve according to the Heisenberg equation

$$i\hbar\dot{\mathcal{O}}_H = [\mathcal{O}_H, H] + i\hbar\partial_t\mathcal{O}_S(t), \tag{1.8}$$

where the last term accounts for the possibility of $\mathcal{O}$ having some externally imposed dynamics in Schrödinger picture. The subscripts S and H denote whether the operator is being considered in the Schrödinger or Heisenberg picture, respectively. In the subsequent chapters, we will often move between these pictures (as well as an intermediate picture called the interaction picture; see §2.2.4) to facilitate calculations and make different results manifest.

(v) Note that sometimes it is useful to generalize the concept of a 'pure' state vector, $|\psi\rangle$, to a so-called 'mixed state' density matrix, ρ. We will briefly consider the

dynamics of such mixed states in §3.4, though the basic details are left to textbook treatments (e.g., see section 2.4 of Ref. 7).

(vi) The above type of measurements, called projective measurements, are quite drastic in that they fully collapse the state onto the eigenvector corresponding to the measurement outcome. A more general class of measurements can be represented by positive operator-valued measures (POVMs) and can be used to describe continuous weak measurements [24]. A POVM is a set of positive operators $\{\Omega_n\}$ that sum to the identity, $\sum_n \Omega_n = \mathbb{1}$ (see App. A.1.1). [So clearly projective measurements are a subclass of POVMs subject to the extra condition $\mathrm{Tr}(\Omega_n \Omega_{n'}) = \delta_{nn'}$; see Eq. (1.3)].

1.3.4 Few-level approximation

Closed, non-relativistic quantum systems can be described, quite generically, by a Hamiltonian of the following form [see Eq. (2.20)]:

$$H_{\mathrm{sys}} = \sum_n \frac{p_n^2}{2m_n} + V(\{\boldsymbol{r}_n\}), \tag{1.9}$$

where the first term is the kinetic energy of a collection of particles with momenta p_n and mass m_n, and V is the Coulomb potential energy of all the particles, which depends on their positions, $\{\boldsymbol{r}_n\}$ (time-dependent external fields are excluded for now). Such a description, though written in a simple form, encodes a lot of DOFs, only a few of which we want to analyze and control. As an emblematic example, we note that even for the simplest composite quantum system—a hydrogen atom consisting of only two particles, a single proton (the nucleus) and an electron bound to it via the Coulomb interaction—understanding this full Hamiltonian, though interesting and

fundamental, is no small task. Accordingly, if we are only concerned with certain transitions or particular DOFs, we should not have to write down a model for all the extraneous ones.

Such a simplified model can be understood by expressing the system Hamiltonian in its energy eigenbasis, i.e., diagonalizing it: $H_{\text{sys}} = \sum_n E_n \, |n\rangle\langle n|$, where $\{|n\rangle\}$ are the energy eigenstates with corresponding eigenenergies $\{E_n\}$. Then suppose that, as is often the case in QIS, one is interested in only a small number of these energy states (or levels). If these levels are well-chosen, one can drive resonant interactions with them specifically, with minimal disturbance to the other levels. In such a case, it is only the levels of interest that exhibit non-trivial dynamics, and hence all the extraneous levels can be omitted from H_{sys}, which has the benefit of taking the state from living in a typically infinite-dimensional Hilbert space to a finite subspace [25].

Here we will focus on the case of an effective two-level system, which might constitute an isolated qubit, in the state

$$|q\rangle = c_g|g\rangle + c_e|e\rangle \tag{1.10}$$

(assumed to be pure here), which is a superposition of a ground state $|g\rangle$ and excited state $|e\rangle$, with the amplitudes subject to the normalization condition $|c_g|^2 + |c_e|^2 = 1$. If other levels become relevant then they too should be included and this discussion naturally generalizes in such cases. The identity operator for this effective system reduces from $\mathbb{1} = \sum_n |n\rangle\langle n|$ for the full Hamiltonian to

$$\mathbb{1}_2 = |g\rangle\langle g| + |e\rangle\langle e| \, . \tag{1.11}$$

The corresponding Hamiltonian is given by projecting H_{sys} onto the subspace spanned by $|g\rangle$ and $|e\rangle$:

$$H'_{\text{sys}} = \mathbb{1}_2 H_{\text{sys}} \mathbb{1}_2 = E_g \, |g\rangle\langle g| + E_e \, |e\rangle\langle e| \, . \tag{1.12}$$

Choosing an energy offset such the ground state energy is zero, the reduced Hamiltonian is

$$H^{(\text{red})}_{\text{sys}} = H'_{\text{sys}} - E_g \mathbb{1}_2 = \hbar\omega_{eg} \, |e\rangle\langle e| \tag{1.13}$$

with $\omega_{eg} = (E_e - E_g)/\hbar$ the resonant-transition frequency. Every qubit has a specific energy scale, $\hbar\omega_{eg}$, and likewise a certain timescale for interacting with it, t_s, where t_s^{-1} is a coupling parameter that depends on how the qubit is being interacted with. For instance, a lone qubit will precess with angular frequency $t_s^{-1} = \omega_{eg}$ (in the Schrödinger picture). When driven, this timescale depends on the strength of the dominant interaction(s), e.g., when driven by a resonant laser field, t_s^{-1} is of order the Rabi frequency (see §2.2.4), which is proportional to the strength of the driving electric field. Similarly, the natural linewidths of the system will impact t_s^{-1}, this includes spontaneous emission rates as well as cavity or resonator decay rates (as applicable).

Thus, quantum systems pick out certain privileged interactions that match their intrinsic energy and time scales. Our goal is to find and leverage these privileged interactions to arrive at simple effective descriptions, such as the qubit, where the multitude of system specific complications (additional states, couplings to other DOFs, etc.) are well encapsulated by a few parameters, i.e., ω_{eg} and t_s. It is worth reemphasizing that experimentalists go through a lot of effort to realize such effective systems (see §1.3.1). For instance, material systems often exhibit degeneracies, where quantum mechanically distinct states have the same energies. In such cases,

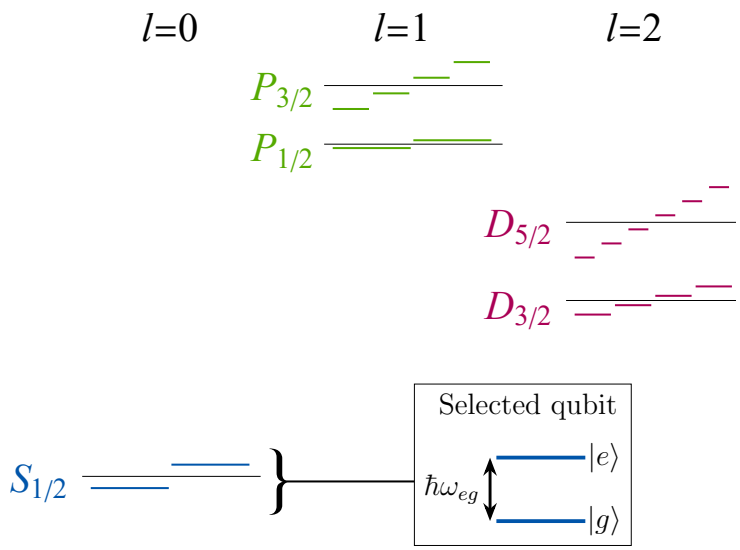

FIGURE 1.1. Selecting a qubit out of the "zoo" of energy states available to the valence electron in a typical monovalent ion (see text for details). A typical low-lying energy state configuration, including fine structure and Zeeman sub-levels, is shown (not to scale). By applying a static magnetic field, the degeneracies of the Zeeman sub-levels (indicated via the gray lines) are lifted. With the energy states separated, the experimentalist can single out two states to encode the state of a qubit by selecting an appropriate drive (laser or RF pulse) to resonantly drive the corresponding transition. The inset illustrates a common selection, where two ground state levels, $|e\rangle$ and $|g\rangle$, with energy difference $\hbar\omega_{eg}$ are used to encode the qubit. Such energy level diagrams are common, though we note that this figure was motivated in part by Fig. 3 of Ref. 26.

experimentalists can still control the "zoo of states" by applying external fields to controllably shift the energy levels, thereby "lifting" such degeneracies, so that particular states can be addressed (e.g., by leveraging the Zeeman effect and ac Stark shifts, while heeding selection rules).

We provide an example of this effort in Fig. 1.1, which illustrates the selection of a particular qubit out of a zoo of possible states. As is common in QIP, we focus on monovalent atoms (both in this figure and largely throughout this dissertation, e.g., see Table 4.1), wherein the energy states of the single valence electron can be used as a qubit that is relatively shielded from the inner electronic structure of the

stable, completed valence band. This includes both neutral alkali atoms, like rubidium (Rb) and cesium (Cs), as well as singly ionized alkaline-earth atoms, like calcium ions (Ca^+), that are commonly used for neutral atom and trapped ion quantum computing, respectively [26–28]. The figure illustrates the lowest-lying energy states of the valence electron for such ions, including the fine structure, as labeled in standard spectroscopic notation.[3] The energy level structure will differ for other systems but the overall idea is the same, e.g., see Extended Data Fig. 1 (b) of Ref. 28 for the level structure of ^{8}7Rb. For simplicity, we focus on the Zeeman magnetic sub-levels (as is valid for atoms with zero nuclear spin, e.g., $^{40}Ca^+$), whose degeneracies are lifted by applying a static magnetic field. Meanwhile, isotopes with non-zero nuclear spin have additional hyperfine structure that further complicate the zoo of states, yet nonetheless can be tamed in a similar fashion. This energy diagram is meant to highlight that, while a lot of work goes into properly understanding the energy structure of atoms and other quantum systems, from a phenomenological point of view, we are afforded the luxury of simply considering effective, few-level systems (like qubits) whose actual, "dressed" energies are handed to us by experiment.[4]

1.3.5 Long-wavelength approximation

In quantum-information processing, the material quantum systems used, e.g., to encode qubits, are often very small compared to the wavelength, λ, of the light

[3]In this spectroscopic (Russell–Saunders) notation, atomic states are denoted via, $^{2S+1}L_J$, where $\boldsymbol{L}$ and $\boldsymbol{J}$ are the total orbital and fine-structure angular momentum quantum numbers, respectively and the spin quantum number label omitted as it ($S = 1/2$) is common to all levels.

[4]This is why our descriptions of the energy level structure are somewhat terse. Phenomenologically, we need not be too concerned with the detailed energy level structure of a system, including their bare values and how they shift when accounting for details such as fine and hyperfine structure as well as shifts due to external fields. For details, see textbook treatments (e.g., chapter 7 of Ref. 20) and review articles [26, 27].

interacting with them. In particular, it is typical that $kr_s \ll 1$, where $k = 2\pi/\lambda$ is the wavevector of light driving a system of characteristic length scale r_s, i.e., the scale over which its wavefunction is appreciable. Thus, in such cases, the field, which varies spatially as $e^{i\boldsymbol{k}\cdot\boldsymbol{r}}$, can be well regarded as a constant on the length scale of the quantum system as is illustrated in Fig. 1.2. Such an expansion of the field for small kr_s is aptly referred to as the long-wavelength approximation (LWA), but also goes by the "dipole approximation" as it allows one to single out the dipole interaction as the dominant light-matter interaction from a more general description (see App. C.3.2). Going to the next order, regarding the field as linearly varying over the length scale of the system, one obtains the electric quadrupole and spin-free magnetic dipole interactions as well, which are suppressed by a factor of order kr_s relative to electric dipole interactions. Thus, under the LWA, there is no need to treat high-frequency (short-wavelength) modes that will remain unoccupied. Hence the LWA serves to reduce the number of DOFs under consideration.

For AMO systems, the characteristic length scale of atoms and ions is on the order of a few Angstrom (10^{-10} m), while visible light has a wavelength of 400–700 nm such that $kr_s \approx 10^{-3}$–10^{-2}. This situation is depicted in Fig. 1.2 (a), where an atom is pictured at an extremum (antinode) of the field as is appropriate for dipole transitions, which depend on the field amplitude itself. Meanwhile, quadrupole transitions depend on the gradient of the field and therefore atoms should be positioned where the field's spatial derivatives are strongest. For the sinusoidal wave considered here, this maximum variation occurs at the field nodes and is $kr_s E_{\max}$ over a distance of r_s (for $kr_s \ll 1$).

For superconducting quantum systems, the LWA often still holds as although the system is much larger than an atom, so is the wavelength of the electromagnetic

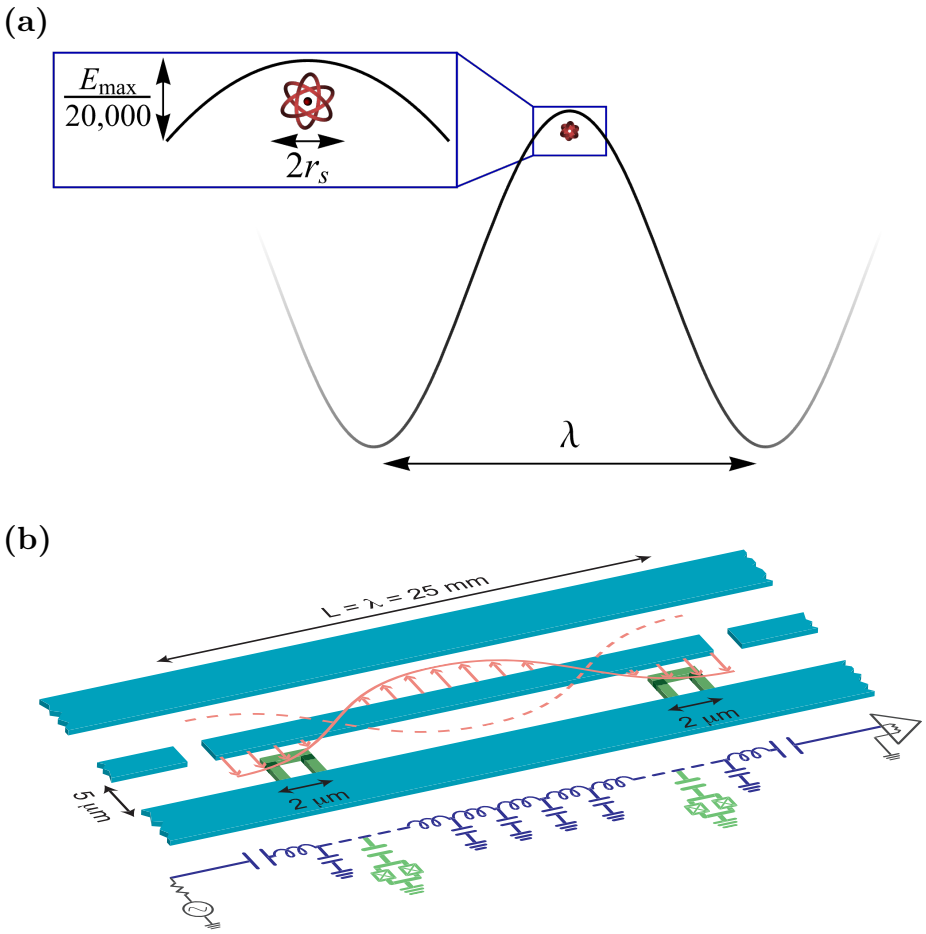

FIGURE 1.2. Visualizing the long-wavelength approximation. A sinusoidal electric field with amplitude $E_{\max}$, wavelength λ, and wavevector $k = 2\pi/\lambda$ interacts with a quantum system of size $r_s \ll \lambda$. **(a)** Illustration for AMO systems with the system visualized as a cartoon atom. The inset highlights the variation in the electric field near its maximum over the length scale of the atom. Specifically, for $kr_s = 2 \cdot 10^{-3}$ (which is the case for the D_2 transition in ^{87}Rb with $\lambda = 780$ nm and atomic radius $r_s \approx 0.25$ nm), the field drops by $5 \cdot 10^{-5} E_{\max}$ over a distance of $5r_s$ from the maximum as illustrated. **(b)** Illustration for superconducting quantum circuit example with $kr_s = 5 \cdot 10^{-4}$ (see text). The shown system (not to scale) consists of two superconducting charge qubits (green) coplanarly fabricated in a 1D transmission line resonator (light blue), which resonator as a "quantum bus" that mediates the transfer of excitations between the qubits when driven by appropriate microwave fields. Reprinted Figure 1 with permission from Ref. 29 by authors Blais and Wallraff, copyright 2007 by the American Physical Society.

radiation driving it. Note that in such contexts, the LWA is tantamount to what is often referred to as the lumped-element model. As an example, Fig. 1.2 (b) depicts charge qubits, each with $r_s = 2$ μm, coupled to a microwave resonator supporting $\lambda = 25$ mm excitations (corresponding to a resonance frequency of $\omega_r = 12$ GHz) [29]. Thus, $kr_s = 5 \cdot 10^{-4}$ in this case, which is clearly consistent with the LWA. Note that other superconducting systems are generally larger than charge qubits, e.g., the prolific transmon qubit has a typical size of a few hundred micrometers (though there are efforts to miniaturize it [30]). Thus, as a concrete instance, suppose $r_s \approx 400$ μm and $\lambda \approx 6$ cm (for a typical $f = \omega/2\pi = 5$ GHz transition frequency), then $kr_s \approx 4 \cdot 10^{-2}$, which is larger than the previous cases but still sufficiently small for a consistent description under the LWA.

1.4 Photons

Light is fundamentally an undulation of the electromagnetic field. Just as the musician can pluck a string and play a note with a distinctive timbre as dictated by the combination of many pure frequency tones (the harmonics of the string), so too can the physicist pluck the electromagnetic field in a way so as to create photon wave packets as a superposition (linear combination) of many pure frequencies. The corresponding "harmonics" of light are the normal vibrational modes of the free electromagnetic field, as characterized by their wavevector $\boldsymbol{k}$ and polarization $\boldsymbol{\varepsilon}$ (vectors are denoted in bold), which correspond to the modes' direction of propagation and electric field. Quantumly, the excitation of such a normal mode is a monochromatic *photon* in mode $\{\boldsymbol{k}, \boldsymbol{\varepsilon}\}$. The addition and removal of such photons from the field can be understood in terms of the aptly named creation operator $a^\dagger_{\boldsymbol{\varepsilon}}(\boldsymbol{k})$ and annihilation operator $a_{\boldsymbol{\varepsilon}}(\boldsymbol{k})$, respectively. We will revisit these operators in more

detail in §2.2, for instance, showing how physical observables, like the electric and magnetic fields, can be written in terms of them.

When acting on the electromagnetic ground state called the vacuum $|\text{vac}\rangle$, which is the state with no photons in any mode, the creation operator $a^\dagger_{\boldsymbol{\varepsilon}}(\boldsymbol{k})$ gives a single photon with polarization $\boldsymbol{\varepsilon}$, $a^\dagger_{\boldsymbol{\varepsilon}}(\boldsymbol{k})|\text{vac}\rangle \equiv |1_{\boldsymbol{\varepsilon}}(\boldsymbol{k})\rangle$, that is completely localized in reciprocal space with wavevector $\boldsymbol{k}$ and hence is entirely delocalized in real space. Accordingly, is often useful and physically necessary to consider localized, and hence multi-mode, photon wave packets whose creation operators are given as superpositions over these monochromatic modes:

$$b^\dagger = \int d^3k \sum_{\boldsymbol{\varepsilon}} f_{\boldsymbol{\varepsilon}}(\boldsymbol{k}) a^\dagger_{\boldsymbol{\varepsilon}}(\boldsymbol{k}). \tag{1.14}$$

Note that as light is a transverse wave, for a given mode the polarization lies in the plane normal to $\boldsymbol{k}$. One can thus evaluate sums over polarization, $\sum_{\boldsymbol{\varepsilon}}$, using an orthonormal basis for this transverse plane: $\{\boldsymbol{\varepsilon}_1, \boldsymbol{\varepsilon}_2\}$ (called linear polarization vectors).

We will focus on the simpler (and often more useful) case, wherein the wave packets are confined to propagate in a single direction by a beam-like geometry (e.g., via a waveguide or optical fiber). We will also consider a fixed polarization (whose label we will omit), though this can easily be extended as necessary (see §2.3 and App. C.2.3). Then $\int d^3k \sum_{\boldsymbol{\varepsilon}} \to \frac{1}{A}\int dk$ in Eq. (1.14), where A is a characteristic transverse area dictated by the confining geometry (though its value will not be important here), and

after using $\omega = ck$ to change variables,[5] we obtain the frequency expansion

$$b^\dagger = \int d\omega\ \varphi(\omega) a^\dagger(\omega), \tag{1.15}$$

where we have defined $\varphi(\omega) := f(\omega/c)/(Ac)$, which can be understood as the spectral amplitude of a photon in the state $b^\dagger|\text{vac}\rangle$. Here $a^\dagger(\omega)$ creates [and $a(\omega)$ annihilates] a photon of frequency ω (with the polarization and transverse spatial degrees of freedom fixed). Due to the bosonic statistics of photons, these operators are subject to the commutation relations

$$[a(\omega), a^\dagger(\omega')] = \delta(\omega - \omega'). \tag{1.16}$$

Note that $a(\omega)$ and related quantities, like the commutator of Eq. (1.16), will never appear by themselves (in a physical quantity), they will always be integrated against a test function as in Eqs. (1.14) and (1.15) [21].

To be a true *single*-photon creation operator, $b^\dagger$ must satisfy the canonical commutation relation $[b, b^\dagger] = 1$, from Eqs. (1.15) and (1.16) we have

$$1 = [b, b^\dagger] = \int d\omega \int d\omega'\ \varphi^*(\omega)\varphi(\omega')[a(\omega), a^\dagger(\omega')] = \int d\omega\ |\varphi(\omega)|^2. \tag{1.17}$$

Thus, we see that the Hilbert space of single photons is the familiar space of square-integrable functions on the real line, $\mathcal{H} = L^2(\mathbb{R})$, e.g., the Hilbert space for a single particle moving in one dimension. This means, among other things, that single-

[5] Here we are abusing notation in a way that is standard but nonetheless worth mentioning. In considering a quasi-1D setup, say along the x-axis, we have $\boldsymbol{k} = k\hat{x}$, where this k is any real number. Clearly, a negative (positive) k corresponds to a leftward (rightward) propagating mode. Making the change of variables to $\omega = ck$, the frequency inherits the ability to be positive or negative, which may look strange at a glance as often $\omega_k \equiv c|\boldsymbol{k}| \geq 0$, but here ω's sign simply encodes the direction of propagation (as a remnant of the initial k-space expansion). This is why, for instance, the ω integral goes from $-\infty$ to ∞ in Eq. (1.15) and many subsequent expressions.

photon wave packets can be expanded in terms of bases of $L^2(\mathbb{R})$, like the Hermite–Gaussian mode functions (corresponding to the energy eigenbasis of a simple harmonic potential).

1.4.1 Visualizing single-photon wave packets

One can nicely visualize a massive quantum mechanical particle and its evolution using its position-space wavefunction. When trying to do this for photons, however, one encounters subtleties because, as a zero rest mass particle, photons cannot be strictly localized (they are inherently relativistic and have no position observable) [31]. Nonetheless, the electromagnetic field operators can be expanded in real space and can be characterized by temporal-mode functions[6] [32]

$$v_j(x,t) = i \int \omega \sqrt{\frac{\hbar|\omega|}{4\pi\varepsilon_0}} \varphi_j(\omega) e^{-i(|\omega|t - \omega x/c)}, \tag{1.18}$$

where $\{\varphi_j(\omega)\}$ is a basis for $L^2(\mathbb{R})$ (we are again assuming a quasi-1D setup aligned along the x axis). Note that if, as is typically the case,[7] $\varphi(\omega)$ has a relatively narrow bandwidth, B_φ, compared to its central frequency, ω_0, then $v(x,t)$ is essentially the

[6]Our 2π factors are chosen to be consistent with our Fourier transform conventions, and thus differ from Ref. 32. Further, heed the absolute values in the definition of v_j in Eq. (1.18). They can be understood, in view of footnote 5, as any proper angular frequencies being given by $|\omega| = c|\boldsymbol{k}|$, whereas effective 1D wavevectors are given by $\omega = ck_x$ (for $\boldsymbol{k} = k_x\hat{x}$). However, typically one considers wave packets that propagate in only a single direction (and not its antiparallel counterpart), so $\varphi(\omega < 0) \equiv 0$, either effectively (e.g., due to exponentially suppressed asymptotics for $\omega < 0$) or by fiat, in which case $|\omega|$ can safely be replaced by ω. For instance, in Fig. 1.3, $\varphi(\omega)$ has small contributions from $\omega < 0$, corresponding to a left propagating part of the wave packet. In particular, the proportion of the wave packet propagating to the left is $\mathrm{erfc}(\omega_0/\sigma)/2$, which even in (b) is only $8 \cdot 10^{-7}\%$. Accordingly in (b) and (c), we are technically only plotting the right propagating part of these temporal modes.

[7]For instance, in optical systems one has carrier frequencies, $\omega_0/2\pi$, on the order of hundreds of THz, whereas the single-photon bandwidth, $B_\varphi/2\pi$, is typically no more than a few THz (for which $\omega_0/B_\varphi \sim 100$). Meanwhile, narrow bandwidth optical photons, $B_\varphi/2\pi \sim$kHz–GHz, can be produced by high-quality single-photon sources, e.g., an atom in a cavity, for which ω_0/B_φ can vary from thousands to billions.

Fourier transform of $\varphi(\omega)$,

$$\tilde{\varphi}(t) = \mathcal{F}[\varphi(\omega)](t) := \int \frac{d\omega}{\sqrt{2\pi}} \varphi(\omega) e^{-i\omega t}, \tag{1.19}$$

namely,

$$v(t_-) \approx v_0 \tilde{\varphi}(t_-), \tag{1.20}$$

up to corrections of order B_φ/ω_0, with $v_0 = i\sqrt{\frac{\hbar\omega_0}{2\varepsilon_0}}$ and $t_- \equiv t - x/c$.

For single photons, $v_j(x,t)$ can *loosely* be thought of as a position space wave function, its precise role can be clarified within the context of input-output theory (see §3.5.3). We use this rough notion to motivate the visualization of single photon wave packets in both the frequency and time domains in Fig. 1.3. Namely, we plot a Gaussian spectral amplitude function

$$\varphi_G(\omega; \omega_0, \sigma) := N_\sigma \exp\left[-\frac{1}{2}\left(\frac{\omega - \omega_0}{\sigma}\right)^2\right], \tag{1.21}$$

where the standard deviation, σ, is comparable to the bandwidth B_{φ_G} and $N_\sigma = 1/\sqrt{\sqrt{\pi}\sigma}$ a normalization constant chosen so that Eq. (1.17) holds. As indicated, the relative widths ω_0/σ in subplots (b) and (c) are 4 and 20, respectively. These relative widths are much smaller than typical cases with $\omega_0 \gg \sigma$. This is done for illustration purposes to show that, even for modest bandwidths, v is effectively proportional to $\tilde{\varphi}$ [see Eq. (1.20)] and the underlying oscillations quickly become cumbersome both for visualization purposes [see (c)] and mathematically. Accordingly, it is often convenient to factor out the fast-oscillating phase factor, $e^{-i\omega_0 t}$, and work with the resulting slowly-varying envelope function (see the interaction picture introduced in §2.2.4).

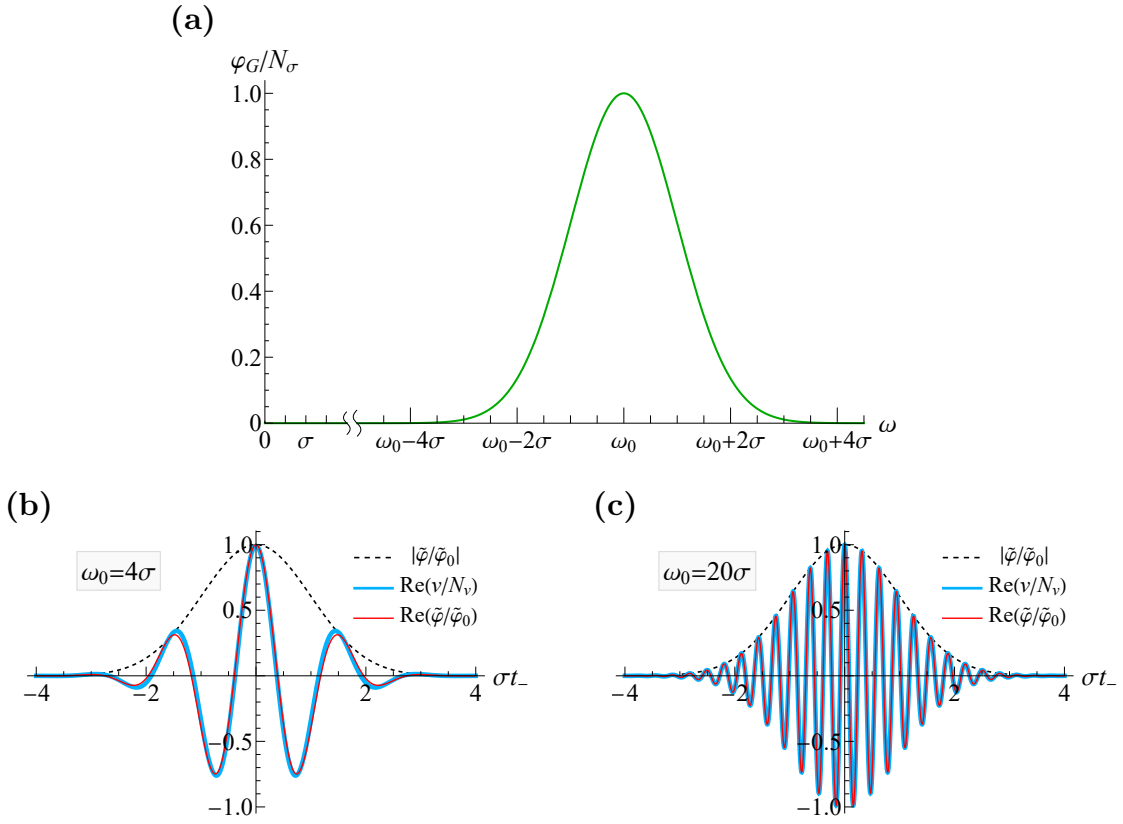

FIGURE 1.3. Visualizing single-photon wave packets via their spectral amplitudes and corresponding temporal modes. **(a)** Plot of a Gaussian spectral amplitude, φ_G, of Eq. (1.21) (green). The discontinuity in the ω-axis is used to indicate that one typically considers $\omega_0 \gg \sigma$. **(b)**–**(c)** Plots of the real parts of the temporal-mode function $v(t_-)$ (thick blue) and Fourier transform $\tilde{\varphi}(t_-)$ (thin overlaid red) corresponding to φ_G, along with their Gaussian envelope (black dashed). The exact form of v is not particularly illuminating, yet we do note that $\tilde{\varphi}(t) = \tilde{\varphi}_0 e^{-i\omega_0 t} e^{-(\sigma t)^2/2}$ here. These functions have all been scaled to have unit maxima; see the legends, with $\tilde{\varphi}_0 = \sqrt{\sigma/2}/\pi^{3/4}$ and $N_v = \tilde{\varphi}_0 v_0$, where v_0 was introduced in Eq. (1.20).

1.5 Hybrid quantum state transfer

In this dissertation, we primarily focus on the task of hybrid quantum state transfer. This task and its motivations are introduced below and extensively analyzed in Chs. III and IV.

1.5.1 The task itself

We analyze the fundamental quantum communication task of reliably transferring the quantum state between remote (spatially separated) quantum systems that are heterogeneous (operating on different energy and time scales). We call this *hybrid* quantum state transfer (QST), to emphasize that we consider connecting heterogeneous systems, whereas the consideration of QST between identical systems is more standard [1]. Being able to interconnect quantum devices in this way is crucial to the development of hybridized and distributed quantum systems for communication, computing, and networking, where the quantum information could be sent between different systems to leverage their individual strengths.

We will focus on the fundamental primitive of transferring the state of a qubit between two systems (labeled as $j = 1, 2$), though the ideas we present could naturally be extended to transferring other states (several qubits, qutrits, etc.) or used as a subroutine in connecting several systems. We assume the state of each qubit is encoded in a long-lived effective two-level system with ground state $|g_j\rangle$ and excited state $|e_j\rangle$ (see §1.3.3 for an overview of quantum mechanics). We suppose that system 1 starts in an arbitrary superposition, $|\psi_1\rangle = c_g|g_1\rangle + c_e|e_1\rangle$, which is the state we want to transfer, and that system 2 starts in its ground state, $|g_2\rangle$. Thus, we want to implement the transformation

$$[\underbrace{c_g|g_1\rangle + c_e|e_1\rangle}_{|\psi_1\rangle}] \otimes |g_2\rangle \longmapsto |g_1\rangle \otimes [\underbrace{c_g|g_2\rangle + c_e|e_2\rangle}_{|\psi_2\rangle}]. \tag{1.22}$$

A standard way to accomplish this transfer for identical (or similar) systems makes use of photons as intermediate quantum information carriers (sometimes called "flying

qubits") that are emitted by system 1, propagate through a quantum communication channel, and are absorbed by system 2 (see Fig. 1.4) [1, 33–35]. Thus, our task, at least in part, will be to understand how photon wave packets (introduced in §1.4 below) interact with material quantum systems. This will require a description of light-matter interactions that will be developed in Ch. II. We will consider systems for which control drives such as laser pulses can be used to deterministically induce the emission and absorption of single photons (see §3.5 for a concrete prescription with three-level Λ-type systems in cavities). In such a scenario (with homogeneous systems), as shown in Ref. 1, one can eliminate the intermediate photonic degrees of freedom (DOFs) and obtain an effective description in which the two systems are directly coupled (see Ch. III). This is a, perhaps less obvious, manifestation of how, in well-controlled quantum systems, extraneous DOFs can be eliminated to obtain a simpler effective description (as discussed in §1.3).

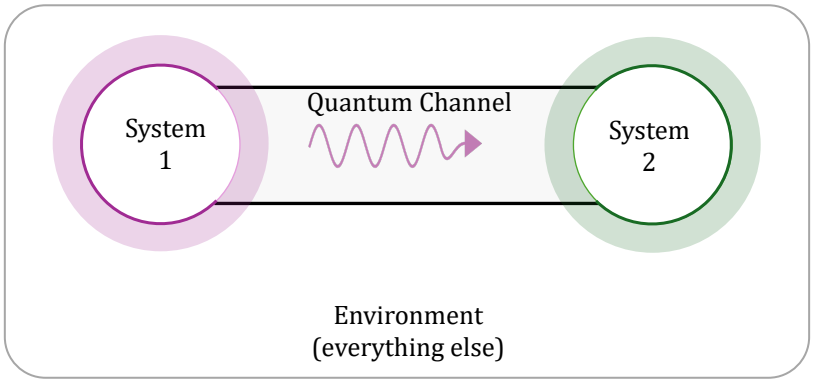

FIGURE 1.4. Schematic depiction of the primary setup considered in this dissertation: two systems that can each controllably emit or absorb photons are coupled together via an intermediate channel. The purple wiggle indicates the electromagnetic field state of the channel, which for QST should correspond to a photon wave packet carrying quantum information between the systems (for hybrid QST, we will also consider a unitary transformation to the photon as part of the channel; see §3.3). The systems and channel will never be perfectly isolated, so there will be undesired couplings to a larger environment. These couplings can be made small so we will neglect them for now, returning to them in Ch. IV.

It is worth noting that although the coupling to the environment or bath is ruinous in some cases (e.g., decoherence in a quantum computation), herein the coupling to the bath is crucial for allowing quantum information to be transferred between the systems via an intermediate photonic state. Accordingly, we will often refer to the intermediate bath a channel or transmission line, meanwhile any other undesired degrees of freedom the systems or channel couple to will be deemed the environment.

However, in the hybrid case we consider, the photon emitted by system 1 is the *wrong* one to be absorbed by system 2, namely, it will only extremely weakly interact with system 2—because it operates on different energy and time scales (i.e., the systems have different resonance frequencies $\omega_1 \neq \omega_2$ and decay rates $\gamma_1 \neq \gamma_2$)—leading to a negligibly low chance of successful QST for heterogeneous systems. We are thus compelled to consider using a unitary transformation (perhaps implemented using nonlinear optics) to change this wrong photon wave packet into the *right* one to be absorbed by system 2. One method for guaranteeing, in principle, that the receiving system 2 absorbs the intermediate photon is to transform the photon's time-frequency shape into the time-inverse of what the receiver would itself emit [36, 37]. Thus, the transformation should time-reverse the photon wave packet and shift its resonance frequency and decay rate to those of system 2 [37–40]. In our work, we study the effective description that results when we thus manipulate the intermediate photon and thereafter eliminate the corresponding DOFs (see Ch. III). The effective description we ultimately obtain corresponds to the receiving system 2 effectively being directly coupled to, and driven by, a fictitious system 1 that evolves backwards in time with a different decay rate and resonance frequency.

1.5.2 Background: Distributed and hybrid quantum technologies

QST and the task of remote entanglement generation (REG), see §1.5.3, are key parts of many quantum communications and networking protocols. Thus, before discussing their hybrid counterparts, we will discuss quantum networks more generally, which are scaled-up counterparts of bipartite quantum communication systems to contain more parties. The culmination of large scale quantum networking is envisaged as a "quantum internet," analogous to the internet, except for the distribution of quantum information across the globe, e.g., via a network of interconnected quantum computers [33]. The quantum internet is envisioned to allow the implementation of various quantum communication, computation, and measurement (sensing) tasks that improve upon their classical counterparts [33]. These tasks include securely sending information between more parties over longer distances, better imaging and sensing [41], and distributed quantum computation.

Scaling the underlying networks to connect a larger numbers of quantum processor systems, often referred to as nodes in the context of quantum communication, improving these processors, and controlling their robustness against noise are among important current practical issues [42, 43]. The fundamental building blocks of these networks are the nodes themselves and the quantum transmission lines (also called quantum channels) that serve as the network edges. Such an edge links together two nodes so that quantum information, say the state of a qubit, can be sent between them at will. These nodes may range from simple devices operating on small numbers of qubits to large-scale quantum computers. When envisaging a large quantum network, or ultimately the quantum internet, many different implementations of an edge will be needed, e.g., to reliably connect close-by units comprising a single computation node, different types of nodes, as well as distant nodes. A schematic representation

of how such a pair of linked nodes might fit into a larger quantum network is given in Fig. 1.5.

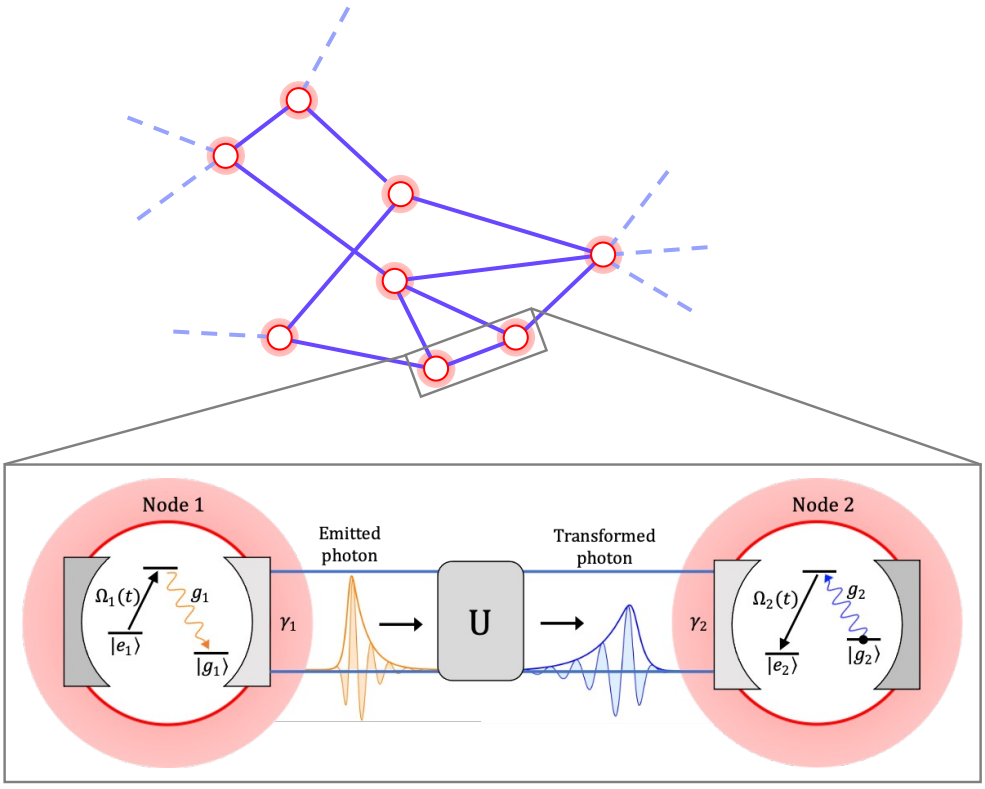

FIGURE 1.5. Subgraph representing part of a quantum network (above) with a zoomed in focus (below) on two nodes (red points) and the quantum channel (blue edges) linking them, along which our QST scheme is implemented (implementation details and symbol definitions are introduced in Ch. III). The graph structure is only for illustration purposes, to show how our scheme can fit into the bigger picture of quantum networking. The dashed lines indicate potential continuations of the network to other nodes. The lower image comes from our work in Ref. 4, and is modified from figures of Refs. 1 and 3.

Two promising research avenues for the scalability of quantum networks are in the development of *distributed* and *hybrid* quantum communication and computation technologies. The utility of distributed quantum technologies lies in the likely scenario that it is easier to connect many high-functioning modestly sized, often homogeneous,

devices (which have been demonstrated), using quantum effects like entanglement as a resource, than to scale a single device to have the same net processing power [44–51].

A complementary means of scaling quantum networks is by developing a hybrid quantum architecture, where either different types of (i) qubits or (ii) nodes are connected so that tasks can be delegated so as to leverage the strengths of a given type of qubit or node [52–57].

Case (i) can be envisaged as a hybrid device that uses different kinds of qubits for different purposes. For instance, using separate types of qubits for local logic operations and for interfacing with quantum channels, which would allow for communication between nodes with minimal disruption to local computation or storage processes [58–63]. In case (ii), heterogeneous nodes (or smaller intranodal units), that are based on different quantum technologies, are connected to form the elementary unit of a hybrid quantum network (or node). Such hybridization would be valuable in making more powerful, large-scale nodes, such as a node that integrates solid-state computation units leveraging fast nanosecond gates (at the expense of relatively short microsecond coherence times for both depolarization and dephasing) [64–67] with atom-based memory units with long coherence times on the order of milliseconds (or seconds for ions, though they can be significantly longer [68], typically limited by dephasing times) at the expense of slower microsecond gate times [26, 69, 70] for hybrid quantum computation [71–73].[8]

[8]Exact times vary wildly between the many different implementations of a solid-state or atom-based qubit and even within a given type of qubit. For instance, the coherence and gate times of semiconductor-spin qubits (a type of solid-state qubit) vary significantly depending on the implementation, say whether the qubits used are encoded in ensembles or single-spins, nuclear or electronic spins, etc. [63, 67]. Also note that in neutral atom quantum computing with Rydberg qubits, the gate and coherence times tend to be longer than for ions yet still much shorter than superconducting circuits [70]. See Ref. 73 for one specific careful comparison of quantum computations on 5 superconducting transmon qubits versus 5 trapped ion qubits. Our point here is to indicate the often present large difference in the orders of magnitude for gate and coherence times in these technologies.

More broadly, realizing such hybrid links would increase the connectivity of quantum networks. Especially as different technologies (trapped ions, superconducting circuits, etc.) become better-established as platforms for qubit implementation, how to interface them is an important question [57, 74–82].

1.5.3 Quantum state versus entanglement transfer

Note that although we tend to focus on just the emitting and receiving systems (e.g., see Fig. 1.5), we are generally concerned with nodes hosting multiple emitters, each encoding the state of a qubit, that can process quantum information locally. That is, nodes which are themselves (modestly sized) quantum computers. Then, QST serves to connect these nodes—effectively creating a larger distributed quantum computer—and, crucially, it maps any entanglement with the sent qubit to the receiver and leaves the entanglement with other qubits unchanged [1]. Thus, the QST protocol we consider can easily be mapped on to one for REG, as visualized in Fig. 1.6. The basic idea is to locally prepare a Bell-state at node 1, say $|\Phi^+_{1',1}\rangle = \frac{1}{\sqrt{2}}\left(|g'_1 g_1\rangle + |e'_1 e_1\rangle\right)$, and then transfer the state of emitter $1'$ to 2. From Eq. (1.22), with the receiving system initialized in $|g_2\rangle$, one then finds (henceforth omitted tensor product signs, $\otimes$, as is standard)

$$|\Phi^+_{1',1}\rangle|g_2\rangle \overset{\text{QST}}{\longmapsto} \frac{|g'_1 g_1 g_2\rangle + |g'_1 e_1 e_2\rangle}{\sqrt{2}} = |g'_1\rangle|\Phi^+_{1,2}\rangle, \tag{1.23}$$

so the QST scheme can map local (intranodal) entanglement to remote (internodal) entanglement. Meanwhile, remote entanglement can be used to implement QST via "quantum teleportation," which is a standard, albeit somewhat fallaciously named, QIP protocol. It leverages remote entanglement, often in the from of a Bell pair,

along with a certain quantum measurement and the transfer of classical information, to achieve QST; see the original article [83] as well as Ref. 84 and the references therein for details. Thus, one can map between QST and REG.

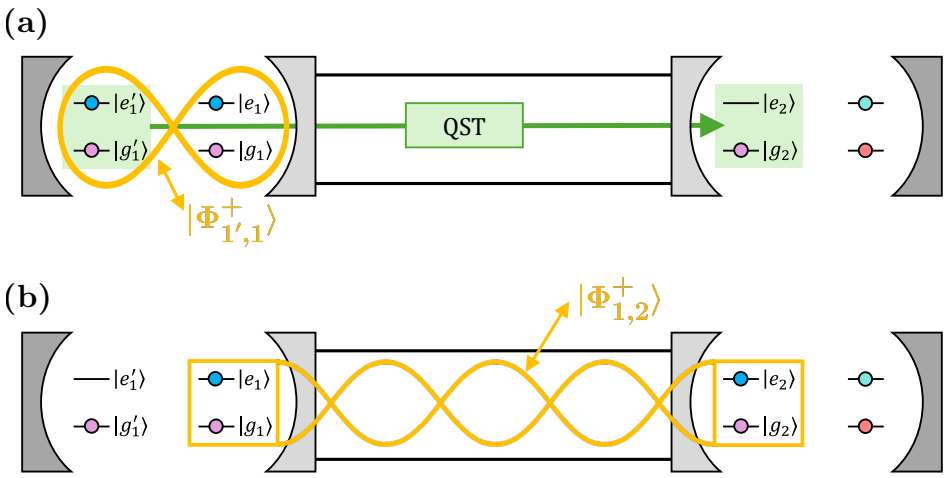

FIGURE 1.6. By transferring half of an entangled Bell-pair at node 1 (left) to node 2 (right), the QST protocol generates remote entanglement between the two nodes. **(a)** A maximally entangled Bell state, $|\Phi^+_{1',1}\rangle$, is prepared at node 1. The QST protocol is then implemented to transfer the state from emitter $1'$ to 2 (shown in green). **(b)** Under an ideal implementation, this transfer generates a remote Bell-pair, $|\Phi^+_{1,2}\rangle$ [see Eq. (1.23)]. Here entanglement is shown schematically using yellow braid-like structures.

The rightmost qubit in the receiving node of Fig. 1.6 is an auxiliary qubit, which is included to indicate that other qubits—beyond those participating in the QST scheme—are not affected by the transfer. In particular, QST is an entanglement preserving map: any entanglement with the transferred qubit ($1'$ here) is mapped to the receiver (2 here), while entanglement between other nodes is unchanged. This justifies why we tend to focus on only emitting and receiving systems (and do not explicitly show any auxiliary qubits). Here we have omitted the unitary transformation, U, for simplicity, though this mapping naturally generalizes in that

case (see App. A.3). Later, we also consider yet another related task, that of heralded REG between such heterogeneous systems (see §4.3.5).

1.5.4 Scope: QST using photonic qubits in guided channels

The implementation of a specific edge depends on the properties of the nodes it is linking, including their underlying technological implementation, natural energy scale, physical separation, and intended function (say communication or computation). In this work we focus on discrete (as opposed to continuous [85]) variable quantum communication in which intermediate 'flying qubits' carry quantum information along an edge realized by a guided quantum channel. Photons are the quintessential flying qubit, and the one we consider here as they can efficiently travel between nodes and they have several degrees of freedom (mode occupation number, polarization, temporal-mode, etc.) that can be used to encode quantum information.

We focus on guided channels (e.g., optical fiber [46, 69, 86, 87] or microwave coaxial cable [35, 88–94]) linking close-by nodes, say within a given lab or device, leaving the consideration of nonguided free-space channels to other work [95–99]. The main issue with distant nodes is that the fidelity of states being transferred (and likewise the degree of entanglement generated) typically decreases exponentially with the length of the connecting channel due to photon absorption and noise in the channel (the rate of this decay can be minimized by using telecom light) [100–103]. We note that, in principle, this issue can be solved using so-called quantum repeaters, which themselves need to be able to repeatedly distribute high-quality entanglement between close-by 'repeater stations.' This entanglement is then propagated to further separated nodes using a probabilistic, repeat until success method called entanglement swapping. Moreover, one potential application of hybrid QST or REG is in interfacing the

end-nodes of a quantum network with an intermediate repeater architecture, which would likely be telecom-based and hence photon manipulation would be necessary (as currently, no standard end-nodes operate in the telecom regime). Further details are beyond the scope of this work, though we note that quantum repeaters are an active area of research [104–107]. Accordingly, we will not explicitly address the difficulties of connecting distant nodes. Note that the error correction protocols we mention are still relevant for distant nodes, though they will accrue additional overhead for larger distances.

Note that this dissertation is molded from a primarily AMO background, so we will tend to focus on atomic and ionic systems as exemplars of the physics underlying our scheme. Though this is with the understanding that the overall scheme applies more generally (which is crucial for its hybrid applicability), so our use of "atom" can often be mapped to other material systems such as an ionic, solid-state, or superconducting qubit in analogous setups. In particular, the phenomenological models we develop apply more broadly to quantum systems beyond atoms, though one should heed that there will be many differences and caveats in the underlying physics and experiment (e.g., see §4.2.3).

CHAPTER II

PHYSICAL UNDERPINNINGS OF INPUT-OUTPUT THEORY

In this chapter we consider the fundamental interaction of light and matter and motivate input-output theory, which is the formalism underlying Chs. III and IV. In particular, the aim is to derive the Hamiltonian of Eq. (2.42), which underpins input-output theory. This Hamiltonian describes the situation depicted in Fig. 1.4 and is broken up into three pieces:

$$H = H_{\rm sys} + H_{\rm B} + H_{\rm int}, \tag{2.1}$$

where $H_{\rm sys}$, $H_{\rm B}$, and $H_{\rm int}$ are the respective Hamiltonians for both systems, the intermediate photonic channel (bath), and the interaction of the systems with the channel. This theory was developed by Gardiner and Collett in 1984 to treat the interaction of open quantum systems with a bosonic reservoir or heat bath, which can be regarded as a large number of harmonic oscillators. In this dissertation we will focus on the case where these oscillators correspond to the photonic modes of the free electromagnetic field [108]. More generally, the reservoir may support other bosonic excitations such as phonons in some optomechanical systems [54, 109–111] and other solid-state systems [112, 113] or magnons in a solid [114]. Input-output theory can be used as a framework for analyzing how different input fields drive the system, the ensuing output fields, and their relation.

2.1 Input-output theory overview

Often times when considering such system-bath interactions, one is only concerned with the system dynamics (not those of the larger bath), in which case one can average over the interaction with the bath (i.e., trace over the bath modes) resulting in a master equation description. Note, however, that such master equation (or corresponding Fokker–Planck or Langevin equation) methods or other previous and concurrently developed treatments, are limited to Gaussian states of the bath, e.g., vacuum, thermal, coherent [115, 116], and squeezed field states. Moreover, squeezed light can be seen as a boundary of the applicability such methods. In particular, the production of squeezed light via degenerate parametric amplification in a cavity [117], the damping of an initially squeezed oscillator, and the interaction of a system with a squeezed bath [118] can be treated using such methods. However, although the damping of the system is naturally included in such contexts, it does not provide any means for determining the output field, which is typically the physical entity accessible to subsequent manipulation or measurement. Input-output theory gives a prescription for calculating such output fields and related quantities such as correlation functions for the bath (provided you know what the system does).

As an early instance, Ref. 119 use the input-output formalism to further analyze the generation of squeezed light in a setup like that of Ref. 117, finding the same resulting intracavity field, yet going a step beyond by also calculating the output field of the cavity. Moreover, input-output theory can also support a wide class of input field states (e.g., Gaussian, multi-photon, and non-Gaussian states) by explicitly including the Hamiltonian describing their sources as part of the model [108, 119–124]. It is also worth noting that the Markovian assumption of the standard input-output theory [108] can be relaxed to treat some non-Markovian open quantum systems

[125–128]. Thus, the input-output formalism and the quantum Langevin equations underlying it are more general than the standard (Markovian) master equations, yet importantly reduces to said master equations (in the appropriate limits), which is useful when determining the dynamics of the system (see §3.6).

In this dissertation, we use the input-output formalism to treat the coupling of two quantum systems via an intermediate continuum-mode photonic bath. We are concerned with transferring quantum information (or entanglement) between these systems by directing the output field of one of them (the emitter) to be the input field driving the other system (the receiver). The theory of such cascaded quantum systems, where the outputs of certain systems are unidirectionally routed to and used as inputs for others, was developed independently by both Gardiner and Carmichael in 1993 appearing in two sequential articles in the same issue of Physical Review Letters [123, 124]. This unidirectionality is enforced by making H_{B} asymmetric between the forward and backward longitudinal directions of the channel, which can be physically accomplished in many ways and leads to a simpler effective description of the systems' interaction. Beyond connecting two systems, as we consider here, this approach can be naturally extended to analyze the connection of multiple quantum systems linked together in a network [129].

2.1.1 Outline

To derive the specific Hamiltonian, Eq. (2.1), that will serve as the starting point of Ch. III, we start by considering the standard electromagnetic Hamiltonian governing light-matter interaction and establishing its connection to multipolar interactions (§2.2). Then, we put the Hamiltonian into the desired form (§2.3), which is known as the Gardiner–Collett model (based on Ref. 108), which underpins this dissertation.

2.2 Light-matter interaction in low-energy systems

In this section we will recapitulate the general framework in which we model and analyze the interactions of light and non-relativistic matter (§2.2.1). We then use the Power–Zienau–Woolley transformation along with the LWA to put the Hamiltonian model in a more illuminating form for our purposes (§2.2.2). Our treatment in these subsections largely follows the methods of Ref. 22, which is a phenomenal textbook reference on quantum light-matter interactions. Thereafter, we further simplify the model (tame DOFs) by leveraging the few-level approximation (§2.2.3) as well as, the yet to be introduced, rotating-wave approximation (§2.2.4).

2.2.1 Quantum electrodynamics in the Coulomb gauge

In this dissertation we consider low-energy (nonrelativistic) quantum systems, wherein the massive particles of interest, such as trapped atoms or ions, are moving with low velocities ($v \ll c$) and additionally the creation and annihilation of said particles can be ignored. Importantly, however, we are concerned with systems in which excitations can be transferred between light and matter, so photons (which are massless) can be created or destroyed due to interactions with matter. The dynamics of a such system of N particles[1] (indexed by n) interacting with electromagnetic fields are determined, quite generically, by a light-matter Hamiltonian operator of the form [22]

$$H_{\mathrm{lm}}(t) = \sum_{n=1}^{N} \frac{1}{2m_n} \left[\boldsymbol{p}_n - q_n \boldsymbol{A}_{\mathrm{tot}}(\boldsymbol{r}_n, t)\right]^2 + V_{\mathrm{tot}}(\{\boldsymbol{r}_n\}, t) + \int d^3k \sum_{\boldsymbol{\varepsilon}} \hbar\omega_k a^\dagger_{\boldsymbol{\varepsilon}}(\boldsymbol{k}) a_{\boldsymbol{\varepsilon}}(\boldsymbol{k}). \tag{2.2}$$

[1]For simplicity, we take the particles to be spin free. A description of spin can be added from the offset, in Eq. (2.2), or post hoc as necessary.

See Table 2.1 for a glossary of the (quite standard) symbols used in Eq. (2.2) as well as throughout this subsection and dissertation more generally. To arrive at the Hamiltonian of Eq. (2.2), one can go through a semi-elaborate but standard quantization procedure (as is done in App. C.2), in which one eliminates all redundant degrees of freedom in the standard presentation of electrodynamics and, in so doing, aptly opts to treat the fields produced by the system in the Coulomb gauge. One is then left with a theory whose fundamental dynamical variables are the particle position and conjugate momentum operators ($\boldsymbol{r}_n$ and $\boldsymbol{p}_n$) and the field creation and annihilation operators ($a^\dagger$ and a), which are subject to the commutation relations:

$$[r_{n,i}, p_{m,j}] = i\hbar\delta_{nm}\delta_{ij} \tag{2.3}$$

and

$$\left[a_{\boldsymbol{\varepsilon}}(\boldsymbol{k}), a^\dagger_{\boldsymbol{\varepsilon}'}(\boldsymbol{k}')\right] = \delta_{\boldsymbol{\varepsilon},\boldsymbol{\varepsilon}'}\delta^3(\boldsymbol{k}-\boldsymbol{k}') \tag{2.4}$$

with all other commutators of these variables being zero.

In addition to the "radiation reaction" fields produced by the particles (encapsulated by $\boldsymbol{A}$ and V), we explicitly allow for and account for the influence of external fields (via $\boldsymbol{A}_{\text{ext}}$ and V_{ext}) on the dynamics of the particles of interest by considering the total vector potential and potential energy function

$$\boldsymbol{A}_{\text{tot}}(\boldsymbol{r}_n, t) = \boldsymbol{A}(\boldsymbol{r}_n) + \boldsymbol{A}_{\text{ext}}(\boldsymbol{r}_n, t) \tag{2.5}$$

and

$$V_{\text{tot}}(\{\boldsymbol{r}_n\}, t) = V(\{\boldsymbol{r}_n\}) + V_{\text{ext}}(\{\boldsymbol{r}_n\}, t), \tag{2.6}$$

TABLE 2.1. Glossary of symbols used in this section and throughout the dissertation more generally. See §1.3.2 for an overview of the notation used. Subscripts denote that a quantity is of particular quality, e.g., m_n is the mass of particle n and $a_{\boldsymbol{\varepsilon}}(\boldsymbol{k})$ is the annihilation operator for a photon with wavevector $\boldsymbol{k}$ and polarization $\boldsymbol{\varepsilon}$. Note that $\boldsymbol{r}_n$ is the position operator (after second quantization) for particle n, whereas $\boldsymbol{r}$ (no subscript) is a spatial coordinate (i.e., a vector in $\mathbb{R}^3$) that parameterizes field variables.

Type	Symbol	Definition
Particle quantities	n	particle label
	m	mass
	q	charge
	$\boldsymbol{r}$	position
	$\boldsymbol{p}$	conjugate momentum
Field quantities	t	time
	$\boldsymbol{r}$	spatial coordinate
	$\boldsymbol{E}$	electric field
	$\boldsymbol{B}$	magnetic field
	$\boldsymbol{k}$	wavevector
	ω_k	angular frequency
	$\boldsymbol{\varepsilon}$	polarization vector
	$\boldsymbol{A}$	vector potential
	$\boldsymbol{A}_{\text{ext}}$	external field vector potential
	V	Coulomb potential energy
	V_{ext}	external potential energy
	a	photon annihilation operator
	$a^\dagger$	photon creation operator
Physical constants	$\hbar$	Planck's reduced constant
	ε_0	permittivity of free space
	c	speed of light
	k_B	Boltzmann's constant

respectively. [Note that for the vector potential, we are summing over terms with different $\boldsymbol{r}_n$, whereas we lumped the potential energy into a single term depending on all of the particle positions, $\{\boldsymbol{r}_n\}$.] By "external field" we mean the electric or magnetic fields produced by an experimental source (such as a laser or current carrying wire) that can be controlled independently of system of interest. In particular, we assume that back reaction of the system (i.e., the fields produced as a result of the particles' motion) either negligibly affects the sources or that the sources are dynamically tuned to compensate for any such effects. If there are no external fields ($\boldsymbol{A}_{\text{ext}}$ and V_{ext} are zero), then $H_{\text{lm}}(t) \to H_{\text{lm}}$ is a constant of the motion. However, in the presence of external fields, H_{lm} acquires time dependence that characterizes the exchange of energy with the external experimental apparatus (the Hamiltonian for which we do not write down).

In the Hamiltonian of Eq. (2.2), and throughout this dissertation, we will be operating in the Coulomb gauge for the system fields:

$$\boldsymbol{\nabla} \cdot \boldsymbol{A}(\boldsymbol{r}) = 0. \tag{2.7}$$

Thus, the longitudinal[2] component of the vector potential operator is zero, $\boldsymbol{A}_{\parallel} = \boldsymbol{0}$, and the central electromagnetic object we must understand is the transverse vector potential operator

$$\boldsymbol{A}(\boldsymbol{r}) \equiv \boldsymbol{A}_{\perp}(\boldsymbol{r}) = \int d^3k \sum_{\boldsymbol{\varepsilon}} \mathcal{A}_k \boldsymbol{\varepsilon} \left[a_{\boldsymbol{\varepsilon}}(\boldsymbol{k}) e^{i\boldsymbol{k}\cdot\boldsymbol{r}} + a^{\dagger}_{\boldsymbol{\varepsilon}}(\boldsymbol{k}) e^{-i\boldsymbol{k}\cdot\boldsymbol{r}} \right], \tag{2.8}$$

[2]This naming comes from reciprocal space, wherein vector fields, such as $\boldsymbol{A}(\boldsymbol{k})$, can be split into *longitudinal* components that are aligned with the wavevector $\boldsymbol{k}$ and *transverse* components that are orthogonal to $\boldsymbol{k}$. Under spatial Fourier transforms, real space vector fields inherent this labeling (see App. C.2.2 for elaboration).

wherein

$$\mathcal{A}_k = \sqrt{\frac{\hbar}{2(2\pi)^3 \varepsilon_0 \omega_k}}, \tag{2.9}$$

with the linear dispersion relation (for the low-energy systems we consider)

$$\omega_k = ck, \tag{2.10}$$

and for each $\boldsymbol{k}$, $\sum_{\boldsymbol{\varepsilon}}$ is a sum over two linear polarization vectors spanning the transverse subspace to $\boldsymbol{k}$. Meanwhile,

$$V(\{\boldsymbol{r}_n\}) = \frac{1}{4\pi\varepsilon_0} \sum_{n=1}^{N} \sum_{m=1}^{n-1} \frac{q_n q_m}{|\boldsymbol{r}_n - \boldsymbol{r}_m|} = \frac{1}{8\pi\varepsilon_0} \sum_{n \neq m} \frac{q_n q_m}{|\boldsymbol{r}_n - \boldsymbol{r}_m|} \tag{2.11}$$

is the Coulomb potential energy of the charge distribution, which is a function of the particle positions only, where in the rightmost expression we are double counting the interaction energy of each pair of particles.

Equation (2.8) can be understood as the second-quantized expansion of the $\boldsymbol{A}$ operator in terms of the normal vibrational modes of the transverse free electromagnetic field in reciprocal space. The importance of the transverse vector potential is endowed by the decoupling of the longitudinal and transverse field components, which allows the longitudinal fields to be eliminated. Namely, $\boldsymbol{E}_{\parallel}$ is not a true dynamical variable as, in the Coulomb gauge, it can be expressed solely as a function of $\boldsymbol{r}_n$,

$$\boldsymbol{E}_{\parallel} = -\boldsymbol{\nabla} V, \tag{2.12}$$

and $\boldsymbol{B}$ is always traverse due to Gauss's law for magnetism. The dynamic fields are thus the transverse electric and magnetic fields, which can be expressed simply in

terms of $\boldsymbol{A} = \boldsymbol{A}_\perp$ as

$$\boldsymbol{E}_\perp = -\dot{\boldsymbol{A}} = i \int d^3k \; \omega_k \mathcal{A}_k \sum_{\boldsymbol{\varepsilon}} \boldsymbol{\varepsilon} \left[a_{\boldsymbol{\varepsilon}}(\boldsymbol{k}) e^{i\boldsymbol{k}\cdot\boldsymbol{r}} - a^\dagger_{\boldsymbol{\varepsilon}}(\boldsymbol{k}) e^{-i\boldsymbol{k}\cdot\boldsymbol{r}} \right] \tag{2.13}$$

(the full system field is $\boldsymbol{E} = \boldsymbol{E}_\parallel + \boldsymbol{E}_\perp$) and

$$\boldsymbol{B} = \boldsymbol{B}_\perp = \boldsymbol{\nabla} \times \boldsymbol{A} = \int d^3k \sum_{\boldsymbol{\varepsilon}} i\mathcal{A}_k \left(\boldsymbol{k} \times \boldsymbol{\varepsilon} \right) \left[a_{\boldsymbol{\varepsilon}}(\boldsymbol{k}) e^{i\boldsymbol{k}\cdot\boldsymbol{r}} - a^\dagger_{\boldsymbol{\varepsilon}}(\boldsymbol{k}) e^{-i\boldsymbol{k}\cdot\boldsymbol{r}} \right], \tag{2.14}$$

respectively.

Note that the expansions of $\boldsymbol{A}$, Eq. (2.8), and of the transverse fields, Eqs. (2.13) and (2.14), can be understood in the Heisenberg or Schrödinger picture (and are valid in both), which is why we did not include a time argument. We note, however, that the Heisenberg picture is often convenient, especially in describing light. For instance, the shown form of $\boldsymbol{E}_\perp$ is not necessarily obvious, yet it can easily be understood in the Heisenberg picture. Therein, the time derivative of $\boldsymbol{A}$ yields $\dot{a}_{\boldsymbol{\varepsilon}}(\boldsymbol{k}, t)$ terms and their adjoints, that are dictated by Heisenberg equations of motion and coalesce to yield Eq. (2.13) (as shown in App. C.2.4).

To interpret the terms in H_{lm}, we note that it can be understood as originating from (or being motivated by) the total energy of a closed system of particles and fields,

$$\sum_{n=1}^{N} \frac{1}{2} m_n \dot{r}_n^2 + \frac{\varepsilon_0}{2} \int d^3r \left[E^2(\boldsymbol{r}, t) + c^2 B^2(\boldsymbol{r}, t) \right], \tag{2.15}$$

which is conserved (a constant of the motion) in standard classical electrodynamics (i.e., Maxwell equations and the Lorentz equation). In particular, we can identify several correspondences between the classical energy of (2.15) and the Hamiltonian operator of Eq. (2.2). The first term in (2.15) is the kinetic energy of the particles

and corresponds to the first term of Eq. (2.2), which is written in terms of the particle's conjugate momenta, which for each particle is given by the sum of its mechanical momentum and the longitudinal[3] field momentum: $\boldsymbol{p}_n = m_n\dot{\boldsymbol{r}}_n + q_n\boldsymbol{A}(\boldsymbol{r}_n)$. Meanwhile, the second term in (2.15) is the energy of the fields. In the Coulomb gauge, wherein one naturally separates the longitudinal and transverse field components, the field energy can likewise be split into longitudinal and transverse contributions, which ultimately correspond to the second and third terms of Eq. (2.2) (i.e., the V_{tot} and $a^\dagger a$ terms), respectively (see App. C.2).

2.2.2 Power–Zienau–Woolley transformation

The Hamiltonian of Eq. (2.2) serves as a good starting point for this work. For instance, the Heisenberg equations of motion (EOMs) for the operators $\boldsymbol{r}_n$ and $a_{\boldsymbol{\varepsilon}}(\boldsymbol{k})$, under this Hamiltonian, ultimately correspond the quantum versions of the Lorentz force law and Maxwell's equations [when using the transverse field operators expansions of Eqs. (2.13) and (2.14)], respectively (as is shown in section III.B.2 of Ref. 22). By "quantum versions" we mean that products of noncommuting Hermitian operators are symmetrized, i.e., $AB \to \frac{1}{2}(AB + BA)$ for operators A, B such that $[A, B] \neq 0$ (see Ref. 130 for some related physical considerations). However, to make use of this Hamiltonian it will be helpful to unravel the interaction between light and matter that is encoded in the $\boldsymbol{p}_n \cdot \boldsymbol{A}_{\text{tot}}(\boldsymbol{r}_n)$ terms. In particular, the conjugate momentum, $\boldsymbol{p}_n$, and vector potential, $\boldsymbol{A}_{\text{tot}}(\boldsymbol{r}_n)$, are not directly observable (they are gauge-dependent). Thus, especially for systems of individual well-isolated particles (such as such as atoms in cavities; see §3.5), it is desirable to write the Hamiltonian in

[3]This component of $\boldsymbol{p}_n$ is called longitudinal, even though it is expressed solely in term of $\boldsymbol{A}_\perp$, because it comes from $\boldsymbol{E}_\parallel$ contributions to the total momentum of the field via terms of the form $\boldsymbol{E}_\parallel \times \boldsymbol{B}$, which are transverse.

terms of physically observable quantities: the electromagnetic fields, $\boldsymbol{E}$ and $\boldsymbol{B}$, and system operators written in terms of the energy levels being accessed in the system under consideration (e.g., the electric dipole moment and higher-order multipolar moments). This "unraveling" can be accomplished by using the Power–Zienau–Woolley transformation [131, 132] to unitarily transform the Hamiltonian, Eq. (2.2), into an ultimately equivalent but more convenient multipolar interaction form. We present the key steps necessary to preface input-output theory here and work through some of the details in App. C.3, leaving further details to textbook treatments.[4]

The Power–Zienau–Woolley (PZW) transformation is given by

$$U(t) = \exp\left[\frac{-i}{\hbar}\int d^3r \boldsymbol{P}(\boldsymbol{r})\cdot\boldsymbol{A}_{\mathrm{tot}}(\boldsymbol{r},t)\right], \tag{2.16}$$

where

$$\boldsymbol{P}(\boldsymbol{r}) = \sum_{n=1}^{N}\int_0^1 du q_n \boldsymbol{r}_n \delta(\boldsymbol{r}-u\boldsymbol{r}_n) \tag{2.17}$$

is the polarization distribution of the N charges; see Fig. 2.1. It is a unitary transformation to the Hamiltonian H_{lm} of Eq. (2.2):

$$H'(t) = U(t)H_{\mathrm{lm}}(t)U^\dagger(t) + i\hbar\dot{U}(t)U^\dagger(t) \tag{2.18}$$

(see §C.3.1). The full result for this transformed Hamiltonian can indeed be calculated, as is done in the references provided in footnote 4. The result is elegant, yet arguably cryptic, as the details of light-matter interactions are compactly tucked

[4]See Refs. 22 and 133 and the references therein for further context and motivations. For instance, among other things, Ref. 22 starts by presenting this transformation in the Lagrangian formalism (see section IV.C), showing that it is tantamount to a gauge transformation, and Ref. 133 (see chapter 9) discusses several extensions, e.g., accounting for the center-of-mass motion (and the corresponding Röntgen interaction).

away in u integrals like that of Eq. (2.17). The key underlying physics can be made more evident by employing the long-wavelength approximation (LWA), which is tantamount to neglecting the spatial variation of the fields on the system's length scale and thus, replacing $\boldsymbol{A}_{\text{tot}}(\boldsymbol{r}, t)$ with its value at the origin (defined as the center of the quantum system of interest, e.g., the nucleus for an isolated atom), $\boldsymbol{A}_{\text{tot}}(\boldsymbol{0}, t)$, and likewise for the corresponding fields. This approximation is valid when the system of interest is much smaller than the wavelength of the light interacting with it, which is almost universally the case in quantum optics (see §1.3.5).

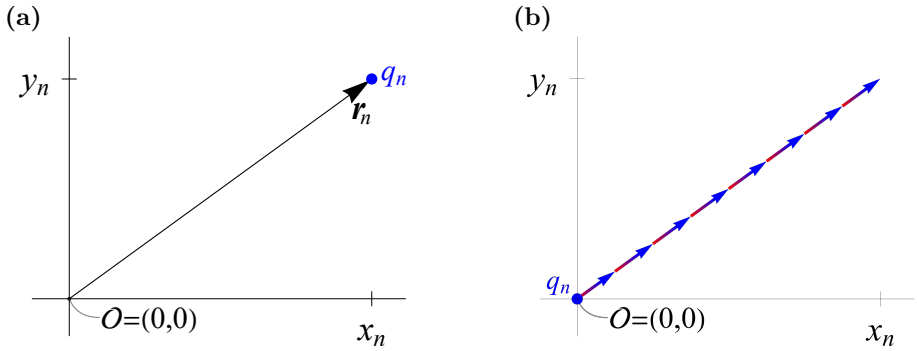

FIGURE 2.1. Visualizing the polarization density of a point charge. **(a)** The physical charge q_n at $\boldsymbol{r}_n = (x_n, y_n)$ relative to the origin $\mathcal{O} = (0, 0)$ (we present a two-dimensional case for graphical clarity). **(b)** An equivalent charge distribution is constituted by a point charge q_n at $\mathcal{O}$ and k physical dipoles ($k = 8$ here), shown as vectors with the blue arrow tip representing a charge $+q_n$ and the red tail representing a charge $-q_n$, arranged along the line from $\mathcal{O}$ to $\boldsymbol{r}_n$ (other curves from $\mathcal{O}$ to $\boldsymbol{r}_n$ could be considered similarly). The equivalence can be seen as the pairwise cancellation of all of the charges except for q_n at $\boldsymbol{r}_n$. The corresponding polarization density, $\boldsymbol{P}_n(\boldsymbol{r})$, can then be defined relative to a reference charge distribution, taken to be q_n at $\mathcal{O}$ here. The form of $\boldsymbol{P}_n(\boldsymbol{r})$ given by the summand of Eq. (2.17) comes from taking the $k \to \infty$ limit, wherein the physical dipoles become ideal, point dipoles [22].

Computing the transformed Hamiltonian, to leading order in the LWA, one obtains

$$H'(t) \approx H_{\text{sys}} + H_B + H_{\text{int}}, \tag{2.19}$$

where the Hamiltonians of the system of particles, electromagnetic fields (or the 'photonic bath'), and their dominant interaction are

$$H_{\text{sys}} = \sum_n \frac{p_n^2}{2m_n} + V_{\text{tot}}(\{\boldsymbol{r}_n\}, t), \tag{2.20}$$

$$H_B = \int d^3k \sum_{\boldsymbol{\varepsilon}} \hbar\omega_k a_{\boldsymbol{\varepsilon}}^\dagger(\boldsymbol{k}) a_{\boldsymbol{\varepsilon}}(\boldsymbol{k}), \tag{2.21}$$

and

$$H_{\text{int}} = -\boldsymbol{d} \cdot \boldsymbol{E}_{\perp,\text{tot}}(\boldsymbol{r} = \boldsymbol{0}, t), \tag{2.22}$$

respectively, where $\boldsymbol{d} = \sum_n q_n \boldsymbol{r}_n$ is the dipole moment of the charge distribution. Note that without the long-wavelength (or "dipole") approximation, one get a whole series of higher-order multipolar interactions (see App. C.3.3). The phenomenological model we are working towards only requires the more general condition of being able to controllably exchange material excitations with photons (via H_{int}). We focus on the dipole interaction here [Eq. (2.22)] to provide a concrete example and because, when it is permitted by selection rules, it is typically the dominant interaction [22, 134]. However, similar analyses, including the ultimate form of H_{int} given in Eq. (2.40), apply more generally in instances where other (non-dipole) interactions are dominant (e.g., trapped ion groups often often leverage electric quadrupole and magnetic dipole transitions [26]).

2.2.3 Dipole interaction with two-level systems

Now that we have molded the Hamiltonian of Eq. (2.19) into a form resembling Eq. (2.1), we are nearly ready to start with input-output theory. However, even after the simplifications we have made so far (including the LWA), H_{sys} and H_{int} are still

too general (complicated) to be reasonably employed to determine the evolution of quantum systems. Thus, we will employ the few-level approximation to eliminate frozen out DOFs (see §1.3.4), and focus on two levels, which we will again denote as $|g\rangle$ and $|e\rangle$ (see Fig. 1.1), and a dipole transition between them.[5] Then, the reduced system and interaction Hamiltonians are given by

$$H_{\text{sys}}^{(\text{red})} = \hbar\omega_{eg}\,|e\rangle\langle e| \tag{2.23}$$

[see Eq. (1.13)] with ω_{eg} the transition frequency and

$$H_{\text{int}}^{(\text{red})} = \mathbb{1}_2 H_{\text{int}} \mathbb{1}_2 = -\boldsymbol{d}^{(\text{red})} \cdot \boldsymbol{E}_{\perp,\text{tot}}(\boldsymbol{0}, t), \tag{2.24}$$

respectively, where we defined the dipole moment operator in the two-level system subspace as

$$\boldsymbol{d}^{(\text{red})} = \mathbb{1}_2 \boldsymbol{d}\, \mathbb{1}_2 = \boldsymbol{d}_{gg}\,|g\rangle\langle g| + \boldsymbol{d}_{ee}\,|e\rangle\langle e| + \boldsymbol{d}_{ge}\,|g\rangle\langle e| + \boldsymbol{d}_{eg}\,|e\rangle\langle g|\,, \tag{2.25}$$

with the shorthand $\boldsymbol{d}_{ab} \equiv \langle a|\boldsymbol{d}|b\rangle$ for the dipole matrix elements. Note that the diagonal matrix elements of the dipole moment operator, $\boldsymbol{d}_{aa}$, vanish for parity

[5] Note that although our derivation of Eq. (2.19) was for spin-free particles, we will consider the actual (dressed) energy levels of the system, which are modified due to interactions including spin-orbit coupling as well as with external fields.

reasons[6] so

$$\boldsymbol{d}^{(\mathrm{red})} = \langle g|\boldsymbol{d}|e\rangle\sigma + \mathrm{Hc}, \tag{2.26}$$

where $\sigma = |g\rangle\langle e|$ is the material annihilation operator and Hc denotes the Hermitian conjugate of the previous term. Assuming the transition is dipole allowed, $d_{eg} \neq 0$, and choosing the phase of the basis states such that the dipole matrix element $\boldsymbol{d}_{eg} \equiv \langle g|\boldsymbol{d}|e\rangle$ is real we have

$$\boldsymbol{d}^{(\mathrm{red})} = \boldsymbol{d}_{eg}(\sigma + \sigma^\dagger). \tag{2.27}$$

In the following sections, we will consider two instances of the electric dipole interaction, first focusing solely on an external drive (§2.2.4), then purely on the system field (§2.3.1).

2.2.4 Rotating-wave approximation and the interaction picture

We will now consider the characteristic dynamics of such a two-level system interacting with a monochromatic, "classical" electric field with fixed wavevector, $\boldsymbol{k}$, polarization, $\boldsymbol{\varepsilon}$, and frequency $\omega = \omega_k = ck$:

$$\boldsymbol{E}_c(\boldsymbol{r}, t) = E_0\boldsymbol{\varepsilon}e^{i(\boldsymbol{k}\cdot\boldsymbol{r}-\omega t)} + c.c., \tag{2.28}$$

[6]Namely, consider the parity operator Π, which negates real space, $\Pi\boldsymbol{r}\Pi^\dagger = -\boldsymbol{r}$, and hence is an involution, $\Pi^2 = \mathbb{1}$ (with $\Pi = \Pi^{-1} = \Pi^\dagger$). Typically, Π commutes with the system Hamiltonian—e.g., the Coulomb interaction of a valence electron with the atomic nucleus is of the form $1/|\boldsymbol{r}_e|$ (neglecting the motion of the nucleus), which clearly commutes with Π—and hence has simultaneous eigenstates, $\{|g\rangle, |e\rangle\}$. Thus, the qubit states have definite parity: $\Pi|a\rangle = \pi_a|a\rangle$ with $\pi_a = \pm 1$ as Π is an involution. Accordingly, focusing on a single particle with $\boldsymbol{d} = q\boldsymbol{r}$, $\boldsymbol{d}_{ab} = \langle a|\Pi^2\boldsymbol{d}\,\Pi^2|b\rangle = q\pi_a\pi_b\langle a|\Pi\boldsymbol{r}\Pi|b\rangle = -\pi_a\pi_b\boldsymbol{d}_{ab}$ (with $|a\rangle, |b\rangle \in \{|g\rangle, |e\rangle\}$). Evidently, $\boldsymbol{d}_{ab}$ vanishes if $\pi_a = \pi_b$. Hence, $\boldsymbol{d}_{aa} = \boldsymbol{0}$ and if $\pi_e = \pi_g$ then the transition is dipole forbidden, $\boldsymbol{d}_{ge} = \boldsymbol{0}$. Note, however, that some systems do have permanent dipole moments leading to non-zero diagonal elements, $\boldsymbol{d}_{aa} \neq \boldsymbol{0}$. In such cases, the corresponding contributions act as energy shifts, rather than excitation changing interactions, and can thus be regarded as an additional dressing of the energy levels (see footnote 5) to be included in H_{sys} rather than H_{int}.

where *c.c.* denotes the complex conjugate of the previous term. Quantumly, this an external field corresponding to an idealized state of a laser. In particular, we simply take the expectation value of the reduced version of Eq. (2.19) with the source-free electric field in the coherent state $|\alpha_{\boldsymbol{k},\boldsymbol{\varepsilon}}\rangle = e^{-|\alpha|^2/2} e^{\alpha a^\dagger_{\boldsymbol{\varepsilon}}(\boldsymbol{k})}|0\rangle$: $\boldsymbol{E}_c(\boldsymbol{r},t) = \langle\alpha_{\boldsymbol{k},\boldsymbol{\varepsilon}}|\boldsymbol{E}_\perp(\boldsymbol{r},t)|\alpha_{\boldsymbol{k},\boldsymbol{\varepsilon}}\rangle$ [see Eqs. (2.13) and (C.54)] with $E_0 \equiv i\alpha\omega_k\mathcal{A}_k$ (which can be taken to be real without loss of generality). The system Hamiltonian is unchanged and the bath expectation value, $\langle\alpha_{\boldsymbol{k},\boldsymbol{\varepsilon}}|H_B|\alpha_{\boldsymbol{k},\boldsymbol{\varepsilon}}\rangle = \hbar\omega_k|\alpha|^2$, is a constant that can be regarded as an energy shift and hence neglected. Then the Schrödinger picture interaction Hamiltonian of Eq. (2.24) becomes

$$H_{\text{int}}^{(\text{red})} = -\hbar\Omega(\sigma + \sigma^\dagger)(e^{i\omega t} + e^{-i\omega t}), \tag{2.29}$$

where $\hbar\Omega \equiv \boldsymbol{d}_{eg}\cdot\boldsymbol{E}_0 = (\boldsymbol{d}_{eg}\cdot\boldsymbol{\varepsilon})E_0$ is called the Rabi frequency.

The dynamics of the two-level system are dictated by the Schrödinger equation. Without the field driving them, the basis states would naturally evolve with phases proportional to their energies, such that σ ($\sigma^\dagger$) would acquire a time dependence of $e^{-i\omega_{eg}t}$ ($e^{+i\omega_{eg}t}$). Thus, when expanding the product in Eq. (2.29), there would be dynamics on two timescales, with certain terms evolving with a slowly varying phase, while those with rapidly varying phases evolving on shorter timescales. To make this more precise, we will now introduce the *interaction picture*, which is an example of using a unitarily equivalent Hamilton or "frame change" to provide a simpler treatment (see App. C.3.1). First lets step back and consider a Hamiltonian of the form $H = H_0 + H_{\text{int}}(t)$, where we assume H_0 is time-dependent (though this method can easily be generalized). Then, one goes into the interaction picture via the unitary transformation

$$U = e^{iH_0 t/\hbar}. \tag{2.30}$$

The Schrödinger picture state, $|\psi_S\rangle$, governed by H, transforms into $|\psi_I\rangle = U|\psi_S\rangle$ and satisfies a Schrödinger equation with the new Hamiltonian

$$\tilde{H} = UHU^\dagger + i\hbar\dot{U}U^\dagger = UH_{\text{int}}U^\dagger, \tag{2.31}$$

where the H_0 term canceled out, with its lingering impact now as part of the transformed H_{int}.

In our case $H_0 \to H_{\text{sys}}^{(\text{red})}$ and $H_{\text{int}} \to H_{\text{int}}^{(\text{red})}$, so

$$U = e^{iH_{\text{sys}}^{(\text{red})}t/\hbar} = |g\rangle\langle g| + e^{i\omega_{eg}t}|e\rangle\langle e| \tag{2.32}$$

and

$$\tilde{H} = -\hbar\Omega\left[\left(e^{i\Delta t} + e^{-i(\omega+\omega_{eg})t}\right)\sigma + \left(e^{-i\Delta t} + e^{i(\omega+\omega_{eg})t}\right)\sigma^\dagger\right], \tag{2.33}$$

where we introduced the detuning, $\Delta \equiv \omega - \omega_{eg}$, which characterizes how close we are to resonance ($\Delta = 0$ is on resonance). Assuming $|\Delta| \ll \omega + \omega_{eg}$, we can make the *rotating-wave approximation* (RWA), which focuses on the slow dynamics (on timescales of order $1/\Delta$), by replacing the rapidly oscillating phases, $e^{\pm i(\omega+\omega_{eg})t}$, by their time average of zero. Moreover, the RWA is a perturbative approximation and relies on $\Omega \ll \omega, \omega_{eg}$. Dropping the rapidly oscillating terms, we obtain

$$\tilde{H}^{\text{RWA}} = -\hbar\Omega\left(e^{i\Delta t}\sigma + e^{-i\Delta t}\sigma^\dagger\right), \tag{2.34}$$

which we can then transform back to the Schrödinger picture as

$$H_{\text{int}}^{\text{RWA}} = U^\dagger\tilde{H}^{\text{RWA}}U = -\hbar\Omega\left(e^{i\omega t}\sigma + e^{-i\omega t}\sigma^\dagger\right). \tag{2.35}$$

This is a very common approximation in quantum optics and it can be extended to other contexts including quadrupole transitions, two-photon Raman transitions, and many other quantum interactions involving the exchange of excitations between modes. To indicate its validity, at least in this context, we briefly consider and contrast the state evolution induced by the Hamiltonians of Eqs. (2.33) and (2.34). This will be a simple analysis to preface a visualization of the RWA (see Fig. 2.2); see Refs. 25, 135, and 136 as well as textbook treatments including chapter 5 of Ref. 133 for more thorough discussions. Denoting the Schrödinger picture state as $|\psi_S\rangle = c_g(t)|g\rangle + c_e(t)|e\rangle$, the state in the interaction picture is $|\psi_I\rangle = \tilde{c}_g(t)|g\rangle + \tilde{c}_e(t)|e\rangle$ with $\tilde{c}_g(t) = c_g(t)$ and $\tilde{c}_e(t) = e^{i\omega_{eg}t}c_e(t)$. From the Schrödinger equation for the full Hamiltonian, $\tilde{H}$, we obtain the amplitude EOMs

$$\dot{\tilde{c}}_g(t) = i\Omega\left(e^{i\Delta t} + e^{-i(\omega+\omega_{eg})t}\right)\tilde{c}_e(t), \tag{2.36a}$$

$$\dot{\tilde{c}}_e(t) = i\Omega\left(e^{-i\Delta t} + e^{i(\omega+\omega_{eg})t}\right)\tilde{c}_g(t), \tag{2.36b}$$

which, under the RWA, reduce to

$$\dot{\tilde{c}}_g(t) \overset{\text{RWA}}{\approx} i\Omega e^{i\Delta t}\tilde{c}_e(t), \tag{2.37a}$$

$$\dot{\tilde{c}}_e(t) \overset{\text{RWA}}{\approx} i\Omega e^{-i\Delta t}\tilde{c}_g(t). \tag{2.37b}$$

Under the RWA, the coupled amplitude EOMs of Eq. (2.37) are easy to solve, however, their full (non-RWA) counterparts, Eq. (2.36), are surprisingly difficult to solve analytically [136]. Accordingly, to glean some intuition about the RWA and its applicability, we opt to simply visualize numerical solutions to these equations in Fig. 2.2.

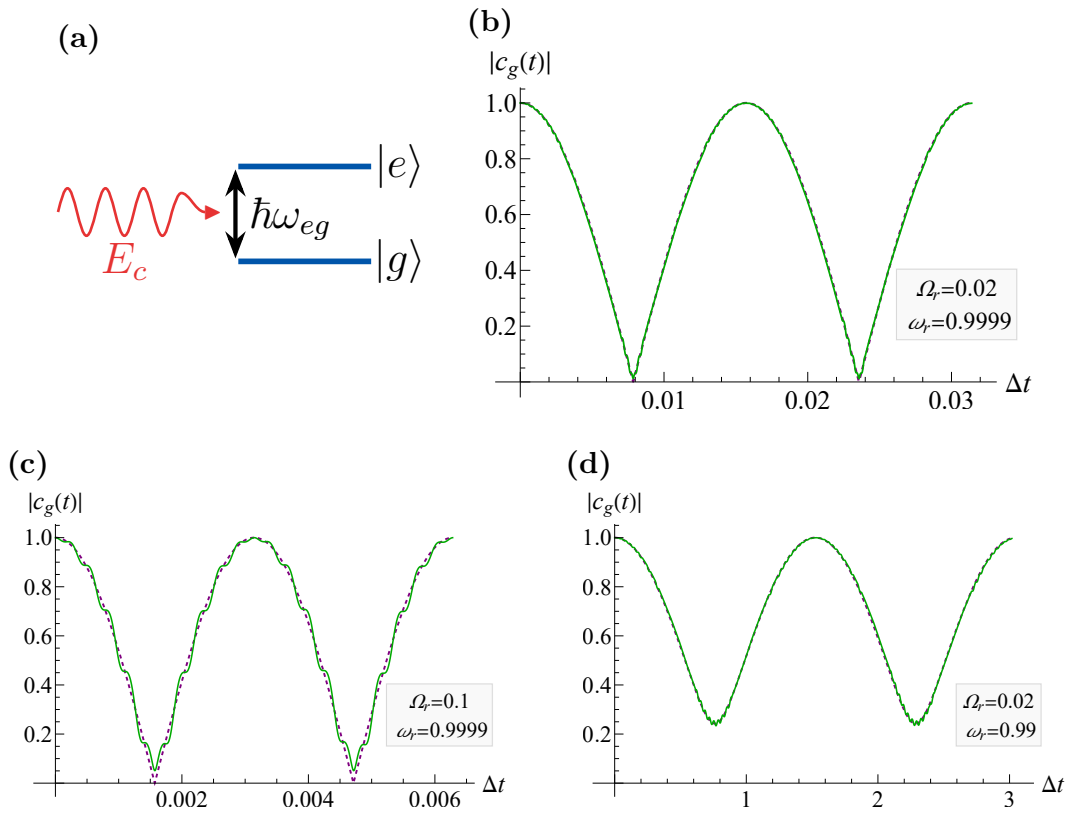

FIGURE 2.2. Visualizing the rotating wave approximation for the situation depicted in **(a)**: a two-level system is driven by an external electric field, E_c of Eq. (2.28), with frequency ω (see text for details). The solid (green) and dashed (purple) lines indicate numerical solutions of Eqs. (2.36) and (2.37), respectively. **(b)** For weak ($\Omega_r \ll 1$), nearly resonant ($\omega_r \approx 1$) drives, the RWA is a very good approximation and the atomic population oscillates sinusoidally, nearly fully between $|g\rangle$ and $|e\rangle$ with frequency $\sqrt{(2\Omega)^2 + \Delta^2}$. These are known as Rabi oscillations. **(c)** For stronger drives, larger Ω_r, we exit the perptubative regime of the RWA's validity as the short-time micromotion (rapid oscillations atop the Rabi oscillations) becomes appreciable. **(d)** When driving further from resonance, i.e., when ω_r gets further from one, the Rabi oscillations are suppressed and the atomic population is biased towards remaining in the initially populated state ($|g\rangle$ here).

We focus on the case, where the driving starts at $t = 0$ with the system initially populated in $|g\rangle$, $\tilde{c}_g(0) = 1$, such that $\tilde{c}_e(0) = 0$ and $\dot{\tilde{c}}_g(0) = 0$. We plot $|c_g(t)|$ as a function of Δt for various values of the dimensionless constants $\Omega_r \equiv \Omega/\omega$ and $\omega_r \equiv \omega_{eg}/\omega$ (specified in the insets); $|c_e(t)|$ can be determined by normalization. Figure 2.2 (b) illustrates a case where the RWA is reasonable. Meanwhile, (c) and (d) illustrate the respective impacts of increases to the drive strength and detuning, which take one out of the parameter regimes wherein the RWA is valid (namley, $\Omega \ll \omega, \omega_{eg}$ and $|\Delta| \ll \omega + \omega_{eg}$). Note that the values in (a) are quite modest, in AMO experiments typical frequency values are on the order of $\Omega \sim$ MHz, $\omega, \omega_0 \sim$ THz and $|\Delta| \sim$ MHz–GHz, corresponding to parameter values of $\Omega_r \sim 10^{-6}$ and $|1 - \omega_r| \sim 10^{-3}$–$10^{-6}$, which more comfortably fall within the validity of the RWA. If the drive is far detuned, $|\Delta|$ is large, i.e., comparable to either ω or ω_{eg}, then the oscillations get very small, approaching zero amplitude [as partially occurs in (d)]. This serves to corroborate the few-level approximation, as it is an explicit example of how driving transitions far from resonance leads to minimal disturbance to the populations.

2.3 Gardiner–Collett model

2.3.1 Quasi-1D interaction model

Now, we will return to interaction Hamiltonian of Eq. (2.24) and focus on the system fields (assuming there are no external fields, for now). Using the transverse field expansion of Eq. (2.13) and Eq. (2.27), we have

$$H_{\text{int}}^{(\text{red})} = i\hbar \int d^3k \sum_{\boldsymbol{\varepsilon}} \kappa_{\boldsymbol{\varepsilon}}(\boldsymbol{k})(\sigma + \sigma^\dagger) \left[a_{\boldsymbol{\varepsilon}}^\dagger(\boldsymbol{k}) - a_{\boldsymbol{\varepsilon}}(\boldsymbol{k})\right] \tag{2.38}$$

with the coupling

$$\kappa_{\boldsymbol{\varepsilon}}(\boldsymbol{k}) = \frac{\omega_k \mathcal{A}_k}{\hbar} \left(\boldsymbol{d}_{eg} \cdot \boldsymbol{\varepsilon}\right) = \sqrt{\frac{\omega_k}{2(2\pi)^3 \hbar \varepsilon_0}} \left(\boldsymbol{d}_{eg} \cdot \boldsymbol{\varepsilon}\right). \tag{2.39}$$

Within standard input-output theory [108, 122–124], and certainly in its application to QST [1], one often wants to controllably route the input and output electromagnetic fields to and from the system they are interacting with. Accordingly, the only propagating degree of freedom is the longitudinal mode of the field, which we will denote as $b(\omega)$ to differentiate it from its 3D counterpart. To focus on this mode, we assume the other three quantum numbers (polarization and two transverse spatial modes) are fixed. Then, the bosonic bath (photonic reservoir) may regarded as a quasi-1D channel. This substantial reduction of DOFs from the full 3D structure to a 1D model is physically facilitated by the experimental setup. In the context of QST, this includes using resonators to preferentially direct the light into (or collect light out of) a guided channel dictating the propagation direction, e.g., in AMO systems this could be an optical cavity coupled to an optical fiber (see §1.5).

This reduction is achieved by evaluating the integrals over the transverse subspace. Doing so from first principles would require details of the confining channel (including its transverse geometry and material properties) and system interaction in order to determine the transverse spatial mode profile, which is beyond the scope of this analysis.[7] Nonetheless, after performing said integrals, one will be left with a reduced

[7]For an explicit example of a full 3D treatment of input-output theory in the context of a strongly focused light beam interacting resonantly with a two-level atom see Ref. 18, which (in part) demonstrates and largely validates the standard reduction from 3D to 1D. Therein, it is noted that—even though the system and treatment thereof is explicitly 3D in character with the electromagnetic fields being expanded in multipole waves—one gets an interaction Hamiltonian of the same form as Eq. (2.40b). In particular, the atomic dipole moment (assumed to be fixed) picks out a particular component of $\boldsymbol{E}$ in the standard electric-dipole interaction Hamiltonian, so one can still characterize

Hamiltonian of the following, phenomenological form

$$H_{\text{int}}^{(1D)} = i\hbar \int d\omega \kappa(\omega)(\sigma + \sigma^\dagger) \left[b^\dagger(\omega) - b(\omega)\right] \tag{2.40a}$$

$$\approx i\hbar \int d\omega \kappa(\omega) \left[\sigma b^\dagger(\omega) - \sigma^\dagger b(\omega)\right], \tag{2.40b}$$

where we made the RWA in the second step. See Ref. 122 for an alternative way of motivating this phenomenological, model Hamiltonian. Here, as was the case in §1.4, ω is taking the role of a 1D wavevector that can be positive or negative, corresponding to forward or backwards propagation in the channel. By integrating out the transverse spatial modes, the full 3D annihilation operator $a_{\boldsymbol{\varepsilon}}(\boldsymbol{k})$ is reduced to a 1D one, $\sqrt{A_\perp c} b(\omega)$, where the prefactor is chosen for dimensionful consistency, with $A_\perp$ is a characteristic transverse area. Here, $b(\omega)$ is the annihilation operator characterizing the longitudinal mode of the quasi-1D bath and satisfies the commutation relation of Eq. (1.16),

$$[b(\omega), b^\dagger(\omega')] = \delta(\omega - \omega'). \tag{2.41}$$

Note this reduction also leads to a modified coupling, where generically, $\kappa(\omega)$ is not a simply function of $\kappa_{\boldsymbol{\varepsilon}}(\boldsymbol{k})$ (though in the paraxial approximation, $|\boldsymbol{k}_\perp| \ll |k_\parallel|$, it would be). Moreover, $\kappa(\omega)$ includes the necessary dimensionful factors ($\sqrt{A_\perp c}$) such that it has the proper dimensions of $[\text{Time}]^{-1/2}$, that is, it is the square root of a frequency.

2.3.2 Quantum state transfer Hamiltonian

We can now write down the standard, full Hamiltonian for quantum state transfer in the input-output formalism. Recall that the task itself is to use an intermediate

the interaction via the single longitudinal-mode DOF $b(\omega)$. The only difference (in this H_{int}), being the exact definition of the coupling $\kappa(\omega)$.

photon to send the state of a qubit between two systems that are coupled via a quantum channel (see §1.5). We will let the positions of systems 1 and 2 be $x_1 = 0$ and $x_2 = c\tau > 0$, respectively, where we let the channel define the x-direction. From Eq. (2.19), we have the total Heisenberg-picture Hamiltonian

$$H_{\rm QST} = H_{\rm sys} + H_{\rm B} + H_{\rm int}. \tag{2.42}$$

Here $H_{\rm sys}$ is the Hamiltonian for both systems within the few-level approximation. We postpone writing it explicitly until §3.5, wherein we model slightly more complicated systems that enable additional control relative to the two-level systems considered above. Meanwhile,

$$H_{\rm B} = \hbar \int d\omega |\omega| b^\dagger(\omega) b(\omega) \tag{2.43}$$

is the Hamiltonian for the photonic bath itself, which, to be consistent with the previous subsection, has been reduced to a quasi-1D description. Note that the absolute value of $|\omega|$ follows from Eq. (2.21), where one has the prefactor $\omega_k = c|\boldsymbol{k}|$ (see footnote 5 in §1.4).

The Hamiltonian characterizing the interaction of the bath with the two systems (in the RWA) is

$$H_{\rm int} = i\hbar \int d\omega \Big\{ \kappa_1(\omega) \left[\sigma_1^- b^\dagger(\omega) - \sigma_1^+ b(\omega)\right] + \kappa_2(\omega) \left[\sigma_2^- b^\dagger(\omega) e^{-i\omega\tau} - \sigma_2^+ b(\omega) e^{i\omega\tau}\right] \Big\}, \tag{2.44}$$

which comes from the using Eq. (2.40b) for each system. The phases for system 2 are due to the interaction Hamiltonian being evaluated at the system itself, e.g., in Eq. (2.22) the field is evaluated at $x_2 = c\tau$ leading to $e^{\pm i\boldsymbol{k}\cdot\boldsymbol{r}} \to e^{\pm i(\omega/c)x_2} = e^{\pm i\omega\tau}$ terms. Here $\sigma_j^+ \equiv \sigma_j^\dagger$ and $\sigma_j^- \equiv \sigma_j$ are the creation and annihilation operators for system

$j = 1, 2$. We introduce the $\pm$ superscripts for later notational convenience. Although we motivated this model in the context of a two-level system, with $\sigma = |g\rangle\langle e|$, these operators can be interpreted as generic system excitation operators, e.g, in §3.5, σ takes the form of a cavity annihilation operator. Zooming out, we note that the form of Eq. (2.44) is phenomenologically clear and apt for QST: each system, can exchange excitations with the quasi-1D channel with some frequency dependent coupling $\kappa_j(\omega)$. This Hamiltonian, H_{QST}, will be our starting point for Ch. III.

Remark:

Note that this treatment naturally extends beyond the dipole-interaction. In particular, the Hamiltonian of Eq. (2.38) can easily account for higher-order interactions by a suitable modification to the coupling $\kappa_{\boldsymbol{\varepsilon}}(\boldsymbol{k})$. For instance, going to the next order in the LWA and considering the electric quadrupole and magnetic dipole interactions (see App. C.3.2), one finds it necessary to modify the electric-dipole coupling, $\kappa_{\boldsymbol{\varepsilon}}(\boldsymbol{k})$ of Eq. (2.39), by adding the coupling

$$\kappa^{(2)}_{\boldsymbol{\varepsilon}}(\boldsymbol{k}) = \frac{\omega_k \mathcal{A}_k}{\hbar} \left(\frac{\boldsymbol{m}_l^{eg} \epsilon_{lij}}{\omega_k} - i Q_{ij}^{eg} \right) k_i \varepsilon_j \tag{2.45}$$

(where the eg labels are moved to superscripts to allow for the indexing of vector and matrix components). As in the electric-dipole case (see footnote 6), this is valid up to the potential additional dressing of the energy eigenstates. This similarly, applies to higher-order terms in the multipolar expansion, yielding

$$\kappa^{(\mathrm{full})}_{\boldsymbol{\varepsilon}}(\boldsymbol{k}) = \frac{\omega_k \mathcal{A}_k}{\hbar} \left[\boldsymbol{d}_j^{eg} + \left(\frac{\boldsymbol{m}_l^{eg} \epsilon_{lij}}{\omega_k} - i Q_{ij}^{eg} \right) k_i + \mathcal{O}(d^{eg} k^2 r_s^2) \right] \varepsilon_j, \tag{2.46}$$

where r_s is the characteristic length scale of the material system. Thus, it is clear that the higher order interaction terms lead to a more intricate reciprocal space coupling, yet the Hamiltonian of Eq. (2.38) is nevertheless of the right form. (This is more clearly manifest when considering the full PZW transformed Hamiltonian; see the references in footnote 4.) Note that the full consideration of these details is not necessary as the dimensional reduction considered in §2.3.1 also serves to modify the coupling, κ, and hence, at least without a lot of system specific additional work, can simply be regarded as a phenomenological quantity.

CHAPTER III

QUANTUM STATE TRANSFER AND INPUT-OUTPUT THEORY WITH TIME REVERSAL

The work of this chapter was published in Physical Review A **108**, 012421 (2023) [3]. It was conceived of by S. J. van Enk, its aim and scope were continually refined jointly by K. J. Randles and S. J. van Enk, and the majority of writing and figure preparation was done by K. J. Randles with continued support, verification, and feedback from S. J. van Enk.

3.1 Introduction

As discussed in §1.5.2, quantum processors can be interconnected to make hybridized and distributed quantum devices that are more powerful than their isolated components [33, 55]. Distributed QIP offers a complementary route towards scaling quantum computers and is essential for quantum networking and the many protocols that seek to leverage it. Hybridization allows for the individual system's strengths to be leveraged so as to create more versatile, robust, and scalable quantum information architectures. A crucial part of this interconnection is achieving quantum state transfer (QST) between different quantum systems that are spatially separated [78, 110, 137, 138] as introduced in §1.5. A standard way to accomplish this transfer of information is by making use of an intermediate information carrier (often deemed a 'flying qubit'), envisaged here as a photon, that is emitted by the first system and absorbed by the second [1, 33, 134]. Such direct transfer can be used to distribute entanglement, e.g., by sending one qubit of a Bell state to another location, with

applications in quantum networking, quantum key distribution, and other protocols [33, 56].

Connecting different quantum systems with high fidelity is challenging because they may have different resonance frequencies and decay rates.[1] In such cases it is well known that one ought to shift the frequency of the light pulse emitted by one system so as to interact resonantly with the receiving system and also stretch or compress the pulse in the time domain to match the receiving system's time scales [38–40, 78]. In addition, one should time-reverse the light pulse, simply because the light pulse that will be optimally absorbed by a system should be the time-reverse of what it would emit [36, 37, 139]. Thus, this challenge can be dealt with by manipulating the light emitted by one system so that it will be absorbed by the next.

Analyzing the state transfer process requires a theoretical description of how light drives quantum systems, which we developed in Ch. II. Describing how a general quantum state of the electromagnetic field interacts with an atom is surprisingly difficult. In 1993, Gardiner and Carmichael developed a strategy called input-output theory that allows one to manage a wider class of field states (see §2.1) [108, 123, 124]. In this theory, one includes a quantum description of the source of the light, and then assumes the light propagates freely and unidirectionally to a cascaded quantum system. That photonic degree of freedom can then be eliminated (by solving the Heisenberg equations for the continuous mode bath operators) to obtain an *effective description* where the source and receiver are directly coupled. The effective Hilbert space is then typically no longer infinite dimensional and in fact it is rather small if

[1] We limit our usage of 'hybrid quantum' to such cases of linking heterogeneous systems, though the phrase is used more broadly, e.g., to indicate hybrid classical-quantum technologies or hybrid continuous-discrete variable systems.

we can model the systems as ones with just a few energy levels (which we can if the interaction is nearly resonant; see §1.3.4).

Employing this formalism, we consider two quantum systems, labeled '1' and '2,' that are coupled indirectly by the ability to exchange photons. We assume this coupling is unidirectional, that is, system 1 can produce a photon that travels to system 2, but no photon travels from system 2 back to system 1. There is no reflection along the quantum channel linking the systems because we assume that the output field of system 2 is directed down a loss channel consisting of a different spatial mode; this could be implemented using a ring cavity or circulator [88]. This unidirectional character of the theory is clear in the effective description, in which there are two types of time evolution: One is by discrete jumps and the other is continuous time evolution governed by a Schrödinger-like equation, but with a non-Hermitian effective Hamiltonian [122, 140, 141]. This effective Hamiltonian will contain a term proportional to $\sigma_1^- \otimes \sigma_2^+$ without the Hermitian conjugate term (see §3.4). Here $\sigma_j^{\pm}$ are the creation and annihilation operators for system $j = 1, 2$. That is, there is a term that annihilates an excitation in system 1 and creates an excitation in system 2, but not vice versa.

In this chapter, our primary motivation concerns what changes in the theoretical description if the light does not simply propagate freely but is manipulated by means of a unitary transformation U. This extends the seminal theoretical work of Cirac and co-workers [1], which describes a method for achieving ideal QST between identical atoms in cavities using time-symmetric pulses. The scheme that Ref. 1 proposes, and likewise the scheme we develop, is reversible, so crucially the state can be transferred from an atom to the field and vice versa (field to atom). This reversible mapping has been experimentally verified [142].

One question we answer is, for the class of unitary transformations, U, we consider, can we still eliminate the light from our description to get a simple effective direct coupling between the two systems? The second question we answer is more subtle: The fact that the effective Hamiltonian contains just a term proportional to $\sigma_1^- \otimes \sigma_2^+$ (naively) seems to indicate that the photon emitted by system 1 will be absorbed by system 2 even without manipulating the photon. However, we know that this alone does not suffice. In fact, the optimal sort of wave packet that would be absorbed by system 2 would have to be the time inverse of the wave packet system 2 would emit itself. So suppose we apply a unitary transformation that time reverses the wave packet emitted by system 1. Then, how can we see from the effective description that system 2 will absorb the photon more efficiently?

We obtain the answers by slightly changing the standard interpretation of the equations obtained in the effective description where the two systems are directly coupled. Doing that will lead us to define a mathematical object $\rho(t)$ consisting of two parts. One part is simply the state of system 2 at time t and the other is the state of a fictitious system $\tilde{1}$ at a time $\tilde{t} = f(t)$ that decreases as a function of t if we apply a time-reversal transformation. The time evolution of that mathematical object thus corresponds to system 2 evolving forward in time in a standard way, yet it is driven by the backward-evolving fictitious system $\tilde{1}$. This is similar in spirit to the theory of the "past quantum state" [143], which likewise introduces a mathematical object consisting of one forward-evolving standard quantum state and a backward-evolving part. In the latter case the backward-evolving part describes retrodiction, whereas in our case it results only if we time reverse the single-photon wave packet.

3.1.1 Outline

In §3.2 we rehearse the input-output methods of Gardiner [124] to model the two systems interacting unidirectionally via a bosonic bath connecting them. We determine the field resulting from the systems' interaction, which is the physical entity we transform in §3.3.2. In §3.3 we describe and analyze a scheme for QST using photon manipulation that could be used for hybrid quantum networking. Modeling the photon manipulation as a unitary transformation, we show how to include field transformations in input-output theory. We analyze how the field is transformed and how equations of motion (EOMs) for system 2 operators are affected. In §3.5 we consider two systems each comprised of a three-level atom in a cavity, where a resonant two-photon Raman process is used to couple each atom to its respective cavity. Here we show that our scheme can be used to achieve hybrid QST. We discuss our results and give some conclusions in §3.6. This includes a discussion of the dynamics of the composite state of systems $\tilde{1}$ and 2, $\rho(t)$, where we add a new interpretation of the state's time argument.

3.2 General setup

We assume that each system ($j = 1, 2$) encodes the state of a qubit in a long-lived effective two-level system with ground state $|g_j\rangle$ and excited state $|e_j\rangle$. We suppose that system 1 starts in an arbitrary superposition $c_g|g_1\rangle + c_e|e_1\rangle$, which is the state we want to transfer, and that system 2 starts in its ground state $|g_2\rangle$. Thus, we want to implement the transformation

$$[c_g|g_1\rangle + c_e|e_1\rangle] \otimes |g_2\rangle \longmapsto |g_1\rangle \otimes [c_g|g_2\rangle + c_e|e_2\rangle]\,. \tag{3.1}$$

For now we assume that we have a way of inducing absorption and emission in these two-level systems via laser pulses. To determine the requisite details of these pulses one needs to specify what the underlying systems encoding the qubits are, which we keep arbitrary for now. In §3.5 we show, following the work of Ref. 1, how this can be done for three-level atoms in optical cavities, where the atomic ground states are coupled by a Raman transition, forming our qubits.

Based on the input-output formalism we model the quantum channel as a quasi-1D bath, with boson annihilation operators, $b(\omega)$, that both systems 1 and 2 are coupled to. Let the positions of systems 1 and 2 be $x_1 = 0$ and $x_2 = c\tau > 0$, respectively (see Fig. 3.1). Based on the formalism developed in §2.3 (which is based on Refs. 122 and 124), we work with the model Hamiltonian specified in Eqs. (2.42)–(2.44), which is of the form $H = H_{\rm sys} + H_{\rm B} + H_{\rm int}$. For neatness of notation, we will henceforth work in natural units, wherein

$$\hbar = 1. \tag{3.2}$$

We delayed this choice til here to facilitate the comparison to other standard treatments. For much of our analysis $H_{\rm sys}$ is left unspecified and can be interpreted as a general operator on the two systems (see §3.5 for a concrete example). We work in the Heisenberg picture, so the operators $\sigma_j^{\pm}$ and b depend on time. The photonic degree of freedom of the channel, $b(\omega)$, can then be eliminated (by solving the corresponding Heisenberg EOM) to obtain an effective description (typically in a much smaller Hilbert space) where the source and receiver are directly coupled. In this formalism we assume the light propagates freely and unidirectionally (as needs to be physically imposed) from the emitter to the receiver.

We now make the Markov approximation of a flat coupling $\kappa_j = \sqrt{\gamma_j/2\pi}$ within a narrow bandwidth of positive ω (e.g., the linewidth for optical cavities). This

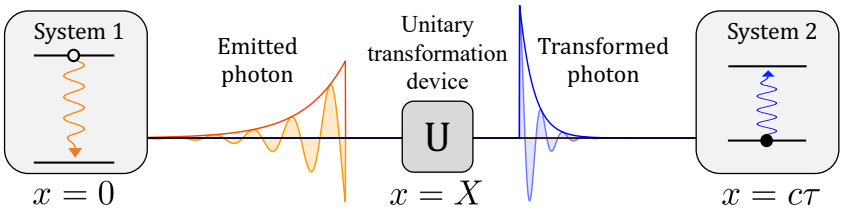

FIGURE 3.1. Scheme to transfer quantum information between distinct quantum systems along a channel. For the sake of illustration, in this figure, we suppose that system 1 is initially excited and emits an exponentially decaying wave packet, which is common to spontaneous emission processes [36].

includes setting $\kappa_j(\omega) = 0$ for negative ω, encoding the unidirectional nature of the coupling [122, 124]. (In particular, see Sec. II B of Ref. 122 for a justification of this approximation and some discussion of the integration limits.) Then we define the forward-traveling 'photon field' operator[2] as

$$A^+(x,t) = \frac{1}{\sqrt{2\pi}} \int d\omega b(\omega,t) e^{i\omega x/c}. \tag{3.3}$$

After solving the Heisenberg EOM for $b(\omega,t)$ with initial condition at $t_0 < t$, this field can be expressed in terms of the rightward- and leftward-propagating 'in fields,'

$$b^r_{\text{in}}(t) = \frac{1}{\sqrt{2\pi}} \int_0^\infty d\omega e^{-i\omega(t-t_0)} b(\omega,t_0) \tag{3.4}$$

and

$$b^l_{\text{in}}(t) = \frac{1}{\sqrt{2\pi}} \int_0^\infty d\omega e^{-i\omega(t-t_0)} b(-\omega,t_0), \tag{3.5}$$

[2]We take this name for the field operator A^+ from Ref. 37. Here A^+ is a vector potential scaled such that $A^+ (A^+)^\dagger$ is a photon flux and under the Markov approximation [122] it is proportional to the electric field (which is what Ref. 124 refers to it as).

respectively. Namely, one finds

$$A^+(x,t) = b^r_{\rm in}\left(t_-\right) + b^l_{\rm in}(t_+) + \sqrt{\gamma_1}u(x)\sigma_1^-\left(t_-\right) + \sqrt{\gamma_2}u(x-c\tau)\sigma_2^-\left(t_-+\tau\right), \quad (3.6)$$

where $t_\pm = t \pm x/c$ and $u(x)$ is the Heaviside step function with $u(0) = 1/2$. Using a "final condition" at $t_1 > t$, one finds a similar expression for $A^+(x,t)$ in terms of the 'out fields' $b^{r,l}_{\rm out}$ defined similarly to $b^{r,l}_{\rm in}$ with $t_0 \to t_1$. Equating these expressions for $A^+(x,t)$ and using the independence of x and t then implies

$$b^l_{\rm out}(t) - b^l_{\rm in}(t) = 0 \quad (3.7)$$

and

$$b^r_{\rm out}(t) - b^r_{\rm in}(t) = \sqrt{\gamma_1}\sigma_1^-(t) + \sqrt{\gamma_2}\sigma_2^-(t+\tau). \quad (3.8)$$

Physically, Eq. (3.7) says that the leftward-propagating free fields are not changed and Eq. (3.8) says that the rightward-propagating free fields are changed by the radiation from the two systems (as is consistent with the unidirectional coupling).

As the leftward-propagating free field is unchanged, we focus on the rightward propagating field and abbreviate $b_{\rm in,out} \equiv b^r_{\rm in,out}$. Then with

$$c_1(t) := \frac{\gamma_1}{2}\sigma_1^-(t) + \sqrt{\gamma_1}b_{\rm in}(t) \quad (3.9)$$

and

$$c_2(t) := \frac{\gamma_2}{2}\sigma_2^-(t) + \sqrt{\gamma_1\gamma_2}\sigma_1^-(t-\tau) + \sqrt{\gamma_2}b_{\rm in}(t-\tau), \quad (3.10)$$

the general Heisenberg EOM for a system operator $s(t)$ as governed by Hamiltonian H_{QST}, see Eq. (2.42), is [124]

$$\dot{s}(t) = -i\left[s(t), H_{\mathrm{QST}}(t)\right] = \sum_{j=1}^{2}\left(c_j^\dagger\left[s, \sigma_j^-\right] - \left[s, \sigma_j^+\right] c_j\right) - i\left[s, H_{\mathrm{sys}}\right], \tag{3.11}$$

in which each operator has the same time argument t and $[\cdot,\cdot]$ is the commutator. Note that b_{in}^l does not appear in this expression due to the assumption that $\kappa(\omega) = 0$ for negative ω, which effectively restricts the ω integral bounds.

Let s_j denote a system j operator. Then as $\left[s_1, \sigma_2^\pm\right] = 0$, Eq. (3.11) implies

$$\dot{s}_1(t) = c_1^\dagger\left[s_1, \sigma_1^-\right] - \left[s_1, \sigma_1^+\right] c_1 - i\left[s_1, H_{\mathrm{sys}}\right], \tag{3.12}$$

so $\dot{s}_1(t)$ depends on system 1 and field operators at the same time t. Similarly, as $\left[s_2, \sigma_1^\pm\right] = 0$,

$$\dot{s}_2(t) = c_2^\dagger\left[s_2, \sigma_2^-\right] - \left[s_2, \sigma_2^+\right] c_2 - i\left[s_2, H_{\mathrm{sys}}\right], \tag{3.13}$$

so $\dot{s}_2(t)$ depends on system 2 operators at the same time t and on the delayed output of system 1 at time $t - \tau$ through $c_2(t)$.

As s_1's EOM depends on a single time, we can shift this time to $f(t) = t - \tau$ to match the time arguments of the system 1 and field operators in s_2's EOM. Using this structure, we can therefore write down an effective description that encapsulates how system 2 is driven. Namely, system 2 is effectively directly coupled to a time-delayed version of system 1, which can be understood as the dynamics of a fictitious Schrödinger picture composite state of the form

$$\rho(t) := \rho_1(f(t)) \otimes \rho_2(t). \tag{3.14}$$

The point is that both the equations for system 1 and system 2 can refer to the same time $f(t)$ for the state of system 1. Importantly, this is true both for Gardiner's original equations [124] and for our transformed equations (see §3.4.2), where $f(t)$ will take a more complicated form.

3.3 Incorporating photon manipulation

3.3.1 Set up

As the systems are spatially separated, the QST of Eq. (3.1) happens indirectly via the exchange of a photon. The *idea* is that laser pulses induce a coherent superposition of an emitted photon (if system 1 is excited) and the vacuum (if system 1 is in the ground state). This transfers the state to the field mode, where the coherent superposition then propagates along the channel to system 2. We then want laser pulses to transfer the state of the field to system 2, inducing absorption if there was a photon.

The *problem* is that a photon emitted by system 1 will not interact strongly with and be absorbed by the heterogeneous system 2. In fact, the optimal photon wave packet for system 2 to absorb is the time-reversed wave packet a lone system 2 would emit [1]. Thus, we consider applying a unitary transformation along the channel that time reverses, frequency translates, and stretches the photon wave packet, transforming it into the time-reversed output of system 2. With an appropriately implemented unitary, carefully designed laser pulses would induce absorption in system 2, thus completing QST, as illustrated in Fig. 3.1.

Transformations of this form could be physically implemented in a single device, as proposed by Ref. 37, or by applying different transformations sequentially, say, a time lens for time reversal and stretching [40, 144], followed by quantum frequency

conversion. The scheme proposed by Ref. 37 relies on nonlinear optical processes, either sum-frequency generation (SFG) or four-wave-mixing Bragg scattering, driven by a short classical pump pulse.

Ref. 1 developed a scheme to achieve QST between distant identical atoms by producing time-symmetric photon wave packets. Incorporating photon manipulation into our scheme makes it more versatile so that we can transfer information between systems with distinct spectral properties [145] and the wave packets need not be time symmetric [146]. [For completeness we note that Ref. 139 demonstrates a method for producing a photon wave packet with a rising exponential shape, thus mimicking a time-reversed wave packet, by producing two photons and measuring one of them to herald the other. It is not clear whether such a heralding-based method could be adapted to our context, in which we need an appropriate superposition of the vacuum state and a single-photon state (conditioned on the state of system 1) in order to transmit the quantum state of one material system to another.]

To narrow our focus to the effect of the transformation, not its physical implementation, we will treat the transformation device as an idealized black box located at position $x = X$, $0 < X < c\tau$. We discuss the correspondence between this abstracted device and a potential physical implementation using SFG [37] in App. A.1.5. Thus, we compound the photon manipulations into a single unitary transformation

$$U(\nu, \nu') = \frac{e^{i\nu T}}{\sqrt{\xi}} \delta\left(\nu' + \frac{\nu - \omega_0}{\xi}\right), \tag{3.15}$$

which acts on a function in frequency space by time reversing it, scaling it by $\xi^{-1/2}$ (such that it will scale the photon flux by ξ in the time domain), and shifting it by

ω_0:

$$\tilde{F}(\nu) = \int d\nu' U(\nu, \nu') F(\nu') = \frac{e^{i\nu T}}{\sqrt{\xi}} F\left(\frac{\omega_0 - \nu}{\xi}\right). \tag{3.16}$$

It satisfies the unitarity condition

$$\int d\nu'' U(\nu, \nu'') U^*(\nu', \nu'') = \delta(\nu - \nu'). \tag{3.17}$$

We start in frequency space because the transformation would be physically implemented using nonlinear-optical processes that modify frequencies [37, 147].

The transformation can be expressed in the more intuitive time domain using Fourier transforms as

$$U(t, t') = \sqrt{\xi} e^{i\omega_0 (T-t)} \delta(t' - \tilde{t}_\xi) \tag{3.18}$$

with

$$\tilde{t}_\xi(t) := \xi(T - t), \tag{3.19}$$

where it acts on functions as

$$\tilde{F}(t) = \int dt' U(t, t') F(t'). \tag{3.20}$$

The time parameter T in the phase sets the time the transformation begins, as justified in §3.3.2. Thus, the parameters ξ, ω_0, and T can be tuned such that the transformation time reverses the slowly varying envelope of the wave packet and shifts the resonance frequency and decay rate of system 1 to those of system 2.[3]

[3]Transformations of this form suffice to realize many hybrid quantum interfaces and, within the context of our model, enable ideal QST (as shown in §3.5.3 below). However, more general wave packet shaping—beyond the time reversal and stretching operations we consider— may be necessary in some scenarios, e.g., in interfacing with the transmission line [148–150].

As the transformation of the photon wave packet occurs over a finite duration (whose start and end times have to be tuned), we may distinguish four different stages:

Stage 1 before transformation ($t < t_i$);

Stage 2 input field processing ($t_i < t < t_s$);

Stage 3 transformed field production ($t_s < t < t_f$);

Stage 4 transformation complete ($t > t_f$).

The initial field produced by system 1 freely propagates during Stage 1 until some time $t = t_i$, at which point the first part of the field to be transformed enters the transformation device at $x = X$. (We interpret these as stages of the wave packet transformation at the transformation device, though they can also be thought of as stages at system 2 with the appropriate time delay $\tau - X/c$.) Let l denote the width of the input field we want to transform with corresponding duration $t_l = l/c$. Then the transformation device will 'process' this portion of the input field (which is ideally a single-photon wave packet) during Stage 2, $t_i < t < t_s \equiv t_i + t_l$. This results in a gap[4] in the field of duration t_l during which a vacuum field $V(x,t)$, $\langle V \rangle = 0$, is produced because our system is 'buffering' until $t = t_s$ when the transformed field production begins. (See App. A.1.5 for a physical description of this buffering stage.)

The transformed wave packet is produced during Stage 3 for $t_s < t < t_f \equiv t_s + t_l/\xi$ as the wave packet is stretched by ξ in the time domain. During this field production

[4] The buffering of Stage 2 can be modeled as the activation of a c mode in the vacuum state that mixes with our input field via a time-dependent beam-splitter transformation. The c mode has creation and annihilation operators $c_{\text{in}}^\dagger$ and c_{in}, respectively, that satisfy the same commutation relations as b_{in}. Then the field being transmitted through the unitary transformation device at $x = X$ is $\cos\theta(t) b_{\text{in}}(t) - i \sin\theta(t) c_{\text{in}}(t)$, where $\theta(t)$ is a switching function that determines whether the c mode is active. Thus, θ should be a smoothed out (for continuity) square wave that is $\pi/2$ during Stage 2 of the transformation and zero elsewise.

we block any incident field from passing through X to ensure that there is always a single $f(t)$ describing the time argument of the field (making it a well-defined function), as was discussed in §3.4.2. This will result in some loss, yet the times T and t_l can be tuned to capture almost the entirety of the initial wave packet, making the loss arbitrarily small. We analyze this loss explicitly for our example in §3.5.4. After the transformation is complete at $t = t_f$, i.e., during Stage 4, any of the original field (including noise) passing through X will be unchanged and the field will freely propagate.

3.3.2 Field transformation

Consider the part of the field in Eq. (3.6) that describes the radiation propagating from system 1 to system 2, $x_1 < x < x_2$,

$$A_i^+(x,t) = A_i^+(t_-) := b_{\text{in}}(t_-) + \sqrt{\gamma_1}\sigma_1^-(t_-)\,, \tag{3.21}$$

where we recall that $t_- = t - x/c$. The first term on the right-hand side is the input to system 1 and the second is the radiation emitted by system 1. The subscript i denotes that this is the *initial* field, which will be transformed at $x = X$, before it is incident on system 2, according to Eq. (3.20) as

$$\tilde{A}_X^+(t) = \sqrt{\xi}e^{i\omega_0(T-t)}A_i^+\left(X, \tilde{t}_\xi\right). \tag{3.22}$$

We can now determine the interval of time for which this transformed outgoing field is valid. For the transformation to be causal the field must depend on past times, $t \geq \tilde{t}_\xi$, such that $t \geq t_s \equiv T/(1+\xi^{-1})$, which defines the physical meaning of T.

The transformed field being produced during Stage 3 will freely propagate for $x \geq X$ after the transformation as

$$\tilde{A}^{+}(x,t) = \tilde{A}^{+}_{X}\left(t - \frac{x-X}{c}\right) = \sqrt{\xi} e^{i\omega_0(T - t_- - X/c)} A_i^{+}\left[\mathcal{T}(t_-)\right], \tag{3.23}$$

with $\mathcal{T}(t_-) := \tilde{t}_\xi(t_-) - (1+\xi)X/c$ as shorthand. To produce a field with a decay rate matching system 2 we select

$$\boxed{\xi = \gamma_2/\gamma_1.} \tag{3.24}$$

Then, comparing the original and transformed fields at system 2, $x = x_2 = c\tau$, we find that the system 1 operators transform as

$$\sqrt{\gamma_1}\sigma_1^{-}(t-\tau) \to \sqrt{\gamma_2} e^{i\omega_0(T - t + \tau - X/c)} \sigma_1^{-}\left[\mathcal{T}(t-\tau)\right] \tag{3.25}$$

and similarly for b_{in}, giving us the transformed, τ-delayed, operators that impact the evolution of system 2 operators via the $c_2(t)$ terms in Eq. (3.13).

Thus, the field propagating between the systems during any Stage is

$$A^{+}(x,t) = \begin{cases} V(x,t), & x \geq X, t_i < t - \frac{x-X}{c} < t_s \\ \tilde{A}^{+}(x,t), & x \geq X, t_s < t - \frac{x-X}{c} < t_f \\ A_i^{+}(x,t), & \text{elsewise} \end{cases}. \tag{3.26}$$

The first case in Eq. (3.26) captures the processing of the portion of the wave packet to be transformed in Stage 2, during which a vacuum field V is produced (see footnote 4). The second case captures the production and free propagation of the transformed field. The third case captures the free propagation of the initial field.

For $x \geq X$, this general expression for the field only depends on x and t in terms of the combined variable t_-, so we can write it in the form

$$A^+(x \geq X, t) = A^+(t_-) = \chi(t_-) A_i^+(f(t_-)). \tag{3.27}$$

Henceforth taking $X = 0$ for simplicity ($X \neq 0$ adds trivial shifts that obfuscate the expression, without affecting our ultimate effective description), we have

$$\chi(t) = \begin{cases} \sqrt{\xi} e^{i\omega_0(T-t)}, & t_s < t < t_f \\ 1, & \text{elsewise} \end{cases} \tag{3.28}$$

and

$$f(t) = \begin{cases} \text{undefined}, & t_i < t < t_s \\ \tilde{t}_\xi = \xi(T-t), & t_s < t < t_f \\ t, & \text{elsewise} \end{cases}, \tag{3.29}$$

where $A_i^+(f = \text{undefined})$ is interpreted to be the vacuum V (see footnote 4).

3.4 Schrödinger picture evolution

Now we can relate the Heisenberg picture evolution of system operators, to the Schrödinger picture evolution of the state. This will allow us to derive the effective Hamiltonian governing the smooth system evolution within the context of the quantum trajectory method.

3.4.1 Without transformation

The identity

$$\mathrm{Tr}(\rho_H \dot{s}(t)) = \mathrm{Tr}(\dot{\rho}_S(t) s) \tag{3.30}$$

connects the Heisenberg picture operator and state on the left to the Schrödinger picture operator and state on the right. Using this identity, the cyclic nature of the trace, and Eq. (3.11), we find the evolution equation for the systems and field to be

$$\dot{\rho}_S = \sum_{j=1}^{2} \left(\left[\sigma_j^-, \rho_S c_j^\dagger \right] - \left[\sigma_j^+, c_j \rho_S \right] \right) - i[H_{\mathrm{sys}}, \rho_S]. \tag{3.31}$$

In the Schrödinger picture the operators no longer evolve with time as any implicit time dependence is shifted onto $\rho_S(t)$.

The transmission can be described in an effective description where the two systems are directly coupled. This effective description is obtained by tracing over the bath, yielding the state of the systems

$$\rho(t) = \mathrm{Tr}_{\mathrm{B}}(\rho_S), \tag{3.32}$$

which is the same state as in Eq. (3.14). Considering coherent input states to the systems $|\beta\rangle\langle\beta|$ such that $b_{\mathrm{in}}|\beta\rangle = \beta|\beta\rangle$ with $\beta \in \mathbb{C}$ and

$$\mathrm{Tr}_{\mathrm{B}}(b_{\mathrm{in}} \rho_S) = \beta \rho, \tag{3.33}$$

we find that ρ satisfies Eq. (3.31) with $b_{\rm in} \to \beta$. After some algebra, we can write this master equation for $\dot{\rho}$ in the Lindblad form

$$\dot{\rho} = i[\rho, H_0] + \mathcal{L}[J]\rho. \tag{3.34}$$

The governing Hamiltonian is $H_0 = H_{\rm sys} + H_c$ with

$$H_c = \frac{-i}{2}\left[\sqrt{\gamma_1\gamma_2}\sigma_2^+\sigma_1^- + \left(\sqrt{\gamma_1}\sigma_1^+ + \sqrt{\gamma_2}\sigma_2^+\right)\beta\right] + \text{Hc} \tag{3.35}$$

describing the coupling between the systems. Relative to the von Neumann equation, the Lindblad superoperator, $\mathcal{L}[J]$, is the 'new object' characterizing damping due to the bath. It acts as

$$\mathcal{L}[J]\rho = J\rho J^\dagger - \frac{1}{2}\left\{\rho, J^\dagger J\right\} \tag{3.36}$$

with jump operator

$$J = \sqrt{\gamma_1}\sigma_1^- + \sqrt{\gamma_2}\sigma_2^- + \beta, \tag{3.37}$$

corresponding to the total output field emanating from the second system, and $\{\cdot,\cdot\}$ is the anticommutator.

Now the connection to the quantum trajectory method can be made. There is smooth evolution governed by a Schrödinger-like equation with a non-Hermitian effective Hamiltonian

$$H_{\rm eff} = H_0 + H', \tag{3.38}$$

where $H' = -iJ^\dagger J/2$ is the non-Hermitian piece. Additionally, random quantum jumps occur, with probability density $\langle\psi|J^\dagger J|\psi\rangle$, leading to wavefunction decay [122]. (This quantum trajectory formalism can be shown to be equivalent to the standard Lindblad master equation dynamics for the density matrix provided we

average $|\psi\rangle\langle\psi|$ over an ensemble of $|\psi\rangle$'s random trajectories [141].) Writing out the effective Hamiltonian explicitly, we find

$$H_{\text{eff}} = H_{\text{sys}} - \frac{i}{2}\left[\gamma_1\sigma_1^+\sigma_1^- + \gamma_2\sigma_2^+\sigma_2^- + 2\sqrt{\gamma_1\gamma_2}\sigma_1^-\sigma_2^+ + 2\beta\left(\sqrt{\gamma_1}\sigma_1^+ + \sqrt{\gamma_2}\sigma_2^+\right) + |\beta|^2\right], \tag{3.39}$$

where the $\sigma_1^-\sigma_2^+$ term survives, not its Hermitian conjugate. This describes an excitation in the first system transferring to the second, but not the other way around.

3.4.2 With transformation

By implementing our transformation, the output of system 1 transforms according to Eq. (3.26) in the Heisenberg picture. Thus, the transformed EOM for s_2 depends on system 1 and field operators at time $\tilde{t} \equiv f(t-\tau)$ and on system 2 operators at the same time t. The transformed EOM for s_1 only depends on operators at a single time $f(t)$, which can be shifted to $\tilde{t} = f(t-\tau)$. Specifically, we start with the transformed Heisenberg EOMs for system operators s_j, which are given by Eq. (3.11) with the replacements $\sigma_1^-(t) \to \chi(t-\tau)\sigma_1^-(\tilde{t})$ for system 1 evolution including via c_1 and $\sigma_1^-(t-\tau) \to \chi(t-\tau)\sigma_1^-(\tilde{t})$ for system 2 evolution via c_2, and likewise for b_{in}.

Then we go to the Schrödinger evolution of the total transformed state of the systems and bath, $\tilde{\rho}_S(t)$, in the same manner as in §3.4.1. Tracing over the bath yields the reduced density operator describing the (fictitious) composite state of the systems that would produce the transformed wave packet

$$\rho(t) = \text{Tr}_{\text{B}}(\tilde{\rho}_S(t)) = \rho_1(\tilde{t}) \otimes \rho_2(t). \tag{3.40}$$

This transformed state satisfies the same Lindblad master equation as before with the transformation being accounted for by the change in the time argument of system 1, and the replacements $\sigma_1^- \to \chi(t-\tau)\sigma_1^-$ and $\beta \to \chi(t-\tau)\beta$, that is, the transformed operators acquire an explicit time-dependent prefactor in the Schrödinger picture. Here $\rho_1(\tilde{t})$ describes the real (τ-delayed) system 1 during Stages 1 and 4, the lack of system 1 during Stage 2, and a fictitious system $\tilde{1}$ at time $\xi(T-t+\tau)$ during Stage 3.

This Heisenberg $\leftrightarrow$ Schrödinger conversion works in a similar way as before because the unitary transformation to the field has the effect of transforming system 1 and field operator arguments from $t-\tau$ to $f(t-\tau)$. In the Schrödinger picture the same unitary is applied to the state, with the same effect on its argument t. Specifically, during the transformation, ρ_1's time argument has slope $-\xi$ corresponding to the fictitious system $\tilde{1}$ evolving backward in time (as the slope is negative) at a new decay rate due to the ξ scaling. Meanwhile system 2 is continually described by $\rho_2(t)$, as in Eq. (3.14).

Naively, the jumps in $f(t)$, and hence $\tilde{t}$ (see Fig. 3.2), seem to indicate that system 2 operators would have discontinuities in their evolution as they are being driven by system $\tilde{1}$, which experiences discontinuities when the Stage changes. Yet at t_i system 1 is just leaving one of its ground states (the cavity ground state in §3.5) and at t_s the decay of the first system is nearly complete (assuming t_l and T are chosen appropriately), so again system 1 will be near a ground state. Hence the coupling between the systems is effectively zero in both cases as system 1 is (at least nearly) in a ground state, which yields zero if acted on by the annihilation operator σ_1^-. This likewise applies to the vertical jump in $f(t)$ at t_f. Moreover, system $\tilde{1}$'s evolution will be smoothed out by the gradual switching to and from the vacuum field $V(x,t)$

during Stage 2 (see footnote 3). Thus, system 2 will evolve smoothly even though $f(t)$ has discontinuities.

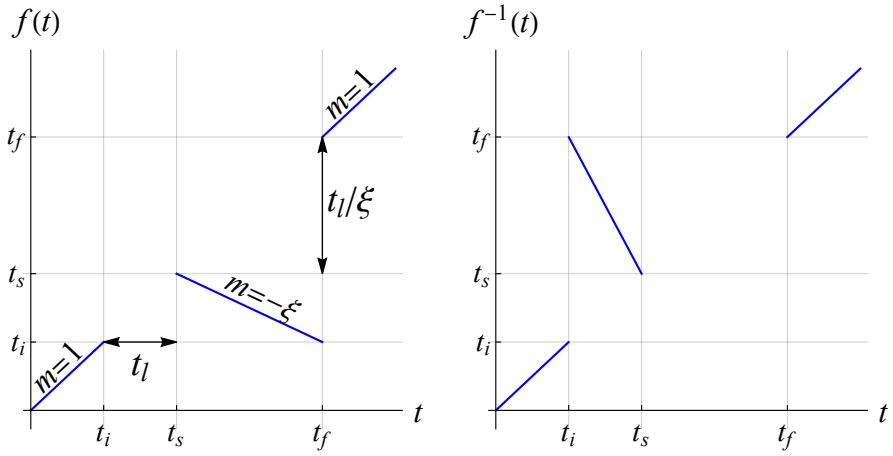

FIGURE 3.2. Plots of $f(t)$ and $f^{-1}(t)$ for $X = 0$, $\xi = 1/2$. $f^{-1}(t)$ is a fictitious time for system 2 as a function of the time for system 1. In the first plot m denotes the slope of different portions of $f(t)$. The horizontal gap of width t_l is due to the buffering of Stage 2 and the vertical gap of height t_l/ξ is due to us blocking the initial wave packet during Stage 3.

3.5 Three-level atoms in cavities

3.5.1 Hamiltonians

We are only concerned with systems that can controllably emit and absorb single photons, i.e., that can realize the Jaynes–Cummings interaction. As a concrete example, we focus on the case where each system, $j = 1, 2$, is comprised of a three-level atom (or ion), in the Λ-configuration with excited state $|r_j\rangle$ and ground states $|g_j\rangle$ and $|e_j\rangle$, that is strongly coupled to a mode of its respective high-Q cavity with frequency ω_{cj} and annihilation operator a_j, which takes the role of σ_j^- (see Fig. 3.3). [Importantly, however, the scheme applies more generally to any systems that can realize such controlled light-matter interaction at the single excitation level, which

includes solid-state and superconducting systems (see §4.2.3 and App. A.1.2).] We take $|g_j\rangle$ to be the zero point of energy, $E_g = 0$, so $|r_j\rangle$ has excitation frequency ω_{rj} and the energy difference between $|e_j\rangle$ and $|g_j\rangle$ is $E_{ej} - E_{gj} = \omega_{ej}$ (previously denoted ω_{eg}). This example and the underlying scheme extend and are based on the pioneering work of Ref. 1 on QST in a quantum network. What we change, relative to Ref. 1, is that the systems are not identical (they can have different parameters including resonance frequencies, ω_{rj}, and decays rates, γ_j) and we incorporate our unitary transformation into the scheme. Additionally, Ref. 1 assumed degenerate ground states as they had a Cs atom in mind. As we want our scheme to apply more generally we do not assume the ground states to be degenerate ($\omega_{ej} \neq 0$). This is a small change to the Hamiltonian but makes it applicable to a larger variety of implementations: trapped ion qubits are generally not degenerate (e.g., two different hyperfine ground states or an S ground state and a metastable D state), superconducting qubits states are never degenerate, etc.

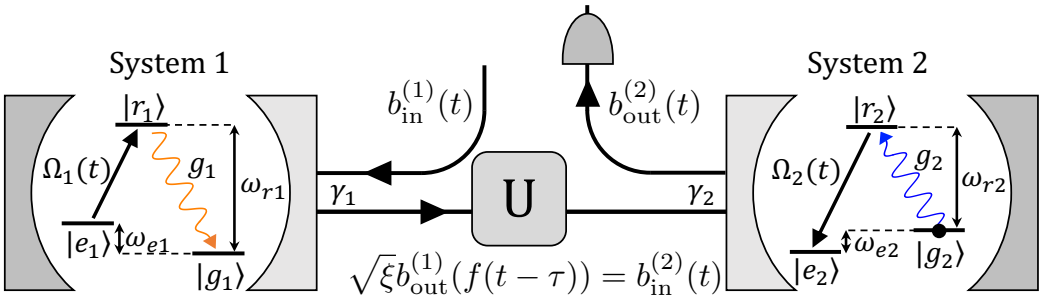

FIGURE 3.3. Schematic depiction of three-level atoms in cavities coupled via a quantum channel along which a unitary transformation is implemented (adapted from Ref. 1). The black arrows indicate laser pulses that induce emission in system 1 and absorption in system 2 (see the text for an explanation). We assume the input field to cavity 1 is in vacuum, $\langle b_{\text{in}}^{(1)} \rangle = 0$.

We will now relay the steps from Ref. 1 that are crucial to this work. The idea is that for each system, $|e\rangle$ and $|g\rangle$ are coupled by a Raman transition and form our qubits. Specifically, we drive an excitation from $|e_1\rangle$ to $|r_1\rangle$ using a laser pulse of frequency ω_{L1} with Rabi frequency $\Omega_1(t)$ and phase $\phi_1(t)$. This is followed by the transition $|r_1\rangle \to |g_1\rangle$ and the corresponding emission of a photon into cavity 1 with coupling g_1. The photon leaks out of the cavity as a wave packet and propagates down the quantum channel and enters cavity 2. Next, atom 2 undergoes the time inverse of the Raman process undergone by atom 1 [with different parameters g_2, ω_{L2}, $\Omega_2(t)$, and $\phi_2(t)$]. The photon is then either absorbed, exciting atom 2 from $|g_2\rangle$ (where it is initialized) to $|e_2\rangle$, such that its state is transferred to atom 2 or reflected down a different spatial mode (e.g., via a ring cavity geometry) and the transfer fails.

We want to design the first laser pulse (including its phase) to ensure that if there is an excitation in atom 1, it is transferred to cavity 1, and then to the channel. Here we assume that a photon emitted by system 1 will make it to system 2, deferring the treatment of absorption in the transmission line and other common errors to Ch. IV. Furthermore, we do not want any other excitations to potentially be transferred to atom 2. Hence we assume a vacuum field input field to system 1, $b_{\text{in}}^{(1)}|\text{in}\rangle = 0$, where the input and output of each cavity are related by [1, 108]

$$b_{\text{out}}^{(j)}(t) = b_{\text{in}}^{(j)}(t) + \sqrt{\gamma_j}a_j(t), \tag{3.41}$$

which comes from splitting up Eq. (3.8) with $\sigma_j^- \to a_j$.

In *our scheme*, the corresponding photon wave packet is manipulated while propagating between the systems, so the input to cavity 2 is the transformed (and time-delayed) output of cavity 1. Thus, we also want to design the unitary transformation and the second laser pulse to minimize loss due to reflection at system

2, and hence achieve ideal QST. The total system Hamiltonian is $H_{\rm sys} = H_1 + H_2$, where

$$H_j = \omega_{cj} a_j^\dagger a_j + \omega_{rj} |r_j\rangle\langle r_j| + \omega_{ej} |e_j\rangle\langle e_j| + g_j \left(|r_j\rangle\langle g_j| a_j + \text{Hc}\right) + \frac{\Omega_j(t)}{2}\left(e^{i\left[\omega_{Lj} t + \phi_j(t)\right]} |e_j\rangle\langle r_j| + \text{Hc}\right) \tag{3.42}$$

is the Hamiltonian for system j. For each system, $j = 1, 2$, we go into rotating frames via transformations of the form $U = \exp\left[i\omega_{\rightsquigarrow} t(a^\dagger a + |r\rangle\langle r|) + i\omega_e t |e\rangle\langle e|\right]$. Here $\omega_{\rightsquigarrow} = \omega_L + \omega_e$ is a parameter of the unitary frame change. Its value is tuned to simplify the dynamics in the rotating frame and it will ultimately correspond to the photon frequency of the corresponding system. Intuitively (and physically) this can be understood as the photon frequency being equal to the laser frequency if the states $|g\rangle$ and $|e\rangle$ are degenerate and, meanwhile, shifting in an energy conserving manner for non-degenerate states. [If you like, you can imagine $\omega_{\rightsquigarrow}$ as a free parameter, whose specific value given above is chosen so that the last term in Eq. (3.43) has the simple phase structure shown.] The $\omega_e |e\rangle\langle e|$ term is used to make the two atomic ground states effectively degenerate, which makes the treatment more similar to Ref. 1.

Then, assuming the lasers are strongly detuned $|\Delta_j| \gg \Omega_j, g_j, |\dot{\phi}_j|$ (where $\Delta_j = \omega_{\rightsquigarrow j} - \omega_{rj} = \omega_{Lj} - \omega_{re,j}$ is the laser detuning relative to transition frequency, $\omega_{re,j} = \omega_{rj} - \omega_{ej}$) to suppress spontaneous emission, we can adiabatically eliminate the excited state $|r\rangle$ [151]. Doing so, the new system Hamiltonians are

$$H_j = \left(\frac{g_j^2}{\Delta_j} |g_j\rangle\langle g_j| - \delta_j\right) a_j^\dagger a_j + \delta\omega_j(t) |E_j\rangle\langle E_j| - iG_j(t)\left(a_j |E_j\rangle\langle g_j| - \text{Hc}\right), \tag{3.43}$$

where $\delta_j = \omega_{\rightsquigarrow j} - \omega_{cj}$, $\delta\omega_j(t) := \Omega_j^2(t)/4\Delta_j$, and $G_j(t) := g_j \Omega_j(t)/2\Delta_j$ are the Raman detunings, the ac Stark shifts to $|E_j(t)\rangle := e^{i\phi_j(t)} |e_j\rangle$, and the Jaynes–Cummings

interaction strengths for the effective two-level atoms, respectively [1]. Note that relative to Eq. (3.42), we rephased $\phi_j \to \phi_j + \pi/2$ so that the pulses G_j are real.

3.5.2 System evolution

Now we want to determine how the state of the systems, expanded as

$$|\psi(t)\rangle = \alpha_1(t)|Eg\rangle|00\rangle + \alpha_2(t)|gE\rangle|00\rangle + \beta_1(t)|gg\rangle|10\rangle + \beta_2(t)|gg\rangle|01\rangle, \qquad (3.44)$$

will evolve. The basis states, read from left to right, give the states of atoms 1, 2 (E or g), and the states of cavities 1, 2 (0 or 1). We leave out a $|gg\rangle|00\rangle$ term because, in the absence of noise, the zero-excitation part of the transfer in Eq. (3.1), $c_g|g_1\rangle|g_2\rangle \mapsto c_g|g_1\rangle|g_2\rangle$, is trivial. That is, the full state is $c_g|gg\rangle|00\rangle + c_e|\psi(t)\rangle$, yet we focus on the nontrivial dynamics of the single-excitation subspace. Now we will go from the Heisenberg picture, in which system operators satisfy Eq. (3.11), to the Schrödinger picture. In doing so, we will work with time-delayed operators and variables for system 1 [e.g., $\sigma_1^-(t-\tau) \to \sigma_1^-(t)$ and so forth for b_{in}, Ω_1, and ϕ_1], effectively eliminating the time delay τ.

As discussed in §3.4, this Heisenberg to Schrödinger picture conversion can be described using the quantum trajectory method, where $|\psi\rangle$ experiences smooth evolution governed by a non-Hermitian effective Hamiltonian H_{eff} as well as discrete quantum jumps, where a jump operator J is randomly applied to the state of our two systems (then the state has to be renormalized $|\psi\rangle \to J|\psi\rangle/\langle\psi|J^\dagger J|\psi\rangle$) [122]. Employing this method, we find that for a vacuum field input to system 1, the effective

Hamiltonian in the rotating frame used above is

$$H_{\text{eff}} = H_1 + H_2 - \frac{i}{2}\Big(\gamma_1 a_1^\dagger a_1 + \gamma_2 a_2^\dagger a_2 + 2\sqrt{\gamma_1\gamma_2} e^{i\zeta t} a_2^\dagger a_1\Big) \tag{3.45}$$

[see Eq. (3.39) with $\beta = 0$ and $\sigma_j^- \to a_j$], where $H_{1,2}$ are the Raman Hamiltonians of Eq. (3.43) and $\zeta \equiv \omega_{\rightsquigarrow 2} - \omega_{\rightsquigarrow 1}$ is a frequency mismatch that degrades the QST when the unitary transformation is not applied. The corresponding phase factor, $e^{i\zeta t}$, comes from two different rotating frames for the two systems.

We find the state amplitude EOMs

$$\dot{\alpha}_1 = -G_1\beta_1, \tag{3.46a}$$

$$\dot{\beta}_1 = G_1\alpha_1 - \frac{\gamma_1}{2}\beta_1, \tag{3.46b}$$

$$\dot{\alpha}_2 = -G_2\beta_2, \tag{3.46c}$$

$$\dot{\beta}_2 = G_2\alpha_2 - \frac{\gamma_2}{2}\beta_2 - \sqrt{\gamma_1\gamma_2} e^{i\zeta t}\beta_1, \tag{3.46d}$$

where we picked laser phases and detunings that satisfy $-\dot{\phi}_j \equiv \delta\omega_j$ and $\delta_j = g_j^2/\Delta_j$, respectively (see App. A.2.5 for further considerations). These laser phase conditions entail that ϕ_j is determined by the pulse Ω_j (up to an initial condition), so as to dynamically compensate for the ac Stark shifts. The condition $\delta = g^2/\Delta$ (for each system, $j = 1, 2$) implies that the laser detunings satisfy

$$\Delta = \omega_{\rightsquigarrow} - \omega_r = \frac{\omega_c - \omega_r}{2} \pm \sqrt{\left(\frac{\omega_c - \omega_r}{2}\right)^2 + g^2}, \tag{3.47}$$

where $|\Delta| \gg g$ so the "+" solution is valid and hence we must pick specific laser frequencies:

$$\omega_L = \omega_c - \omega_e + \frac{g^2}{\omega_c - \omega_r} + \mathcal{O}\left(\frac{g^4}{(\omega_c - \omega_r)^3}\right). \tag{3.48}$$

It follows that, up to the energy shift of $|e\rangle$ relative to $|g\rangle$, we need to lase near the cavity resonance: $\omega_L \approx \omega_c - \omega_e$ (note that $|\omega_e|$ is typically small relative to ω_c). Thus, as one might expect, the photon frequency will be close to the cavity resonance: $\omega_{\rightsquigarrow} \approx \omega_c$. We assume these conditions are met, that is, we assume the Raman process is two-photon resonant once all shifts are taken into account. We do not consider errors due to a nonzero Raman detuning, though they can naturally be incorporated into the formalism.

Remarks:

(i) The EOMs for system 2 are the same as those for system 1 except for the β_1 term in Eq. (3.46d), which encapsulates how an excitation in cavity 1 is transferred to cavity 2. Because G_j are real, with the phases $\phi_j(t)$ factored out and tuned to satisfy $-\dot{\phi}_j \equiv \delta\omega_j$, α_1 and β_1 are real. Meanwhile, α_2 and β_2 will be complex for $\zeta \neq 0$ (which is why we will tend to plot their magnitudes).

(ii) We provided some context for 'rotating frames' when considering the interaction picture in §2.2.4. The utility and physical basis for such frame changes is nicely summarized by Gardiner and co-authors on the first page of Ref. 122 as "Choosing the interaction picture leaves all the fast but uncomplicated optical time development in the operators, while the slower, but more difficult fluctuation and damping phenomena take place in the state vector, and are thus represented by a linear equation."

(iii) In Ref. 3, we, admittedly somewhat cryptically, mixed frames considering the transformed states $|e'\rangle = U|e\rangle = e^{i\omega_e t}|e\rangle$ within the simplified system Hamiltonian analogous to Eq. (3.43). Doing so, although technically fine, obfuscates the physical description including physical quantities such as laser and photon frequencies. Accordingly, here we opted to directly account for the impact of ω_e on the laser frequency, through its inclusion in the rotating frame frequency $\omega_{\rightsquigarrow} = \omega_L + \omega_e$.

3.5.3 Photon transformation

So far, this section is just a generalization of Ref. 1 to non-identical, non-degenerate systems. Our larger modification is incorporating the effect of the unitary transformation so that the two non-identical systems naturally interact with each other. Thus we will now analyze the impact of the unitary transformation on the amplitude EOMs. The photon wave packet emitted by system 1 can be specified by the mode function

$$\Psi_1(t) := \langle gg|\langle 00|b_{\text{out}}^{(1)}|\psi(t)\rangle, \tag{3.49}$$

whose modulus squared is the expectation value of the number operator for the output of cavity 1, $N_1 = \left(b_{\text{out}}^{(1)}\right)^\dagger b_{\text{out}}^{(1)}$, with respect to the state $|\psi\rangle$:

$$\langle N_1(t)\rangle = |\Psi_1(t)|^2. \tag{3.50}$$

For a vacuum field input

$$\Psi_1(t) = \langle gg|\langle 00|\sqrt{\gamma_1}a_1|\psi\rangle = \sqrt{\gamma_1}\beta_1(t). \tag{3.51}$$

The transformed (tilded) cavity creation operator can be found using Eq. (3.25) at system 1 (again with $X = 0$) with $\sigma_1^- \to a_1$ to be

$$\tilde{a}_1(t) = \chi(t) a_1(f(t)). \tag{3.52}$$

It follows that the transformed wave packet is

$$\tilde{\Psi}_1(t) = \langle gg|\langle 00|\sqrt{\gamma_1}\tilde{a}_1|\psi\rangle = \sqrt{\gamma_1}\chi(t)\beta_1(f(t)) \tag{3.53}$$

so that system 2 is driven by the transformed amplitude

$$\beta_1(t) \to \tilde{\beta}_1(t) = \chi(t)\beta_1(f(t)), \tag{3.54}$$

whose form varies depending on what Stage of the transformation we are considering and we interpret $\beta_1(f = \text{undefined}) \equiv 0$. Hence under the transformation, Eq. (3.46d) becomes

$$\dot{\beta}_2 = G_2\alpha_2 - \frac{\gamma_2}{2}\beta_2 - \sqrt{\gamma_1\gamma_2}e^{i\zeta t}\tilde{\beta}_1 \tag{3.55}$$

with the other equations (3.46a-c) remaining the same. For $t_s < t < t_f$ this gives

$$\dot{\beta}_2 = G_2\alpha_2 - \frac{\gamma_2}{2}\beta_2 - \gamma_2 e^{i\omega_0 T}e^{i(\zeta-\omega_0)t}\beta_1(\tilde{t}_\xi), \tag{3.56}$$

which motivates the choice

$$\boxed{\omega_0 = \zeta \equiv \omega_{\rightsquigarrow 2} - \omega_{\rightsquigarrow 1} = \omega_{L2} - \omega_{L1} + \omega_{e2} - \omega_{e1}} \tag{3.57}$$

for the frequency shift of the transformation in order to cancel out the time-dependent phase in the last term of Eq. (3.55) during Stage 3.

Note that, as we are working in a carefully chosen rotating frame for the cavity modes at the photon frequency $\omega_{\rightsquigarrow 1} = \omega_{L1} + \omega_{e1}$, the transformed wave packet, $\tilde{\Psi}_1(t)$, corresponds to a slowly varying envelope function (at least during Stage 3). Thus, the corresponding wave packet in the Schrödinger picture is $\Psi_S(t) = e^{-i\omega_{\rightsquigarrow 1}t}\Psi(t)$ such that during the transformation, assuming the transformation parameters are ideal, $\Psi_S(t_s < t < t_f) = \sqrt{\gamma_2}e^{-i\omega_{\rightsquigarrow 2}t}\beta_1(\xi(T-t))e^{i\zeta T}$, which makes the shift in central frequency from $\omega_{\rightsquigarrow 1}$ to $\omega_{\rightsquigarrow 2}$, decay rate change from γ_1 to γ_2, and time reversal manifest (up to the known phase $e^{i\zeta T}$).

Now the problem is to find the pulse shapes $G_j \propto \Omega_j$ such that ideal QST occurs when we implement our unitary transformation, that is, we want

$$\alpha_1(-\infty) = 1 \tag{3.58a}$$

$$|\alpha_2(+\infty)| = 1 \tag{3.58b}$$

(with the other amplitudes equal to zero at these times due to normalization). The condition of Eq. (3.58a) can be accomplished via standard local state preparation methods. Additionally, we want to ensure that the relative phase between $|g\rangle$ and $|e\rangle$ is transferred. This can be done using a local oscillator at the location of each system, $j = 1, 2$, with frequency ω_{ej} to serve as a well-defined frequency reference that the fast varying phase of the qubit can be tracked with respect to. We assume this is done, that the noise in each local oscillator is negligible, and that the two local phases are stabilized relative to each other [152, 153]. Under these assumptions, we may regard

the probability of excitation transfer as the success probability of the protocol:

$$P_{\text{success}} \equiv |\alpha_2(t \to \infty)|^2. \tag{3.59}$$

Here we are guided by the expectation that the laser pulse inducing absorption in system 2, G_2, must be time reversed and stretched relative to the pulse inducing the emission of system 1, G_1. Specifically, we let

$$G_2(t) = \xi G_1(\tilde{t}_\xi) \tag{3.60}$$

such that given solutions α_1 and β_1 there are corresponding solutions $\beta_2(t) = -e^{i\omega_0 T}\beta_1(\tilde{t}_\xi)$ and $\alpha_2(t) = e^{i\omega_0 T}\alpha_1(\tilde{t}_\xi)$. Note that we are not optimizing G_2 for every parameter value (starting time t_i, duration t_l, etc.). Rather, we select this pulse as it is agnostic to such details, working generally as long as l is large enough for (almost) all of wave packet to be transformed. With this choice for G_2, constructing G_1 such that $\alpha_1(-\infty) = 1$ ensures that $|\alpha_2(+\infty)| = 1$ for sufficiently large l (assuming both pulses are implemented correctly). Moreover, note that there is an intrinsic limit to the success probability of deterministic QST based on how good the emitters and cavities are at coupling to the desired modes (as quantified by so-called cooperativity parameters) [154, 155], we will return to this and other realistic errors in §4.2.5.

To guarantee that the state's phase is transferred one must do two things: Use the local oscillators mentioned above to define clocks relative to which one can account for free precession, and account for the extra phase $e^{i\omega_0 T}$ that appears in α_2 due to the unitary.[5] This argument implicitly assumes that $\tilde{\beta}_1(t) = \sqrt{\xi}e^{i\omega_0(T-t)}\beta_1(\tilde{t}_\xi)\ \forall t$, which

[5]We get the phase factor $\exp(i\omega_0 T)$ only when we apply the unitary (Stage 3). So if some of the untransformed portion of the photon is absorbed by system 2, we would induce a phase error.

is only valid during Stage 3. However, if we transform enough of the wave packet (make l big) β_1 will be negligibly small outside of Stage 3, making this an increasingly good approximation as l increases.

Now our task is to find a pulse G_1 such that the boundary conditions of Eq. (3.58) are satisfied. From Eqs. (3.46a–b) we find that α_1 and G_1 uniquely determine each other. Thus, we can reframe the task as specifying an α_1 that goes from 1 at $t = -\infty$ to 0 at $t = +\infty$,[6] from which the first pulse is uniquely specified:

$$G_1(t) = \frac{-\dot{\alpha}_1 e^{\gamma_1 t/2}}{\sqrt{e^{\gamma_1 t_p}\beta_1^2(t_p) - 2\int_{t_p}^{t} dt' e^{\gamma_1 t'}\dot{\alpha}_1(t')\alpha_1(t')}}. \tag{3.61}$$

Here t_p is some early time by which the first atomic state is *prepared* in the desired superposition state, $c_g|g_1\rangle + c_e|e_1\rangle$, so $\beta_1(t_p)$ should be zero.[7]

A natural choice of α_1 is the logistic function

$$\alpha_1(t) = \frac{1 + \tanh(-kt)}{2}, \tag{3.62}$$

from which we can find the corresponding pulse G_1 via Eq. (3.61) and $\beta_1 = -\dot{\alpha}_1/G_1$ from Eq. (3.46a). We assume the laser pulse applied to system 1, G_1, is implemented perfectly. The ability to control the shape and timing of single-photon pulses has been demonstrated experimentally for similar systems [156]. Then we can solve for

---

We assume either that the frequency shift $\omega_0 = \zeta$ is so large that the photon will not be absorbed without our unitary, or that we control ω_0 and T such that $\omega_0 T = 0$ (modulo 2π) when ω_0 is small.

[6]Note that only some amplitude functions $\alpha_1(t)$ have a corresponding pulse $G_1(t)$ that produces them because the argument of the square root in Eq. (3.61) must be positive as G_1 is real (the corresponding phase $\phi_1(t)$ has already been taken out). However, any positive α_1 that monotonically decreases, as we have here, can be produced. The class of possible solutions $\{\alpha_1, \beta_1\}$ will be studied in App. A.2.5.

[7]Note that in Eq. (48) of Ref. 3, we mistakenly claimed that Eq. (3.61) was only specified up to a sign. This is incorrect as the sign is dictated by Eq. (3.46a), see App. A.2.2.

α_2 and β_2 numerically using Eqs. (3.46c), (3.55), and (3.60). We plot the solutions and the corresponding laser pulses below in Fig. 3.4. Additionally, we plot the photon wave packet's square modulus for the various stages of the transformation in Fig. 3.5. In our plots we work in natural units based on the rate γ_2 and the speed of light c; so times are in units of γ_2^{-1}, lengths are in units of $c\gamma_2^{-1}$, etc.

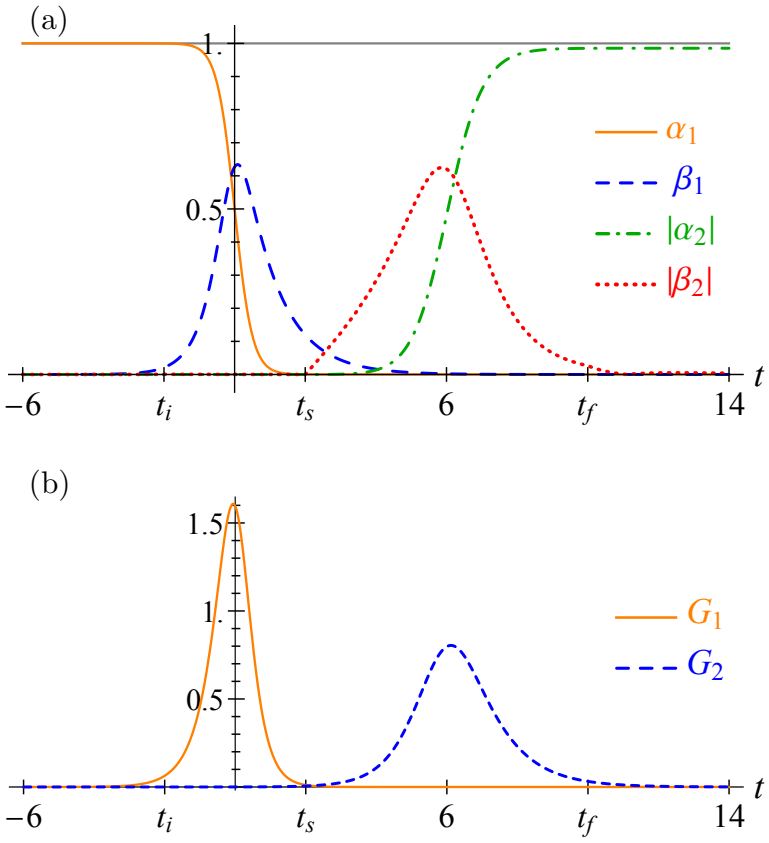

FIGURE 3.4. (a) Probability amplitudes and (b) corresponding laser pulses $G_{1,2}$ plotted as functions of time t (all quantities are in units where $\gamma_2 = 1$). Here α_1 is a logistic function of the form of Eq. (3.62) with $k = 2$ and we take $T = 6$, $\xi = 1/2$, $\omega_0 = \zeta = 50$, and $t_l = 4$. Atom 1 is initially excited, $\alpha_1^2(-\infty) = 1$, and this excitation is transferred to atom 2 with probability $|\alpha_2(\infty)|^2 = 0.97$ ($|\alpha_2|$ falls just below 1, the upper line, for large t).

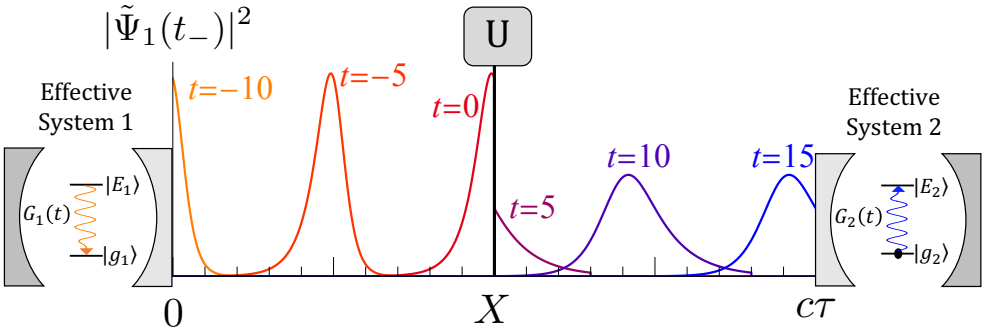

FIGURE 3.5. Plot of $|\tilde{\Psi}_1(t_-)|^2$ vs x for various t (in units of γ_2^{-1}), illustrating the propagation of the photon for a logistic α_1 with the same parameters as in Fig. 3.4. The wave packet propagates until $t_i = -2$, at which point it begins being processed until $t_s = 2$. The transformed wave packet is produced until $t_f = 10$, and then it propagates freely and induces absorption in system 2 with 97% success rate. Here we let $X = c\tau/2$ for illustration.

3.5.4 Two types of loss

We can quantify whether we succeeded in transferring the quantum state from system 1 to 2 by analyzing two kinds of loss that are present in our scheme: loss due to blocking the incident field from propagating through $x = X$ during Stage 3 and loss due to an imperfect photon wave-packet shape leading to the field being reflected from system 2 out another spatial mode, which occur with probabilities of P_b and P_p, respectively. The probability density functions for these losses are

$$\dot{P}_b = \begin{cases} \gamma_1 |\beta_1|^2, & t_s < t < t_f \\ 0, & \text{elsewise} \end{cases}, \tag{3.63}$$

as we block the incident field during Stage 3, and

$$\dot{P}_p = \left| \sqrt{\gamma_1} e^{i\zeta t} \tilde{\beta}_1 + \sqrt{\gamma_2} \beta_2 \right|^2, \tag{3.64}$$

which comes from looking at the decay of the norm of the effective state due to the unitary transformation and accounts for the interference between the cavity amplitudes. Without the unitary, $\dot{P}_p$ is simply minus the time derivative of the norm state of $|\psi\rangle$.[8] The total quantum jump rate up to time t is then

$$P_{\text{jump}}(t) = \int_{t_p}^{t} dt' \left[\dot{P}_b(t') + \dot{P}_p(t')\right] \tag{3.65}$$

as illustrated in Fig. 3.6.

For Figs. 3.4–3.6 we selected the parameter values $T = 6$, $\xi = 1/2$, $\omega_0 = \zeta = 50$, and $l = 4$ such that $t_i = -t_s = -2$ because G_1 is large during this window (see Fig. 3.4b). This is a good choice but not the ideal choice, which for the same values of ξ, ω_0, ζ, and l involves choosing $T = 7.8$ such that $t_i = -1.4$. The corresponding results are plotted in Fig. 3.7, in which the errors are spread out among the stages due to delaying the start of the transformation from $t_i = -2 \to -1.4$. This change in starting time was beneficial as it led to larger portions of β_1 being transformed and hence more destructive interference between $\tilde{\beta}_1$ and β_2 in Stage 3 [see Eq. (3.64)]. Both of these losses can be reduced by transforming more of the pulse. This can be accomplished by either increasing l for a given G_1 or picking G_1 (or equivalently α_1) such that the wave packet is more localized.

In Fig. 3.8 we illustrate how the probability of success, see Eq. (3.59), approaches 1 as l is increased. Note that if the first pulse is implemented correctly so that $\alpha_1 \to 0$

[8] One can equivalently write the probability density of loss due to an incorrect photon wave packet as $\dot{P}_p = -\frac{d}{dt}\left(\frac{|\tilde{\alpha}_1|^2+|\tilde{\beta}_1|^2}{df/dt} + |\alpha_2|^2 + |\beta_2|^2\right)$, where the quantity in parentheses acts as a norm for system 2 and the fictitious system $\tilde{1}$ driving it. Here $\tilde{\alpha}_1$ is defined in a manner analogous to $\tilde{\beta}_1$ in Eq. (3.54).

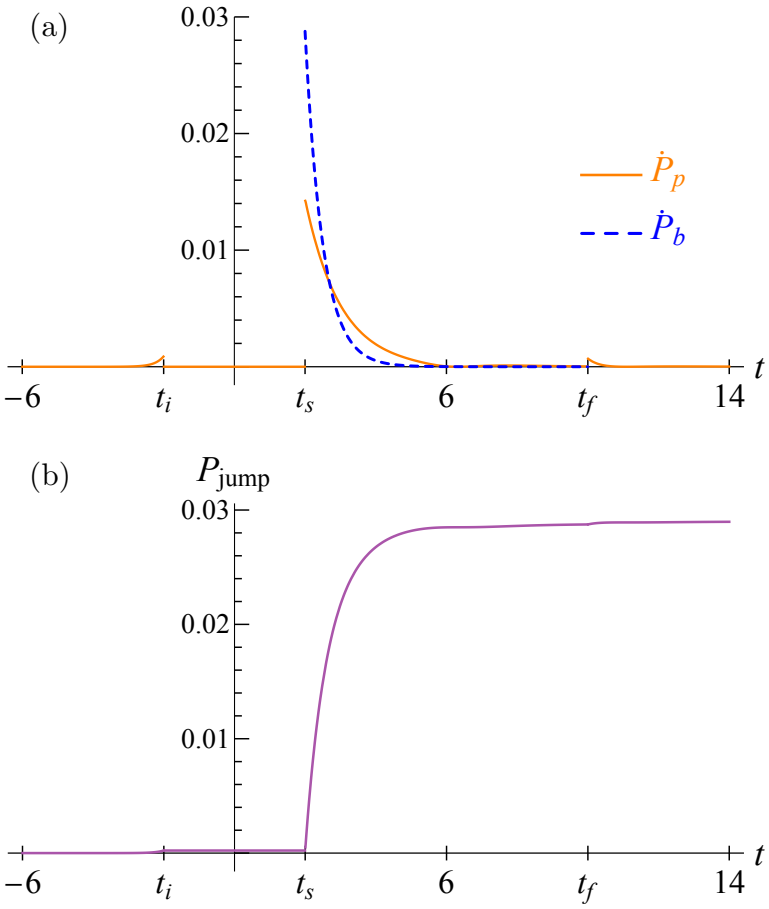

FIGURE 3.6. (a) Probability density functions for loss due to blocking (dashed line), which is only plotted during Stage 3 where it occurs, and due to imperfections in the shape of the photon wave packet (solid line). (b) Probability of a quantum jump up to time t (in units of γ_2^{-1}). The parameter values are the same as in Fig. 3.4. Note that P_{jump} tends to 0.029, as is consistent with the 0.97 success rate we found previously.

for large times, then one finds that

$$P_{\text{success}} = 1 - P_{\text{jump}}(t \to \infty). \tag{3.66}$$

For $\zeta = 0$, the systems are already resonant so no frequency shift is needed and hence P_{success} decreases if only a small amount of the photon wave packet is transformed (as then much of it is blocked). We see that when the frequencies of the lasers driving

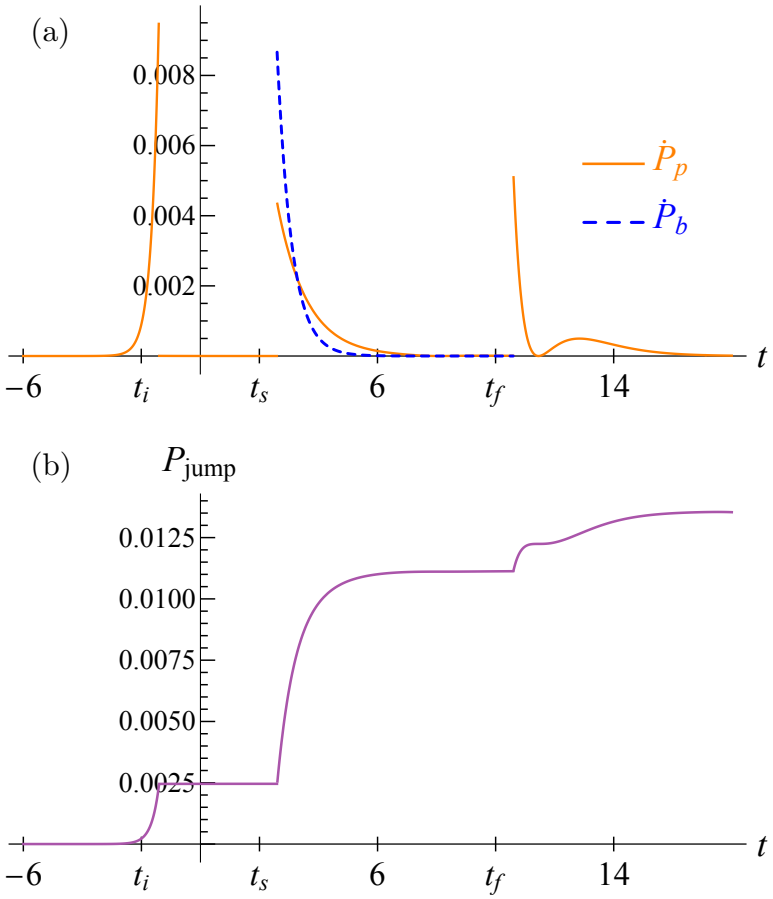

FIGURE 3.7. Plots of (a) the probability density functions and (b) the total jump probability, choosing the ideal value of T (keeping $\xi = 1/2$, $\omega_0 = \zeta = 50$, and $t_l = 4$) such that $t_i = -1.4$ (all quantities are in units where $\gamma_2 = 1$). Here $P_{\text{jump}} \to 0.014$ for large t, which is slightly less than half of the loss probability we found previously with $t_i = -2$.

the systems differ appreciably, i.e., when $|\zeta|$ is large, P_{success} is nearly 0 without the unitary (when $l = 0$) and so performing a transformation is critical for QST. Recall that, in our numerics, frequencies are measured relative to the cavity decay rate γ_2, which is typically on the order of kHz. Thus, 'large $|\zeta|$' is relative to γ_2. Note that the photon frequency mismatch, ζ, will be similar in magnitude to the cavity resonance frequencies, see Eq. (3.48), for which typical values are on the order of THz $= 10^9$ kHz (this is consistent with our high-quality factor assumption for each cavity). So

generically $|\zeta| \gg \gamma_2 = 1$ (in our units) and then P_{success} monotonically increases from 0 at $l = 0$ to 1 for large l (see the $|\zeta| = 50$ curve in Fig. 3.8, which does not change significantly as $|\zeta|$ is further increased;[9] we keep $|\zeta|$ relatively small in our numerics to avoid issues with highly oscillatory integrals).

Experimentally, increasing l would necessitate using more nonlinear optical media to control the unitary transformation, whereas tailoring G_1 to produce a narrow wave packet demands more precise control of the timing so that deviations from the ideal value of T are more costly. An analysis of the benefits and limitations of each of these solution methods is beyond the scope of this dissertation. However, we do consider many additional error mechanisms in Ch. IV, including loss due to a frequency mismatch $\omega_0 \neq \zeta$.

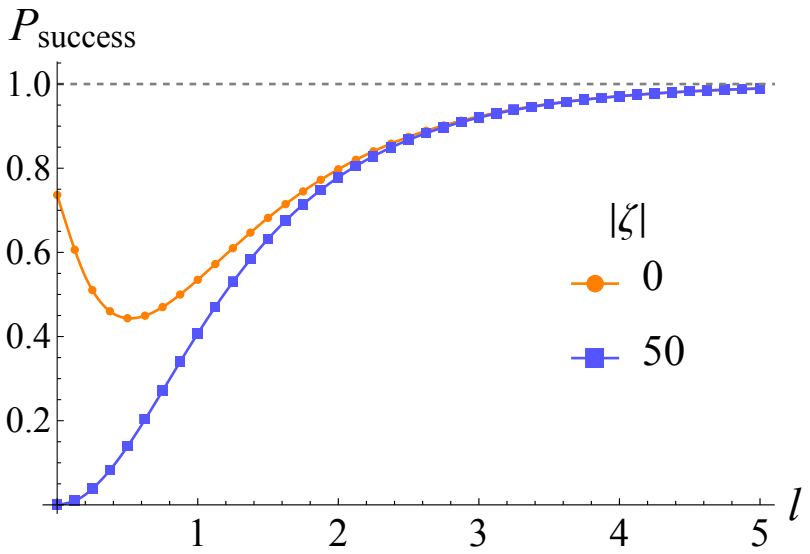

FIGURE 3.8. Plot of P_{success} vs l for identical photon frequencies, $\zeta = 0$, and for a frequency mismatch of $|\zeta| = 50$ (all quantities are in units where $\gamma_2 = c = 1$). Here we use the ideal frequency shift $\omega_0 = \zeta$, and $\xi = 1/2$, $T = 3t_l/2$ such that $t_s = t_l/2$. (See the text for further discussion.)

[9]For completeness, we note that there is ζ-dependent interference between the cavity fields, $\exp(i\zeta t)\tilde{\beta}_1$ and β_2 [see Eq. (3.64)], which results in P_{success} oscillating about the large-$|\zeta|$ limit. However, this effect is only pronounced for small but non-zero $|\zeta|$. For instance, for $|\zeta| = 10$ the oscillations are visually discernible, while for $|\zeta| = 25$ they are not.

3.6 Discussion

In this chapter, we have demonstrated that photon manipulation can be incorporated into input-output theory to achieve, in principle, ideal quantum state transfer (QST) between non-identical systems. This offers a potentially versatile scheme for QST in hybrid quantum networks. We showed, using analytical and numerical means, how this scheme can be applied to systems of three-level atoms in cavities to achieve ideal QST. Our scheme could be generalized to systems with more levels, where more laser pulses and their time-reversed counterparts need to be used to induce emission and absorption in the systems, respectively [157–159]. Furthermore, our scheme could readily be adapted to any other material system that can controllably emit and absorb single photons (e.g., by leveraging cavity or circuit QED to realize the Jaynes–Cummings interaction; see App. A.1.2), with the details contingent on the forms of the system Hamiltonians.

A main result is a new interpretation of system 1's time argument in the effective description where the systems are directly coupled. In particular, we find that the mathematical object

$$\boxed{\rho(t) = \tilde{\rho}_1(\tilde{t}) \otimes \rho_2(t)} \tag{3.67}$$

describes the composite state of system 2 coupled to a fictitious system $\tilde{1}$, which would produce the transformed wave packet. Then we can eliminate the bath and unitary transformation from the description and obtain an evolution equation for the state ρ, in the standard Lindblad form

$$\dot{\rho} = i[\rho, H_0] + J\rho J^\dagger - \frac{1}{2}\left\{\rho, J^\dagger J\right\}. \tag{3.68}$$

Yet crucially, the effects of the transformation (the scaling by a factor ξ and time reversal) are accounted for by the change in the time argument of the state of system 1, $t \to \tilde{t} = \xi(T - t + \tau)$, during the transformation (see §3.4 for details). This has the interpretation that the unitary transformation can be incorporated into the effective description of the dynamics of system 2 by simply letting system 1 (which drives system 2) run backward in time at a new decay rate and frequency (see Fig. 3.9). Thus, the effective description in the quantum trajectory method is unchanged, yet the interpretation of the state does change.

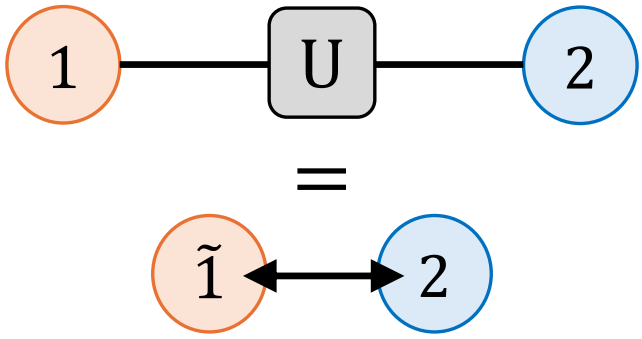

FIGURE 3.9. Schematic illustration of the interpretation of Eq. (3.67). After eliminating the channel as well as the unitary transformation device from the description, system 2, $\rho_2(t)$, is effectively directly driven by a fictitious, time-reversed and mode-matched version of system 1, $\tilde{\rho}_1(\tilde{t})$ (see the main text for details).

Clearly, implementing the unitary transformation device in our scheme would be challenging. Reference 37 propose a nonlinear optical based method to implement the transformation we consider in the optical domain. However, if we wanted to perform microwave to optical transduction we would need a different implementation of our transformation, e.g., using atomic ensembles or electro-optical systems for frequency conversion [138], followed by our shaping and time-reversal procedure. Accordingly, modeling a more realistic, imperfect transformation device is an important extension of this work. We leave for Ch. IV the analysis of additional losses and limitations in

the transformation. In App. A.1.5, we discuss the method of Ref. 37 and direct the reader to potential implementations in other regimes.

CHAPTER IV

SUCCESS PROBABILITIES IN TIME-REVERSAL BASED HYBRID QUANTUM STATE TRANSFER

The work of this chapter was published in Physical Review A **110**, 012415 (2024) [4]. It was developed jointly by K. J. Randles and S. J. van Enk, and follows up on our previous work in Ch. III [3]. The majority of writing, supporting analysis, and figure preparation was done by K. J. Randles with continued guidance and feedback from S. J. van Enk.

4.1 General introduction

4.1.1 What about errors?

In this chapter, we focus on the theoretical implementation of a deterministic quantum state transfer (QST) scheme capable of linking hybrid quantum nodes via itinerant photons. In particular, we consider connecting two different types of spatially separated nodes, with potentially different spectral properties (resonance frequency and decay width). The state of a qubit prepared at the 'sender' node 1 is mapped to the state of an emitted photon wave packet (facilitated by local controls) that is sent to a 'receiver' node 2 via a guided channel. To optimally be absorbed at node 2, and hence to map the photonic state to a material qubit state, this wave packet must be modified, tailoring its time-frequency shape.[1]

[1]In contrast to wave packet shaping methods, quantum state transfer by adiabatic passage between two cavities via an intermediate fiber (channel), which is also deterministic, can mitigate losses due to absorption in the cavities [154, 160, 161]. However, consideration of the hybridization of such an adiabatic passage based QST scheme for a case where transduction is needed is beyond the scope of this work.

In the previous chapter, Ch. III, we showed how this can be accomplished by incorporating a unitary transformation, U, that time reverses (see App. A.1.4 for some discussion of why we emphasize time reversal), frequency shifts, and stretches or compresses the intermediate photon wave packet along the quantum channel (as was depicted in Fig. 1.5). In the time domain, U is given by Eq. (3.18):

$$U(t,t') = \sqrt{\xi} e^{i\omega_0(T-t)} \delta(t' - \xi(T-t)). \tag{4.1}$$

With the inclusion of this unitary transformation, we showed how to design system controls (laser pulses) that will transfer the state of a qubit at node 1 to one at node 2 even if the nodes have significantly different resonance frequencies and decay rates (provided we can implement U correctly). This is especially important in hybrid cases, where without U the likelihood of node 2 absorbing a photon emitted by node 1, even for well-designed controls, is very small.

In this chapter we consider and analyze realistic errors that can occur in the hybrid QST scheme of Ch. III, which demonstrated how the scheme works in ideal conditions. We focus on errors in the implementation of the unitary transformation, as other common errors, such as those due to photon absorption in the transmission line, incorrect laser controls, and cavity loss, are well-known and understood [2, 14, 162–164]. This lets us show our protocol's utility in the presence of these realistic errors especially when it is supplemented by known error correction protocols [2, 164] that can correct these common errors as well as errors in the unitary transformation using local quantum computations with auxiliary quantum emitters at each node (see §4.3.4). Nonetheless, error mitigation remains a crucial part of making such error correction protocols viable, specifically to keep the expected number of repetitions of a primitive transfer operation low and moreover to lessen additional overhead.

We also show that the probability of successfully transferring the state from one node to another, P_{success}, is determined (rather intuitively) by the overlap between the actual and ideal single-photon wave packets to be incident on node 2 denoted by Ψ and Φ, respectively. Specifically, we find

$$\boxed{P_{\text{success}} = |\langle\Phi|\Psi\rangle|^2 = \left|\int_{-\infty}^{\infty} dt\ \Phi^*(t)\Psi(t)\right|^2} \tag{4.2}$$

(see §4.3.1 for the corresponding derivation in the particular case we focus on in this work, where each node is comprised of a three-level atom in a cavity and see App. A.1 for a general argument for this result, which ultimately amounts to the Born rule). This can be understood by interpreting the successful completion of the protocol as a photodetection event in which the receiving node can be thought of as a photodetector, that (in the case of a "click") would project onto a particular single-photon wave packet Φ, which is determined by the parameters of node 2 and the laser driving it.

4.1.2 Outline

We outline the model for the interaction of the nodes and present our QST scheme in §4.2. This includes specifying the corresponding Hamiltonian and equations of motion (EOMs) for the amplitudes of various excitations as well as giving an overview of the standard errors present in such a scheme. In §4.3 we consider errors in the unitary transformation. In §4.3.1 we show how these errors can be described in the context of quantum measurement theory in terms of positive operator-valued measures (POVMs). Then in §4.3.2 we show how the ideal value of the unitary transformation's timing parameter can be determined and in §4.3.3 we perform some

further numerical analysis of the probability of successful state transfer in the presence of unitary errors. In §4.3.4 we highlight how known error correction protocols could be used to reliably perform this state transfer procedure in the presence of realistic errors. In §4.3.5 we consider the relevance of our work in heralded, as opposed to deterministic, schemes. Finally, in §4.4 we discuss the utility of our scheme and provide an outlook of other contexts where it could be employed. Additional analysis and supporting details regarding the scope of our results are provided in App. A.

4.2 Scheme and model

Here we summarize the model and methods used for analyzing two linked nodes of a quantum network interacting via a quantum channel. (This model was introduced in §2.3 and analyzed in Ch. III; see Refs. 108, 122 and the textbook 165 for further details.) Starting from the Gardiner-Collett model [108], one can show that in the quantum trajectory formalism [122], the dynamics (during time intervals when no quantum jump occurs) are determined by an effective non-Hermitian Hamiltonian of the form

$$H_{\text{eff}} = H_1 + H_2 + H_{\text{tl}} \tag{4.3}$$

[see Eq. (3.39)]. Here H_j is the Hamiltonian for node $j = 1, 2$ and H_{tl} accounts for the nodes' interaction via the *transmission line*.

4.2.1 Node implementation

Here we consider nodes that can encode the state of a qubit in an effective two-level system with a controllable coupling to a well-defined electromagnetic field mode. Such a node is readily realized, at least theoretically, by a three-level Λ-type atom (or ion) in a high-Q optical cavity [1] and there has been significant recent experimental

progress in such systems [59, 154, 166, 167] (see §4.2.6). As discussed in §1.5.4, we focus on such atom in cavity systems (both here and in Ch. III) to exemplify the physics underlying our scheme, though the scheme applies more generally. These atomic systems along with the rest of our QST scheme are highlighted back in Fig. 1.5 of the introduction. In this case, at each node the state of a qubit is encoded in the ground states of the atom, $|e\rangle$ and $|g\rangle$, which are coupled via a Raman transition through an auxiliary atomic excited state $|r\rangle$. We consider asymmetric cavities that preferentially couple to the transmission line, e.g., by using a partially transmitting mirror to interface with the transmission line and a (near) perfectly reflective outer mirror.

That is, the dynamics of the first Raman qubit are controlled using a laser pulse that drives a transition from $|e_1\rangle$ to $|r_1\rangle$, which is followed by the transition $|r_1\rangle$ to $|g_1\rangle$ and the emission of a photon into cavity 1, and meanwhile leaves $|g_1\rangle$ undisturbed with no corresponding emission. Thus, if atom 1 was in the 'excited' state $|e_1\rangle$, an emitted photon would leak out of cavity 1, propagate down the transmission line along which it would be transformed via U, before its incidence on node 2. Then atom 2, which is prepared in $|g_2\rangle$, can simply undergo the Raman process analogous to that undergone by atom 1 but in the backwards order, with the goal of inducing absorption of the photon. This is possible as by implementing U we have effectively equalized the spectral properties of the two nodes (analogous to impedance matching).

By linearity, this process can thus be used to implement our QST scheme, where the state of atom 1, $c_g|g_1\rangle + c_e|e_1\rangle$, is transferred to the photon, $c_g|0\rangle + c_e|1\rangle$, and then to atom 2, $c_g|g_2\rangle + c_e|e_2\rangle$. Here we take the photonic qubit to be encoded in the occupation number degree of freedom, i.e., either the vacuum $|0\rangle$ or single-photon $|1\rangle$ state in a certain mode [168, 169]. Other encodings could potentially be used

with appropriate modifications to our scheme. There are of course tradeoffs between different encodings, e.g., the polarization encoding $\{|H\rangle, |V\rangle\}$ is more robust in some scenarios [134, 170], yet the occupation number encoding is necessary for the known error correction protocols we consider (see Apps. A.1.6 and A.3 for further discussion).

For these nodes, the effective dynamics in the single (or zero) excitation subspace are ultimately determined by the Hamiltonian ($\hbar = 1$) [1]

$$H_j = iG_j(t)\left(a_j^\dagger |g_j\rangle\langle e_j| - a_j |e_j\rangle\langle g_j|\right). \tag{4.4}$$

The operators $a_j^\dagger$ and a_j are the creation and annihilation operators for cavity j, respectively. Likewise $|e_j\rangle\langle g_j|$ and $|g_j\rangle\langle e_j|$ are the raising and lowering operators for the effective two-level atom j, respectively. Here, we recall from §3.5.1 that, $G_j(t) = g_j\Omega_j(t)/2\Delta_j$ is the Jaynes–Cummings interaction strength between the effective two-level atom and cavity at node j, where g_j is the bare atom cavity coupling, $\Omega_j(t)$ is the user-controlled Rabi frequency envelope of the driving laser, and $\Delta_j = \omega_{Lj} - \omega_{re,j}$ is the laser detuning. Note $G_j(t)$ is real with the implicit time-dependent laser phase, of the form $e^{i\phi_j(t)}$, factored out. To obtain this form for H_j [as compared to Eq. (3.43)], we selected specific laser frequencies ω_{Lj} to eliminate shifts to the cavity energy states and chose the laser phases $\phi_j(t)$ (the chirps specifically) to compensate for the ac Stark shift to $|e_j\rangle$ (see App. A.2.1). Additionally, we assumed far off-resonant driving lasers (to suppress spontaneous emission [151]) so that we could adiabatically eliminate the excited states $|r_j\rangle$, and we went into a rotating frame at the photon frequency, $\omega_{\rightsquigarrow j} = \omega_{Lj} + \omega_{ej}$, for each system.

4.2.2 Interaction model

Assuming a vacuum field input, or less strictly that no light is incident on the nodes in relevant modes, the connection of the nodes is ultimately described by

$$H_{\mathrm{tl}} = -\frac{i}{2}\left(\gamma_1 a_1^\dagger a_1 + \gamma_2 a_2^\dagger a_2 + 2\sqrt{\gamma_1\gamma_2}e^{i\zeta t}a_2^\dagger \tilde{a}_1\right), \tag{4.5}$$

as we found in Eq. (3.45), which provides an effective description of the transmission line in which node 2 is effectively directly coupled to the transformed output of node 1. This is accounted for by the operator $\tilde{a}_1$, which is an annihilation operator for the transformed photon that exits the unitary transformation device. Note that both a_1 and $\tilde{a}_1$ are time-delayed operators, which implicitly account for the time delay of light propagating between the nodes. This description highlights the role of the transmission line as an intermediary for the transfer of excitations from node 1 to node 2 (via the $a_2^\dagger \tilde{a}_1$ term). Here γ_j is the decay rate for cavity j into the transmission line. The relative phase of $\zeta = \omega_{\rightsquigarrow 2} - \omega_{\rightsquigarrow 1}$ in the excitation transfer term corresponds to oscillations at the mismatch in the photon frequencies and, mathematically, is due to going into the aforementioned rotating frames for each node.

Within this model, we assume the coupling to be unidirectional with photons only propagating from system 1 to 2 (there is no $a_2 a_1^\dagger$ term in H_{tl}), at least during the QST procedure. Ideally, this unidirectionality should be a consequence of atom 2 being prepared in a stable ground state $|g_2\rangle$, yet it can be physically imposed as necessary. This unidirectionality can be imposed using a circulator as proposed by Refs. 1, 124 and used by some microwave implementations [35, 88, 89] or by directing signal reflected by system 2 down a different spatial mode, say using a ring cavity geometry. Even if we do not explicitly impose unidirectionality, the presence of a

$a_2 a_1^\dagger$ term does not necessarily doom the QST scheme [92]. This is because, just as the present term has the implicit time dependence $a_2^\dagger(t)a_1(t-\tau)$ (with τ the time delay for light propagating between the nodes), the opposing term behaves as $a_2(t)a_1^\dagger(t+\tau)$. Thus, even if reflection from node 2 occurs, we would not be driving the corresponding transition for node 1 to reabsorb the now transformed photon wave packet. [Note this is only true for wave packets that are short relative to τ, as is often the case optically. Additional considerations may be warranted, e.g., Ref. 171's use of a circulator helps them ensure the photon is emitted into a Markovian environment (channel).] Accordingly, QST and remote entanglement generation experiments often do not use circulators in practice, especially as they come with their own losses and errors, e.g., those due to back reflections.

Then, for a unidirectional coupling, however it may be achieved, U does not affect system 1 dynamics and a_1 acts in the Heisenberg picture in a standard way, i.e., on $|C\rangle_1 = c_0|0\rangle_1 + c_1|1\rangle_1$ it acts as

$$ {}_1\langle 0|a_1(t)|C\rangle_1 = c_1(t). \tag{4.6}$$

Meanwhile, in this effective description, the second system is effectively directly coupled to the *unitarily transformed* output of system 1. This is accounted for by the $a_2^\dagger \tilde{a}_1$ term of Eq. (4.5), where $\tilde{a}_1$ encodes the effect of U, acting as

$$ {}_1\langle 0|\tilde{a}_1(t)|C\rangle_1 = \chi(t)c_1(f(t)) \tag{4.7}$$

in contrast to Eq. (4.6), where[2]

$$\chi(t) = \begin{cases} 0, & t_i < t < t_s \\ \sqrt{\xi} e^{i\omega_0(T-t)}, & t_s < t < t_f \\ 1, & \text{elsewise} \end{cases} \tag{4.8}$$

and

$$f(t) = \begin{cases} \text{undefined}, & t_i < t < t_s \\ \xi(T-t), & t_s < t < t_f \\ t, & \text{elsewise} \end{cases} . \tag{4.9}$$

Here t_s is the time at which the transformed field starts to be produced and it is controlled via the relation $T = t_s(1 + 1/\xi)$. These functions are broken up into intervals as the part of the photon wave packet to be transformed, taken to be of duration $t_l = l/c$, must pass through the unitary transformation device (in the time interval $t_i \equiv t_s - t_l < t < t_s$), before the transformed wave packet is produced (in the interval $t_s < t < t_f \equiv t_s + t_l/\xi$). Outside of the time interval where the transformation is happening $\tilde{a}_1$ reduces to the standard a_1. The form of these functions for $t_s < t < t_f$ comes directly from Eq. (4.1), assuming that the untransformed pulse is blocked at the transformation device during the production of the transformed field. [This assumption is not necessary, but it leads to a simpler description of how the unitary transformations effect can be encoded in the time argument of a fictitious system $\tilde{1}$ that is, effectively, directly driving system 2 (see §3.4.2). Furthermore, the distinction of whether we block the original field for $t_s < t < t_f$ does not matter if the photon

[2]These formulae for χ and f follow from Eqs. (3.28) and (3.29). Note that the difference in $\chi(t_i < t < t_s)$ is used to more explicitly indicate the behavior of mode functions [as considered here and in Eq. (3.53)], rather than field operators. See §3.3.2 and §3.5.2 for details.

frequencies are substantially different: $|\zeta| = |\omega_{\rightsquigarrow 2} - \omega_{\rightsquigarrow 1}| \gg \gamma_{1,2}$ (see §4.3.2). Assuming $|\omega_{L2} - \omega_{L1}| \gg |\omega_{e2} - \omega_{e1}|$, this is tantamount to the drive frequencies differing appreciably.] The crucial part is that the transformed part of the field (which should be the entirety of the single-photon wave packet assuming the control parameters are suitably picked and implemented) has the time-reversed and stretched argument $\xi(T - t)$.

4.2.3 Model generality

Importantly, our focus on a particular kind of node does not limit the scope of this dissertation, which is meant to concern hybrid links, as the ideas behind our scheme apply to many other analogous controllable systems that could be used for either (or both) node(s). In fact, the Hamiltonian governing the system dynamics we analyze [given in Eqs. (4.3)–(4.5)] is quite general for deterministic QST schemes like ours, so the physics should be identical after an appropriate mapping of physical parameters. This is provided the unitary transformation U can be implemented to transduce the intermediate photon between the emitting and receiving nodes energy and time scales. [Note that U has a proposed implementation in the optical regime [37]. In other regimes, say for microwave systems or hybrid cases, such as the coupling of microwave and optical nodes, some aspects of such a transformation have been considered yet to our knowledge the entire unitary we consider has not been (see App. A.1.5 for further discussion).]

In particular, we assume that we utilize nodes for which individual excitations can controllably and reversibly be transferred from the material system to a photonic mode (emission) and vice versa (absorption), often at the single-photon level, say mediated by a cavity or resonator [1, 170, 172]. It should then be possible to recast

the Hamiltonians for the nodes themselves into the standard Jaynes–Cummings form [as was done for Eq. (4.4)] through the appropriate adiabatic elimination of auxiliary states, selection of unitary transformations to the node Hamiltonian, and tuning of the system and control parameters. One benefit of such coherent and reversible interactions is that you can generate different kinds of target states, e.g., tune the wave packet's shape, amplitude, and phase (see App. A.2 for further discussion). This is to be contrasted against heralded, probabilistic approaches such as those based on spontaneous emission (see §4.3.5). The form of the Hamiltonian describing the coupling of the nodes, Eq. (4.5), is also common within the context of input-output theory in which one eliminates the channel from the description (via its corresponding continuous mode field operators) to obtain a simpler description where the two nodes are effectively directly coupled (see App. A.1.2 for further details and examples).

4.2.4 System evolution

Starting from Eq. (4.3), the zero-excitation ground state evolves trivially $|gg\rangle|00\rangle \to |gg\rangle|00\rangle$ as

$$i\frac{d}{dt}|gg\rangle|00\rangle = H_{\text{eff}}|gg\rangle|00\rangle = 0 \tag{4.10}$$

in the interaction picture. Meanwhile the dynamics of a state in the single-excitation subspace,

$$|\psi(t)\rangle = \alpha_1(t)|eg\rangle|00\rangle + \alpha_2(t)|ge\rangle|00\rangle + \beta_1(t)|gg\rangle|10\rangle + \beta_2(t)|gg\rangle|01\rangle, \tag{4.11}$$

are encoded by α_j and β_j, which are the state amplitudes for an excitation being in atom j ($|e_j\rangle$) and cavity j ($|1_j\rangle$), respectively. The corresponding amplitude EOMs

are

$$\dot{\alpha}_1 = -G_1\beta_1, \tag{4.12a}$$

$$\dot{\beta}_1 = G_1\alpha_1 - \frac{\gamma_1}{2}\beta_1, \tag{4.12b}$$

$$\dot{\alpha}_2 = -G_2\beta_2, \tag{4.12c}$$

$$\dot{\beta}_2 = G_2\alpha_2 - \frac{\gamma_2}{2}\beta_2 - \sqrt{\gamma_2}e^{i\zeta t}\Psi(t), \tag{4.12d}$$

where

$$\Psi(t) := \sqrt{\gamma_1}\chi(t)\beta_1(f(t)) \approx \sqrt{\gamma_1}\xi e^{i\omega_0(T-t)}\beta_1(\xi(T-t)), \tag{4.13}$$

is the transformed wave packet emitted by system 1 that is driving system 2 [see §3.5, Eq. (3.53) in particular with $\tilde{\Psi}_1 \to \Psi$ for ease of notation]. The approximation in Eq. (4.13) is exact during the transformed field production $t_s < t < t_f$ and hence holds in the large l limit. Note that by tuning the laser frequencies and phases to obtain the simple Jaynes–Cummings type node Hamiltonians of Eq. (4.4) we are fixing α_1 and β_1 to have the same constant phase, so without loss of generality we take them both to be real. This simplified case, where we tune the control parameters so that the system 1 amplitudes are real, is of course not general, though it entirely suffices for our QST scheme and makes our analysis easier. It is worth mentioning that one can controllably modulate the phase of the emitted photon wave packet, $\Psi(t) = \sqrt{\gamma_1}\beta_1(t)$, in time by adjusting the parameters of the driving laser, namely the phase (though this can exacerbate non-Markovian effects, which need more careful treatment [128]), and then α_1 also acquires a time-dependent phase (see App. A.2.1 for more details).

Note that in our setup the transfer $|g_1\rangle \to |g_2\rangle$ happens by default, see Eq. (4.10), and so the principal goal is to transfer any excitation from the first qubit to the second, $|e_1\rangle \to |e_2\rangle$. Thus, in the single-excitation subspace, we want $|\alpha_1(t \to -\infty)| = 1$ and $|\alpha_2(t \to \infty)| = 1$; the former condition is satisfied via appropriate local state preparation while the latter requires the transmission process to be implemented correctly. Accordingly, we deem the probability of successful QST to be $P_{\text{success}} \equiv |\alpha_2(t \to \infty)|^2$, with the caveat that one need also transfer the relative phase of the qubit states, which requires an interferometrically stable channel (see the discussion at the end of §4.3.1 for further details).

4.2.5 Simplified treatment

As we have alluded to, we want to highlight the role of the unitary transformation U in our QST scheme. Accordingly, we use several simplifying strategies that allow us to set aside other well known kinds of errors and quantify the impact of U by the single parameter P_{success}. In this subsection, we list these strategies and briefly discuss how they can naturally be incorporated into our analysis (see App. A.3.1 for further details). These strategies include that:

1) emission of the Λ system into modes other than the desired cavity mode is treated post hoc,

2) cavity field loss into modes other the relevant transmission line mode is treated post hoc,

3) transmission line loss is treated post hoc,

4) we assume the laser pulses (or other control drives) are implemented correctly, and

5) we do not account for dispersion in the transmission line.

Strategies 1) and 2) are worded for the emission process from node 1, yet we likewise (due to time-reversal symmetry) apply them during absorption at node 2.

The post hoc treatment in strategies 1), 2), and 3) is performed by multiplying our probability of success by the respective survival probabilities P_1, P_2, and P_3 of the photon being transferred to the desired mode during emission into (or absorption out of) the cavity (see App. A.2.3), the cavity-channel interactions, and its propagation through the channel [150, 154, 155]. That is, the evolution described in §4.2.4 is conditioned on attempts where the photon is not lost (absorbed or in an orthogonal mode). Thus, the modified success probability of our scheme is

$$\tilde{P}_{\text{success}} = P_1 \cdot P_2 \cdot P_3 \cdot P_{\text{success}}. \tag{4.14}$$

One can naturally separate the first two survival probabilities into contributions from each of the individual nodes. Namely, letting $\mathcal{P}_{\text{em-j}}$ and $\mathcal{P}_{\text{cav-j}}$ denote the respective probabilities of the emitter and cavity at node j coupling to the desired mode (which are the same for emission and absorption due to time-reversal symmetry), we have $P_1 = \mathcal{P}_{\text{em-1}}\mathcal{P}_{\text{em-2}}$ and $P_2 = \mathcal{P}_{\text{cav-1}}\mathcal{P}_{\text{cav-2}}$.

As an instructive example, here we consider the case where nodes 1 and 2 undergo the same amount of loss. In particular, we take $\mathcal{P}_{\text{em-1}} = \mathcal{P}_{\text{em-2}} = C_{\text{em}}/(1 + C_{\text{em}})$ and $\mathcal{P}_{\text{cav-1}} = \mathcal{P}_{\text{cav-2}} = C_{\text{cav}}/(1+C_{\text{cav}})$. Here C_{em} and C_{cav} are cooperativity parameters that quantify how well the emitters and cavities, respectively, are able to produce photons in the desired output mode. Meanwhile, for strategy 3), we consider exponential transmission line loss $P_3 = e^{-x/x_{\text{tl}}}$ with attenuation distance x_{tl}. (See App. A.3.1 for further explanation and motivation of these parameters and the corresponding

survival probabilities; realistic values are given in §4.2.6.) In this case, we have

$$\tilde{P}_{\text{success}} = P_{\text{success}} \cdot \left(\frac{C_{\text{em}}}{1 + C_{\text{em}}} \frac{C_{\text{cav}}}{1 + C_{\text{cav}}} \right)^2 e^{-x/x_{\text{tl}}}. \tag{4.15}$$

Strategies 4) and 5) are used for simplicity and could be accounted for implicitly via modifications to the actual and target wave packet shapes Ψ and Φ in P_{success} of Eq. (4.2). Strategy 4) is well-founded in that laser errors in the amplitudes G_j and phases ϕ_j are typically negligible compared to the other errors we consider, yet such errors could easily be included in our model and numerics if necessary. One point of note that is obfuscated by the effective treatment of Eq. (4.5) is the role of the relative timing of the laser pulses (which is implicitly encoded in the time-delayed operators for node 1). A relative timing error of δt would result in P_{success} being determined by the overlap of $\Psi(t+\delta t)$, instead of $\Psi(t)$, with the target $\Phi(t)$, degrading the excitation transfer. Thus, in strategy 4), we additionally assume that no such relative timing errors are made, which demands care, but can be accomplished by characterizing and controlling the photon propagation time through the channel and using a common reference clock for both nodes. In regards to strategy 5), distortion to the wave packet Ψ induced by channel dispersion can be (partially) compensated for by modifying the control pulses [128] as well as the unitary transformation U (see App. A.1.4). However, the comprehensive modeling and treatment of such distortion effects is beyond the scope of this dissertation. We note that channel dispersion poses less of a problem when using short channels and/or small bandwidth (large duration) photons, making strategy 5) more justified in these cases.

4.2.6 Realizable parameters in cavity QED experiments

We will now consider realistic values of the parameters $C_{\rm em}, C_{\rm cav}$, and $x_{\rm tl}$ for atom or ion in an optical cavities type nodes. This allows us to quantify the impacts of the standard loss mechanisms that we set aside in the previous subsection. For transmission line loss we consider two cases that are employed or sought in the literature: optical and telecom light, for which $x_{\rm tl}^{\rm (opt)} \approx 1.2 - 1.5$ km and $x_{\rm tl}^{\rm (tele)} \approx 15 - 25$ km, respectively.[3] For emitter and cavity losses, we consider several references that use nodes similar to our exemplar case and in Table 4.1 we list the corresponding cooperativities and survival probabilities they are (or would be) able to achieve. The average cooperativities based on this table are $C_{\rm em}^{\rm (avg)} = 9.0$ and $C_{\rm cav}^{\rm (avg)} = 5.9$, whereas if the maximum and minimum values are disregarded in each case, the averages become 3.6 and 5.8, respectively.

We note that the reported ion experiments tend to have lower emitter and cavity cooperativities than the neutral atom experiments. One main reason for this is that small mode volumes are needed to obtain large ion-light couplings g, yet they also result in a stronger disturbance to the trapping field due to stray fields caused by charge build up on the dielectric mirrors in a typical Fabry-Perot type cavity setup. This can be largely circumvented using a fiber-based Fabry-Perot cavity, in which the two cavity mirrors are each an end face of an optical fiber, wherein the accumulated charge is distributed over the fibers' dielectric surfaces [173]. In §4.3.4 we use these realistic $x_{\rm tl}$ values and the tabulated cooperativity values to inform how

[3]These values come from optical and telecom attenuation rates in the ranges of 0.17 dB/km $\leq X_{\rm tele} \leq$ 0.3 dB/km and 3 dB/km $\leq X_{\rm opt} \leq$ 3.5 dB/km [103, 154, 167], respectively, which are translated to our notation via $x_{\rm tl}^{-1} = X \ln(10)/10$.

implementable our scheme is (in consonance with an error correction protocol) in different parameter regimes (see Fig. 4.6).

4.3 Unitary errors

Here we consider errors in the unitary parameter values of ω_0, ξ, and T. We focus on cases where the transformation duration, t_l, is long enough to transform essentially all of the pulse. That is, we do not analyze errors due to the unitary not being implemented for long enough, which (at least in non-linear optical setups) could be due to not using a long enough medium for the transformation device. Errors such as photon absorption or distortion can be corrected for [2, 164], though the corresponding protocols do not correct for errors due to the undesired production of a photon. Hence we assume there is no other mechanism for atom 2 to absorb an excitation, which is consistent with the assumption of a vacuum field input to system 1 needed to obtain the effective Hamiltonian of Eq. (4.3). In particular, we assume that there are no relevant thermal excitations, which is only valid for systems at low temperatures relative to their operation frequency such that the average thermal occupation number $\bar{n}_{\text{th}} = 1/(e^{\hbar\omega/k_B T} - 1)$ is nearly zero (it is desirable to have it be far less than 1) [180]. Accordingly, even though true $T = 0$ is unphysical, we can define *effective* zero temperature as the regime wherein $\hbar\omega \gg k_B T$, which is typically what is meant when one encounters a "zero temperature bath" in the literature.

An effective zero temperature bath is a very good approximation for optical systems, though systems that operate at lower frequencies need to be cooled. For instance, at room temperature $T = 293$ K optical light with wavelength $\lambda \approx 700$ nm will have $\bar{n}_{\text{th}} \approx 3{\cdot}10^{-31}$, whereas microwave light with $\lambda \approx 20$ mm will have $\bar{n}_{\text{th}} \approx 400$. Hence adequate cooling is crucial in reducing thermal noise and loss experienced by

TABLE 4.1. Overview of realizable emitter and cavity parameter values based on several recent experimental analyses that consider nodes comprised of a neutral atom or ion coupled to an optical cavity (in experiments that use two such nodes, we list the values for each, labeled A and B). Here we list the emitter and cavity cooperativities (C_{em} and C_{cav}) as well as the corresponding maximum probabilities that a photon is emitted by the atom or ion into the correct cavity mode $\mathcal{P}_{\mathrm{em}} = C_{\mathrm{em}}/(1 + C_{\mathrm{em}})$ and then from the cavity into the desired output mode (in the transmission line) $\mathcal{P}_{\mathrm{cav}} = C_{\mathrm{cav}}/(1 + C_{\mathrm{cav}})$. In Refs. 166, 174 and 34, C_{cav} was not given and could not be calculated directly, yet an analog to $\mathcal{P}_{\mathrm{cav}}$ is reported. In these cases we infer the values of C_{cav} by backtracking. Here $P_{\mathrm{tot}} = P_1 P_2 = (\mathcal{P}_{\mathrm{em}}\mathcal{P}_{\mathrm{cav}})^2$ is the combined probability of this full emission process at node 1 and symmetrically of absorption at node 2, assuming both nodes have the same cooperativities. The emitter in each of the neutral atom experiments is a ^{87}Rb atom. In the trapped ion experiments, Refs. 175 and 174 use a single $^{174}Yb^{+}$ atom and up to 5 $^{40}Ca^{+}$ ions, respectively, while the others [166, 173] use a single $^{40}Ca^{+}$ ion. An extended version of this table is given in App. A.3.1 (see Table A.1).

Emitter type	Ref(s)	C_{em}	$\mathcal{P}_{\mathrm{em}}$ (%)	C_{cav}	$\mathcal{P}_{\mathrm{cav}}$ (%)	P_{tot} (%)
Neutral atom	[34]	2.8	74	9.0	90	44
	[176, 177]	6.0	86	11.9	92	62
	[178]	66.7	99	1.3	57	31
	[150]	2.9	75	8.0	89	44
	[179] A	7.7	89	11.5	92	66
	[179] B	6.9	87	6.0	86	56
Ion	[175]	0.05	5	0.5	32	0.02
	[154, 174]	0.3	24	6.7	87	4
	[166] A	0.8	45	0.3	20	0.8
	[166] B	1.9	66	3.5	78	26
	[173]	3.2	76	0.3	20*	2

$*$: The setup of Ref. 173 is not intended to preferentially produce photons out of one mirror. Accordingly, the cavity parameter values reported here appear small (and are excluded from the reported $C_{\mathrm{cav}}^{(\mathrm{avg})}$) yet they could readily be increased by modifying the setup.

guided microwave channels such as cryogenic microwave links [94, 171]. Note that the effects of a non-zero temperature bath can be incorporated in the input-output formalism (see Refs. 118 and 165 for corresponding textbook treatments), though doing so requires a good deal of extra work that we can largely avoid by assuming adequate effort will be taken to the isolate the setup from thermal noise.

The ideal values of the frequency and stretching parameters are $\omega_0 = \omega_{0i} \equiv \zeta = \omega_{\rightsquigarrow 2} - \omega_{\rightsquigarrow 1}$, which compensates for the difference in frequencies of the two systems, and $\xi = \xi_i \equiv \gamma_2/\gamma_1$, which stretches the wave packet to match the receiving time scale of cavity 2 [see Eqs. (3.24) and (3.57)]. Unlike for ω_0 and ξ, there is not a similarly 'nice' expression for the ideal value of the timing parameter $T = t_s(1 + 1/\xi)$, which controls the starting time for the transformation t_s. However, the goal is simple: for a given l one need simply select a t_s (and hence T) such that the largest contributions to $\beta_1(t)$ are transformed. We can be more precise in finding the optimal value of T, though we defer this to §4.3.2, where the analysis will be made easier using the machinery we will develop in the following section. For now we simply note that such an optimal T, which we will call T^*, must exist.

As we are focusing on errors in the unitary parameters in this section, we assume that the drives are implemented correctly [see strategy 4) above]. Namely, we assume that G_1 is implemented such that α_1, β_1 are as desired (see App. A.2 for a discussion of how an appropriate α_1 or β_1 can be used to determine the corresponding G_1) and, based on Eq. (3.60), that

$$G_2(t) = \xi_i G_1(\xi_i(T_i - t)) \tag{4.16}$$

with $T_i = T|_{\xi=\xi_i}$.[4] Note that with this choice, the laser phase $\phi_2(t)$ for system 2 is also time reversed and scaled relative to that for system 1. Hence the second laser pulse is not affected by an error in the unitaries' values of ξ and T. (In fact T_i need not take on its optimal value T_i^* as long as it is consistent in U and G_2 and l is long enough for the entire wave packet to be transformed.) One can show that the above choices for the unitary parameters and G_2's relation to G_1 are an optimum, in that given solutions α_1 and β_1, there are corresponding solutions for system 2

$$\alpha_2^i(t) = e^{i\omega_{0i}T_i}\alpha_1(\xi_i(T_i - t)) \tag{4.17}$$

and

$$\beta_2^i(t) = -e^{i\omega_{0i}T_i}\beta_1(\xi_i(T_i - t)) \tag{4.18}$$

(assuming l is long enough for the entire wave packet to be transformed), which act in a time-reversed manner relative to their system 1 counterparts. Hence, with the above choices and assumptions, if atom 1 loses an excitation, α_1 goes from one to zero, then atom 2 will absorb it, as $|\alpha_2^i|$ goes from zero to one.

4.3.1 Unitary parameter errors

If an excitation is sent from atom 1, we want atom 2 to absorb it and hence to achieve $|\alpha_2(t \to \infty)| = 1$. Thus, we analyze here the structure of α_2's EOM, which,

[4]This simple relationship between the drives G_j, and the corresponding class of ideal solutions for hybrid QST, simply relies on the validity of the Jaynes–Cummings Hamiltonian, Eq. (4.4), which as discussed in App. A.1.2 is quite general as an effective theory.

after eliminating β_2 in the coupled Eqs. (4.12c–d), can be found to be

$$\ddot{\alpha}_2 = \left(\frac{\dot{G}_2}{G_2} - \frac{\gamma_2}{2}\right)\dot{\alpha}_2 - G_2^2\alpha_2 + \sqrt{\gamma_2}e^{i\zeta t}G_2\Psi(t). \tag{4.19}$$

Rearranging the terms, it follows that

$$L(t)\alpha_2(t) = \Psi(t) \tag{4.20}$$

with

$$L(t) := \frac{e^{-i\zeta t}}{\sqrt{\gamma_2}G_2}\left[\frac{d^2}{dt^2} - \left(\frac{\dot{G}_2}{G_2} - \frac{\gamma_2}{2}\right)\frac{d}{dt} + G_2^2\right] \tag{4.21}$$

a linear operator (we *assume* it is invertible) and so it has some Green's function $\Gamma^*(t,t')$:

$$\alpha_2(t) = \int_{-\infty}^{\infty} dt'\ \Gamma^*(t,t')\Psi(t'). \tag{4.22}$$

[We choose to define the complex conjugated Green's function, $\Gamma^*(t,t')$, so that Eq. (4.23) takes a more standard form for a complex inner product.] Here we treat $\Psi(t)$ as some generic (possibly subnormalized) wave packet of arbitrary shape. This is justified mathematically as, in terms of the differential equation Eq. (4.20), $\Psi(t)$ is just some non-homogeneous source term, and the Green's function solution is indifferent to the origin of Ψ. Note we cannot design the first laser pulse G_1 (even if it is supplemented by our unitary) to deterministically produce arbitrary wave packets from system 1 (see App. A.2.5 for further discussion).

We will now use this Green's function to derive an expression for the limiting value of α_2 at some *end* time t_e by which the amplitudes have reached steady values (in practice t_e can be taken to be $+\infty$ mathematically). Physically, we know that

$|\alpha_2| \leq 1$, so with the shorthand $\Gamma(t = t_e, t') = \Gamma_e(t')$, we have

$$1 \geq |\alpha_2(t_e)|^2 = \left| \int_{-\infty}^{\infty} dt' \; \Gamma_e^*(t') \Psi(t') \right|^2 = |\langle \Gamma_e | \Psi \rangle|^2 , \tag{4.23}$$

where we are assuming Γ_e is well-defined and unique (in practice, this is typically the case with appropriate boundary conditions, and our numerics in §4.3.3 substantiate the validity of the solution we find), yet we do not yet know its norm. [We focus on $\Gamma_e(t')$ because our primary goal is that the excitation is ultimately transferred (as part of the QST scheme), not to know the exact dynamics of the excitations. Accordingly, we do not attempt to compute $\Gamma(t, t')$ for all times t, though we do note that it must be causal so $\Gamma(t, t' > t) = 0$.] This is true for arbitrary Ψ, which will be normalized (in the single-excitation subspace) unless there are losses, say due to photon absorption. Thus, we can select

$$|\Psi\rangle = \frac{|\Gamma_e\rangle}{\sqrt{\langle \Gamma_e | \Gamma_e \rangle}} \tag{4.24}$$

(up to a phase) to maximize $|\alpha_2(t_e)|^2 = |\langle \Gamma_e | \Psi \rangle|^2$ via the Cauchy–Schwarz inequality. With this selection, by Eq. (4.23) we have

$$1 \geq |\alpha_2(t_e)|^2 = \left| \sqrt{\langle \Gamma_e | \Gamma_e \rangle} \right|^2 = \langle \Gamma_e | \Gamma_e \rangle \tag{4.25}$$

so $|\Gamma_e\rangle$ is either a normalized or subnormalized quantum state.

We know that with ideal parameters $\omega_0 = \omega_{0i}$ and $\xi = \xi_i$ (again, for sufficiently long l with appropriate timing $T = T_i$) our unitary will produce the ideal wave packet

$$\Phi(t) = \Psi(t)|_{\omega_0 = \omega_{0i}, \xi = \xi_i, T = T_i, l \to \infty} = \sqrt{\gamma_2} e^{i\omega_{0i}(T_i - t)} \beta_1(\xi_i(T_i - t)), \tag{4.26}$$

which evidently is the time reversed, stretched, and frequency shifted counterpart of the wave packet to be emitted by system 1. Crucially, note that for properly designed α_1 that start at 1 at some early *preparation* time t_p, from Eq. (4.17) we have $|\alpha_2^i(t = t_e)| = |e^{i\omega_{0i}T_i}| = 1$ for $t_e \geq T_i - t_p/\xi_i$ and hence the corresponding normalized $\Phi(t)$, $\langle\Phi|\Phi\rangle = 1$, would lead to perfect absorption at system 2. Thus, again using Cauchy–Schwarz, we have that

$$1 = |\alpha_2^i(t_e)|^2 = |\langle\Gamma_e|\Phi\rangle|^2 \leq \langle\Gamma_e|\Gamma_e\rangle \langle\Phi|\Phi\rangle = \langle\Gamma_e|\Gamma_e\rangle \leq 1, \tag{4.27}$$

where we used Eq. (4.25) in the last step. It clearly follows that

$$\langle\Gamma_e|\Gamma_e\rangle \equiv 1 \tag{4.28}$$

and hence $|\Gamma_e\rangle$ corresponds to a normalized state vector, and moreover

$$|\Gamma_e\rangle = |\Phi\rangle \Longleftrightarrow \Gamma_e(t) = \Phi(t) \tag{4.29}$$

(again, up to a phase) as the states must be linearly dependent to saturate Cauchy–Schwarz. [This whole argument applies more generally as long as the EOM for α_2 is linear and there exists an ideal solution with $|\alpha_2^i(t_e)| = 1$.]

It thus follows that the probability of success is

$$P_{\text{success}} \equiv |\alpha_2(t_e)|^2 = |\langle\Phi|\Psi\rangle|^2 = \left|\int_{-\infty}^{\infty} dt'\ \Phi^*(t')\Psi(t')\right|^2 \tag{4.30}$$

as claimed in Eq. (4.2). That is, the probability of success is given by the norm squared overlap of the incident photon wave packet $\Psi(t)$ with the ideal wave packet $\Phi(t)$. Thus, if no errors occur, the transformed wave packet $\Psi(t)$ will be equal to the

normalized $\Phi(t)$ and hence $P_{\text{success}} = 1$. It follows that system 2 can be thought of as a photodetector that in the case of a click would project on the ideal state via the POVM element

$$\hat{\Pi}_{\text{success}} = |\Phi\rangle\langle\Phi| \,. \tag{4.31}$$

Note we would only register such a click (or not) if we appended an atomic measurement of the receiving qubit state. Then, we see that for the pure input state $\rho_{\text{in}} = |\Psi\rangle\langle\Psi|$,

$$P_{\text{success}} = \text{Tr}\Big(\rho_{\text{in}}\hat{\Pi}_{\text{success}}\Big) = |\langle\Phi|\Psi\rangle|^2 \,, \tag{4.32}$$

which matches Eq. (4.30). Note that this does not assume that Ψ is normalized, it could be subnormalized due to an error at system 1, an error in the unitary, or loss during the transformation.

More generally, such a POVM would be a weighted sum of projectors (mixed) but here it is a lone projector (pure) as our process is reversible. For instance, if the system parameters, such as g_j, varied due to fluctuations in the position of the atoms or cavities, then averaging over these fluctuations would give a mixed POVM [159]. Another relevant situation would be fluctuations in the unitary transformation parameters (ω_0, ξ, and T), which would result in the input state ρ_{in} of Eq. (4.32) being an incoherent mixture of states Ψ with different parameters according to some underlying classical probability distribution. Specifically, if there is classical uncertainty or variation in the unitary transformation parameters, e.g., variation in ω_0 due to the finite linewidth of a control laser, then the actual probability of success would be $P_{\text{success}}(\omega_0, \xi, T)$ averaged over the corresponding classical probability distribution. Note that the ideal wave packet should remain the same as it is purely determined by the parameters of node 2 and the laser driving it, G_2.

Note that P_{success} is actually just the probability that an excitation from atom 1 is transferred, via the intermediate photonic degree of freedom, to atom 2. This assumes that no other excitations that can excite atom 2 are produced during the transmission. We additionally assume that the phase of the initial state of atom 1 is correctly transferred to atom 2, i.e., the channel needs to be interferometrically stable [59, 168, 169]. This can be accomplished using stable local oscillators as frequency references at each system to establish a common phase reference for both nodes. Then phase stabilization techniques can be used to maintain (and control) the phase induced by the channel, which is easier for shorter channels [84, 153, 168, 169]. We assume such considerations are taken so we can focus on the impact of U rather the examination of such phase errors. Even if such phase errors do occur, error correction protocols could be used to eliminate them (see §4.3.4). We will proceed under these assumptions so that P_{success}, as defined in Eq. (4.30), is a good measure of the success of the entire QST scheme. Note that what 'success' ultimately means is up to the particular scheme. For instance, the quantum state fidelity $\mathcal{F}$ may be a more apt measure of successful QST. Here $\mathcal{F}$ is given by the magnitude squared of the overlap of the initial (qubit) state of atom 1 with the final state of atom 2. Notably in the absence of phase errors $\mathcal{F}(|c_e|)$ is bounded below by $P_{\text{success}} = |\alpha_2(t_e)|^2$ (see App. A.1.3 for details).

4.3.2 Optimal timing

Now that we have shown this new perspective, where system 2 can be thought of as a single-photon detector, we will derive an expression that the optimal unitary timing parameter T^* must satisfy. (Note this is new within the context of this problem; that POVMs play a key role in describing photodetection [181–186] and

measurements more generally [7, 187, 188] is well known.) We compute T^* assuming that the transformation is implemented correctly in all ways except that it has a limited duration t_l. Then the probability of success based on the Green's function argument above is

$$P_{\text{success}}(t_s) = |\langle\Phi|\Phi_l\rangle|^2 , \tag{4.33}$$

where $\Phi_l(t) = \Psi(t)|_{\omega_0=\omega_{0i},\xi=\xi_i,T=T_i}$ is the actual transformed wave packet for some finite l, assuming the ideal frequency and stretching parameters as well as consistent timing; $\Phi_l(t)$ is equal to $\Phi(t)$ for $t_s < t < t_f$. Maximizing $P_{\text{success}}(t_s)$ can thus be accomplished by solving for the t_s (and hence T_i) such that

$$\frac{d}{dt_s} P_{\text{success}}(t_s) = 0 \tag{4.34}$$

(and verifying that the optimum is a maximum).

Note that

$$\langle\Phi|\Phi_l\rangle = \sqrt{\gamma_1\gamma_2} \int_{-\infty}^{\infty} dt \, \Big[e^{-i\zeta(T_i-t)} \beta_1(\xi_i(T_i-t))\chi(t)\beta_1(f(t)) \Big], \tag{4.35}$$

where $\chi(t)$ and $f(t)$ characterize the different stages of the transformation and are implicitly evaluated at $\omega_0 = \omega_{0i}$, $\xi = \xi_i$, and $T = T_i$ here. The parameters T_i, t_i, and t_f (which are related to the different stages) all implicitly depend on t_s and so Eq. (4.34) should be solved numerically in general. However, in typical cases the contribution to Eq. (4.35) due to the untransformed portion of the wave packet (i.e., outside the interval $t_s < t < t_f$) will be negligible. This is due to some combination of l being long enough for the β_1 product in the integrand to be small over the relevant domain and the term being far off-resonant, with $|\omega_{0i}| \gg \gamma_{1,2}$, such that the phase

rapidly oscillates and the integrand averages to zero. In such a case, effectively none of the untransformed wave packet emitted from system 1 will induce a transition at system 2 and so we have

$$\langle \Phi | \Phi_l \rangle \approx \int_{t_s}^{t_f} dt \ |\Phi(t)|^2 = \gamma_2 \int_{t_s}^{t_f} dt \ \beta_1^2(\xi_i(T_i - t)) = \gamma_1 \int_{t_i}^{t_s} dt \ \beta_1^2(t) \tag{4.36}$$

(the approximation gets better for large $|\omega_{0i}|$ and/or l). As this inner product is real, we can maximize $P_{\text{success}}(t_s)$ by finding the t_s such that

$$0 = \frac{d}{dt_s} \int_{t_s - t_l}^{t_s} dt \ \beta_1^2(t) = \beta_1^2(t_s) - \beta_1^2(t_s - t_l). \tag{4.37}$$

This is a much simpler condition than in the general case and it can easily be solved for numerically once G_1 is specified and hence β_1 is determined. The corresponding solution is the ideal value of t_s, which we will denote by $t_s^* \equiv T_i^*/(1 + 1/\xi_i)$.

4.3.3 Numerical results

To makes plots illustrating errors in the different unitary parameters, we must specify the first laser pulse G_1. A natural case to consider is the G_1 such that the amplitude for atom 1, α_1, logistically decreases from 1 to 0

$$\alpha_1(t) = \frac{1 + \tanh(-kt)}{2}. \tag{4.38}$$

Note, for any monotonically decreasing α_1, one can compute the corresponding laser pulse G_1 that would generate it [see Eq. (A.27)]. Then the amplitude for cavity 1 can be determined as $\beta_1 = -\dot{\alpha}_1/G_1$, which in turn gives the exact form of the ideal emitted photon wave packet Φ of Eq. (4.26). (See App. A.2.2 for β_1 in this logistic

α_1 case.) We can thus compute how errors in the unitary transformation parameters, i.e., incorrect values of ω_0, ξ, and T, degrade the transfer resulting in a decreased P_{success}. The impact of such errors on P_{success} can be seen graphically as in Fig. 4.1, where we compare a wave packet Ψ due to a unitary transformation with stretching and timing errors to the corresponding ideal wave packet Φ.

Furthermore, we can compute how P_{success} varies as a function of the amount of error in the various transformation parameters. For instance, we illustrate the effect of errors in the unitary parameters ω_0, T, and ξ by plotting P_{success} versus one of these parameters assuming the other parameters are ideal in Figs. 4.2, 4.3, and 4.4, respectively. We work with a set of shifted 'error variables' that are centered at zero: $\Delta\omega_0 \equiv \omega_0 - \omega_{0i}$, $\Delta\ell_\xi \equiv \log_2 \xi - \log_2 \xi_i$, and $\Delta T \equiv T - T_i^*$. We consider the logarithm of ξ in most of our plots as its ideal value is a ratio of two decay widths, $\xi_i = \gamma_2/\gamma_1$, so errors in ξ should scale multiplicatively, e.g., doubling ξ (with respect to its ideal value) should be (about) as bad as halving it. In each of these plots (Figs. 4.2-4.4), the solid black lines are a cubic interpolation between 201 points with the independent variable's values distributed evenly over the intervals shown. The corresponding value of P_{success} is given by the overlap calculation $|\langle\Phi|\Psi\rangle|^2$. The overlaid colored points are calculated by numerically solving the coupled ordinary differential equations (ODEs) of Eqs. (4.12a-d) for various values of the independent variable (with larger separations because the relevant numerics are more computationally expensive).

For concreteness we focus on the specific case of a logistic α_1 with $k = 2$ and the physical parameters $\omega_{0i} = 50$ and $\xi_i = 1/2$. Additionally, we assume a long transformation length $l = 10$, for which $T^* = 19.7$, such that in the absence of errors in the unitary, effectively all of the wave packet would be transformed with $P_{\text{success}} = 0.999995 \approx 1$. Here all quantities are given in natural units in which

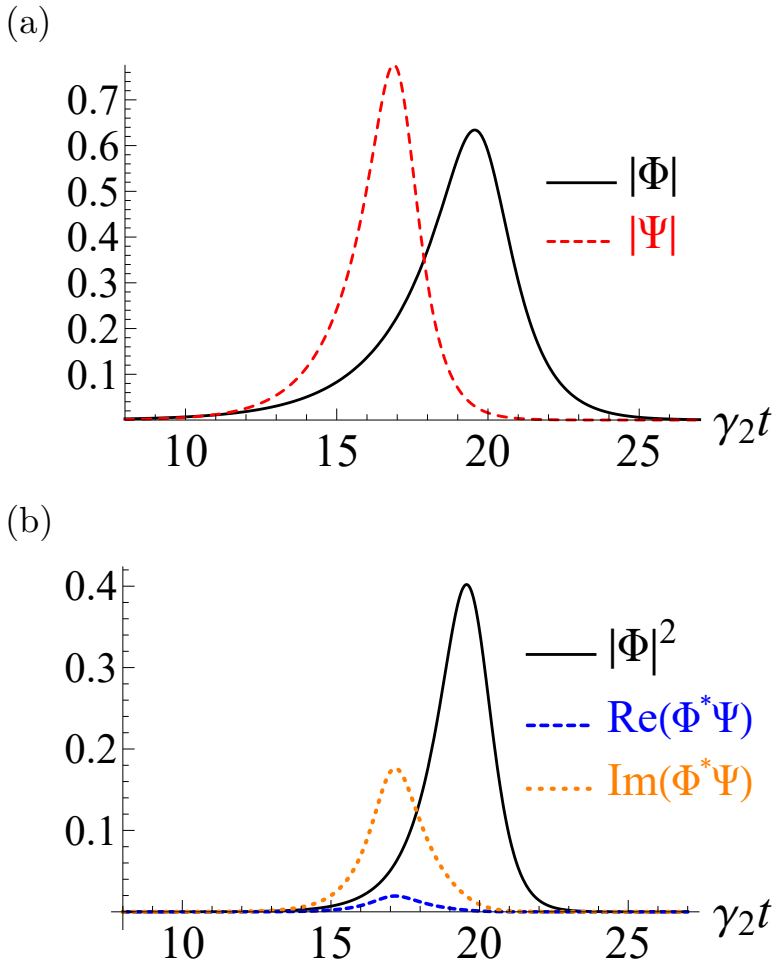

FIGURE 4.1. (a) Plot of the ideal wave packet modulus $|\Phi|$ for $k = 2$, with the unitary parameters taking on their ideal values $\omega_0 = \omega_{0i} = 50$, $\xi = \xi_i = 1/2$, $T = T_i^* = 19.7$ for transformation duration $t_l = 10$, and a non-ideal wave packet modulus $|\Psi|$ still with $\omega_0 = \omega_{0i}$, but with stretching and timing errors $\xi = 0.75$ and $T = 17$. (All quantities are in units where $\gamma_2 = 1$.) (b) Plot of the integrand in Eq. (4.30) for computing P_{success} in the ideal case (solid line) and the real and imaginary parts in the non-ideal case (dashed and dotted lines, respectively). Here, for visualization purposes, we decompose Eq. (4.30) as $P_{\text{success}} = \left[\int dt\, \mathrm{Re}\,(\Phi^*\Psi)\right]^2 + \left[\int dt\, \mathrm{Im}\,(\Phi^*\Psi)\right]^2 = 0.186$, whereas $P_{\text{success}} = \int dt |\Phi|^2 = 1$ for the ideal wave packet (which assumes the entirety of the wave packet emitted from node 1 is transformed).

$\gamma_2 = c = 1$. Importantly, these underlying parameter values are not crucial as, at least for large l as we have here, only the error variables (made dimensionless with appropriate factors of γ_2) and the wave packet shape (as effectively controlled by α_1)

matter (see App. A.3.2). Hence the results gleaned from this specific case apply more generally. The largest discrepancy in calculating P_{success} between the original coupled ODEs solution method and the POVM wave packet overlap method is $1.1 \cdot 10^{-6}$, which we assume to be numerical error (in particular, we see that this specific error value goes down if we increase our error tolerance when solving the ODEs). Hence this numerical comparison serves as a strong indicator of the validity of the POVM based results we found.

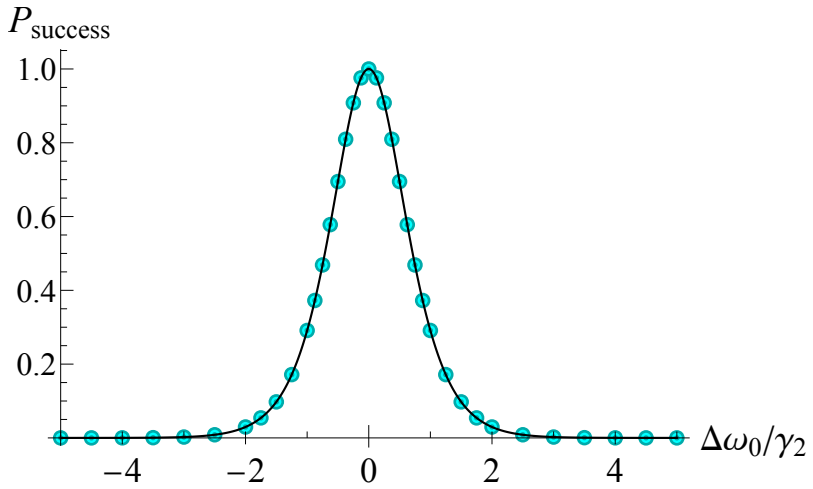

FIGURE 4.2. Plot of P_{success} as a function of the detuning $\Delta\omega_0$ assuming the other unitary parameters are ideal. We take the underlying parameter values to be the same as in Fig. 4.1 (that is, $k = 2$, $\omega_{0i} = 50$, $\xi_i = 1/2$, and $t_l = 10$ in units where $\gamma_2 = 1$). The probability of success quickly falls off away from resonance, $\Delta\omega_0 = 0$. The solid line is from a state overlap calculation using Eq. (4.30) and the overlaid points are from directly numerically solving coupled EOMs for the state amplitudes (see main text).

The probability of success quickly falls off away from its peak value near unity as ω_0, T, and ξ are shifted from their ideal values. The narrow peak around $\omega_0 = \omega_{0i}$ in Fig. 4.2, which has a full width at half maximum (FWHM) of $1.4\gamma_2$, illustrates the importance of frequency conversion. We note that the shape and width of the P_{success} versus ω_0 curve do not change appreciably as the central frequency $|\omega_{0i}|$ is further

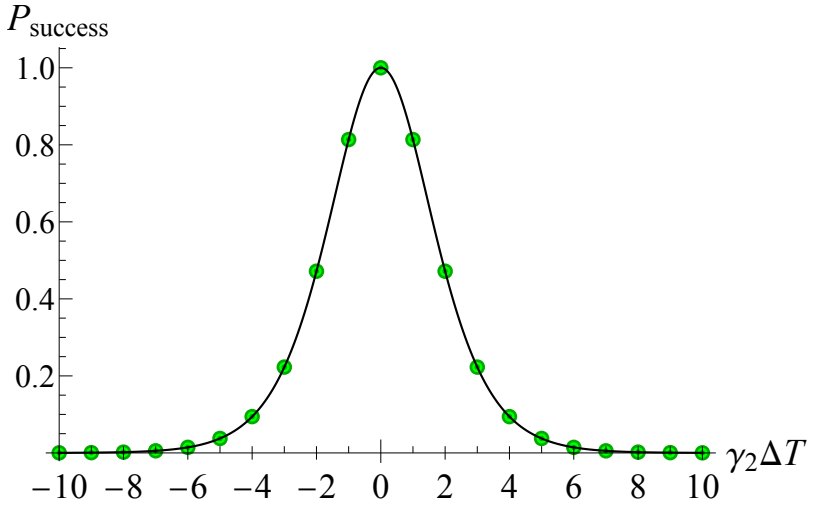

FIGURE 4.3. Plot of P_{success} versus ΔT assuming the other unitary parameters are ideal (with the same underlying physical parameters as the previous figures). The solid line is from an overlap calculation and the overlaid points are from solving coupled amplitude EOMs (see main text).

increased. This is because, as alluded to above, only the detuning of the transformed wave packet from resonance with system 2 relative to γ_2, $|\Delta\omega_0|/\gamma_2$, significantly matters during the transformation. Moreover, for large $|\omega_{0i}|$ the untransformed portions of the wave packet will not induce an excitation in atom 2. Thus, even when $|\omega_{0i}|$ is very large, e.g., $|\omega_{0i}|/\gamma_2 \sim 10^6$ is typical, the FWHM will be stable. Here it remains at $1.4\gamma_2$ (for this logistic α_1 with $k = 2\gamma_2 = \gamma_1$), and hence it is critical to control against frequency errors. Note that wave packets with narrower temporal shapes are less susceptible to such frequency errors, though this will be limited by emitting node parameters (see App. A.2.4).

The couplings γ_j tend to be on the order of kHz-MHz, and are typically smaller in the microwave regime as compared to the optical. Hence, typical values of γ_j can vary by 2 to 3 orders of magnitude between different systems and so $\xi_i = \gamma_2/\gamma_1 \sim 100-1000$ is reasonable for hybrid interconnects (assuming $\gamma_2 > \gamma_1$, otherwise ξ_i would be the reciprocal of this). Experiments across different platforms have demonstrated the

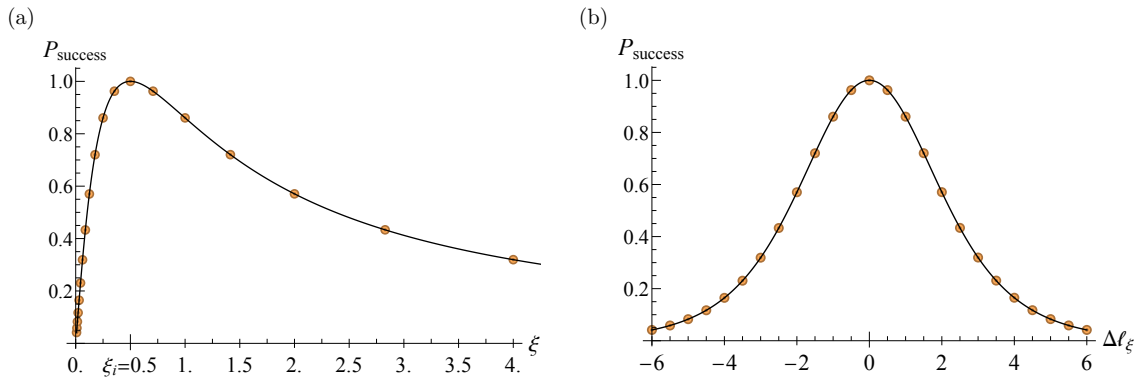

FIGURE 4.4. Plots of P_{success} versus ξ on (a) a linear scale and (b) a logarithmic scale with $\Delta\ell_\xi = \log_2 \xi/\xi_i$, assuming the other unitary parameters are ideal (with the same underlying physical parameters as the previous figures). The solid line is from an overlap calculation and the overlaid points are from solving coupled amplitude EOMs (see main text).

ability to shape photon wave packets, which includes stretching and compression by these orders of magnitude [147, 149, 150, 189]. Note that the results for different ξ_i can be mapped between one another because, as mentioned above, P_{success} is predominantly determined by the error variables, $\Delta\ell_\xi$ in this case. Importantly, the narrow width of P_{success} as a function of $\Delta\omega_0/\gamma_2$ does not doom us as sub-kHz-MHz level precision in frequencies (necessary to obtain $|\Delta\omega_0| < \gamma_2$) is possible using tunable, narrow-linewidth lasers [190–193], mid-infrared and terahertz laser sources based on difference frequency generation [194, 195], and for many other standard lasers. For instance, in an optical setup with atoms or ions (see Ref. 166 as a good example) typical laser linewidths and cavity jitters are on the order of $10 - 100$ kHz, meanwhile γ_j are around $1 - 10$ MHz (see Table A.1) so one could reasonably achieve $|\Delta\omega_0|/\gamma_2$ of 10^{-2} to 10^{-3}, for which $P_{\text{success}} > 99\%$ in Fig. 4.2.

We can quantify how much two of the dimensionless error variables $\{\Delta\omega_0/\gamma_2, \Delta\ell_\xi, \gamma_2\Delta T\}$ depend on one another by computing their "index of

separability" $\mathcal{S}$.[5] For an $m \times n$ matrix A we define $\mathcal{S}$ in terms of its singular values $\{\sigma_i(A)\}$ with maximum $\sigma_{\max}(A)$ as

$$\mathcal{S}(A) := \frac{\sigma_{\max}^2(A)}{\sum_i \sigma_i^2(A)}, \tag{4.39}$$

which is the square of the ratio of the induced 2-norm and Frobenius norm of A. This index of separability is bounded as $0 < 1/\min\{m,n\} \leq \mathcal{S}(A) \leq 1$, where the maximum $\mathcal{S}(A) = 1$ entails that A is separable, i.e., can be written as an outer product of two vectors, and the minimum $\mathcal{S}(A) = 1/\min\{m,n\}$ (which is nearly zero for large matrices) entails A is full rank with all equal singular values. However, practically the smallest observed values will be much larger than this (~ 0.75 here), which comes from comparing to random matrices (see App. A.3.2).

For instance, with the same underlying physical parameters as in Figs. 4.1–4.4, we take the joint probability distribution for $\gamma_2 \Delta T$ and $\Delta \ell_\xi$ assuming ω_0 takes on its ideal value, $P_{\text{success}}(\Delta T, \Delta \ell_\xi)|_{\omega_0 = \omega_{0i}}$, compute it on a grid of equally spaced values for ΔT and $\Delta \ell_\xi$ yielding a matrix, and then compute its index of separability to be

$$S_{T,\xi} \equiv \mathcal{S}[P_{\text{success}}(\Delta T, \Delta \ell_\xi)|_{\omega_0 = \omega_{0i}}] = 0.87. \tag{4.40}$$

[5] Reference 196 uses and analyzes this index in a much different, neuroscience-based context, though such a measure is often considered in principal component analysis, in which case this index is the percent of variance captured by the first principal component of the data. Such an index is quite natural based on the Eckart–Young theorem [197] for low-rank matrix approximations [198]. An analogous quantity often considered in quantum information, e.g., in multipartite entanglement characterization, is the 'Schmidt number,' which is encoded in the Schmidt decomposition (which is nothing but a singular value decomposition in disguise) of a quantum state [199]. See App. A.3.2 for further method details and discussion.

Similarly, for the other two variable pairs (keeping the third variable at its ideal value) we find

$$S_{\omega_0,\xi} \equiv \mathcal{S}[P_{\text{success}}(\Delta\omega_0, \Delta\ell_\xi)|_{T=T^*}] = 0.87 \tag{4.41}$$

and

$$S_{\omega_0,T} \equiv \mathcal{S}[P_{\text{success}}(\Delta\omega_0, \Delta T)|_{\xi=\xi_i}] = 0.998. \tag{4.42}$$

[Each of these $\mathcal{S}$ values is computed on a 121 by 121 grid (matrix) with the same spacings as described in the Fig. 4.5 caption over a rectangular region twice as large in each direction as those depicted. These reported values ultimately serve as upper bounds for the separability index for large grids. Corresponding lower bounds can be calculated using the zero-mean counterparts of the P_{success} matrices used here, yielding respective $\mathcal{S}$ values of 0.80, 0.80, and 0.97 compared to Eqs. (4.40)–(4.42). (See App. A.3.2 for additional method details.)]

Hence ω_0 and T errors are largely independent of one another (as the corresponding probability distribution is almost separable, $\mathcal{S} \approx 1$), whereas errors in ω_0 and T are distinctly dependent on what ξ error occurs. The corresponding joint probability distributions are given in Fig. 4.5 and can be used to get visual intuition for the index of separability. For instance, Fig. 4.5 (a) illustrates that errors in T and ξ are dependent on each other, which can intuitively be explained as wave packet timing errors in T will reduce the overlap, yet there will be relatively more overlap if one also elongates the wave packet in the time domain by choosing $\xi < \xi_i$ ($\Delta\ell_\xi < 0$). This analysis accounts for dependencies of the errors on one another that are intrinsic to our model. We leave considerations of other error dependencies that may be due to a particular implementation of the transformation U to other work.

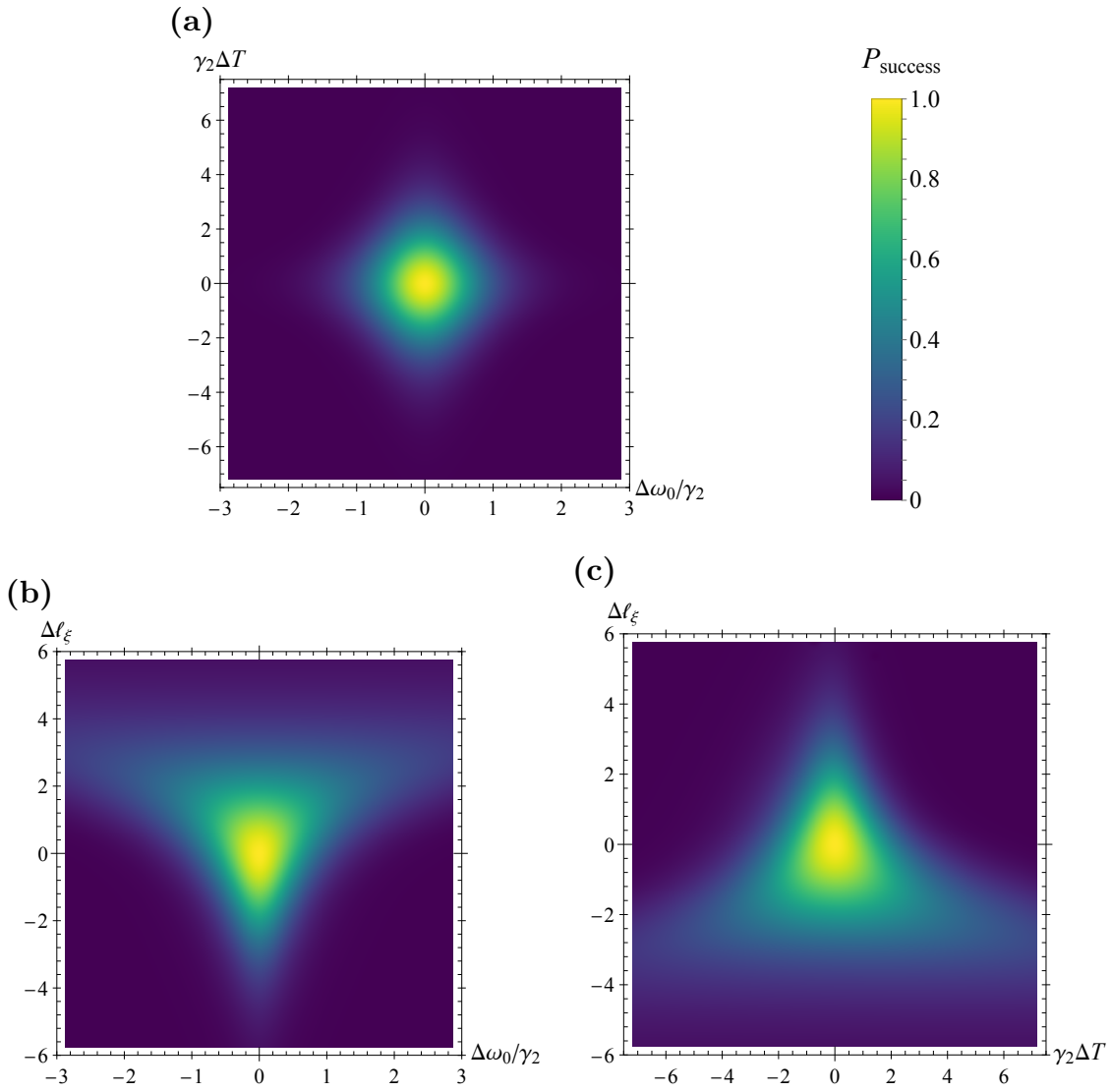

FIGURE 4.5. Density plot of P_{success} as a function the error variable pairs for the transformation parameters (a) T and ξ, (b) ω_0 and ξ, and (c) ω_0 and T assuming the other unitary parameter is ideal (with the same underlying physical parameters as the previous figures). Each plot is computed as the cubic interpolation of a 61 by 61 grid of points that are evenly spaced over the region shown and is colored according to the legend.

4.3.4 Error correction

We have highlighted many things can go wrong in the implementation of the unitary itself, which is in addition to standard errors due to incorrect driving laser

pulses, incorrect laser frequencies, fluctuating system parameters, as well as photon absorption or other losses in the transmission line, cavities, material qubits, or transformation device. With all of these possibilities, the presence of errors on a single attempt of a QST scheme like ours is inescapable, though crucially we can correct for these errors. Accordingly, we will now discuss the applicability of a few error correction protocols to our scheme as well as their limitations.

ECZ protocols. By using the occupation number encoding our scheme could naturally be improved by utilizing one of two relatively low overhead error correction protocols [2, 164] that capitalize on the feasibility of suppressing photon production errors $|0\rangle \to |1\rangle$. We refer to these as the 'ECZ protocols' after their authors' last names. These protocols can correct for photon loss and phase errors, which are recurrent in standard transmission lines, e.g., optical fibers and waveguides. They do so using auxiliary quantum emitters, again envisaged as atoms in a cavity, that can encode the state of a qubit at each node and serve as a form of redundancy. They cannot correct for errors caused by the creation of photons in the relevant mode, which is often reasonable as the production of photons can be suppressed in a well-isolated setup operating at an appropriate temperature (such that there is low thermal occupation, $\bar{n}_{\rm th} \ll 1$, which as previously discussed is more of a problem in microwave-based systems).

Each ECZ protocol is based on repeating a certain primitive transfer operation, which we will refer to as a trial, that includes 1 or 2 QST attempts (typically 2), local single-qubit and two-qubit entanglement gate operations, and measurements of auxiliary qubits or states. These local gate and measurement operations are assumed to be implemented perfectly, though in practice these operations will also be error prone and hence limit how close to unity the ultimate transfer fidelity can be. In the

earlier protocol [2], measurements are performed on each trial, a successful outcome of which validates the state transfer. In the later protocol [164], a given trial serves as a 'purification' step to be iterated so that a target state is approached exponentially, at a rate that gets faster for smaller net errors in the protocol, and hence can be reached up to some error threshold in fidelity. (See App. A.3 for further discussion of these protocols.)

Both ECZ protocols consider an effective channel in which on a single transmission attempt (which forms an integral part of both protocols) the initial state will evolve for large times (so that no excitations remain in the cavities) according to a map of the form[6]

$$\begin{matrix} |g_1\rangle|g_2\rangle \\ |e_1\rangle|g_2\rangle \end{matrix} \longrightarrow \begin{matrix} \alpha|g_1\rangle|g_2\rangle \\ \beta|g_1\rangle|e_2\rangle + \Upsilon_1|g_1\rangle|g_2\rangle + \Upsilon_2|e_1\rangle|g_2\rangle \end{matrix}, \tag{4.43}$$

where α, β, and $\Upsilon_{1,2}$ are constants. These are the form of the long time limit of the solutions to EOMs analogous to Eq. (4.12) with $|\beta| = |\alpha_2(t_e)|$ and $|\Upsilon_2| = |\alpha_1(t_e)|$, but with additional possible errors included. Importantly for our scheme, *an error in the unitary transformation falls under this class of channel* as it will contribute to photon loss. Chiefly, an incorrectly shaped incident wave packet will not be absorbed by node 2 and hence will be directed out a different spatial mode. This is in addition to losses that are in intrinsic to the transformation device. Such errors can be accounted for via the amplitudes β and Υ_1. Thus, our scheme can naturally be incorporated as an extended version of the transmission steps in the ECZ protocols, which can aptly be utilized in our context for reliable QST between hybrid nodes.

[6]This is analogous to Eq. (3) of Ref. 2 using our notation for the states. They consider emitters with a slightly modified level structure compared to the Λ-type systems we consider due to the presence of an additional ground state (see Fig. A.11).

We acknowledge that such a protocol would slow down the rate of entanglement generation due to the time it takes to repeat the primitive transfer scheme as well as to perform the requisite local computations. Importantly, however, if we can achieve reasonably small error probabilities in the necessary operations the slowdown in rate can be manageable. We will now illustrate this by considering the expected number of repetitions $E[n]$ of the earlier ECZ protocol (until success) [2] in the case where $|\alpha| = 1$, as we have previously assumed in our scheme, yet its phase could be nontrivial due to a relative phase error (see App. A.3.4). Consider an error on a given transmission of $|\Upsilon_1|^2 + |\Upsilon_2|^2 = \varepsilon$ such that $|\beta|^2 = 1 - \varepsilon$ by normalization. In this model the worst case, that with the largest $E[n]$, is when we are dominated by Υ_1 errors (i.e., $|\Upsilon_1|^2 = \varepsilon$ and $\Upsilon_2 = 0$). In this worst case we find

$$E[n] = \frac{4}{(1-\varepsilon)(2-\varepsilon)^2}, \tag{4.44}$$

which starts at 1 for $\varepsilon = 0$, corresponding to only needing a single trial without errors, and monotonically increases as a function of $\varepsilon \in [0, 1]$, tending towards $+\infty$ as $\varepsilon \to 1$ as the state transfer entirely fails for $\beta = 0$ (see App. A.3 for the general derivation and further details). Note in fact we expect to be in this regime, $|\Upsilon_1| \gg |\Upsilon_2|$, with photon loss and unitary transformation errors being dominant such that

$$\varepsilon \approx |\Upsilon_1|^2 \approx 1 - \tilde{P}_{\text{success}}, \tag{4.45}$$

see Eq. (4.14). In Fig. 4.6 we use Eqs. (4.44) and (4.45) to show how $E[n]$ depends on the bare P_{success} value with the inclusion of realistic standard errors (informed by the parameter values of Table 4.1). Knowing the dependence of $E[n]$ on P_{success} for experimentally achievable parameter regimes can inform how much

unitary transformation loss or error (quantified by P_{success}) can be tolerated in a given implementation. Importantly, we find that if small unitary transformation error probabilities, $1 - P_{\text{success}}$, can be achieved, then few trials (protocol repetitions) will typically be needed when linking nodes with good (yet realizable) cooperativities linked by relatively short channels (e.g., with lengths around an order of magnitude smaller than the attenuation distance x_{tl} or less).

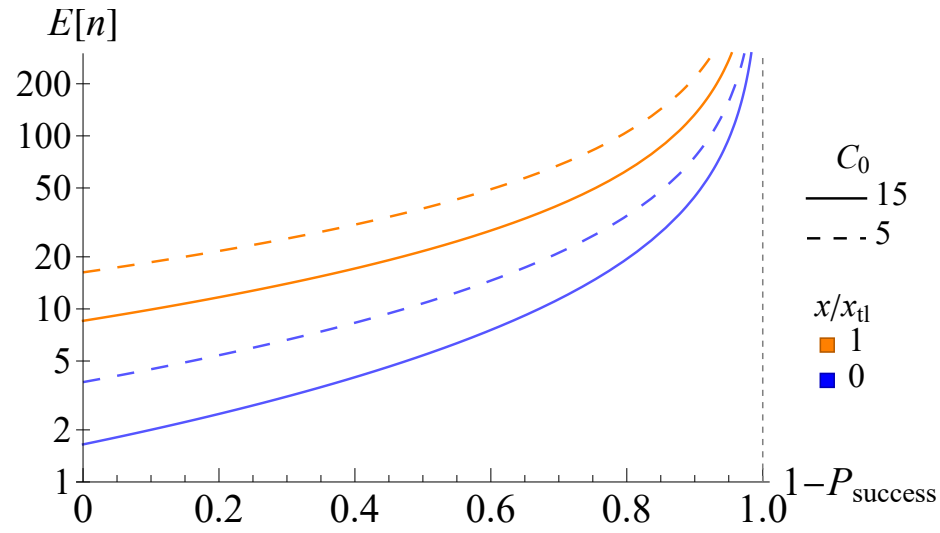

FIGURE 4.6. Plot of the expected number of ECZ [2] error correction trials, $E[n]$ from Eq. (4.44), on a log scale versus the error in the itinerant photon's temporal-frequency shape, $1 - P_{\text{success}}$. This is done for realistic cooperativities informed by the values listed in Table 4.1. Here for simplicity we take $C_{\text{em}} = C_{\text{cav}} = C_0$, as in both cases currently achievable cooperativity values are around $C_0 = 5$ (dashed lines), while $C_0 = 15$ (solid lines) is more optimistic yet plausible. These plotted cases could equivalently represent other cooperativity pairs with the same respective combined probabilities $P_{\text{tot}} = P_1 P_2$ of 48% and 78%. For each C_0 value, we consider two cases: no transmission loss ($x/x_{\text{tl}} = 0$, $P_3 = 1$) and transmission loss over one attenuation distance ($x/x_{\text{tl}} = 1$, $P_3 = 1/e \approx 37\%$), which are shown in the lower (blue) and upper (orange) lines, respectively, for a given line type (solid or dashed). See §4.2.6 for standard values of x_{tl} for optical and telecom light in fiber. As P_{success} gets small, tending towards zero ($\varepsilon \to 1$), the expected number of trials quickly grows, diverging like $1/P_{\text{success}}$ to leading order (indicated via the dashed vertical asymptote). For instance, $E[n]$ reaches 10 when $\varepsilon \approx 0.75$, which in the above cases with cooperativities of 15 and 5 corresponds to bare P_{success} values of about 33% and 53%, respectively, for $x/x_{\text{tl}} = 0$.

Alternate protocols and their scope. Depending on the achievable $E[n]$, the magnitude of errors in the local operations needed for the ECZ protocols, and other implementation details, the employment of another correction protocol or even a nondeterministic heralded approach may be appropriate (see §4.3.5). There are several alternate error correction protocols that can be used for deterministic quantum communication via photons. For consistency, here we focus on protocols that use the mode occupation number encoding (see App. A.1.6 for a discussion of other encodings). Such protocols can be realized using multi-photon states as a type of redundancy, e.g., using so-called binomial [200] or cat [93] codes, or using photonic graph states (such as cluster states) generated from a single emitter [201–203]. Each of these alternate protocols comes with their own technical challenges, especially in hybrid interfacing contexts like ours where we would need to transform all the itinerant photons in a logical state preserving way. Moreover, both the sender and receiver would need to be able to interface with these multiphoton logical states. For instance, such binomial codes are realizable with superconducting circuit technology [88] but are more challenging for other implementations with less control of the requisite multiphoton states. Similarly, only a few emitters, including quantum dots and atoms in cavities, have demonstrated viability in the generation of such photonic graph states. Accordingly, one advantage of the ECZ protocols, especially for hybrid interconnects, is their relative simplicity as the generation of single photon states is a standard, feasible task for a wide variety of node implementations.

To make such protocols (including those of ECZ) applicable in the NISQ (Noisy Intermediate-Scale Quantum [204]) era with error prone operations on small numbers of qubits one has to compromise between the potential noise reduction of a given error correction protocol versus the realistic 'cost' of its implementation in

a given deterministic QST proposal or experiment. This cost includes additional resources such as local operations and controls as well as auxiliary emitters that can simultaneously be coupled at each node, which all come with their own potential errors as well as slower rates. For instance, when adapted to our hybrid case, the earlier ECZ protocol [2] is contingent on the errors in the unitary parameters, laser pulses, and system parameters [specifically α and β in Eq. (4.43)] being consistent between subsequent transmissions in a given trial. If this systematic condition breaks down, then the later ECZ protocol [164] should potentially be used as it can iteratively purify more general random errors in the channel even with potentially non-Markovian decoherence. However, this more comprehensive nature of the later protocol is at the expense of additional overhead, in the form of additional local operations, especially for large errors, so a compromise must be made.

4.3.5 Relevance in heralded schemes

At this point, it is useful to contrast our deterministic scheme against commonly employed heralded schemes for QST and/or remote entanglement generation. Here we give the basic idea of such heralded schemes and discuss how the ideas underlying our work can be applied to them. Such a heralded scheme may be appropriate if the ECZ or alternate error correction protocols discussed above for a deterministic scheme are not realizable (see App. A.1.7 for some discussion of the pros and cons of deterministic versus heralded schemes). In many such schemes [166, 168, 169, 205–207], two nodes each emit a photon that encodes the state of a qubit in one of its degrees of freedom (typically using a polarization encoding). Said photonic qubits states are (ideally) maximally entangled to their emitter's qubit state. Then a photonic Bell-state measurement is implemented in which the two photons interfere at a 50:50 beam

splitter and a subsequent coincident detection of photons with orthogonal qubit states ideally heralds the creation of a remote entangled state between the matter qubits at each node, otherwise the procedure is repeated until success.

The quality of the generated remote entanglement is ultimately determined by how indistinguishable the two photons are, whose states we denote by $|\psi_A\rangle$ and $|\psi_B\rangle$. Namely, the fidelity of the remote entangled state relative to a target maximally entangled state is determined by the mode overlap of the two photons $\mathcal{C} \equiv \langle\psi_A|\psi_B\rangle$ as [205]

$$\mathcal{F} = \frac{1 + |\mathcal{C}|^2}{2} \tag{4.46}$$

(note this ignores detector background counts and imperfect emitter-photon entanglement, which will further degrade $\mathcal{F}$ [166]). The key physics behind this is that for indistinguishable photons, $|\mathcal{C}| = 1$, the beam splitter removes which-path information leading to the entanglement swapping from the emitter-photon pairs to the emitters with unit fidelity (after an appropriate heralded measurement). Meanwhile, the interference of distinguishable photons at the beam splitter results in the addition of a classical mixture to the otherwise entangled (heralded) joint state of the emitter qubits. This combination preserves the joint state populations yet reduces the coherences, thereby lowering the state fidelity (i.e., it is a two-qubit dephasing channel).

Thus, having nearly indistinguishable photons as inputs to the photonic Bell-state measurement of such a heralded scheme is crucial for obtaining high fidelity remote entanglement. This can be connected to our work in that a transformation like our U (but without time reversal) could be used to make the photons emitted by heterogeneous nodes nearly indistinguishable and thus to achieve heralded hybrid remote entanglement generation (or QST via an additional quantum teleportation

step). Moreover, the analysis of the errors in such a transformation, to be employed in a heralded scheme, carries over almost directly from our work with $|\mathcal{C}|^2$ effectively replacing P_{success} as a figure of merit for the success of the scheme.

4.4 Discussion

In this chapter we have demonstrated theoretically how unitary transformations to the temporal-spectral mode of a photon serving as a flying qubit between hybrid quantum nodes can be used to drastically improve the probability of successfully transferring quantum information between the nodes. We showed that the probability of transferring an excitation from one node to another, which is a good measure of successful quantum state transfer, is given by the modulus squared of the overlap of the spectral shapes of the actual and ideal photon wave packets. Doing so makes the role of the unitary transformation apparent: it should transform the emitted photon to one with this ideal spectral shape (which can be calculated). Importantly, our scheme applies quite generally to any nodes in which controlled quantum light-matter interaction can be realized to reversibly transfer the state of a material qubit to a photonic degree of freedom and back, not just for the three-level atom in a cavity type nodes we focus on.

We analyzed the impact of errors in the implementation of the unitary transformation. This includes showing how the success of the protocol depends on the deviations from the ideal parameters as well as quantifying how much these parameter errors depend on one another. This analysis, along with our considerations of more standard errors, can be used to determine what kinds of errors dominate in a given physical setup, say to form an error budget. Furthermore, we discussed how our scheme can naturally be incorporated with and aid known error correction

protocols to significantly suppress or potentially eliminate unavoidable errors in deterministic quantum state transfer, even between hybrid systems. Such an error-corrected adaptation of our scheme could be used to distribute entanglement in a quantum network or for distributed quantum computing. As a next step, our methods could be applied to other material systems and the unitary transformation's physical implementation could be further considered, especially for cases outside of the optical regime.

CHAPTER V

INTERFERENCE OF INTERFERENCE EFFECTS

This chapter contains currently unpublished work that is under a second round of review at the American Journal of Physics and a preprint is available, arXiv:2501.03505 (2025) [5]. It was originally conceived of by S. J. van Enk, and its revitalization was spurred by K. J. Randles. It was developed by K. J. Randles and S. J. van Enk, who jointly conducted the main analysis. The figure production, appendix preparation and analysis, and a majority of the writing was done by K. J. Randles with continued guidance, feedback, and editing from S. J. van Enk. Once published, see American Journal of Physics for a shorter version of this work intended for physics instructors.

As we prefaced in Ch. I, this chapter explores a second, self-contained direction of this dissertation that has more of a pedagogical aim. It should be accessible to a wider audience as the underlying methodology is arguably much simpler than that of the previous chapters, e.g., it does not require an understanding of the input-output formalism. To this end, we note that with this chapter's pedagogical basis, we choose to include explanations of some content that is likely well-known to the reader (§5.2). Accordingly, readers may reasonably opt to skip to §5.3.

5.1 Introduction

In this chapter, our focus shifts from the interaction of light with matter and wave packet manipulation, to the control of photons using passive elements like beamsplitters along with measurement. We will explore how two quantum interference effects of light, namely, single-photon Mach–Zehnder interference (MZi)

and two-photon Hong–Ou–Mandel interference (HOMi), manifest in consonance with one another. (We will review each of these interference effects in Sec. 5.2.) This exploration naturally leads us to consider the setup depicted in Fig. 5.1 (see Sec. 5.3). This setup consists of two Mach–Zehnder interferometers (MZIs) linked via a common central beam splitter, forming a network of seven beam splitters that direct incident light along well-defined paths that can intersect one another. We focus on single-photon inputs into each MZI and on a diagrammatic method of analyzing the resulting path interference.

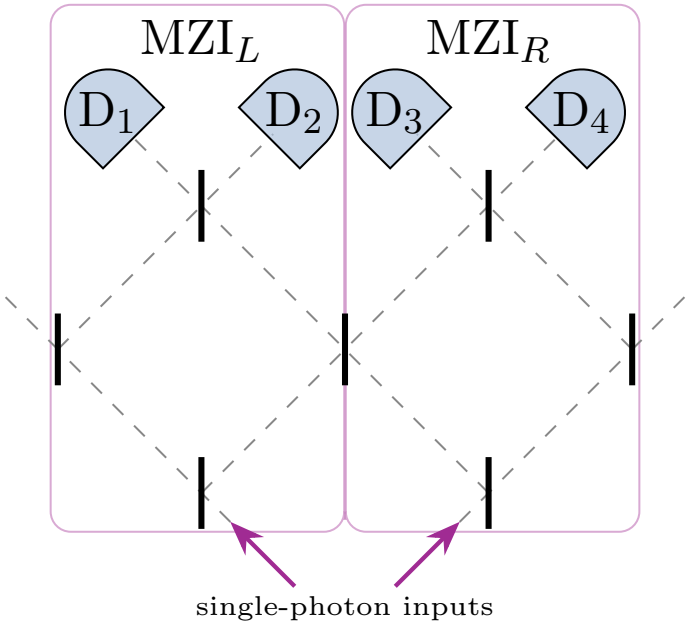

FIGURE 5.1. Diagram of the beam-splitter (BS) network setup we consider, which consists of two balanced MZIs linked by a common central BS. The left and right MZIs (denoted with L and R subscripts, respectively) are both indicated via the bordered regions. All the BSs (shown as vertical black lines) are taken to be 50:50. The incident light is comprised of two identical single photons (shown as arrows), one incident on each of the initial BSs. After traversing the setup (the possible paths are indicated by the dashed lines), each photon will either impinge on one of the four detectors (D_1−D_4) or exit the setup via one of the outer BSs (see text for further explanations).

5.1.1 Pedagogical context

We note that tutorials, simulations (see App. B.1 and Ref. 208), and experiments exploring the interference of individual photons can be made quite accessible (e.g., appropriate for a quantum optics or laboratory course for advanced undergraduate or early graduate students) [209–212], which is important as quantum interference can be a confusing topic to students [213–216]. Part of the intrigue of our setup is that, even if one successfully engages with such material and learns about MZi and HOMi, they may be tempted to follow a line of reasoning (similar to that presented in Sec. 5.3.2) that is partially quantumly informed, yet nevertheless leads to incorrect conclusions. In this chapter, we highlight several examples of such incorrect reasonings and provide "resolutions" that explicitly address corresponding misunderstandings (see §5.3.4) [213].

Our exposition is designed to be accessible and serve as a bridge from the unadorned interference effects that are often introduced to students (MZi and HOMi in our case) to understanding more complicated setups and related fundamental physics, including photonic quantum computing,[1] tests of quantum mechanics [225–227], and complementarity [228–230]. Moreover, related setups have applications in quantum communication and quantum sensing [231–233]. Throughout the chapter (see Sec. 5.3.5 especially), we highlight connections between our work and these

[1]References 217–221 provide a carefully selected subset of the literature on quantum computing with photons, intended to serve as a useful starting point for the reader. The seminal work of Ref. 217 demonstrated that linear-optical quantum computation (LOQC) was possible. Ref. 218 presents a key experiment that demonstrated many LOQC primitives in an MZI-based system. Refs. 219 and 220 provide reviews on LOQC, the former being an extensive early review, and the latter providing a more concise overview focused on recent advances in the field and photonic quantum information processing more generally. Lastly, Ref. 221 details a (quite technical) "fusion-based" approach to quantum computation that offers a promising route toward fault-tolerant quantum computation with photons. Additionally, related linear-optical networking experiments (e.g., boson sampling [222, 223]) have been used to demonstrate that quantum computations can achieve things that are (probably [224]) hard classically.

broader topics, and refer interested readers to the cited references for details. In App. B.1, we provide some resources and exercises that readers can use to further engage with the concepts of this chapter and to explore extensions of our setup. For completeness, we provide solutions to these exercises in App. B.2.

We note that many closely related setups have been analyzed in the literature (starting with Ref. 225), due to the rich underlying physics. Moreover, the setup we consider has already been thoroughly experimentally investigated in Ref. 226. However, the focuses and intended audiences of these works are quite different than this chapter (see Sec. 5.3.4 for some additional discussion).

5.2 General approach and background

We want to analyze and understand how individual photons will propagate through our setup and the resulting probabilities of them being incident on the various detectors placed at possible output ports of the setup (see Fig. 5.1). In order to focus on the relevant physics and highlight the interference effects we are concerned with, we consider an idealized setup where the photons are confined to a particular finite collection of possible paths (as dictated by the geometry of the setup), the photons are not lost during their propagation through the setup, and the detectors are perfect.[2]

5.2.1 Underlying principles of quantum mechanics

To calculate the probability of an initial state transitioning to a certain final state, we will employ the general principles of quantum mechanics outlined by Feynman

[2]Such issues would undoubtedly be present in a real setup, though they can be largely mitigated via careful experimental design. Moreover, in an actual realization of such a setup, such error mechanisms can (and should) be characterized, so that they can be accounted for when analyzing detection statistics.

[234, 235]. These principles are that (1) the probability of a particular outcome, $\mathcal{O}$, is given by taking the square of the absolute value of a complex number $\mathcal{A}_\mathcal{O}$ called the probability (transition) amplitude, $P_\mathcal{O} = |\mathcal{A}_\mathcal{O}|^2$, and (2) when $\mathcal{O}$ can occur via multiple processes, the total amplitude $\mathcal{A}_\mathcal{O}$ is given by adding up the quantum mechanical amplitudes, $\mathcal{A}_p$, for each such process p as $\mathcal{A}_\mathcal{O} = \sum_p \mathcal{A}_p$. Together these imply

$$\boxed{P_\mathcal{O} = \left| \sum_{p \in p_\mathcal{O}} \mathcal{A}_p \right|^2,} \tag{5.1}$$

where the sum is over the subset $p_\mathcal{O}$ of all possible processes (or paths) that lead from the initial state of the system to outcome $\mathcal{O}$. Equation (5.1) assumes that no measurement takes place on any path before the final measurement. Here an "outcome" corresponds to a possible measurement result of a physical observable such as energy, spin, or—as we consider in this chapter—the location reached by a photon. Moreover, measuring a red photon at location 1 and a blue photon at location 2 is a different outcome than measuring blue at 1 and red at 2 (see Sec. 5.3.5).

This formula encodes the fundamental notions of quantum mechanics, that amplitudes *interfere* and this interference happens at measurement. This can be constructive interference, where the individual amplitudes $\mathcal{A}_p$, for a given outcome $\mathcal{O}$, have similar phases (as complex numbers) so they build on each other when added up, enhancing $|\mathcal{A}_\mathcal{O}|$. Alternatively, this can be destructive interference, where the amplitudes have substantially different phases so they tend to cancel each other out when added up, reducing $|\mathcal{A}_\mathcal{O}|$. The corresponding ability of amplitudes to nicely combine, as opposed to remaining disjoint, is inherited from the linearity of the Schrödinger equation. This "superposition principle" likewise applies to many

waveforms more generally (e.g., those governed by the wave equation or Maxwell's equations in linear media) and leads to a propensity for interference effects in nature.

An important demonstration of such interference is Young's famous double-slit experiment (DSE), wherein light is shone through two small slits in an otherwise opaque slide. The transmitted light is then incident on a screen, on which one finds interference fringes—a series of alternating regions where the light is prominent and absent—which is quite different than the two bright spots one might expect based on superposing the single-slit diffraction patterns of the two lone slits. At its inception [236], the outcome of the DSE was (classically) well explained by describing light as a wave that goes through both slits and interferes with itself. However, an amazing experimental fact of reality is that the same interference pattern occurs even if the light is sent in one photon at a time [212, 237]. Thus, such setups can be used to demonstrate single-photon interference, wherein, for each final location on the screen, the intermediate photon state is in a superposition of having taken one of two separate paths, through one slit or the other. It is the quantum mechanical amplitudes for the photon taking either path that interfere and ultimately (after repeated trials) give rise to the standard double-slit interference pattern.

As we will explore in Sec. 5.2.3, the interference phenomena observed in MZIs can similarly be observed with single photons [214, 215, 238], where the two arms of the interferometer take the roles of the two slits in the DSE. Accordingly, although both double-slit interference and MZi can be regarded as phenomena emblematic of the wave-like nature of "classical" light, they can each be seen (more fundamentally) as the persistence of a deep-rooted quantum interference effect, wherein the interference happens photon by photon (both phenomena can also be seen when using electrons or

other particles [239, 240]). In contrast, the second interference effect we use, HOMi, is not reducible to a classical effect (see Sec. 5.2.4).

5.2.2 Beam-splitter relations

A beam splitter (BS) is a linear-optical device that splits light incident on it, letting some transmit and reflecting the rest (up to absorption or scattering loss). In this chapter, as is standard, we will model the (well-known and characterized) effect that BSs and mirrors have on light propagating through the system without having to worry about the precise nature of their interactions. In particular, the relevant amplitudes, $\mathcal{A}_p$, can be determined using so-called BS input-output relations, which amount to "update rules" for how single-photon amplitudes will change due to a given optical element (BS or mirror).

Namely, consider the situation shown in Fig. 5.2, wherein a single photon is in a superposition of being incident on a BS from two directions, 1 and 2, with amplitudes $\mathcal{A}_{\text{in}}^{(1)}$ and $\mathcal{A}_{\text{in}}^{(2)}$, respectively. The interaction with the BS transforms this input photon into an output photon in a new superposition of directions 1 and 2 with respective amplitudes of $\mathcal{A}_{\text{out}}^{(1)}$ and $\mathcal{A}_{\text{out}}^{(2)}$. Focusing on the case of symmetric BSs,[3] these single-photon amplitudes are related as

$$\mathcal{A}_{\text{in}}^{(1)} = t\mathcal{A}_{\text{out}}^{(1)} + ir\mathcal{A}_{\text{out}}^{(2)}, \tag{5.2a}$$

$$\mathcal{A}_{\text{in}}^{(2)} = ir\mathcal{A}_{\text{out}}^{(1)} + t\mathcal{A}_{\text{out}}^{(2)}, \tag{5.2b}$$

[3]Symmetric BSs are common in optics laboratories, though other phases are possible (for a given t and r), as determined by the optical properties and construction of the BS interface [241]. Moreover, provided the relative phases acquired along different paths are appropriately tuned and stabilized, the exact BS phases will not change our ultimate conclusions and can be treated as a convention.

where t and r are the real transmission and reflection coefficients, respectively, that satisfy $t^2 + r^2 = 1$. We will mostly consider 50:50 BSs that equally transmit and reflect light: $t = r = 1/\sqrt{2}$. Note, perhaps more familiarly, that BSs transform electric fields in a manner analogous to Eq. (5.2). More fundamentally, this transformation applies to creation operators yet the corresponding second-quantized treatment, although present elsewhere in this dissertation, is not needed in this chapter. Accordingly, we will present a simpler schematic approach in terms of single photon amplitudes, with the occasional more technical remark or footnote.[4] This is done in accordance with this works pedagogical motivations to limit barriers of accessibility, including mathematical ones. We refer the curious reader to the Exercise 5 solution, Eqs. (B.17)–(B.20) in particular, wherein we draw the connection between our approach and the second-quantization formalism quite explicitly.

These relations provide us with an intuitive way to track the phases acquired by light (in the form of individual photons) traveling different paths through a linear-optical setup. Each time light is reflected from a BS or mirror (which is a purely reflective, $r = 1$, BS), it acquires a $\pi/2$ phase shift, i.e., the corresponding amplitude is multiplied by $e^{i\pi/2} = i$. Meanwhile, no phase is imparted on transmission through a BS. Thus, the phase factor acquired along a path due to interacting with BSs and mirrors is i^{N_r}, where N_r is the number of reflections undergone, and hence light taking different paths to a given destination will interfere. This "counting method" allows us to track the phases and magnitudes of each path's contribution *diagrammatically* and thus avoid the underlying matrix formalism while still capturing the fundamental

[4]The transformation induced by a BS or indeed an entire linear-optical network (such as the setup of Fig. 5.1) is a unitary map from input annihilation (or creation) operators to output ones: $a_k^{\text{out}} = \sum_{j=1}^{m} U_{kj} a_j^{\text{in}}$, where m is number of relevant modes the photon(s) can occupy. For instance, in our setup, the $n = 2$ photons are restricted to $m = 6$ modes at any given time (including vacuum contributions and outputs not incident on a detector). Especially for larger n and m, this relates to boson sampling, a problem believed to be classically hard [222, 242].

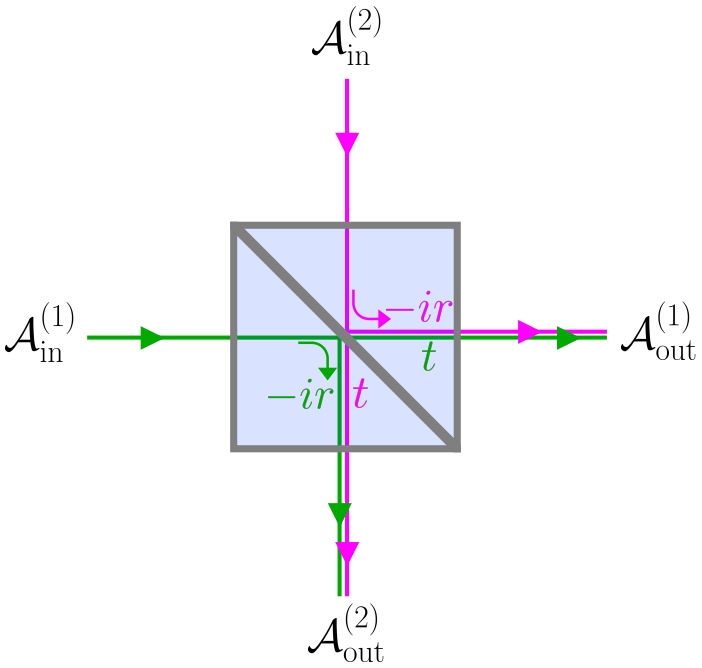

FIGURE 5.2. Diagram of a single-photon's interaction with a symmetric BS (see text for further details). The input amplitudes $\mathcal{A}_{\text{in}}^{(1)}$ (green) and $\mathcal{A}_{\text{in}}^{(2)}$ (pink) are transformed into the outputs as $\mathcal{A}_{\text{out}}^{(1)} = t\mathcal{A}_{\text{in}}^{(1)} - ir\mathcal{A}_{\text{in}}^{(2)}$ and $\mathcal{A}_{\text{out}}^{(2)} = t\mathcal{A}_{\text{in}}^{(2)} - ir\mathcal{A}_{\text{in}}^{(1)}$. Here we show how the output is formed from the input. However, one often knows the initial state and wants to track the output, in which case it is typically more useful to solve for the inputs in terms of the outputs, as in Eq. (5.2).

physics. In setups like ours, the single-photon BS update rules can be generalized to analyze more complicated incident states of light [243–245]. However, writing down how the output state amplitudes depend on the initial input state can be cumbersome [222, 242], and is unnecessary here.

5.2.3 Mach–Zehnder interference

Now that we are equipped with the above rules of Feynman and the BS relation of Eq. (5.2), we can examine the contributions of different paths that photons could take in propagating from a prescribed starting location to one of the possible outputs. We will start by demonstrating the interference of such paths in a Mach–Zehnder

interferometer (MZI), which is a fundamental physical instrument for measuring phase shifts between two beams with classical and quantum sensing applications. Additionally, the MZI and related setups have offered a platform for testing and exploring some of the fundamental predictions of quantum mechanics [218, 246–248]. Moreover, the MZI is a key part of the full setup we consider, so it will be useful to identify the underlying physics.

A typical MZI setup is comprised of a light source, two 50:50 BSs, two mirrors, and two detectors as shown in Fig. 5.3 [209, 249]. We consider light incident on the left port of BS_1 from a collimated light source (represented schematically in Fig. 5.3 by the purple flashlight). Meanwhile, no light is incident on the top port of BS_1 (it is in the vacuum state, indicated by thin dashing). The incident light can then either transmit through or reflect from BS_1 (with equal probability) and then propagate through the upper or lower arm of the interferometer, which are shown as the solid pink and dashed green paths in Fig. 5.3, respectively. Along each path, the light encounters a mirror (M_1 or M_2) and then the beams are recombined at BS_2, from which the light can exit via two possible output ports after which it will impinge on a detector: D_1 and D_2, for the rightward and downward outputs, respectively.

Focusing on a single-photon input, we will use the counting method introduced above to track the amplitudes acquired along each path through the interferometer (see Ref. 238 for a related experiment). We assume a *balanced* interferometer, wherein light acquires the same net phase during propagation along both arms. This balancing can be accomplished by ensuring that the arms share a common optical-path length, and is often a key preparatory (alignment) step in the operation of such an interferometer and in many optics experiments. Importantly, in a balanced setup one can neglect the common phase induced by traversing each arm as it is global, so

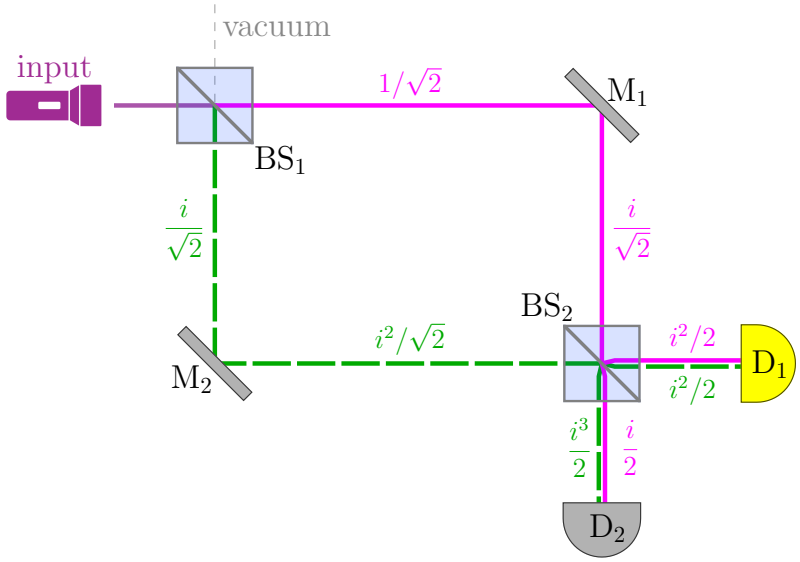

FIGURE 5.3. Diagram of a balanced MZI with a single input. The incident light can take either the upper (solid, pink) or lower (dashed, green) path through the interferometer, after which it is directed to one of two detectors, D_1 or D_2. At each detector, the contributions of these two paths interfere, constructively at D_1 and destructively at D_2, i.e., the light only impinges on D_1 (emphasized in yellow) and never on D_2 (see text for details). Here we use the abbreviations: 50:50 beam splitter (BS), ideal mirror (M), and photodetector (D).

we only need to track the phases induced by reflections from the BSs and mirrors. (We operate under this assumption throughout this chapter.)

We can now determine the amplitudes, $\mathcal{A}_j$, for the incident photon to reach detector $j = 1, 2$ as well as the corresponding probability of detection, $P_j = |\mathcal{A}_j|^2$. For each detector, light can reach it through either the upper or lower arm, so $\mathcal{A}_j = \mathcal{A}_{j,\text{upper}} + \mathcal{A}_{j,\text{lower}}$. The amplitude of a given path can be found by tracking the contribution acquired due to interacting with all the optical elements (BSs and Ms) encountered along the path. Namely, in the prescribed setup, the BSs split the light 50:50, inducing $1/\sqrt{2}$ factors, the mirrors are perfectly reflective, and a reflection always induces a $\pi/2$ phase corresponding to multiplying by i. The two paths that exit BS_2 via its bottom output port are both attenuated by two BSs, but the solid

(pink) and dashed (green) paths undergo one and three reflections, respectively. Thus, the corresponding amplitude is

$$\mathcal{A}_2 = \overbrace{\frac{1}{\sqrt{2}} \cdot i \cdot \frac{1}{\sqrt{2}}}^{\text{upper path}} + \overbrace{\frac{i}{\sqrt{2}} \cdot i \cdot \frac{i}{\sqrt{2}}}^{\text{lower path}} = \frac{i + i^3}{2} = 0, \tag{5.3}$$

so these paths entirely *destructively* interfere. Accordingly, D_2 should never detect the incident photon, $P_2 = |\mathcal{A}_2|^2 = 0$. Meanwhile, the two paths that exit BS_2 to the right undergo the same number of reflections (namely two), acquiring a common phase of π, and thus interfere entirely *constructively*:

$$\mathcal{A}_1 = \overbrace{\frac{1}{\sqrt{2}} \cdot i \cdot \frac{i}{\sqrt{2}}}^{\text{upper path}} + \overbrace{\frac{i}{\sqrt{2}} \cdot i \cdot \frac{1}{\sqrt{2}}}^{\text{lower path}} = \frac{i^2 + i^2}{2} = -1, \tag{5.4}$$

so D_1 will always detect the incident photon, $P_1 = |\mathcal{A}_1|^2 = 1$. This Mach–Zehnder interference (MZi) is shown diagrammatically in Fig. 5.3, where next to each MZI path segment we display the corresponding amplitude for light that has traversed up to that point.

5.2.4 Hong–Ou–Mandel interference

When considering multiple photons, one can find surprising interference effects that do not manifest classically. In particular, we will focus on Hong–Ou–Mandel interference (HOMi) [250], wherein two photons are incident on a 50:50 BS (which we will henceforth represent as a thick vertical black line), one on each input port. For the effect to be most prominent, we take the photons to be indistinguishable at measurement (i.e., identical in timing, frequency, polarization, and transverse

spatial mode) and pure.[5] Such photon pairs might be obtained from a spontaneous parametric down-conversion apparatus [211, 226, 255, 256], though other synchronized sources, such as quantum dots [257] or cavity QED based emitters [4], could be used. Each photon can either transmit or reflect (acquiring a $\pi/2$ phase), so the possible processes for both photons can be schematically summarized as

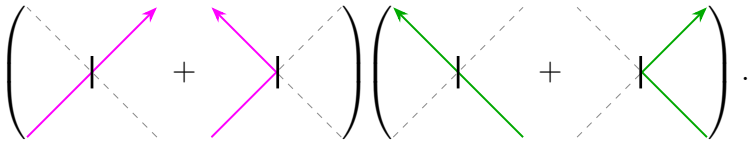

(5.5)

[For completeness, note that the pictorial representation of different photon paths in Eq. (5.5) is being used to represent the final state of the system (a vector in Hilbert space), whereas in subsequent expressions, including Eqs. (5.6)–(5.8), such symbols are used to denote amplitudes (complex numbers).] In the shown orientation, the two identical photons propagate up the page as time goes on, ending up either on the left (L) or right (R). Faux coloring is used to schematically keep track of the different processes with pink and green denoting the left and right side inputs, respectively (this is done throughout this subsection and in Fig. 5.6).

[5] For distinguishable photons, the interference of Eq. (5.6) no longer occurs, nor does the Bose enhancement of Eqs. (5.7) and (5.8), as the possible outcomes ($L\&L$, $R\&R$, $L\&R$, and $R\&L$) are physically distinguishable (these effects are merely suppressed if the photons are partially distinguishable). These four outcomes are equiprobable, so coincident detections ($L\&R$ or $R\&L$) occur with probability 1/2. Thus, for the HOM effect to be most pronounced, and for the conclusions of Sec. 5.3 to be valid, it is crucial that the photons are indistinguishable. In particular, it is the distinguishability at measurement that matters (e.g., that the photons could initially be distinguished by their differing paths is of no concern as long as they are not measured at that time). Photon indistinguishability plays a similarly crucial role in many quantum information processing applications [219, 242, 251–253], including hybrid QST as seen in Ch. IV. For simplicity, we focus on pure photon states. More generally, in addition to indistinguishability, the state's "mixedness" [which is a classical-like uncertainty that can be quantified by the linear entropy, $1 - \mathrm{Tr}(\rho^2)$, of the state ρ] also degrades interference [253, 254].

The possible outcomes can be organized into three possibilities: the photons exit opposite ports (either both transmitting or both reflecting) with amplitude

$$\mathcal{A}_{L\&R} = \quad + \quad = \frac{1}{\sqrt{2}} \cdot \frac{1}{\sqrt{2}} + \frac{i}{\sqrt{2}} \cdot \frac{i}{\sqrt{2}} = 0, \tag{5.6}$$

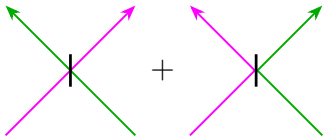

the photons both go left with amplitude[6]

$$\mathcal{A}_{L\&L} = \quad = \sqrt{2}\left(\frac{i}{\sqrt{2}} \cdot \frac{1}{\sqrt{2}}\right) = \frac{i}{\sqrt{2}}, \tag{5.7}$$

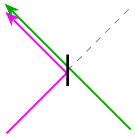

or the photons both go right with amplitude

$$\mathcal{A}_{R\&R} = \quad = \sqrt{2}\left(\frac{1}{\sqrt{2}} \cdot \frac{i}{\sqrt{2}}\right) = \frac{i}{\sqrt{2}}. \tag{5.8}$$

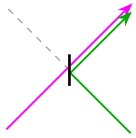

The two amplitudes for ending up with one photon in L and one photon in R are equal in magnitude yet differ in phase by π (due to the difference of two reflections). Hence, they fully destructively interfere: $\mathcal{A}_{L\&R} = 0$. Accordingly, if detectors are placed after the BS, there will never be a coincident detection at both outputs (L and R), $P_{L\&R} \equiv |\mathcal{A}_{L\&R}|^2 = 0$. Thus, the two input photons always exit together, either both left or both right with equal probability: $P_{L\&L} = P_{R\&R} = |i/\sqrt{2}|^2 = 1/2$. This phenomenon is often deemed the HOM effect.[7]

[6]The additional $\sqrt{2}$ factor present in Eqs. (5.7) and (5.8) is necessary for normalization. More fundamentally, it encodes the phenomenon of Bose enhancement, which is reflected in the action of a creation operator on a number state, $a^\dagger|n\rangle = \sqrt{n+1}|n+1\rangle$, such that $\left(a^\dagger\right)^2|0\rangle = \sqrt{2}|2\rangle$ [or $\left(a^\dagger\right)^n|0\rangle = \sqrt{n!}|n\rangle$, more generally; see chapter 4, sections 2 and 3 of Ref. 234, as well as Ref. 245].

[7]The HOM effect was first demonstrated in the eponymous work of Hong, Ou, and Mandel [250], by varying the time delay between two otherwise identical single photons being interfered via a 50:50 BS. Up to experimental constraints, this allowed them to interpolate between coincident detection probabilities of 0 (for identical photons) and 1/2 (for distinguishable photons, see footnote 5). See

5.3 Full setup

Here we consider a setup that naturally combines the two interference effects we have discussed (MZi and HOMi). This full setup is comprised of two adjacent balanced MZIs connected via a common central 50:50 BS that allows light from one MZI to couple to the other. We imagine using four detectors $D_1 - D_4$ (taken to be photon-number resolving for simplicity, though one can avoid this by postselecting on coincident detections at different detectors) to monitor the output of the setup, as shown in Fig. 5.1. To make each MZI symmetric we also replace the two other (outer) central mirrors by 50:50 BSs (hence every BS in the setup is 50:50). We consider the case where one photon is in the left input and one otherwise identical photon is in the right input, so that ostensibly HOMi should take place at the central BS and MZi should take place on both sides. [We will not be concerned with the precise source of these pairs of input photons so long as they are identical and pure. We do note that one common means of producing such photon pairs is by leveraging the parametric-down-conversion process in certain nonlinear crystals [226, 255, 256, 258], though two synchronized quantum emitters (such as atoms in cavities, see §3.5) or other controllable sources could be used.]

We will focus on answering the seemingly innocuous question: *What is the probability of a coincident detection at both inner detectors, D_2 and D_3?* We denote this probability as $P_{2,3}$. Note that because the previously perfectly reflective central mirrors have been replaced by 50:50 BSs, the photons can be lost out of the setup (via either outer central BS, as indicated by the outermost dotted lines in Fig. 5.1 that do not impinge on a detector).

Ref. 211 for an example of how this experiment can be adapted for the undergraduate laboratory (using either time delays or relative polarization to control distinguishability).

5.3.1 MZ interference revisited

We will start by considering single-photon (MZ) interference in this setup. Suppose only one photon is sent through the full setup, for concreteness, we will take it to be in the left input. Relative to the MZI considered in Sec. 5.2.3, we have replaced the previously perfectly reflective ($r = 1$) mirrors by partially transmissive ones ($r = 1/\sqrt{2}$). The photon will now either be reflected by one of these partially transmissive mirrors and remain in the left MZI, MZI_L, or exit MZI_L by transmitting through one of these mirrors. If the photon remains in MZI_L, the amplitudes for reaching the corresponding detectors D_1 and D_2 can be computed in the same manner as in Eqs. (5.4) and (5.3), respectively. The only change is that the path contributions are each reduced by r, so $\mathcal{A}_2$ remains 0 and $|\mathcal{A}_1|$ decreases from 1 to r. Thus, if the photon stays in MZI_L, full MZi occurs: the photon will always go to D_1, never to D_2, $P_2 = |\mathcal{A}_2|^2 = 0$. Otherwise, the photon will exit MZI_L, either crossing into the right MZI or being lost out the leftmost central BS. Likewise, as the setup is left-right symmetric, if a single photon was sent into the right MZI, it would never be detected at the corresponding inner detector D_3.

5.3.2 Two-photon input: Semi-naive treatment

Now we will consider what happens when two identical single photons are sent into the setup, one on each side, as depicted in Fig. 5.1. We will start by presenting a series of quantumly-informed[8] premises from which one can ostensibly deduce whether $P_{2,3}$ is zero.

[8]We deem this treatment to be "semi-naive" in that it leverages actual quantum interference effects (MZi and HOMi) in its reasoning yet misuses them in consonance with one another. One might similarly refer to such reasonings as semi-classical [216].

(i) Based on the previous subsection, it seems that neither photon should reach the inner detector on its own side due to MZi. That is, the left photon should not arrive at D_2 nor should the right photon arrive at D_3.

(ii) Thus, ostensibly the only way to get a D_2D_3 coincident detection event would be for the photons to both cross into the other half of the setup, with the initially left photon crossing to the right and being detected at D_3, and the right photon crossing and being detected at D_2.

(iii) However, when two identical photons are incident on a 50:50 BS, they will always exit the BS together, either both going left or both going right with equal probability. This is the HOM effect discussed in Sec. 5.2.4. Accordingly, HOMi seems to prevent such a crossing.

Thus, it appears that a coincident detection at D_2 and D_3 should be impossible (such that $P_{2,3} = 0$) as, ostensibly, the photons cannot reach the inner detectors each from their original sides due to MZi and they cannot cross to the opposite sides due to HOMi.

However, the above qualitative reasoning is ultimately wrong, as, in fact, $P_{2,3} > 0$, which is predicted by quantum mechanics (under a more proper treatment). Thus, we have an apparent contradiction (or "paradox") between the above reasoning, which predicts $P_{2,3} = 0$, and quantum mechanics. In the next subsections, we will show that quantum mechanics predicts $P_{2,3} > 0$ and then contrast the two treatments to clarify what went wrong in the above semi-naive reasoning.

5.3.3 Two-photon input: Proper treatment

As was done in Eq. (5.5), the amplitude for each possible detection event can be calculated by identifying *all* of the two-photon paths leading to it (visualized in Fig. 5.4 for coincident detections), applying the counting method to determine the contribution of each path, and then adding up these contributions [in accordance with general principle (2)] [244, 245]. Here we focus on a D_2D_3 coincidence (though other outcomes can be analyzed similarly). In particular, we want to compute the amplitude, $\mathcal{A}_{2,3}$, and corresponding probability $P_{2,3} = |\mathcal{A}_{2,3}|^2$ for this event. The two-photon paths leading to this event can be organized in terms of whether the paths cross or not. Letting $\mathcal{A}_{S\to j}$ denote the single-photon amplitude for the photon starting on side $S \in \{L, R\}$ to reach detector j, we can thus write the total amplitude for this outcome as

$$\mathcal{A}_{2,3} = \mathcal{A}_{L\to 2}\mathcal{A}_{R\to 3} + \mathcal{A}_{L\to 3}\mathcal{A}_{R\to 2}. \tag{5.9}$$

The processes corresponding to $\mathcal{A}_{L\to 2}$ and $\mathcal{A}_{R\to 3}$ can happen via either the "outer path" (i.e., the corresponding photon transmits, reflects, and then transmits at the subsequent BSs) or the "zigzag path" (the photon reflects thrice) with amplitudes O_S and Z_S, respectively, for starting side S. That is, $\mathcal{A}_{L\to 2} = O_L + Z_L$ and $\mathcal{A}_{R\to 3} = O_R + Z_R$. Meanwhile, the processes corresponding to $\mathcal{A}_{L\to 3}$ and $\mathcal{A}_{R\to 2}$ can only happen via the "crossing path" (where the photon reflects, transmits, then reflects) with amplitude C_S, so $\mathcal{A}_{L\to 3} = C_L$ and $\mathcal{A}_{R\to 2} = C_R$. The corresponding single-photon amplitudes for these paths can be determined via the counting method to be $O_S = i/2^{3/2}$, $Z_S = i^3/2^{3/2}$, and $C_S = i^2/2^{3/2}$ (they are the same for each starting side S as our setup is left-right symmetric). These amplitudes can be understood and determined diagrammatically, as demonstrated for C_L in Fig. 5.5.

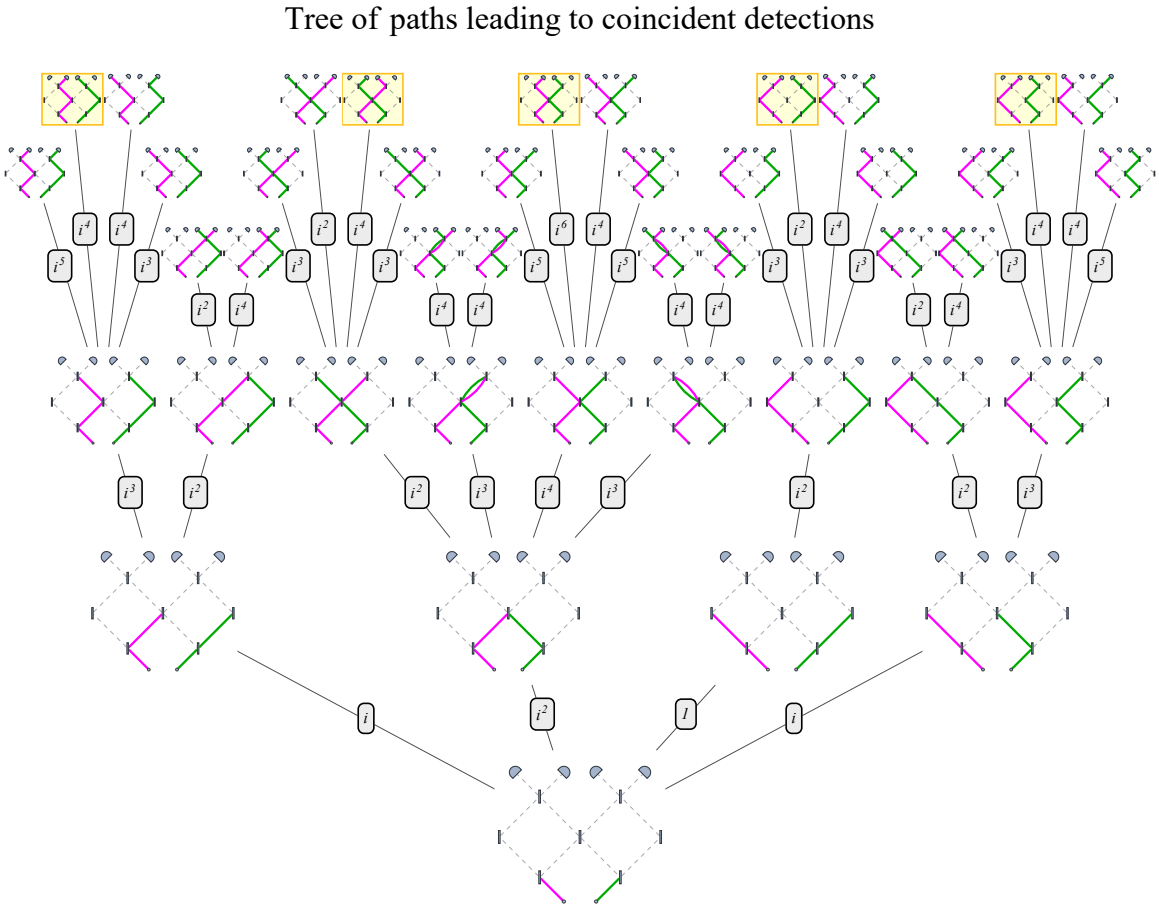

FIGURE 5.4. Visualizing all paths the photons can take through the setup that lead to a coincident detection event and counting the phase acquired (i.e., same detector two-photon detection and loss events are not shown). The five amplitudes corresponding to a D_2D_3 coincidence are highlighted in yellow.

Thus, we can rewrite Eq. (5.9) as

$$\mathcal{A}_{2,3} = (O_L + Z_L)(O_R + Z_R) + C_L C_R. \tag{5.10}$$

We can leverage either MZi ($O_S + Z_S = 0$ for both sides S) or HOMi ($Z_L Z_R + C_L C_R = 0$) to simplify Eq. (5.10) as

$$\mathcal{A}_{2,3} = C_L C_R = 1/8 \tag{5.11}$$

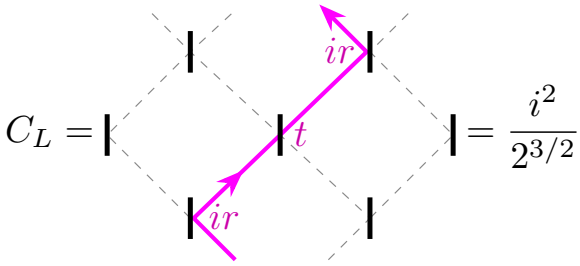

FIGURE 5.5. Illustrating the counting method for determining the amplitude, C_L, of the shown path. We annotate the diagram here with the contribution of each transmission and reflection, which are t and ir, respectively [see Eq. (5.2)]. Thus, the path amplitude is $C_L = ir \cdot t \cdot ir$, which, for the case of all 50:50 BSs, becomes $C_L = i^2/2^{3/2}$ as indicated. The other path amplitudes O_L and Z_L can be calculated similarly (and likewise for side R) and are shown in Fig. 5.6.

or

$$\mathcal{A}_{2,3} = O_L O_R + O_L Z_R + Z_L O_R = 1/8, \tag{5.12}$$

respectively. These two reductions are shown diagrammatically in Fig. 5.6. In Eq. (5.12), we could leverage MZi to further cancel the $O_L O_R$ term with exactly one of the $O_L Z_R$ or $Z_L O_R$ terms (but not both). Either way, we have that $P_{2,3} = |\mathcal{A}_{2,3}|^2 = 1/64 > 0$. One can likewise compute the probabilities of the other possible detection events, the results of which are summarized in Fig. 5.7.

5.3.4 Resolutions to apparent contradiction

Thus, the qualitative reasoning of the semi-naive treatment, which predicts $P_{2,3} = 0$, contradicts the proper quantum mechanical treatment, which predicts $P_{2,3} = 1/64$. We will now discuss several ways of "resolving" this apparent contradiction. Note that $P_{2,3} > 0$ can be and has been confirmed experimentally [226], so the semi-naive treatment is fundamentally wrong. Accordingly, these resolutions each amount to highlighting a different perspective on where the semi-naive treatment went wrong.

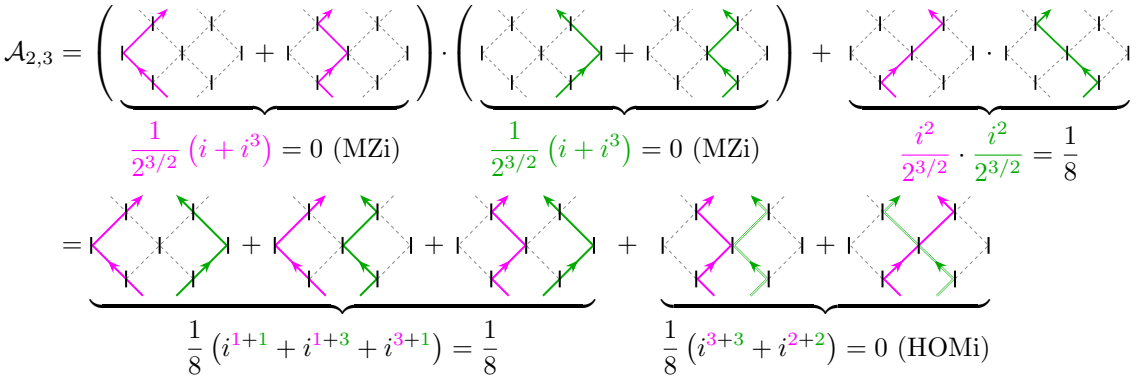

FIGURE 5.6. Diagrammatic calculation of the amplitude $\mathcal{A}_{2,3} = 1/8$. Here we visually show how the sum in Eq. (5.10) can be rearranged in two ways to emphasize either MZi (top row) or HOMi (bottom row), as in Eqs. (5.11) and (5.12), respectively. The underbraces highlight how the contributions of different terms can be gleaned by simply counting the number of reflections in a given path. [In the bottom row, we merged products of two single-photon amplitudes into single two-photon amplitudes to emphasize that HOMi is inherently a two-photon interference effect. Additionally, in the HOMi terms, the $S = R$ (green) paths are subtly striped to make it easier to disambiguate the overlapping paths.]

We focus on three such resolutions, each corresponding to a specific issue in the semi-naive treatment, namely, it wrongly assumes that

(1) MZ and HOM interference happen in isolation,

(2) the two photons are independent, and

(3) intermediate probabilities add.

The first resolution constitutes our new perspective on this setup and is intended to be intuitive and accessible. The latter resolutions highlight perspectives that have been extensively analyzed in previous works; we include them here to illustrate how issues in the semi-naive treatment can guide one to fundamental quantum mechanical concepts. We elaborate on these resolutions in Sec. 5.3.5, highlighting their relation to said previous (more technical) works and to each other. Pedagogically, we present

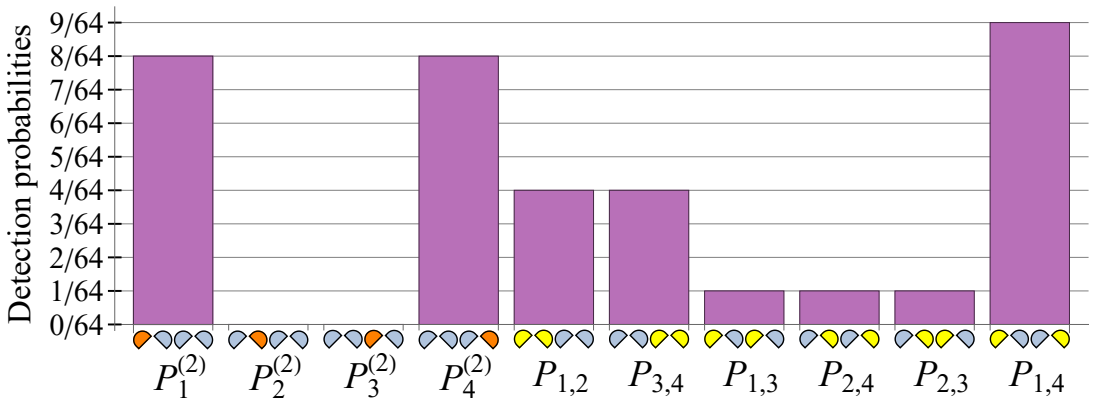

FIGURE 5.7. Probability distribution for all possible two-photon detection events in the setup shown in Fig. 5.1. Here $P_i^{(2)} = P_{i,i}$ is the probability of the two photons (see footnote 6) being incident on the same detector D_i (emphasized in orange) and $P_{i,j}$ is the probability of coincident detection at detectors D_i and D_j (yellow) with $i, j \in \{1, 2, 3, 4\}$. Here we are not showing cases where at least one of the photon exits the setup via of one of the outer central BSs. The probability of losing either individual photon is $|t^2|^2 = 1/4$, so the probability of not losing either photon is $(1 - 1/4)^2 = 36/64 = 56.25\%$, which is the sum of the probabilities shown above.

the semi-naive treatment—even though it is incorrect—as an example of a flawed line of reasoning that students (even those who know about MZi and HOMi) may be susceptible to, given the challenges often faced when learning about such interference effects (see Sec. 5.1.1).[9]

Resolution 1: Interference of interference effects. In our setup, MZi and HOMi do not occur independently; rather, a more intricate combination of them occurs. This can be seen via the two different reductions of Eq. (5.10) to either Eq. (5.11) or Eq. (5.12), which are illustrated in the top and bottom rows of the diagrammatic equation in Fig. 5.6, respectively. Mathematically, these reductions

[9]The conceptual difficulties that students experience in learning about single-photon interference were explored in Ref. 213. One difficulty they identified was students "Ignoring the interference of a single photon at the detectors after passing through the MZI" (section V, page 4). This difficulty is worth highlighting as it provides pedagogical context for why we emphasize that interference happens upon measurement in Sec. 5.4.

are simply an algebraic rearrangement of the complex number $\mathcal{A}_{2,3} = 1/8$ into a sum of different parts. However, each reduction highlights a different effect: MZi is manifest in Eq. (5.11) and HOMi is manifest in Eq. (5.12), yet one cannot make both interference effects manifest at the same time. This is because

the zigzag amplitudes, Z, enter both effects, and can cancel either the O or C terms but not both.

This impossibility can be seen by counting: there are five total two-photon paths leading to D_2D_3 [see Eq. (5.10) or Fig. 5.6], MZi requires four paths (two per side S), and HOMi requires two paths, yet

$$4 + 2 \neq 5, \tag{5.13}$$

so not all amplitudes can be canceled. That is, the two interference effects interfere with each other via these shared Z amplitudes.

Accordingly, MZi and HOMi do not happen in isolation in this setup and, moreover, one cannot even say that either effect in particular happens (the physical interpretation of an event should not depend on how we rearrange a sum; see Fig. 5.6). Hence, premises (i) and (iii) in the semi-naive treatment are certainly not valid together and, at the very least, they are individually misleading. Moreover, we did not properly distinguish between there being an amplitude for the photons to traverse a given set of paths and the photons actually traversing said paths. For instance, in premise (iii), after leveraging MZi, it was incorrect to consider two *photons* incident on the center-most BS. Rather, a single two-photon *amplitude* ($C_L C_R \neq 0$) describing both photons taking the crossing path remained, as in Eq. (5.11).

Resolution 2: Photonic entanglement. In our semi-naive treatment, we implicitly assumed that the two photons behave independently when we reasoned that the probability for a coincident inner detection could be decomposed in a classical way as a sum of two disjoint probabilities:

$$P_{2,3} \overset{\text{sn}}{=} P_{L\to 2\&R\to 3} + P_{L\to 3\&R\to 2}. \tag{5.14}$$

Here $P_{L\to 2\&R\to 3}$ and $P_{L\to 3\&R\to 2}$ are the respective semi-naive probabilities (indicated via the overset "sn") for the photons to either both stay on their initial sides or both cross in a D_2D_3 coincident detection. According to premises (i)[10] and (iii), respectively, these probabilities should each be zero, implying $P_{2,3} \overset{\text{sn}}{=} 0$. However, this reasoning clearly neglects the possibility of the two photons being entangled, i.e., their joint final state being quantumly correlated. In fact, the presence of nonmaximal entanglement in the photons' state after interacting with the central BSs can be used to account for why $P_{2,3} > 0$ (see Sec. 5.3.5 for additional context) [226, 259]. Thus, such entanglement invalidates the semi-naive reasoning here. However, more broadly, entanglement serves as a fundamental resource in quantum-information processing [260].

Resolution 3: Amplitudes versus probabilities. When analyzing particles that are quantum-mechanically identical, one needs to be careful when attributing specific

[10]Premise (i) can be phrased alternatively in terms of interaction-free measurements [226, 246]. If the initially left photon reaches D_2, there must have been an obstruction to its MZi and, from the context of this problem, we can infer that this obstruction was the right photon being at the center-most BS. Similarly, if the initially right photon reaches D_3, we can infer that the left photon being at the center-most BS obstructed it. Accordingly, if each photon reaches the inner detector on its original side, it would seemingly follow that both photons obstructed the other's MZi and hence have traversed the inner arms of their respective MZIs, yet such photons would have bunched (due to HOMi), leading to a contradiction. Thus, we again find that ostensibly $P_{L\to 2\&R\to 3} \overset{\text{sn}}{=} 0$.

behavior to an individual particle. For instance, if a $D_i D_j$ coincident detection ($i \neq j$) occurs in our setup, assuming the two photons are in fact identical, one cannot say which photon went to D_i and which went to D_j as these outcomes cannot be distinguished (even in principle): they lead to the same final state. In such a situation, two different processes contribute to the outcome (a $D_i D_j$ coincident detection): the initially left photon going to D_i and the right to D_j or vice versa. However, according to the general principles of Feynman, as summarized in Eq. (5.1), in such a context, the amplitudes for these alternatives add,

$$\mathcal{A}_{i,j} = \mathcal{A}_{L\to i}\mathcal{A}_{R\to j} + \mathcal{A}_{L\to j}\mathcal{A}_{R\to i} \quad (i \neq j) \tag{5.15}$$

[as in Eq. (5.9)], not the corresponding probabilities, $P_{i,j} \neq P_{L\to i\&R\to j} + P_{L\to j\&R\to i}$, which invalidates the semi-naive reasoning.[11] Thus, in effect, the semi-naive reasoning wrongly assumes that identical outcomes can be distinguished.

5.3.5 Further context and resolution relations

We intentionally chose these issues and resolutions because their further considerations provide valuable insight into fundamental concepts in physics. For instance, the independence of the photons in Resolution 2 can be made quantitative and precise by assuming that the photons are described by a local hidden variable theory (LHVT). For the purposes of this work, we simply note that such a theory

[11] The astute reader may note that if one defines these semi-naive "probabilities" in a different quantumly informed way as $P_{L\to i\&R\to j} \equiv |\mathcal{A}_{L\to i}\mathcal{A}_{R\to j}|^2$, then Eq. (5.14) appears to be valid. Indeed, for $i = 2$ and $j = 3$, this yields the correct probability, $P_{2,3}$, so long as there is full MZi (namely, $\mathcal{A}_{L\to 2}\mathcal{A}_{R\to 3} = 0$) as then there are no cross terms in Eq. (5.1). However, this approach is not valid as it cannot be applied for $i, j \in \{1, 4\}$ or, more generally, when full MZi does not occur, i.e., so long as both such "probabilities" are nonzero. See the solutions to Exercises 3 and 5 for some related discussion.

predicts $P_{2,3} = 0$, just as our semi-naive treatment did (though the specific reasoning is quite different), which again seemingly contradicts quantum mechanics. This apparent contradiction is deemed "Hardy's Paradox" as it arose in a thought experiment of Lucien Hardy regarding a setup analogous to ours, except with an electron and positron in the overlapping MZIs (instead of photons) [225].

Much like the situation we present, the "paradox" is that a coincident detection at the inner detectors can occur, even though this suggests that both the particle and anti-particle went through their inner arm and should have annihilated, e.g., forming gamma rays (this is analogous to the photon bunching at the center-most BS in our setup). Related setups have had a rich history as potential means of demonstrating Bell's theorem, which (in brief) says that quantum mechanics cannot be consistently described by any LHVT [261]. For instance, a setup nearly identical to the one we consider was analyzed by Hardy [258] and later experimentally tested in Ref. 226, serving as a striking demonstration of Bell's theorem. Note that the (nonmaximal) entanglement of the final photonic state is what ultimately makes it possible to demonstrate Bell's theorem using such a setup [259]. A more complete exposition of entanglement and LHVTs (e.g., what they are and their role in the development of quantum mechanics) is left to other work,[12] though we note that corresponding Bell and Hardy tests of local realism (LHVTs) versus quantum mechanics can be explored in the undergraduate laboratory [255, 256].

Spurred by Resolution 3, one might ask "What if the photons are distinguishable?" and thus consider a variant of the setup wherein the photons have a differing degree

[12]Reference 260 review entanglement and explain various measures for quantifying it such as the "entanglement entropy" and "concurrence." The corresponding story of why local realism clashes with quantum mechanics (including the "EPR paradox" [262], Bell's theorem, and the ensuing related experiments and discourse) is not only important to the history of quantum physics but has also provoked research that probes the fundamentals of physics. As a good starting place, see the aforementioned references, the review article of Ref. 263, and Ref. 264.

of freedom by which final measurements could distinguish them (e.g., perhaps one is red and the other is blue). Indeed, we ask this question in Exercise 3 (and extend it in Exercise 5). The short answer is that *distinguishability diminishes interference*, which connects Resolutions 1 and 3. [This short answer applies to single- and two-particle interference effects, as considered here (see Solutions 3 and 5 in App. B.2). Systems of more than two particles exhibit rich collective interference, e.g., which underlies boson sampling, with a more intricate dependence on indistinguishability [242, 265].] Thus, the use of indistinguishable photons is critical for the two-photon interference and concomitant interference of interference effects in our setup. In particular, it is the distinguishability of the outcomes of different processes, i.e., the final state, that determines interference (see Sec. 5.4).

This interplay between interference and distinguishability is a manifestation of the principle of *complementarity*, that quantum systems can possess properties that are equally real (and hence measurable) but exclusive (i.e., they cannot be observed simultaneously). In our setup, and multi-port interferometers more generally, this can be expressed as a quantitative tradeoff between interference visibility and distinguishability,[13] which can be regarded as a manifestation of wave-particle duality (see Refs. 228–230 and the references therein for details).

The conceptual similarity of Resolutions 2 and 3 hints at a similar connection between entanglement and distinguishability (as well as mixedness [254]). Indeed, many quantum-information-processing protocols for generating and manipulating entanglement [e.g., remote entanglement generation (see §4.3.5), entanglement

[13]Note that we have focused on particle distinguishability in this chapter (and throughout the dissertation more generally, through photon wave packet overlaps). However, in the above complementarity contexts, distinguishability is typically expressed as a measure of potential "which-path information," which is related to particle distinguishability in some contexts, yet more generally characterizes the extent to which one can determine which path a particle took through an interferometer or other setup [210, 214, 215].

swapping, and photonic fusions [221]] rely on high-quality interference and thus require indistinguishable photons (or other particles) [231, 242, 251–253]. In certain cases, a precise relationship between entanglement and indistinguishability can be given, yet there are subtleties in quantifying the entanglement of indistinguishable particles [266], and the general relation between multipartite entanglement and partial distinguishability is an open question (see Ref. 242 for a tutorial on this topic, including analysis of the impact of indistinguishability on boson sampling). Moreover, note that our list of issues and resolutions is not exhaustive. For instance, Ref. 227 experimentally explores a linear-optical analog of Hardy's thought experiment (which is quite different than that of Ref. 226) and they offer another way of resolving Hardy's Paradox via weak measurement.

5.4 Conclusions

In this chapter, we analyzed a linear-optical setup comprised of two overlapping Mach–Zehnder interferometers, showcasing how single-photon Mach–Zehnder interference and two-photon Hong–Ou–Mandel interference interplay. We provided a semi-naive line of reasoning to illustrate how someone who knows about these two interference effects separately could easily misapply them in combination with one another and wrongly predict that a certain coincident detection outcome is impossible. We then showed how the possibility of this outcome can be understood as resulting from the interference of these two interference effects (as shown visually in Fig. 5.6). This new perspective is intended to be quite accessible, yet (as we briefly considered) is connected to deeper perspectives and topics explored in the literature, such as Bell's theorem.

Central to these various perspectives (i.e., the resolutions of Sec. 5.3.4) is the notion that interference (of quantum amplitudes) does not happen at any specific interaction or part of an experiment. Rather,

interference happens upon measurement.

This is in accordance with the rules of Feynman summarized in Eq. (5.1) and is why we have emphasized the *final* state of the photons (just before measurement). For instance, interference effects that seem to require indistinguishable photon amplitudes (including MZi and HOMi) can still occur for photons that were fully distinguishable when the interference nominally could have taken place, yet were appropriately made indistinguishable thereafter (but before measurement). The quantum-eraser experiment is a single-photon example of this [210, 228, 267]. Such phenomena can likewise occur in two-photon interference effects. For instance, Refs. 268 and 269 explore setups in which photons with different timing and color, respectively, interfere (see also Sec. III D of Ref. 231 and the references therein). This notion is apparent in our setup, as HOMi does not happen at the center-most BS, nor does MZi happen at each MZI. Such impressions could mislead one to the semi-naive premises of Sec. 5.3.2. Rather, aspects of both interference effects are imprinted in the final state amplitudes as dictated by the entire setup.

CHAPTER VI

CONCLUSION

This dissertation analyzes methods for controlling photons and their interactions with matter for quantum information processing. A unifying theme of this work is the criticality of controlling the shape and indistinguishability of photons. A main conclusion of Chs. III and IV is that the probability of successful hybrid quantum state transfer (QST) is dictated by the overlap of two photon wave packets:

$$P_{\text{success}} = |\langle\Psi|\Phi\rangle|^2 . \tag{6.1}$$

Here $|\Psi\rangle$ the is photon wave packet incident on the receiving node, i.e., the transformed output of the emitting node, and $|\Phi\rangle$ is a target photon wave packet dictated by the receiving node. Similarly, in heralded hybrid remote entanglement generation (REG), two nodes each emit a photon that is entangled with a qubit encoded in the emitter. Then a photonic Bell-state measurement is performed on these photons, $|\Psi_1\rangle$ and $|\Psi_2\rangle$ (at least one which having been transformed), which, on a successful herald, results in the two nodes becoming entangled with a Bell-state fidelity dictated by the photonic overlap:

$$\mathcal{F} = \frac{1 + |\langle\Psi_1|\Psi_2\rangle|^2}{2}. \tag{6.2}$$

Hence, both QST and REG, especially between heterogeneous nodes, demand precise control over the shape, frequency, and time scales of single photons—achieved via carefully tuned production and manipulation methods—to match a target wave packet. The importance of controlling photons is probably quite intuitive.

Nonetheless, seeing how the success of a complicated quantum protocol emerges from the underlying physical description is both fascinating and important for understanding how to actually achieve said control.

More broadly, many quantum-information-processing tasks rely on indistinguishable photons (or processes) [251–253, 265]. These include Mach–Zehnder and Hong–Ou–Mandel interference as well as setups that leverage them. As emphasized in Ch. V, it is the distinguishability of processes at measurement that matters, as is often quantifiable by an overlap of photon wave packets. Therein we showed that the possibility of a certain coincident detection event can be understood as the result of the interference of two interference effects, a phenomena that relies on the photons being indistinguishable at measurement. Moreover, in hybrid QST, it does not matter that the emitted photon is initially the wrong photon to be absorbed by the receiver; what matters is that the final transformed photon incident on the receiver matches the target.

It is hoped that our light treatment of such quantum processing tasks underscores the power and intrigue of controlling and manipulating photons.

APPENDIX A

SCOPE, ADORNMENTS, AND FURTHER CONSIDERATIONS: HYBRID QUANTUM STATE TRANSFER

Here we provide quite extensive additional discussion, calculations, and background to supplement Chs. III and IV. This content is a slightly extended version of the supplemental online material for Ref. 4, which was written by K. J. Randles, who also performed the calculations and made the figures, with the continued guidance, conceptual input, and methodological verification from S. J. van Enk. Because of its appreciable length, we break down the contents of this appendix below.

Contents

A.1 Scope of results

The atom in cavity type node we focus on in Chs. III and IV is meant to be an elucidating example, which should be contrasted against other implementations of controlled light-matter interaction of individual quanta. As mentioned in §4.2.3, our general theory aims to capture many of such implementations, which we will further substantiate here. In this section we discuss the applicability of our work beyond such atom in a cavity type nodes, the impact of various choices we made in the QST scheme, and relevant alternatives to said choices. This includes a more general argument for the probability of successful excitation transfer formula derived in Ch. IV, P_{success}, in Sec. A1 and moreover a discussion of why our model Hamiltonians themselves are quite general in Sec. A2. In Sec. A3 we discuss the quantum fidelity of the initial and final qubit states as a different measure of a successful QST scheme than P_{success}. In Sec. A4 we discuss the impact of including time reversal as part of the unitary transformation to the itinerant single photons. In Sec. A5 we highlight relevant implementations of the proposed unitary transformation. In Sec. A6 we discuss the

impact of using a mode occupation number encoding for the photonic qubits and contrast it to other commonly used encodings, especially polarization. Finally, in Sec. A7 we contrast our deterministic scheme to heralded implementations, showing that heralded schemes, especially hybrid ones, could benefit from (or be made possible by) a unitary photon transformation similar to the one we consider.

A.1.1 Generality of $P_{success}$

To illustrate the wide-reaching applicability of our scheme for quantum networking and communications we will now show how and why Eq. (4.2) applies quite generally, under modest assumptions, for nodes implemented using other systems including those just mentioned. To see this we interpret the receiving node to be a binary-outcome photodetector (the simplest possibility), which either "clicks" if the incident light is in a certain small fraction of all possible modes or does not click, corresponding to a null response where there was either no light or the incident light was in a mode the detector was not sensitive to. [Note that this is just a thought experiment as in our actual QST scheme it is crucial that we do not actually perform a measurement (which would cause the state to collapse out of the desired superposition state). In particular, we do not check the measurement outcome, which could be done by appending an atomic measurement of the state of qubit at node 2 (doing so would turn our QST scheme into an actual measurement).]

As is contemporarily standard (see the clarifying note in §4.3.2), such a quantum measurement can be mathematically represented as a positive operator-valued measure (POVM), which is a set $\{\hat{\Pi}_n\}$, where one can associate a POVM element $\hat{\Pi}_n$ (a positive Hermitian measurement operator) with each of the possible measurement outcomes labeled by n. The fact that upon measurement, one of the possible outcomes

must occur is encapsulated by the completeness relation $\sum_n \hat{\Pi}_n = \mathbb{1}$, where the sum runs over all n and $\mathbb{1}$ is the identity operator on the Hilbert space associated with the system being measured. Here the outcomes are "click" or "no click" with corresponding POVM elements

$$\hat{\Pi}_{\text{click}} = \sum_i w_i |\phi_i\rangle\langle\phi_i| \tag{A.1}$$

(this form results from diagonalizing the POVM element, which is possible as it is positive and Hermitian), where the sum runs over an orthonormal set of modes $\{|\phi_i\rangle\}$ with weights $0 \leq w_i \leq 1$, and $\hat{\Pi}_{\text{no-click}} = \mathbb{1} - \hat{\Pi}_{\text{click}}$, respectively. The probability of a click can then be expressed as

$$P_{\text{click}} = \text{Tr}\Big(\rho_{\text{in}} \hat{\Pi}_{\text{click}}\Big). \tag{A.2}$$

In our case of single-photon detection, time reversibility guarantees that (under ideal conditions[1]) our effective photodetector (the receiving node) will project onto one single-photon wave packet. That is, the POVM element (and corresponding ideal wave packet) is pure (rank one). This is simply because the absorption process is reversible, it is time reversed and complex conjugated relative to the pure (under the aforementioned ideal conditions) emission process [1, 155]. Thus, here with the deterministic (and reversible) production of single-photon wave packets, we have the

[1]These ideal conditions include that, as previously assumed, no thermal or other unexpected excitations will interact with the receiving node, that the system parameters are fixed (do not fluctuate), that there are no dark counts, which would be represented by an additional term in the click POVM element that projects onto the vacuum, and moreover we do not consider multiple incident photons in the detection time. These are realistic assumptions in situations like ours, where the single photon excitation is mapped onto a material qubit. This is to be contrasted against standard photodetectors that are destructive and hence irreversible (as considered in Ch. V).

pure POVM element

$$\hat{\Pi}_{\text{click}} = |\Phi\rangle\langle\Phi|, \tag{A.3}$$

where $|\Phi\rangle$ is one of the orthornomal basis vectors. Inserting this into Eq. (A.2) for a pure input state $\rho_{\text{in}} = |\Psi\rangle\langle\Psi|$ we obtain[2]

$$P_{\text{click}} = P_{\text{success}} = |\langle\Phi|\Psi\rangle|^2 \tag{A.4}$$

as given by Eq. (4.2).

A.1.1.1 Remark on 3D treatment. This treatment makes it clear that this formula for P_{success}, Eq. (A.4), is valid in a full 3D treatment with the wave packets given by

$$|\Xi\rangle = b_\Xi^\dagger|\text{vac}\rangle \quad \text{with} \quad b_\Xi^\dagger = \int d^3k \sum_{\boldsymbol{\varepsilon}} \Xi_{\boldsymbol{\varepsilon}}(\boldsymbol{k}) a_{\boldsymbol{\varepsilon}}^\dagger(\boldsymbol{k}) \tag{A.5}$$

[see Eq. (1.14)] with $\Xi = \Phi$ or Ψ such that

$$P_{\text{success}}^{(3D)} = \left|\langle\text{vac}|b_\Phi b_\Psi^\dagger|\text{vac}\rangle\right|^2 = \left|\int d^3k \sum_{\boldsymbol{\varepsilon}} \Phi_{\boldsymbol{\varepsilon}}^*(\boldsymbol{k})\Psi_{\boldsymbol{\varepsilon}}(\boldsymbol{k})\right|^2. \tag{A.6}$$

Then to arrive at a quasi-1D treatment—as was done in Chs. III and IV—we assume a fixed polarization, $\boldsymbol{\varepsilon}_\Xi$, and transverse spatial mode, i.e., $\Xi(\boldsymbol{k}) = \Xi_\perp(\boldsymbol{k}_\perp)\Xi_\parallel(k_\parallel)$ for each wave packet. Doing so, making the change of variables $k_\parallel = \omega/c$ to focus on the longitudinal mode ω, and defining $\Xi(\omega) := \Xi_\parallel(k_\parallel)/\sqrt{c}$ we have

$$P_{\text{success}}^{(3D)} = \eta_\perp P_{\text{success}}^{(1D)}, \tag{A.7}$$

[2]Note that this click outcome corresponds to the successful transfer of an excitation, which is why we call it P_{success}, though additional considerations (e.g., the use of local oscillators as phase references) are needed to ensure that the phase is transferred.

where the previously considered 1D overlap

$$P_{\text{success}}^{(1D)} = \left| \int d\omega \ \Phi^*(\omega)\Psi(\omega) \right|^2 = \left| \int dt \ \Phi^*(t)\Psi(t) \right|^2 \tag{A.8}$$

is reduced by the 'mode-mismatch' factor

$$\eta_\perp = \left| \boldsymbol{\varepsilon}_\Phi^* \cdot \boldsymbol{\varepsilon}_\Psi \int d^2k_\perp \Phi_\perp^*(\boldsymbol{k}_\perp)\Psi_\perp(\boldsymbol{k}_\perp) \right|^2 . \tag{A.9}$$

A.1.1.2 Premature detection. Now we return to the quasi-1D model (omitting the corresponding subscript), noting that above we assumed the receiving system is given enough time to click. One can easily generalize this, defining the probability of success for a premature detection time $t_p \leq t_d \leq t_e$ [as discussed surrounding Eq. (4.23), t_e is the steady state 'end' time] as

$$P_{\text{success}}(t_d) := \left| \int_{t_p}^{t_d} dt \ \Phi^*(t)\Psi(t) \right|^2 , \tag{A.10}$$

which is zero at the preparation time $t = t_p$ and approaches the probability of success $P_{\text{success}}(t_e)$ as t_d increases towards t_e. This can be thought of as the overlap of our state Ψ with the ideal state up until time t_d, that is, with the subnormalized state $\Phi_{t_d}(t') := \Phi(t')\Theta(t_d - t')$ with Θ the Heaviside step function. Thus we can consider the corresponding (unnormalized) POVM element

$$\hat{\Pi}_{\text{success}}(t_d) = |\Phi_{t_d}\rangle\langle\Phi_{t_d}| . \tag{A.11}$$

Equivalently, we can factor out the subnormalization and write the above POVM element as

$$\hat{\Pi}_{\text{success}}(t_d) = W(t_d) \left|\tilde{\Phi}_{t_d}\right\rangle\!\left\langle\tilde{\Phi}_{t_d}\right| \tag{A.12}$$

with

$$W(t) := \int_{t_p}^{t} dt' \; |\Phi(t')|^2 = \int_{t_p}^{\infty} dt' \; |\Phi(t')\Theta(t-t')|^2 = \langle \Phi_t | \Phi_t \rangle \tag{A.13}$$

interpreted as an efficiency $0 \leq W \leq 1$ and $|\tilde{\Phi}_t\rangle = W^{-1/2}(t)|\Phi_t\rangle$ a normalized single-photon state [270]. Importantly, no matter how we write the success POVM element describing a click, the effective photodetector is (and in fact must be[3]) independent of the actual incident wave packet Ψ and only depends on the detection time t_d and on the measurement parameters (those of the receiving system and the controls used to manipulate it), which determine the ideal wave packet Φ. However, we cannot specify the form of the ideal wave packet $\Phi(t)$ without further system details, namely, the particular form of the effective Hamiltonian describing our scheme, which can be obtained by focusing on specific kinds of nodes. In this work we focus on nodes comprised of a three-level atom in an optical cavity, though, as we will next discuss, the corresponding Jaynes–Cummings interaction Hamiltonian is quite general. This allows us to explicitly determine the ideal wave packet $|\Phi\rangle$ in the temporal mode $\Phi(t)$ as in §4.3.1.

A.1.2 Generality of model Hamiltonian

As we have discussed, the broad scope of Eq. (4.2) is quite intuitive. Potentially more surprising (at least at first thought) is that our Hamiltonian itself H_{eff}, Eq. (4.3), is quite general. To obtain H_{eff} one starts by considering two spatially separated

[3]Just as a POVM element of a general measurement never depends on the input state on which the measurement is performed.

systems (nodes) interacting via an intermediate channel that hosts a quasi-one-dimensional electromagnetic field [122] for which the only propagating degree of freedom of light in the channel is the longitudinal mode (the polarization and two transverse spatial modes are fixed, though this can straightforwardly be extended, e.g., see §A.1.1.1). Then, by employing the standard rotating-wave approximation and a Markov approximation (detailed in [122]) that includes assuming a flat coupling[4] $\kappa_j(\omega) = \sqrt{\gamma_j/2\pi}$ within a narrow bandwidth of positive frequencies, one can eliminate the continuum mode bosonic bath operators of the channel, as is standard in input-output theory [122–124], to obtain the Heisenberg EOMs for system operators. The corresponding dynamics of the state of both systems in the Schrödinger picture can then be described by a Lindblad master equation or equivalently in the quantum trajectory formalism [122, 140, 141] in which a given pure state trajectory of the effectively directly coupled systems is induced by an effective Hamiltonian. This Hamiltonian will be of the same three part form as H_{eff} of Eq. (4.3), where $H_{1,2}$ are the node Hamiltonians and H_{tl} accounts for their interaction [it takes on the specific form of Eq. (4.5) assuming a unidirectional coupling and a vacuum field input to system 1; the phase ζ depends on what rotating frames we go into for each node].

In our QST scheme and often in quantum networking, it is desirable to use nodes in which some internal state of a material encoding a qubit can be reversibly converted into a quantum excitation (often a single photon). Hence, almost by construction, in the appropriate parameter regime(s), each node must be describable by a standard Jaynes–Cummings-like interaction, i.e., via a Hamiltonian of the general form

$$H_{\text{a}\sigma} = g(t)a^\dagger\sigma^- + g^*(t)a\sigma^+ \tag{A.14}$$

[4] Our use of the symbols γ and κ here and in Chs. III and IV follows the notation of Refs. 122 and 124.

in the interaction picture, under the rotating wave approximation (as was already assumed to obtain H_{tl} via input-output theory). Here a and σ^- are annihilation operators ($a^\dagger$ and σ^+ are their Hermitian conjugate creation operators) for a photonic and material excitation (the cavity and atom in our case), respectively, and $g(t)$ is a time-dependent coupling between them. This Hamiltonian describes a system in which excitations with similar energies are transferred between light and matter. When an excitation is removed from the material, a photon is produced, $a^\dagger\sigma^-$, (though other excitations of light could potentially be used, say in a two-photon transition) or vice versa during absorption, $a\sigma^+$. This form assumes we are in the single-excitation regime as we focus on material dynamics in the two-level subspace encoding the state of the qubit, $\{|g\rangle, |e\rangle\}$ here. As emphasized by Ref. 33, for quantum networking applications it is desirable for the light-matter coupling $g(t)$ to be 'user controlled' so that one can tune its amplitude and phase (say using lasers driving the system) so as to deterministically induce emission and absorption of photon wave packets of particular shapes. Our effective node Hamiltonians Eq. (3.43), obtained in the case where each node is comprised of an atom in cavity, are of this same form with $\sigma^- = |g\rangle\langle e|$ and $g(t) = iG(t)$, though the phase can be tuned more generally, see Sec. B1.

The generality of the Jaynes–Cummings (JC) model beyond systems of atoms or molecules in a cavity (our setting here) was not obvious from its conception [271]. In fact it took decades for the strong coupling regime, which is necessary to realize JC physics, to be reached in cavity QED experiments [163, 272]. Since then, additional groundbreaking cavity QED experiments have demonstrated the ability to engineer highly-controllable interactions of individual photons with a small number of quantum emitters (single atoms interacting with single photons in our

case) with the corresponding weak light-matter interaction enhanced by a high-Q cavity. Such advances are relevant for our scheme, which is a modified and extended version of a seminal cavity QED based QST protocol [1], and for quantum networking more generally. See Refs. 170 and 273 for relevant reviews (we point to Refs. 34, 142, 274, 275 for some innovative demonstrations).

Meanwhile, other technologies have emerged that can similarly facilitate such highly-controllable quantum light-matter interactions to implement fundamental primitives like QST and entanglement generation (which in some cases are heralded as opposed to deterministic). These include experimental implementations (and accompanying theory) using trapped ion qubits [167, 276–278], collective atomic excitations [279], various forms of superconducting qubits [35, 88, 89, 92, 93, 280], and electronic spin qubits [nitrogen-vacancy (NV) centers in diamond are a common realization] [207]. These are not limited to photonic flying qubits; notably see Ref. 113 which uses an intermediate phonon for hybrid quantum state transfer between a superconducting microwave qubit and a solid-state spin qubit. In their main text they do this using a direct coupling, though in their Supplementary Note 1 they also consider a 'pitch-and-catch' protocol with the phonon serving as a flying qubit that could propagate between distant versions of such nodes connected by a waveguide.

These many implementations make the generality of JC physics manifest. They also make clear that this generality is the result of tremendous efforts in experiment and theory to "tame DOFs" as discussed in §1.3. See Ref. 281 for further exposition of the JC model including its applicability in many experimental settings, including those just mentioned, as well as its history, theoretical details, and extensions.

The precise means of obtaining a Hamiltonian of this form depend on the nodes' physical implementation, though some common steps (as mentioned in the main text;

see §3.5.1) include adiabatically eliminating other states, selecting an appropriate rotating frame to go into (i.e., selecting which unitary transformations to perform on the node Hamiltonians), and tuning the system parameters to eliminate undesired terms. The physical interpretation of the operators in $H_{a\sigma}$ and the methods of controlling the coupling $g(t)$ likewise depend on the node. However, as long as such a Hamiltonian is realizable with a given node implementation (as it often is for deterministic QST schemes), then the analysis presented here and in Chs. III and IV should be applicable. In particular, the equations we derive, such as the excitation amplitude EOMs Eq. (4.12) and other subsequently derived expressions (or similar variations thereof), should apply more generally to these other types of nodes. Thus, even though we emphasize connecting two nodes that are each comprised of an atom in a cavity, our results are relevant to hybrid cases where two different types of nodes are connected.

A.1.3 Fidelity as a measure of success

The probability of successfully transmitting an excitation between the systems $P_{\text{success}} = |\alpha_2(t_e)|^2$, given in Eq. (4.30), is a useful measure of the success of a state transfer attempt. This can be contrasted to the quantum state fidelity

$$\mathcal{F} = |\langle\psi_i|\psi_f\rangle|^2 \tag{A.15}$$

(some authors refer to the square root of this quantity as 'the fidelity'), which accounts for impact of phase errors in addition to excitation loss. Here the initial state (of atom 1) is $|\psi_i\rangle = c_g|g\rangle + c_e|e\rangle$ (using the same notation for the coefficients as §4.2.1) and

the final state (of atom 2) is of the form

$$|\psi_f\rangle = e^{i\theta_f}\sqrt{1-|c_e|^2|\alpha_2(t_e)|^2}|g\rangle + c_e|\alpha_2(t_e)||e\rangle, \tag{A.16}$$

where θ_f encodes any relative phase errors between $|g\rangle$ and $|e\rangle$ (we already factored out any phase error in the term $\alpha_2(t_e)e^{i\phi_2(t_e)}$ and included it in θ_f, up to an unphysical global phase).[5] Note there is no phase error if $\theta_f = \arg(c_g)$ so using the relation $|c_g|^2 + |c_e|^2 = 1$ along with shorthand[6] $x = |c_e|^2$, $a = |\alpha_2(t_e)|$, and $\delta\theta = \arg(c_g^* e^{i\theta_f})$ we have

$$\begin{aligned}\mathcal{F} &= \left|e^{i\delta\theta}\sqrt{(1-x)(1-a^2x)} + ax\right|^2 \\ &= a^2x^2 + (1-x)(1-a^2x) + 2\cos(\delta\theta)\sqrt{(1-x)(1-a^2x)}ax.\end{aligned} \tag{A.17}$$

Note this dramatically simplifies for $|c_e| = 1 \implies x = 1$ to $\mathcal{F}|_{x=1} = a^2 = |\alpha_2(t_e)|^2$, which is the probability of successfully transferring an excitation P_{success} considered above. The more general behavior of $\mathcal{F}(x,a)$ depends on what the phase error $\delta\theta$ is, three possibilities of which are illustrated in Fig. A.1. In the ideal case without phase errors $\delta\theta = 0$, achieved by phase matching for a given α_2, the fidelity $\mathcal{F}$ monotonically decreases from 1 to a^2 as x goes from 0 to 1, see Fig. A.1 (a). Hence in this ideal

[5]Note that it does not matter if the unitary induces a relative phase ϕ during the transmission from node 1 to 2, as long as a $-\phi$ phase is induced during the reverse transmission from node 2 to 1. For instance, say $(a|0\rangle_1 + b|1\rangle_1)|0\rangle_2 \to |0\rangle_1(a|0\rangle_2 + be^{i\phi}|1\rangle_2)$ under a QST procedure, then the basis $\{|0\rangle_2, |1'\rangle_2 = e^{i\phi}|1\rangle_2\}$ can be used for system 2, effectively relabeling the excited state to account for this relative phase. This is ok provided this phase error is systematic and reversible. That is, if when the state is transferred back to system 1, it obtains the opposite phase $-\phi$, e.g., $|0\rangle_1(a|0\rangle_2 + b|1'\rangle_2) \to (a|0\rangle_1 + be^{-i\phi}|1'\rangle_1)|0\rangle_2 = (a|0\rangle_1 + b|1\rangle_1)|0\rangle_2$, which is the original state. Otherwise, this is a genuine phase error (which is assumed to be the case for $\delta\theta$ in this section).

[6]Note that within given appendix sections we occasionally represent a new variable with a symbol that has already been used. For instance, here we define the excited state population x, which is not to be confused with the transmission line propagation distance. The quantity under consideration should be clear from context.

phase matched case the considered P_{success} is a lower bound for $\mathcal{F}$. This fidelity is clearly minimized if $\delta\theta = \pi$, yet one should be able to tailor the scheme so that, at least for large a near 1, the phase error is negligibly small. The simplest possible realization of this is the phase error model $\delta\theta = \theta_0(1-a)$, where assuming the phase error gets smaller as a increases then $0 \leq \theta_0 \leq \pi$. Even in the worst such case with $\theta_0 = \pi$, corresponding to a phase flip error for $a = 0$, the average value of $\mathcal{F}$ as a function of x is always well above a^2, and moreover for $a \geq 1/2$ in the model we again find (as in the ideal case) that $\mathcal{F}$ monotonically decreases from 1 to a^2, see Fig. A.1 (b). Thus $P_{\text{success}} = a^2$ again serves as a lower bound provided the transfer satisfies the modest condition $a \geq 1/2$. This lower bound restriction on a of $1/2$ gets smaller as θ_0 decreases, approaching $a \geq 0$ for the ideal case $\theta_0 = 0$ considered above. This may be overly simplistic, though the development of a general phase error model is beyond of the scope of this dissertation and would likely depend on many system-specific figures of merit. We note that similar results seem to hold for other phase error models provided $\lim_{a\to 1} \delta\theta = 0$. If this does not happen, i.e., if $\lim_{a\to 1} \delta\theta = \delta\theta_1 \neq 0$, then even for perfect excitation transfer $a = 1$, the fidelity will drop below one $\forall\ 0 < x < 1$ (which just excludes the end points) and will reach a minimum value of

$$\min_x \mathcal{F}(x, a = 1) = \cos^2\left(\frac{\delta\theta_1}{2}\right) = 1 - \frac{\delta\theta_1^2}{4} + \mathcal{O}\left(\delta\theta_1^4\right) \tag{A.18}$$

at $x = 1/2$ (assuming $\delta\theta$ is independent of x). See Fig. A.1 (c) for an example of this behavior in the case of a constant error of $\delta\theta = \pi/5$.

Due to the presence of $|e_1\rangle|g_2\rangle \to |g_1\rangle|g_2\rangle$ (photon loss) errors, the fidelity tends to be much lower when the excited state population x is large (at least for small a, see Fig. A.1). One way to quantify the typical fidelity of an arbitrary initial state $|\psi_i\rangle$

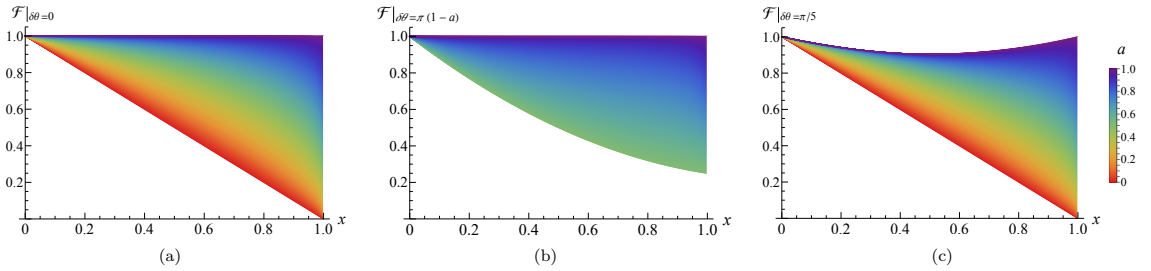

FIGURE A.1. Plots of the fidelity $\mathcal{F}$ as a function of x for various a as indicated by the legend. In each of the subfigures we consider a different case of the phase error: (a) $\delta\theta = 0$, (b) $\delta\theta = \pi(1-a)$, and (c) $\delta\theta = \pi/5$. In each of case $\mathcal{F}(x)$ increases monotonically as a function of a pointwise for each x over the shown values of a. To obtain this behavior in case (b), and hence to avoid crossings (which would make this type of figure futile), we only includes curves for $a \geq 1/2$.

is by averaging over the x parameter. In particular, we express the initial state in the Bloch sphere representation as $|\psi_i\rangle = \cos(\theta_{Bs}/2)|g\rangle + e^{i\phi_{Bs}}\sin(\theta_{Bs}/2)|e\rangle$ and average $\mathcal{F}$ over the polar angle θ_{Bs}. Doing so using Eq. (A.17), wherein $x = \sin^2(\theta_{Bs}/2)$, and again assuming $\delta\theta$ is independent of x, we find

$$\langle\mathcal{F}\rangle_x \equiv \int_0^\pi \frac{d\theta_{Bs}}{\pi}\mathcal{F}[x(\theta_{Bs})] = \frac{1}{2} + \frac{a^2}{4} + \frac{\cos(\delta\theta)\left[a\sqrt{1-a^2}(2a^2-1) + \sin^{-1}(a)\right]}{2\pi a^2}, \tag{A.19}$$

which is plotted in Fig. A.2 for several phase error models. As $a \to 1$, corresponding to $P_{\text{success}} = a^2$ near unity, this averaged fidelity approaches $\lim_{a\to 1}\langle\mathcal{F}\rangle_x = 1 - \delta\theta_1^2/8 + \mathcal{O}(\delta\theta_1^4)$, which is near one for small residual phase offsets $\delta\theta_1$, similar to Eq. (A.18).

A.1.4 Utility of time reversal

We emphasize the time reversal aspect of our protocol, and of the transformation specifically, both because it naturally fits within the quantum networking goal of being able to realize controlled reversible light-matter interactions to transfer the state of a qubit to and from a material system and a photon and because it is not typically

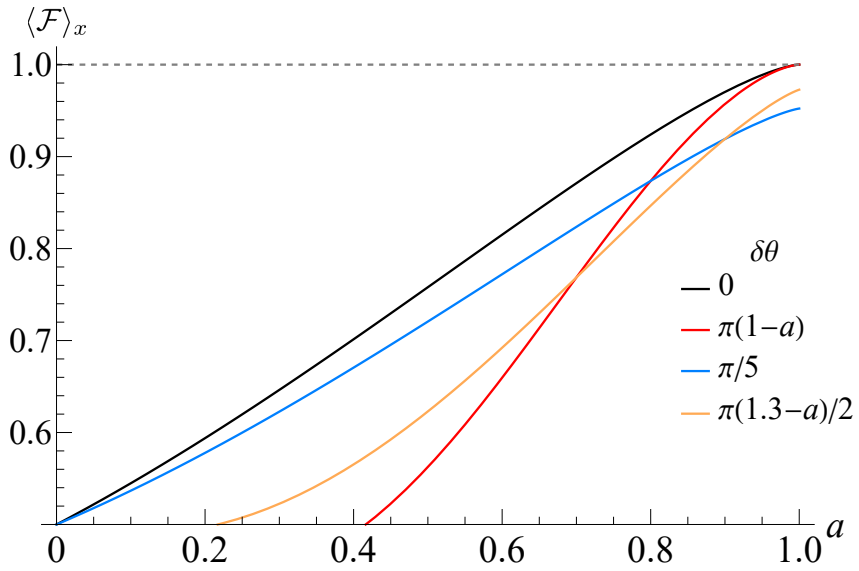

FIGURE A.2. Plots of the average fidelity $\langle \mathcal{F} \rangle_x$ for the three error models for $\delta\theta$ considered in Fig. A.1 (a-c) as well as an additional model that combines the simple phase error model with $\theta_0 = \pi/2$ (see above text) with a small residual offset: $\delta\theta = \pi(1-a)/2 + 3\pi/20$ (these respective cases are shown as black, red, blue, and orange lines).

emphasized by other researchers considering similar QST schemes to ours. For the former point, we note that the incorporation of a time-reversal operation as part of the unitary transformation in our scheme is motivated by the notion that the absorption of a flying qubit is the time-inversed complex conjugate of the emission process [155], and moreover, that this still holds for nodes with different resonance frequencies and decay rates, provided we implement a transformation to effectively match up these quantities. Note that including the time-reversal operation to the intermediate photon is redundant in the often considered special case where the produced photon [34, 35, 78, 88, 89, 280, 282] or phonon [112, 113] wave packet envelope is time-symmetric (as in seminal proposal by Ref. 1). However, in some cases, an asymmetric wave packet may be preferable, such as if it is easier to produce the corresponding drives, e.g., laser pulses, (note that errors in the drives will generally lead to an

asymmetric shape even when the target shape is time symmetric [150, 283]) or if a certain wave packet shape is less susceptible to errors [for instance, wave packets with longer durations (e.g., due to slow driving) can be emitted with higher efficiency (see Sec. B3) yet they take longer to produce (potentially reducing the QST rate) and are more susceptible to frequency errors (see Sec. B4)]. Even in cases where the intended wave packet is symmetric, a time-reversal transformation may correct for any error-induced time asymmetry, assuming the error is systematic in that it effects the receiving and sending nodes in the same way. For instance, dispersion (or other distortion) during propagation in the channel can make an initially time-symmetric wave packet asymmetric and it can induce a nontrivial relative phase to the photonic qubit state. Hence, the unitary transformation we propose could be used in the middle of the channel to cancel out such asymmetric distortions and phase errors, analogous to a spin-echo. If only time reversal was implemented, this would typically still result in a wave packet that is broadened and frequency shifted due to dispersion. However, assuming this happens in a systematic and characterizable way, these net shifts could be compensated for using our stretching and frequency shift parameters of ξ and ω_0, respectively. Note that such distortion can alternatively be taken into account by modifying the drives themselves. For instance, the emission inducing drive $G_1(t)$ could be designed to produce wave packets that are less-susceptible to reshaping and the absorption inducing drive $G_2(t)$ could be modified to better receive the distorted wave packet [128].

Accordingly, to not restrict ourselves to this special time-symmetric case, we include time reversal in our unitary transformation. This is nice theoretically, as then our QST scheme is applicable more generally for asymmetric photon wave packets, and in fact is indifferent to the photon wave packet shape (provided we know

the temporal window it occupies). Furthermore, it may be natural to incorporate the time-reversal transformation as part of the photon manipulation scheme along with frequency conversion and mode stretching or compressing, as is the case in Ref. 37. Importantly, much of our analysis would still apply if a time-reversal transformation was not implemented. There would just be a corresponding error due to how asymmetric the wave packet is. Moreover, such analysis would still hold if a different transformation was implemented or no transformation was implemented at all (which is relevant when small frequency shifts, small time asymmetries of the photon, and compression or stretching factors of near unity are needed). This is because the result for P_{success}, Eq. (4.2), does not depend on how or whether the incident wave packet $\Psi(t)$ has been transformed.

Returning to the latter point of a lack of emphasis, we note that recent work on hybrid quantum interconnects and networking often emphasizes the need for frequency conversion and wave packet shaping, in the form of bandwidth conversion, of the intermediate photon wave packet with little explicit mention of correcting for time asymmetry [57, 78, 150, 284, 285]. Some QST experiments produce photons with manifestly time-asymmetric temporal shapes, often producing wave packets that are smoothed-out versions of an exponentially decaying function [167, 276, 278, 286]. This may suffice for establishing photonic entanglement (see §A.1.7 for such a case) but would lead to issues in achieving state transfer or entanglement generation across material systems realized using absorption unless the corresponding photons' shapes are modified or a time-reversal transformation (or more general wave packet shaping) is employed. Perhaps this lack of emphasis is because the intermediate photon can often be engineered to have a symmetric (or nearly symmetric) temporal shape or because it is well-known and currently a less pressing issue than frequency and decay

rate matching (especially in the current era where hybrid frequency conversion can only be achieved with low probability).

To illustrate the impact of temporal shape – and hence how pressing errors in it may be – we consider the highly asymmetric, though typical [148], case of a normalized wave packet with an exponentially decaying envelope $\Psi(t) = \sqrt{\gamma}\Theta(t)e^{-\gamma t/2}$ being sent between two identical nodes. Assuming the absorption process is the reverse of the emission process that generated this wave packet (including any time-dependent system controls used), the ideal wave packet for absorption will be the time inverse of $\Psi(t)$ up to a delay T_d, i.e., $\Phi(t) = \Psi(T_d - t)$. Then the probability of success as determined by Eq. (4.2) is $P_{\text{success}} = \gamma^2 T_d^2 \Theta(T_d) e^{-\gamma T_d}$, which has a maximum value of $4/e^2 \approx 0.54$ for $T_d = 2/\gamma$. This indicates that while time-reversal transformations (or the use of time-symmetric photon wave packets) is necessary for optimal transfer, it is only responsible for relatively small inefficiencies in a QST scheme like ours as compared to the impact of suboptimal frequency, stretching, and timing. The practical utility of time-reversal should thus be deferred to a case-by-case basis depending on experimental details including how naturally a time-reversal operation can be included (say as part of an already needed transformation) and what success probabilities are desired (namely whether a potential increase by a factor of $\lesssim 2$ is worth the effort of including time reversal).

A.1.5 Unitary implementations

The hybrid QST scheme we propose is contingent on being able to implement the unitary transformation, U, of Eq. (3.18) to transduce the intermediate photon between the emitting and receiving nodes' disparate energy and time scales. The form of the unitary transformation we consider was inspired by Ref. 37, which

proposed an optical implementation of a transformation that amounts to U, including time reversal, via a three or four wave-mixing process that can be achieved in realistic nonlinear media. Here we describe how our simple model for the unitary transformation device is related to their three wave-mixing, sum-frequency generation (SFG) based physical implementation in a nonlinear medium of length L. Then we mention related experimental efforts in other electromagnetic regimes.

Reference 37 considers a transformation that takes in two signals, 1 and 2, with frequencies ω_1 and ω_2, that are initially a temporal mode in an arbitrary state and a vacuum state, respectively. (In their notation, $\omega_1 = \omega_s$, $\omega_2 = \omega_r$, and $\xi = M = -1/m > 0$.) These signals are connected using SFG driven by a short classical pump pulse of frequency $\omega_p = |\omega_2 - \omega_1|$ that mixes the signals in the medium. They derive conditions for the output of the transformation to be signal 1 in the vacuum state and signal 2 in a temporal mode that is the time reversed and stretched by ξ counterpart of the initial signal 1 yet is still centered at ω_2. These conditions include that the group slownesses $\beta'_\eta = 1/v_\eta$ ($\eta = 1, 2, p$), which are the inverse group velocities in the medium, are ordered as $\beta'_1 > \beta'_p > \beta'_2$ (for $\omega_2 > \omega_1$, otherwise it is reversed), as well as things such as phase matching. They verify that these conditions can occur for realistic media. Importantly for QST, they show that the entanglement between the transformed field (which here is the output from system 1) and the pump pulse (and hence the unitary transformation device) stays arbitrarily small in the limit of a classical (i.e., strong and coherent) pulse. Note that their signals 1 and 2 are our input and output to the unitary transformation device, respectively.

Our Stage 2 and 3 are captured by their transformation. Stage 2 begins at t_i when signal 1, the input field, first enters the transformation device (nonlinear medium). Signal 1 is followed by signal 2 and the pump pulse, which enter the medium at

the same time. A three-wave-mixing process (SFG) then begins, and signal 2 (the transformed output) exits the medium, followed by signal 1 and the pump pulse at the same time. Using these conditions it follows that to transform a duration $t_l = l/c$ of the input pulse we need a medium of minimum length

$$L = t_l(\beta_1' + \beta_2' - \beta_p' - 1/c)^{-1} > \frac{l}{c\beta_1' - 1}. \tag{A.20}$$

Let t_{exit} be the time that signal 2 begins exiting the medium at $x = X + L$. Then $t_s = t_{\text{exit}} - L/c$ is the effective time that the transformed output begins to be produced at $x = X$. Thus, the buffering of Stage 2 can physically be interpreted as the effective time between signal 1 entering the medium at $x = X$ and when the transformed signal 2 would have been at $x = X$ had it been traveling at the speed of light rather than β_2' (i.e., what happens in our simplified device).

In our scheme we need to be able to control both laser frequencies ω_{Lj} and convert the frequency of the emitted wave packet by their difference, $\omega_{L2} - \omega_{L1}$ [more properly by ζ, see Eq. (3.57), though we assume the bare ω_{ej} are stable and well characterized], all at a precision less than γ_2, which is typically on the order of kHz-MHz. If a wave-mixing unitary implementation, like that of Ref. 37, is used one must thus be able generate a pump pulse at the difference frequency $|\zeta|$. For atomic systems, as considered here, standard optical lasers could typically be used. However, when doing intraband frequency conversion, e.g., microwave-optical transduction, lower frequency lasers or alternate drives may be necessary, which may be limiting.

Considering systems in the optical to near-infrared domain is a convenient starting point, not only because of proposal of Ref. 37, but because several aspects of it have been demonstrated experimentally including implementations of optical and telecom frequency conversion [100, 103, 147, 287–290] and shaping (typically bandwidth

conversion).[7] Additionally, such systems can reasonably be connected via optical fiber (over modest distances) [101]. Hence direct connection is not detrimental for short distances, though relatively small frequency conversion to the telecom band (by a factor of $\sim$2), that can be achieved using nonlinear optical methods, can still be valuable if employed. One such experiment worth mentioning is Ref. 78, which demonstrated the heralded hybrid QST of a spin-wave excitation of a laser cooled atomic ensemble to a collective optical excitation of a receiving rare-earth doped crystal. They did so by employing quantum frequency conversion at both nodes to transduce from the atomic ensemble's natural optical frequency to the telecom for transmission along a fiber followed by conversion back to the optical for interfacing with the crystal. Their method is notably different from our scheme as it heralded as opposed to deterministic and hence they do not have to be as concerned with the precise control pulses and the corresponding wave packet temporal shape.

The development of methods to control the wave packet shape of microwave photons is an active area of research [149, 280, 291] as are microwave channels (see §1.5.4). For instance, with some adaptations, the microwave temporal and spectral mode converter of Ref. 149 could potentially be used to implement the considered unitary in the microwave regime. Their mode converter uses the vibration of the aluminum drumhead to catch, modify (which includes shaping and small frequency shifting), and then release the quantum microwave signal.

The extent of frequency conversion needed to link optical-optical systems, microwave-microwave systems, or even optical-telecom is modest compared to the order $\sim 10^5$ frequency discrepancy that needs to be bridged for microwave to optical (or telecom) transduction. Even with the associated difficulties, microwave-optical

[7] We already mentioned relevant optical photon wave packet shaping experiments in §4.3.3, namely see Refs. 147, 149, 150 and 189.

transduction is rapidly developing area of research in which there have been many recent developments in various approaches (including those leveraging electro-optic transducers [292, 293], Rydberg atomic ensembles [294], as well as other methods [295]; see Ref. 180 for a review) and in applications such as the hybrid interfacing of microwave and optical nodes and for optically linking microwave nodes [94, 296–298]. Note these approaches emphasize frequency conversion, over shaping operations like time reversal and stretching or compression, because naturally it is the largest obstacle in microwave-optical interfacing. An implementation of our scheme in such a microwave-optical case could include cascaded transformations, somewhat like Ref. 78, say microwave to optical frequency conversion followed by optical tailoring of the photon wave packet, though significant advancement in current methods or new methods would be needed for this to be viable.

Remark:
This subsection draws from the appendiceal content of Ref. 3 in addition to the supplemental material of Ref. 4.

A.1.6 Photonic qubit encodings

In Chs. III and IV we focused on using an occupation number encoding for the photonic qubit state in which there is either a photon (in a particular singled-out mode), represented by $|1\rangle$, or there is not, $|0\rangle$. We do so for simplicity and so that the ECZ error correction protocols could be utilized, which would allow us to maintain a deterministic scheme even with errors and loss. However, this is not the only encoding that could be used for our scheme. Accordingly, in this section we compare the utility of different ways of encoding the state of a qubit in the degrees of freedom of a photon with a focus on occupation number versus polarization encodings.

Polarization encoding. We will start by considering the polarization encoding in which the photonic qubit is encoded in an orthogonal polarization basis, we will refer to the linearly polarized horizontal and vertical basis $\{|H\rangle, |V\rangle\}$ for concreteness though others, such as right and left circularly polarized basis, could equally well be used. Note that one can easily change polarization basis, e.g., change between linear and circular polarized light using a quarter-wave plate. Such a polarization qubit can be mapped to and from many quantum emitters that have polarization dependent transitions. This can be achieved by appropriately selecting which electronic or spin states of the material are used to encode the qubit, e.g., considering selection rules, as well as using polarized drives. One realization of this, which is a straightforward modification of our scheme, uses two well-chosen states (typically ground states, though other long-lived states may be appropriate), such as two hyperfine states of an ion split by a magnetic field [134, 166], that are both coupled to an auxiliary level, which we will denote $|r\rangle$ here, via their own Raman transition through an intermediate upper level $|i\rangle$. The material qubit state is encoded in these states, which we will denote by $|g\rangle, |e\rangle$ for consistency. Thus, if the emitter was in state $|g\rangle$ we could apply a properly polarized pulse $\Omega_g(t)$ to induce a transition to $|r\rangle$ which would be accompanied by the production of a photon with polarization state $|H\rangle$ say. Otherwise, if the emitter was in state $|e\rangle$ we would apply a different pulse $\Omega_e(t)$ with different polarization, again inducing a transition to $|r\rangle$, except a photon with a relatively orthogonal polarization, $|V\rangle$, would be produced. (This uses the level structure of the 'ECZ atoms' shown later in Fig. A.11 with $\Omega = \Omega_e$ and an additional Raman field Ω_g applied to the $|g\rangle \leftrightarrow |r\rangle$ transition. The dynamics of both cases are the same as for three-level Λ-type atoms we have detailed.) Hence by applying both pulses, i.e., a bichromatic Raman field, a single photon should always

be generated but its polarization will depend on the emitter state such that for a generic superposition we would achieve QST from the material qubit to the photonic polarization qubit: $c_0|g\rangle + c_1|e\rangle \rightarrow c_0|H\rangle + c_1|V\rangle$. Note that in practice, this transfer is difficult to implement (see the discussion of photon production in heralded setups below in Sec. A7).

Now returning to our context of QST between hybrid material nodes, we would first need to deterministically generate such a photon in a superposition of two polarization states. The photon would then propagate down a transmission line, along which it should be transformed so as to be absorbed by the receiving node. One notable difference here for the polarization, as opposed to the occupation number, encoding is that one would typically need two different transformations, one for each polarization, as different unitary parameters ω_0, ξ, and T would generally be needed to 'impedance match' both Raman transitions, e.g., due to different relative energy splittings of the states of both nodes as well as different phase matching conditions in the implementation of U for each polarization. One way of achieving this would be by using a polarizing beamsplitter to direct the two different polarization components into different transmission lines along which the two separate unitary transformations are performed, after which the lines are recombined, say using another polarizing beamsplitter. Note that this splitting of modes into different fibers is already necessary for the transmission of a polarization encoded state as in a single fiber, even if it is 'polarization maintaining,' the relative phase between two orthogonal modes in superposition, say $|H\rangle$ and $|V\rangle$, will rapidly drift. However, by using a polarizing beamsplitter one can ensure that the initial polarizations in each of the split channels are linear and orthogonal with respect to each other. By using a polarization maintaining fibers for these channels, with the now linearly-polarized

light properly aligned to either the fast or slow axis of the fiber, the states $|H\rangle$ and $|V\rangle$ will be stable and their relative phase can be made to be preserved or to be systematic at least. Finally, the time reversed and stretched counterpart of the original bichromatic Raman field would be applied to the receiving node, initialized in $|r\rangle$, to induce absorption and hence QST between the two nodes.

Tradeoffs. We will now contrast the advantages and disadvantages of the occupation number versus polarization encodings in our scheme. In the occupation number encoding, photon production $|0\rangle \to |1\rangle$ errors can be highly suppressed (note microwave systems must be cooled down for this to be the case) but photon loss errors $|1\rangle \to |0\rangle$ are common. This entails that one cannot distinguish the zero photon state $|0\rangle$ from a lost photon, $|1\rangle \to |0\rangle$, which is a major downside in a single QST trial. However, this can be rectified using error correction such as the ECZ protocols [2, 164]. Alternatively, in the polarization encoding different basis states, say horizontal $|H\rangle$ and vertical $|V\rangle$ polarizations, can mix while propagating in a fiber or when interacting with systems. That is, an initial state $|\psi\rangle = h|H\rangle + v|V\rangle$ can be mapped onto a new state by a nonidentity unitary (neglecting absorption) matrix $|\psi\rangle \to U_{\text{mix}}|\psi\rangle$ so both $|H\rangle \to |V\rangle$ and $|V\rangle \to |H\rangle$ errors can occur. Importantly this can be highly suppressed through careful mode-matching to the transmission line for each polarization and/or appropriate use of polarization maintaining fibers as described above. Nonetheless error correction protocols like those of ECZ, that capitalize on the ability to suppress one of the encoding states turning into the other, cannot be employed for the polarization encoding because of this mixing.

Therefore, in realizations where the polarization encoding has been deemed appropriate, alternative heralded schemes are likely preferable compared to deterministic schemes supplemented by costly full-fledged error correction (that can

correct for both photonic bit flip errors). For instance, one can post select (a means of heralding) on cases where the photon has not been lost, say by detecting if the receiver remains in the auxiliary state $|r\rangle$ (in the above example) [170]. This allows one to detect photon loss errors but not amplitude nor phase errors in the transferred state. Accordingly, if one can suppress bit-flip (mixing) errors, e.g., $|H\rangle \leftrightarrow |V\rangle$, and ensure the phase stability of the channel (similar to the occupation number encoding), then this type of heralding for a pitch-and-catch scheme using the polarization encoding (or using another dual-rail code such as the time-bin encoding [78, 299]) is a promising, currently implementable, alternative to the occupation number encoding. One additional prerequisite for such a scheme is that both polarizations need to undergo nearly identical amplitude damping (photon loss) as elsewise, if $|r\rangle$ is measured and not occupied, the relative populations in $|e\rangle$ and $|g\rangle$ will be incorrect. Such a scheme is more applicable for the QST of half of a relatively easy to generate Bell pair, i.e., remote entanglement generation, which could then be used for quantum teleportation (see §1.5.3), as opposed to the QST of an arbitrary qubit whose preparation is likely more demanding so one would not want to lose its state.

Another notable difference between these encodings is in the control and stability of the transferred qubits phase, which is crucial for QST as discussed at the end of §4.3.1 and Sec. A3 (which shows how phase errors degrades the fidelity of the received state). As we have noted, in the occupation number encoding one needs to track and stabilize the relative phase between $|0\rangle$ and $|1\rangle$ using local oscillators and active phase stabilization, which is additional work but the methods to do so are well established (see the discussion and references at the end of §4.3.1). This can be contrasted with polarization, which is interferometrically stable so one does not need be as concerned with active phase stabilization (e.g., maintaining the length of the

transmission line) though one still needs well-defined clocks at both nodes to serve as phase references. Moreover, in the polarization encoding, one needs to be careful to not induce phase errors during transmission in the two split channels or by the separate unitary transformations discussed above (when applicable). Notably, many of the aforementioned optical to optical or telecom frequency conversion experiments (in Sec. A5) are polarization preserving and thus the polarization encoding can be made robust to phase errors even with a unitary transformation [103, 287, 288, 290].

The polarization basis is commonly used in QST experiments, especially in the optical regime, where standard devices that are useful for manipulating and maintaining polarization can be employed [34, 170, 276, 300]. Ref. 142 is a notable exception that explicitly demonstrated a reversible cavity-based mapping of a coherent superposition between an optical field and an atom using the occupation number encoding. In the microwave regime it is more common to use the occupation number encoding [35, 88, 89, 280, 282], due at least in part to a lack of microwave analogs of standard optical elements for manipulating polarization. This discrepancy in the suitability of different photonic encodings from heterogeneous nodes is one reason we focus on the occupation number encoding (as discussed in §4.3.4).

Alternative encodings. Some other possibilities are encoding in temporal modes (wave packets with orthogonal time-frequency shapes), in arrival time (as done by Refs. 78 and 299), in space (path taken), or in frequency. Using temporal modes is less viable in our scheme as their generation is typically achieved using parametric down-conversion as controlled by an applied pump field [301], which is quite different than the controlled emission (and absorption) processes we are concerned with. Additionally, the unitary transformation and distortion in the fiber may disrupt the temporal modes used so that they are no longer orthogonal leading to mixing errors as

mentioned for polarization. Such state mixing can likewise be a problem for time- or frequency-bin encoding if there is too much overlap between the basis states or if the spacing of these states changes (say due to propagation in the channel or the unitary) in their respective domain (time or frequency). The task of getting nodes to emit (and absorb) one of the specific basis states in a time or frequency bin encoding, dependent on the state of a material qubit, is quite system specific. In the frequency encoding transitions with different frequencies could be utilized. Different transitions could also be utilized to distinguish arrival-time encoded flying qubit basis states, or local gates could be used to perform SWAP-like operations, systematically rearranging the amplitudes of given material states. Similar to polarization, using these encodings, would typically require the use of two unitary transformations one for each of the basis states. This need not be the case when encoding in arrival time if a suitably long transformation is employed, provided one correspondingly changes the timing of the controls at the receiving node. Note that it can be highly nontrivial to map between different photonic encodings in an efficient quantum state preserving manner. For instance going between the occupation number and polarization encodings is nontrivial, whereas polarization and path can be converted between using a polarizing beamsplitter.

A.1.7 Heralded protocol comparison

Here we contrast deterministic QST and remote entanglement generation (REG) protocols against commonly employed heralded (non-pitch-and-catch) protocols with the same aims. In §4.3.5, we introduced the general setup of such heralded protocols and described the relevance of our work to them. Here we contrast (mostly qualitatively) the merits and downsides of deterministic versus heralded protocols.

For concreteness, we focus on comparing deterministic QST protocols with the occupation number encoding, like the one analyzed in this work, against heralded REG protocols using the polarization encoding such as that employed by Ref. 166 (see Fig. A.3 for a schematic comparison). Recall that QST and REG protocols can be mapped onto each other by transferring half of a local Bell-pair (QST $\rightarrow$ REG) and quantum teleportation (REG $\rightarrow$ QST). We will make this comparison across several categories: resource overhead, photon production and absorption, photon detection, and photon transmission, which are displayed in a list with each category being followed by a comparison of corresponding details relevant to deterministic and heralded protocols individually (labeled via D and H, respectively) or both.

– **Resource overhead.**

D: A single deterministic QST attempt has the glaring problem of being highly susceptible to photon loss errors. Especially when using the occupation number encoding, one cannot distinguish between a photon loss error $|1\rangle \rightarrow |0\rangle$ and the transmission of the ground state. Error correction, such as the ECZ protocols, can be used to address this; however, it requires an appreciable overhead, e.g., in the ability to perform local quantum operations at the nodes being connected (for ECZ) or for generating more exotic photonic states to encode the state of the qubit being transferred (see §4.3.4).

H: This additional overhead is avoided in heralded REG protocols, as although photon loss will lower the entanglement generation rate, it does not itself degrade the fidelity of a successfully heralded entangled state. Note that there is an intrinsic maximum heralding probability of 50% due to the photonic Bell-state measurement (as identical photonic qubit states do not lead to a remote entangled state).

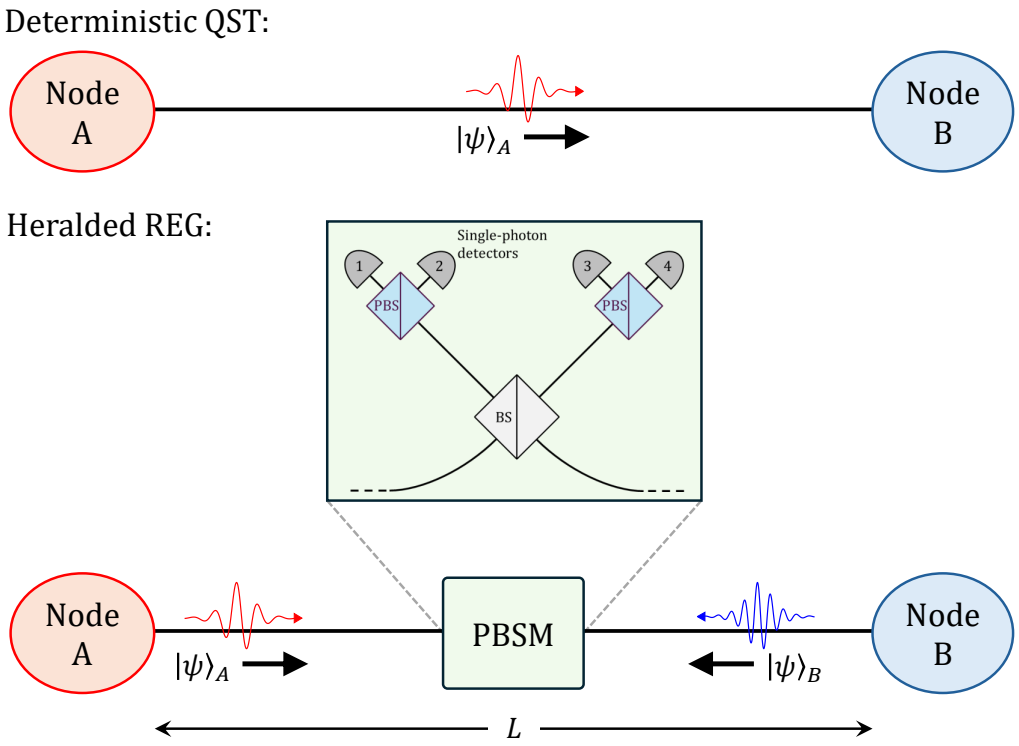

FIGURE A.3. Schematic overview of a deterministic QST protocol versus a heralded REG protocol linking two nodes, A and B, separated by a distance L in both cases. The unitary transformation is omitted in both diagrams for simplicity yet would generally be needed when interfacing heterogeneous nodes. See §4.2 for an overview of the deterministic case. In the prototypical heralded case, a photonic Bell-state measurement (PBSM) is employed, wherein two photons, one emitted from each node, are interfered at a balanced beam splitter (BS) and output photonic state is measured (in the photonic qubit encoding basis) using single-photon detectors. The coincident detection of orthogonal photonic qubit states heralds a remote entangled state of the qubits at nodes A and B. Further, note that entanglement swapping protocols, as necessary for quantum repeaters, leverage PBSMs in a related manner to propagate entanglement over larger distances (typically to well-separated counter-propagating photons that were initially entangled with the photons being measured) [302]. Here we illustrate the PBSM for a linear polarization photonic encoding, $\{|H\rangle, |V\rangle\}$, for which the BS outputs are each further split using a polarizing beam splitter (PBS) so that the photons' polarizations can be measured.

– **Photon production and absorption.**

Both: In each case there is loss due to emitter-cavity and cavity-channel couplings as quantified by the probabilities $\mathcal{P}_{\text{em}}$ and $\mathcal{P}_{\text{cav}}$, respectively, at each nodes. Because these probabilities are the same for emission and absorption at a given node, they will equally affect both deterministic QST (emission from one node followed by absorption at the other) and heralded REG (emission from both nodes), assuming each node has the same cooperativity in both cases.

H: One potential drawback of heralded REG schemes is that they require the challenging controlled production of a photon whose qubit state is in a particular entangled state with its emitter's qubit, e.g., in the polarization encoding this can be accomplished by simultaneously driving two polarization-dependent transitions (as discussed in the previous subsection), which often experience some cross-coupling. For instance, Ref. 166 were able to achieve ion-photon fidelities (relative to a target maximally entangled state with best-fit relative phase) of 92.9% and 95.5% for their nodes A and B, respectively.

– **Photon detection.**

Both: Controlling the presence of undesired photons due to spontaneous emission of the nodes or environmental noise (especially in microwave systems) is crucial.

D: If such an undesired photon is produced due to spontaneous emission from the upper level in the Raman process it will lead to some combination of amplitude damping, photon loss, and phase errors, i.e., β and Υ_1 errors in Eq. (4.43). Notably, such an error can potentially be corrected for using the ECZ protocols. Otherwise, if the error is caused by some other spurious photon causing the unwanted transition $|g_2\rangle \rightarrow |e_2\rangle$ for the component of the first

qubit in the zero-excitation subspace, then it cannot be corrected for the ECZ protocols. Fortunately, the receiving node is quite selective as a photodetector, in that only input photons with an appreciable overlap with the target shape $\Phi(t)$, as quantified in Eq. (4.30), will cause this ruinous $|g_2\rangle \rightarrow |e_2\rangle$ error, which would require the incident light to have a component with a specific timing, frequency, and wave packet shape. This is likewise the case for the dual-rail code (the heralded pitch-and-catch scheme) mentioned in §A.1.6, in which case spontaneous emission will likely lead to a (detectable) photon loss error as opposed to a qubit error.

H: In heralded schemes that leverage conventional single-photon detectors, such a spontaneously emitted photon is likely to lead to a detection event, yet it is distinguishable from the desired photon so it gives which-path information and thus ultimately lowers the remote state fidelity. Accordingly, one must compromise between entanglement quality and generation rate, i.e., using smaller coincidence windows to lessen the impact of spontaneous emission [166]. This is likewise an issue for any environmental photons at a frequency the photodetectors are sensitive too (this can be partially alleviated by filtered out light at frequencies away from the photon's central frequency). Moreover, the success of heralded schemes heavily relies on how good the single-photon detectors used are, which is not an issue faced by our deterministic QST scheme. Namely, detector imperfections, including their bare inefficiency, timing jitter, and dark counts, reduce the achievable rates and can contribute to apparent (false) coincidence events.

– **Photon transmission.**

Both: The role of fiber-cavity alignment (mode matching) is similar in both

cases and must be done at each node. Transmission-line loss typically occurs exponentially with propagation distance. Thus, as discussed in §4.2.5, the probability to propagate a distance x in a given transmission line with attenuation distance x_{tl} is $e^{-x/x_{\mathrm{tl}}}$ (referred to as P_3 in §4.2.5). Thus, when linking nodes over a set distance L, as in Fig. A.3, the probability of retaining a single photon over its full-propagation in a deterministic scheme is $e^{-L/x_{\mathrm{tl}}}$, which is equal to the probability of retaining both photons in a heralded scheme no matter where the heralded measurement is performed $0 < x_{\mathrm{meas}} < L$ (with 0 and L the respective positions of nodes 1 and 2) as $e^{-x_{\mathrm{meas}}/x_{\mathrm{tl}}} e^{-(L-x_{\mathrm{meas}})/x_{\mathrm{tl}}} = e^{-L/x_{\mathrm{tl}}}$ (ignoring additional fiber length needed for the photonic Bell-state measurement itself). (The situation is slightly different for heralded protocols implemented using the occupation number encoding. For instance, Ref. 169 and 168 only want one of two potential photons to be detected, as two-photon contributions lead to an error in their cases.)

H: Dispersion can be made less of a problem in heralded protocols if it is undergone symmetrically for each of the photons emitted by the separate nodes, as the particular shape of the interfered photons is not as important as them being nearly indistinguishable. This would require the Bell-state measurement to take place near the center of both locations via the transmission line.

Outlook. As more complex quantum networking nodes with multiple interacting qubits, each constituting a small quantum computer, become more commonplace, error corrected deterministic QST and REG using a photon-number encoding become more viable as an alternative to analogous heralded methods. Moreover, we note that if one can controllably produce polarization (or time- or frequency-bin) encoded photonic qubits in a given heralded REG experiment (which is requisite for producing

indistinguishable photons and obtaining high-fidelity remote entangled states), they should be able to controllably produce a single-photon (in a particular well-chosen mode) for occupation number encoding (likely with higher success rate). Therefore, we recommend the further consideration of deterministic quantum state transfer using the photon number encoding in such setups and more generally as a potential means of progressing distributed and hybrid quantum computing technologies.

A.2 Determining the wave packet

Here we consider how to design the laser pulse $G_1(t)$ to produce a specific amplitude $\alpha_1(t)$ or $\beta_1(t)$. Without the unitary transformation, the wave packet emitted by system 1 is $\Psi(t) = \sqrt{\gamma_1}\beta_1(t)$ [see Eq. (3.51)], whereas with the transformation the wave packet is $\Psi(t) = \sqrt{\gamma_1\xi}e^{i\omega_0(T-t)}\beta_1(\xi(T-t))$, assuming l is large enough so that the entire wave packet is transformed. We start by discussing the Hamiltonians for the nodes and the corresponding amplitude EOMs as well as their limitations in §A.2.1. We then show how G_1 and the corresponding β_1 can be determined from α_1 in a 'nice' case where we select certain laser frequency and phase in §A.2.2. Next, in §A.2.3 we analyze the impact of spontaneous emission during the Raman processes employed at both nodes, ultimately giving credence to our post hoc treatment of it [strategy 1)]. In §A.2.4 we provide a formal solution to β_1 that makes its relation to the driving pulse G_1 intuitive and lets us analyze frequency errors. Ultimately, in §A.2.5 we show that even with the unitary transformation we cannot produce a wave packet $\Psi(t)$ with arbitrary shape, though there is a large class of wave packets we can produce that are useful for QST.

A.2.1 Node Hamiltonians

In Chs. III and IV we made several choices to put the Hamiltonians describing the dynamics of the atom in a cavity type nodes into the simple JC form of Eq. (3.43). Doing so allowed us to emphasize the crucial aspects of our QST scheme. However, we can obtain more control of the photon wave packet, namely its phase, if we do not fix the laser frequency and phase in the previously mandated way. Hence, here we consider a more general node Hamiltonian in which we have not yet selected the phase and frequency of the lasers driving each system, though we have already adiabatically eliminated the excited state and gone into an appropriate rotating frame. Then H_j is given by Eq. (3.43), which in the single- (or zero-) excitation subspace simplifies slightly to

$$H_j = d_j a_j^\dagger a_j + \delta\omega_j(t)|e_j\rangle\langle e_j| - iG_j(t)\left(e^{i\phi_j(t)}a_j|e_j\rangle\langle g_j| - \text{Hc}\right), \tag{A.21}$$

with $d_j \equiv g_j^2/\Delta_j - \delta_j$, $\delta\omega_j(t) := \Omega_j^2(t)/4\Delta_j$, and $G_j(t) := g_j\Omega_j(t)/2\Delta_j$, where $\delta_j = \omega_{\rightsquigarrow j} - \omega_{cj}$ is the Raman detuning between the jth photon and cavity frequency and the other parameters are defined in §3.5.1. We see that there is still a Jaynes–Cummings like atom-cavity coupling term, which relative to the generic node JC Hamiltonian of Eq. (A.14) has a and $\sigma^- = |g\rangle\langle e|$ as cavity and atomic lowering operators, respectively, and $g(t) = iG(t)e^{-i\phi(t)}$; however, there are additional energy shifts. With these system Hamiltonians as well as Eqs. (4.3) and (4.5)[8] for the state

$$|\psi(t)\rangle = \alpha_1(t)e^{i\phi_1(t)}|eg\rangle|00\rangle + \alpha_2(t)e^{i\phi_2(t)}|ge\rangle|00\rangle + \beta_1(t)|gg\rangle|10\rangle + \beta_2(t)|gg\rangle|01\rangle, \tag{A.22}$$

[8]Note that in the same frame as Eq. (A.21), H_{tl} is given by Eq. (4.5) precisely as written.

now with the laser phases explicitly factored out, we obtain the following single-excitation dynamics:

$$\dot{\alpha}_j = -G_j\beta_j - i\left(\dot{\phi}_j + \delta\omega_j\right)\alpha_j \qquad (j = 1, 2), \tag{A.23a}$$

$$\dot{\beta}_1 = G_1\alpha_1 - \left(\frac{\gamma_1}{2} + id_1\right)\beta_1, \tag{A.23b}$$

$$\dot{\beta}_2 = G_2\alpha_2 - \left(\frac{\gamma_2}{2} + id_2\right)\beta_2 - \sqrt{\gamma_2}e^{i\zeta t}\Psi(t). \tag{A.23c}$$

Note that α_j are slowly varying complex amplitude envelopes as we factored out the laser phases $e^{i\phi_j(t)}$. We see that our simpler dynamics given in Eq. (4.12) result from this if we select 'nice' laser phases such that $\dot{\phi}_j + \delta\omega_j \equiv 0$ and laser frequencies such that $d_j = 0$.

Alternatively, we can obtain these simpler dynamics of Eq. (4.12) by first going into a rotating frame via the unitary transformation $U = U_1U_2$ with

$$U_j = \exp\left\{i\left[d_j t a_j^\dagger a_j + \int dt\ \delta\omega_j(t)\,|e_j\rangle\langle e_j|\right]\right\} \tag{A.24}$$

for $j = 1, 2$. In this frame the system Hamiltonians of Eq. (A.21) become

$$H_j = -iG_j(t)\left(e^{i\theta_j(t)}a_j\,|e_j\rangle\langle g_j| - \mathrm{Hc}\right) \tag{A.25}$$

with $\theta_j(t) := \phi_j(t) + \int dt\ \delta\omega_j(t) - d_j t$. Note that H_{tl} is also modified in this new frame, in particular $\zeta \to \zeta' \equiv \zeta + d_2 - d_1$ in Eq. (4.5). Now by selecting the 'nice' laser frequencies and phases for each node, such that $\theta_j \equiv 0$,[9] we obtain the effective node Hamiltonians of Eq. (3.43). Note that as $d_j = 0$ in this case, H_{tl} is ultimately

[9]Technically we just have that θ_j are constants, as with $\dot{\phi}_j + \delta\omega_j \equiv 0$ and $d_j = 0$ we have $\theta_j(t) = \phi_j - \int dt\ \dot{\phi}_j =$ constant. However, we can fix their value by redefining the phase of $|e_j\rangle$ or equivalently fixing an appropriate lower bound of the improper integrals.

unchanged in this frame, with $\zeta' = \zeta$, so we still can still report Eq. (4.5) as the transmission line interaction Hamiltonian in this frame (considering the specification of footnote 8). Note we must also account for the modification to the state $|\psi\rangle$ in this new frame as

$$|\psi'\rangle = U|\psi\rangle = \alpha_1 e^{i\left(\phi_1 + \int dt\ \delta\omega_1\right)}|eg\rangle|00\rangle + \alpha_2 e^{i\left(\phi_2 + \int dt\ \delta\omega_2\right)}|ge\rangle|00\rangle$$
$$+ \beta_1 e^{id_1 t}|gg\rangle|10\rangle + \beta_2 e^{id_2 t}|gg\rangle|01\rangle \tag{A.26}$$

such that for the selected laser parameters the additional phases cancel out and we simply obtain Eq. (4.11).

We will work with this simpler case in the following two subsections as the extra freedom in possible amplitudes we could have by making other choices is not necessary for conveying the points we want to make. We will return to this more general case without specifying a specific laser frequency or phase in §A.2.5 where we consider the class of β_1 and hence wave packets that can possibly be produced. This includes analysis of the possible dynamical phases of β_1, which have been constant thus far as we have assumed the 'nice' laser frequency and phase are used. We note that several other groups have conducted similar analysis of the controlled generation of single-photon wave packet shapes from quantum emitters in the context of cavity QED [145, 150, 155, 303]. Also see Ref. 128 for analysis showing how dynamically tuning the system controls [$G_j(t)$ and $\phi_j(t)$ in our work] can be used to compensate for errors caused by distortion of photons in the quantum channel [related to strategy 5) in §4.2.5] as well as non-Markovian effects induced by quickly modulating the coupling of a quantum emitter to a corresponding photonic mode.

To this end, we note that one needs to be careful when considering wave packets with more complicated phases, especially if they are fast varying, as they may be incompatible with the Markov approximation used to obtain the tractable amplitude EOMs considered here, Eq. (A.23). This Markov approximation is standard in input-output theory, as mentioned in §A.1.2, and effectively assumes that the produced photon wave packet only experiences small variations about a central carrier frequency. However, this will not be the case when using large frequency bandwidth photons, which can be useful in achieving faster rates [additionally, in our protocol they are more robust to frequency errors, see Eq. (A.43)], as then corrections beyond the Markov approximation are needed to obtain analogous EOMs that take into account non-trivial memory kernels and can be used to engineer improved system controls [128]. A similar photon bandwidth dependent tradeoff exists between protocol rates and material dispersion. Namely, larger frequency bandwidth photons are more susceptible to dispersion effects while small bandwidth photons are temporally long so the drives must be comparably slow, ultimately leading to a decreased rate of QST or entanglement generation.

A.2.2 Wave packet for a given α_1

In Ch. III we found that in the special case mentioned above, where we select the laser phases and frequencies such that $\dot{\phi}_j + \delta\omega_j \equiv 0$ and $d_j = 0$, by specifying α_1 (which can be taken to be real in this case without loss of generality; see §4.2.4) the corresponding laser pulse (if it exists) is given by Eq. (3.61):

$$G_1(t) = \frac{-\dot{\alpha}_1 e^{\gamma_1 t/2}}{\sqrt{e^{\gamma_1 t_p}\beta_1^2(t_p) - 2\int_{t_p}^{t} dt' e^{\gamma_1 t'}\dot{\alpha}_1(t')\alpha_1(t')}}. \tag{A.27}$$

Note that this formula has been derived in the large atomic cooperativity limit. Similar formulae that explicitly account for cooperativity can also be derived, though they often rely on different approximations [150, 155]. Importantly, in §A.2.3 we find that the losses due to not accounting for the presence of spontaneous decay in the drives G_j themselves are minimal and so the above formula can still be used for nodes with moderate cooperativities. The overall minus sign here encodes that of Eq. (A.23a) starting from the initial condition at $t = t_p$. However, the amplitudes EOMs are preserved (remain true) if precisely two of the functions $\{G_j, \alpha_j, \beta_j\}$ are negated for both $j = 1, 2$. Here t_p is some early time by which the first atomic state is *prepared* in the desired superposition state, $c_g|g_1\rangle + c_e|e_1\rangle$, so $\beta_1(t_p) = \sqrt{1 - \alpha_1^2(t_p)}$ should be zero. The corresponding wave packet is then determined by $\beta_1(t) = -\dot{\alpha}_1(t)/G_1(t)$ as given by Eq. (3.46a). From Eq. (A.27) we see that only some amplitude functions $\alpha_1(t)$ have a corresponding pulse $G_1(t)$. Specifically, we have the consistency condition that G_1 is real though it need not be positive (this is by construction as the corresponding phase has already been taken out and used to cancel the ac Stark shift of the qubit) so that the argument of the square root in Eq. (A.27) must be positive and hence we have the condition on α_1:

$$1 - \alpha_1^2(t_p) - 2\int_{t_p}^{t} dt' e^{\gamma_1(t'-t_p)}\dot{\alpha}_1(t')\alpha_1(t') \geq 0. \tag{A.28}$$

As an intuitive example, we cannot sustain Rabi-like oscillations $\alpha_1(t) = \cos(\Omega t)$ unless the cavity does not let any excitations decay out of it, i.e., if $\gamma_1 = 0$. Note, however, that any $\alpha_1 \geq 0$ that monotonically decreases, as is appropriate for QST, can be produced (at least in principle, in practice this is limited due to a finite emitter cooperativity). Qualitatively, this restriction dictates that we cannot make $|\alpha_1|$ increase too much relative to the natural transmission rate out of the first cavity.

For the logistic α_1 of Eq. (4.38), we can use Eq. (A.27) to solve for the corresponding pulse G_1, and then find the first cavity amplitude

$$\beta_1(t) = z\sqrt{\frac{1}{(1+z^2)^2} + (1-r)\left(\frac{1}{1+z^2} - r\Phi_L(-z^2, 1, 1+r)\right)} \tag{A.29}$$

with $z(t) := e^{kt}$ and $r \equiv \gamma_1/2k$. Here Φ_L is the analytically continued Lerch transcendent (for general parameter values a special function is needed to express the exact solution). For $r = 1/2$ (which aligns with the case used for most plots within the main text with $k = \gamma_1 = 2$) we have

$$\beta_1(t)|_{r=1/2} = \sqrt{\frac{z^2-1}{2(z^2+1)} + \frac{\arctan(z)}{2z}} = \frac{1}{2}e^{-kt/2}\sqrt{2\arctan(e^{kt}) + \operatorname{sech}(kt)\tanh(kt)}, \tag{A.30}$$

which is not symmetric in time t, as can be seen in Fig. 3.4 (a), whereas for $r = 1$ (so $k = \gamma_1/2$) we have

$$\beta_1(t)|_{r=1} = \frac{z}{1+z^2} = \frac{\operatorname{sech}(kt)}{2}, \tag{A.31}$$

which is symmetric in time. In the special limit $r \to 0$ ($k \to \infty$ with $\gamma_1 > 0$ constant) we find that

$$\alpha_1(t) \xrightarrow{r\to 0} \Theta(-t), \tag{A.32}$$

with $\Theta(t)$ the Heaviside step function. Meanwhile the leading-order asymptotics for β_1 and G_1 are [304]

$$\beta_1(t) \overset{r\ll 1}{\approx} \begin{cases} \sqrt{1 - \frac{1}{\left(1+e^{2kt}\right)^2}}, & t < 0 \\ \sqrt{e^{-\gamma_1 t} - \frac{1}{\left(1+e^{2kt}\right)^2}}, & t \geq 0 \end{cases} \xrightarrow{r\to 0} \Theta(t)e^{-\gamma_1 t/2} \tag{A.33}$$

and

$$G_1(t) \overset{r\ll 1}{\approx} \frac{k\,\mathrm{sech}(kt)}{\sqrt{2+e^{2kt}}} \xrightarrow{r\to 0} \frac{\pi}{2}\delta(t). \tag{A.34}$$

The normalization of the delta function laser pulse, $\lim_{r\to 0} G_1$, comes from computing the area of $G_1(t)\forall t$ for small r, yielding $\pi/2 + \mathcal{O}(r)$.[10]

A.2.3 Impact of spontaneous decay

Here we further justify why, under the limits we consider in this work (of large detuning Δ_j and cooperativity C_j for each node), the impact of spontaneous decay of the material qubit, with rate Γ_j, can be set aside [see strategy 1)]. We start by explicitly incorporating spontaneous decay into our model effective Hamiltonian and computing the resulting dynamics in the single-excitation subspace. We then show how our dynamics are retrieved in the aforementioned limits. Next, we numerically investigate the impact of spontaneous decay and find that for moderate cooperativities and large (yet achievable) detunings, we obtain a survival probability for emission (or absorption) of just under $\mathcal{P}_{\text{em-max}} = C_{\text{em}}/(1+C_{\text{em}})$ with $C_{\text{em}} \to C_j = 4g_j^2/(\gamma_j\Gamma_j)$ for node j, validating it as a nearly achievable C_{em}-dependent maximum. Moreover, we show that, without even modifying our drives G_j, the emitted wave packet shape does not substantially change for nonzero Γ_j (again, under the above limits) as compared to the ideal case with no spontaneous emission. In particular, once photon loss has

[10]Note that the given $r \ll 0$ ($k \gg \gamma_1$) asymptotics of the functions β_1 and G_1 converge pointwise, whereas the given $r \to 0$ limits do not converge at $t = 0$, where the product kt is undefined. This can lead to confusion when trying to verify that these limits are consistent with Eqs. (4.12a-b) due to indeterminate limiting values at $t = 0$. For instance, even though G_1 approaches an impulse response with $\pi/2$ normalization as $k \to \infty$, and $\alpha_1(t = 0) = 1/2\forall k$, consideration must be taken when considering their product $G = G_1\alpha_1$ as $\lim_{k\to\infty} G(t) = \delta(t) \neq \lim_{k\to\infty} G_1(t) \lim_{k\to\infty} \alpha_1(t) = \frac{\pi}{2}\delta(t)\Theta(-t) = \frac{\pi}{4}\delta(t)$ because more carefully $G_1(t) \xrightarrow{r\to 0} \frac{\pi}{2}\delta(t + \mathcal{O}(r))$. Importantly, there are only seeming discrepancies in the unphysical limit where $k \to \infty$. For large but finite values of k, the functions α_1, β_1, and G_1 are smoothed out and we avoid any pathologies in dealing with $\Theta(t)$ and $\delta(t)$.

been accounted for via $\mathcal{P}_{\text{em}}$, for moderate C_j one can obtain a near unity state overlap (fidelity) of the wave packet emitted in the presence of spontaneous emission with the target wave packet. As an example, for the achievable value of $C_1 = 5$, these overlaps are around 99% across each of several instances we consider below (see Fig. A.6). Thus, the ensuing analysis serves as a partial validation of the post hoc treatment of strategy 1) (see §4.2.5 and §A.3.1) and further, it demonstrates why, in the rest of our analysis, we do not need to consider errors caused by the drives G_j not being tuned for specific decay rates Γ_j (such errors do occur yet they are significantly less relevant than $\mathcal{P}_{\text{em}}$). Our numerical treatment is meant to be indicative rather than fully comprehensive; see Refs. 150, 154, 155 for some related analysis, e.g., Ref. 155 are able to explicitly show the existence of the aforementioned upper bound $\mathcal{P}_{\text{em-max}}$ for emission and/or absorption, albeit in slightly different parameter regimes.

When employing the quantum jump (stochastic wavefunction) method we use in our work, the effective system dynamics are governed by a non-Hermitian Hamiltonian, H_{eff} of Eq. (4.3) in our case. In this context, the role of spontaneous emission from the upper level in the Raman process can be accounted for using a complex detuning parameter $\Delta_j \to \Delta_j + i\Gamma_j/2$ in H_{eff} [1]. Here Γ_j is the spontaneous decay rate of the upper level $|r_j\rangle$ (elsewhere in this appendix it is referred to as Γ_{sd} for a generic node). As the transmission line Hamiltonian does not depend on Δ_j, we need only analyze the impact of spontaneous decay on the system Hamiltonians H_j and the resulting amplitudes EOMs. Thus, we apply the map $\Delta_j \to \Delta_j + i\Gamma_j/2$ to Eq. (A.21) and as Δ_j only appears in the denominator of part of d_j, $\delta\omega_j$, and G_j we consider the map (for each $j = 1, 2$)

$$\frac{1}{\Delta} \to \frac{1}{\Delta + i\Gamma/2} = \frac{1}{\Delta}\frac{1}{1 + i\Gamma_r} \approx \frac{1}{\Delta}\left(1 - i\Gamma_r + \mathcal{O}(\Gamma_r^2)\right), \tag{A.35}$$

where we have defined the rescaled decay rate $\Gamma_r = \Gamma/(2\Delta)$. Therefore, in the system Hamiltonians, we have the replacements: $d \to \frac{g^2}{\Delta(1+i\Gamma_r)} - \delta$, $\delta\omega \to \frac{\delta\omega}{1+i\Gamma_r}$, and $G \to \frac{G}{1+i\Gamma_r}$ for each j. Thus, the ensuing amplitude EOMs, previously Eqs. (A.23a-c), likewise undergo this map and become

$$\dot{\alpha}_j = \frac{-G_j}{1+i\Gamma_{r,j}}\beta_j - i\left(\dot{\phi}_j + \frac{\delta\omega_j}{1+i\Gamma_{r,j}}\right)\alpha_j \qquad (j=1,2), \tag{A.36a}$$

$$\dot{\beta}_1 = \frac{G_1}{1+i\Gamma_{r,1}}\alpha_1 - \left[\frac{\gamma_1}{2} + i\left(\frac{g_1^2}{\Delta_1(1+i\Gamma_{r,1})} - \delta_1\right)\right]\beta_1, \tag{A.36b}$$

$$\dot{\beta}_2 = \frac{G_2}{1+i\Gamma_{r,2}}\alpha_2 - \left[\frac{\gamma_2}{2} + i\left(\frac{g_2^2}{\Delta_2(1+i\Gamma_{r,2})} - \delta_2\right)\right]\beta_2 - \sqrt{\gamma_2}e^{i\zeta t}\Psi(t), \tag{A.36c}$$

where the G_j and $\delta\omega_j$ shown here are the original functions with the Γ_j dependence already factored out.

To make the resulting EOMs more tractable (and ultimately more useful), we will again select the 'nice' laser frequency and phase satisfying $\delta = g^2/\Delta$ and $\dot{\phi} = -\delta\omega$ for each node. Recalling $\Gamma_{r,j} = \Gamma_j/(2\Delta_j)$, noting that $\delta\omega_j = \Delta_j G_j^2/g_j^2$, defining the cooperativity $C_j \equiv 4g_j^2/(\gamma_j\Gamma_j)$, and doing some algebra we find

$$\dot{\alpha}_j = \frac{-G_j}{1+i\Gamma_{r,j}}\beta_j - \frac{2G_j^2}{\gamma_j C_j(1+i\Gamma_{r,j})}\alpha_j \qquad (j=1,2), \tag{A.37a}$$

$$\dot{\beta}_1 = \frac{G_1}{1+i\Gamma_{r,1}}\alpha_1 - \frac{\gamma_1}{2}\left(1 + \frac{\Gamma_{r,1}^2 C_1}{1+i\Gamma_{r,1}}\right)\beta_1, \tag{A.37b}$$

$$\dot{\beta}_2 = \frac{G_2}{1+i\Gamma_{r,2}}\alpha_2 - \frac{\gamma_2}{2}\left(1 + \frac{\Gamma_{r,2}^2 C_2}{1+i\Gamma_{r,2}}\right)\beta_2 - \sqrt{\gamma_2}e^{i\zeta t}\Psi(t). \tag{A.37c}$$

Note that if we take the large cooperativity $C_j \to \infty$ and large detuning $|\Delta_j| \to \infty$ limits (namely, $\Gamma_{r,j} \to 0$ here)[11] we obtain the original EOMs Eqs. (4.12a-d). If we only take the large detuning limit (as is consistent with the adiabatic elimination of

[11]For these simultaneous limits to be defined, specifically in the $\dot{\beta}_j$ equations, we consider the single $\Gamma_j \to 0$ limit with the other parameters constant such that $\Gamma_{r,j}^2 C_j \to 0$.

the upper level already performed), the β_j EOMs are the same as in the main text, yet the atomic excitation amplitude EOMs acquire a new term:

$$\dot{\alpha}_j = -G_j\beta_j - \frac{\tilde{\Gamma}_j}{2}\alpha_j \qquad (j = 1, 2), \tag{A.38}$$

with $\tilde{\Gamma}_j(t) := \frac{4G_j^2(t)}{\gamma_j C_j} = \left(\frac{\Omega_j(t)}{2\Delta_j}\right)^2 \Gamma_j$, which is the same as equation (41) of Ref. 154.

Now we want to solve these amplitude EOMs and determine how well an excitation is transferred from the first emitter to its cavity at node 1 and then from cavity 2 to the emitter at node 2. For concreteness, we will focus on emission from node 1 as absorption at node 2 is the effective time-reversed process so the impact of spontaneous decay can be gleaned from either. In particular, we aim to analyze the impact of spontaneous decay (nonzero Γ_j) on the produced wave packet $\Psi(t) = \sqrt{\gamma_1}\beta_1(t)$, i.e., how Ψ's normalization and shape compare to the target wave packet $\Psi_0(t) := \Psi(t)|_{\Gamma_1 \to 0}$. The same kinds of degradations will likewise occur during and affect absorption (with potentially different parameters). As even the node 1 EOMs for α_1 and β_1, which are uncoupled from node 2, are analytically quite unwieldy, we will solve them numerically focusing on the case considered in §4.3.3 with a target logistically decreasing α_1, see Eq. (4.38). The corresponding applied drive G_1 is given by Eq. (A.27) such that in the ideal, target case (with $\Gamma_1 \to 0$) the cavity amplitude is given by Eq. (A.29), which here we deem $\beta_1^{(\text{target})}(t)$. Based on this target case, we will work in terms of the dimensionless time $\tau = kt$ (e.g., $1/k$ is the natural unit of time), often making a change of variables to $z = e^\tau$ for ease of our numerics.

Thus, our current task is to analyze the wave packets $\Psi(\tau) = \sqrt{2r}\beta_1(\tau)$ produced when applying the unaltered $G_1(\tau)$ (calculated based on the idealized target case) in the presence of spontaneous decay, i.e., with nonzero Γ_1 and hence finite C_1, and compare them to the target wave packet $\Psi_0(\tau) = \sqrt{2r}\beta_1^{(\text{target})}(\tau)$. Note that here

$r = \gamma_1/2k$, as in the previous subsection, and the prefactor of β_1 has changed to maintain wave packet normalization after the change of variable: $\int_{-\infty}^{\infty} d\tau |\Psi_0(\tau)|^2 = 1$. We make this comparison across various cooperativity values, C_1, and under two spontaneous decay models for node $j = 1$:

i) in the large detuning $\Gamma_{r,1} \to 0$ limit given in Eq. (A.38) for α_1 and Eq. (3.46b) for β_1 and

ii) for finite Δ_1 using Eq. (A.37), where as a reasonable instance we will consider cases with $\Gamma_1 = \gamma_1$ (as is often nearly the case, see Table A.1) and take the modest $\Delta_1 = 5\max\{g_1, 2\gamma_1\}$, which will typically be on the order of $\sim$100 MHz for optical nodes (we do not want it so large that we cannot distinguish this case from model i), such that $1/\Gamma_{r,1} = 5\max\{\sqrt{C_1}, 4\}$.

We denote the respective wave packets produced under these the models as $\sqrt{2r}\beta_1^{(m)}(\tau)$ with $m =$ i, ii.

In Fig. A.4 we plot $\Psi(\tau)$ for the cavity amplitudes $\beta_1^{(\text{target})}(\tau)$, $\beta_1^{(\text{i})}(\tau)$, and $\beta_1^{(\text{ii})}(\tau)$ (broken up into real and imaginary components) for several C_1 values and two disparate r values. Under both models, for large C_1, the wave packets produced closely match the target shape. We can quantify the extent to which the wave packets match by considering two key parameters for each model: the probability of an excitation being transferred from the emitter to the desired cavity mode

$$\mathcal{P}_{\text{em}} = \int_{\tau_0}^{\tau_f} d\tau \big|\Psi(\tau)\big|^2 \leftrightarrow 2r \int_{\tau_0}^{\tau_f} d\tau \big|\beta_1^{(m)}(\tau)\big|^2 \equiv \eta_m^2, \tag{A.39}$$

where η_m is the subnormalization of the wave packet, and the overlap (fidelity) of the renormalized wave packet with the target wave packet

$$\mathfrak{o}_m \equiv \left| 2r \int_{\tau_0}^{\tau_f} d\tau \left(\frac{1}{\eta_m} \beta_1^{(m)}(\tau) \right)^* \beta_1^{(\text{target})}(\tau) \right|^2 . \tag{A.40}$$

By using these two parameters we separate the impacts of spontaneous decay on photon loss ($\mathcal{P}_{\text{em}}$) and photon shape ($\mathfrak{o}_m$). The integrals bounds should extend over all times in principle, yet in practice the β_1 functions we consider here decay rapidly away from $\tau = 0$ so the bounds we use here of $\tau_0 = -15$ and $\tau_f = 15$ more than suffice for our purposes.[12]

In Fig. A.5 we plot $\mathcal{P}_{\text{em}} = \eta_m^2$ (in several forms) as a function of C_1 for several r values. We find that $\mathcal{P}_{\text{em}}$ approaches 1 as C_1 tends to infinity for each r and this approach happens faster for larger r, which correspond to a slower driving with small k relative to γ_1. Accordingly, there is a trade off between photon generation rate (where one wants want large k) and successful emission. Notably, η_{i}^2 nearly saturates the $\mathcal{P}_{\text{em-max}} = C_1/(1 + C_1)$ bound for relatively large $r \gtrsim 5$, as is consistent with Refs. 150, 154, 155 and our strategy 1). This near saturation also happens in model ii for suitably large detunings. Beyond subnormalization, the shape of the wave packets produced for finite C_1 will differ from target shape as is quantified by the overlap $\mathfrak{o}_m$. If this shape difference is considerable, then additional considerations would be required in our analysis to quantify this spontaneous decay induced shape mismatch as it would implicitly degrade the wave packet overlap in P_{success}. Accordingly, in Fig. A.6 (a) we

[12]Note that over this interval the target wave packets are slightly subnormalized. Namely, for the considered r values of $\{1/4, 1/2, 1, 2, 5\}$ we find $1 - \int_{\tau_0}^{\tau_f} d\tau |\Psi_0(\tau)|^2$ of $\{4.6 \cdot 10^{-4}, 2.3 \cdot 10^{-7}, 1.9 \cdot 10^{-3}, 2.7 \cdot 10^{-7}, 6.5 \cdot 10^{-6}\}$, respectively. For comparisons between r values, we account for these slight subnormalizations by dividing the corresponding β_1's by $\left[\int_{\tau_0}^{\tau_f} d\tau |\Psi_0(\tau)|^2 \right]^{1/2}$. Note these deviations are small enough that this step could suitably be omitted as each target wave packet is essentially normalized.

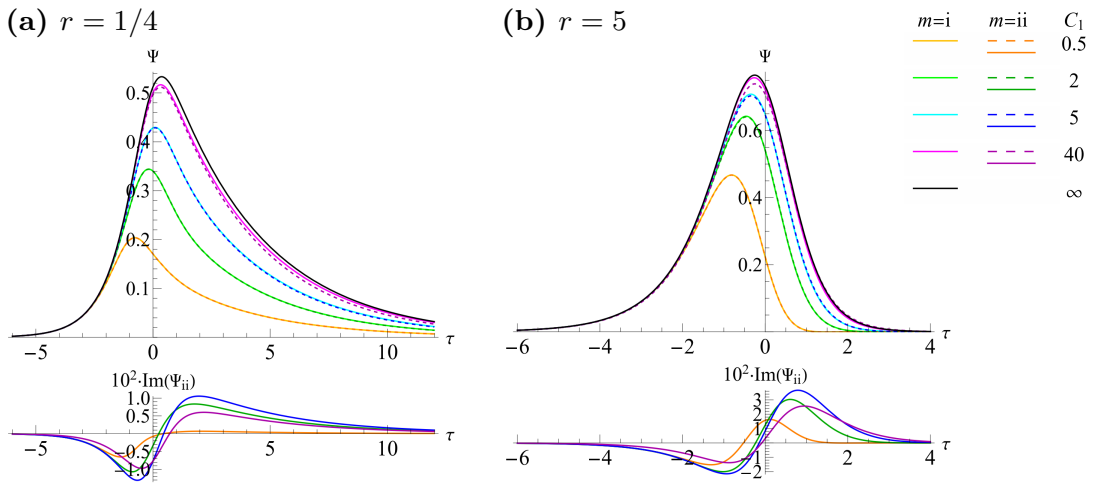

FIGURE A.4. Plots of Ψ as a function of τ for each model $m =$ i, ii, with several C_1 values including the ideal $C_1 \to \infty$ case, and for two disparate r values. In the model ii, a nontrivial phase is acquired so in the upper panel we are actually just plotting the real component (dashed dark lines) with the small imaginary component (solid dark lines) being plotted in the lower panel (note the scaling). This does not affect model i (solid light lines), wherein Ψ is real. (a) Faster driving case with $r = 1/4$, which closely resembles Eq. (A.33). (b) Slower driving case with $r = 5$, which under model ii acquires a larger relative imaginary component as compared to the small r case in (a) (which encourages the use of a larger detuning). For each r and under each model, the wave packets quickly approach the target shape as C_1 is increased as quantified in Figs. A.5 and A.6.

plot $\mathfrak{o}_\mathrm{i}$ versus C_1 for the extremal values of r we consider and in Fig. A.6 (b) we show the overlap deviations between the models i and ii. We find that the overlaps quickly approach 1 as C_1 increases so the shape is largely left unchanged. Moreover, if nodes 1 and 2 have similar cooperativities, the impact of this shape mismatch will be further suppressed. For instance, in model i, simulating emission and absorption between nodes with identical cooperativities C (and assuming the unitary transformation is implemented perfectly with no other errors) one finds that $|\alpha_2(t_f)| = \mathcal{P}_\mathrm{em}$ exactly, so the subnormalization fully accounts for excitation loss in the whole process. [We have performed some similar analysis of η_m and $\mathfrak{o}_m$ for other drives (including a

smoothed out square wave, a sech shape, and a sech shape with an additional small constant drive for $t > 0$) and the corresponding wave packets, finding the same general behaviors as shown for this example.] Thus, we do not need to modify the drives themselves as wave packet shape mismatch errors due to spontaneous decay are essentially negligible (for large Δ_j and moderate C_j). Accordingly, the impact of spontaneous decay can justifiably be treated post hoc via strategy 1) for large detuning and $\mathcal{P}_{\text{em}}$ nearly saturates its maximum value for relatively slow drives G_j.

A.2.4 Formal β_1 and frequency errors

Note that Eq. (3.46b) has the formal solution

$$\beta_1(t) = \int_{t_p}^{t} dt' e^{-\gamma_1(t-t')/2} G_1(t') \alpha_1(t'), \tag{A.41}$$

which is for the case where one selects the 'nice' laser frequency and phases. Note that, as above, t_p is a preparation time at which any excitation is solely in atom 1, it can mathematically be taken to be $-\infty$; doing so and defining $H(t) := \Theta(t) e^{-\gamma_1 t/2}$ and $G(t) := G_1(t)\alpha_1(t)$ it follows that

$$\beta_1(t) = \int_{-\infty}^{\infty} dt' G(t') H(t-t') = (G * H)(t). \tag{A.42}$$

We thus see that G_1 and α_1, through their product G, act to "smear out" H via the convolution of Eq. (A.42). This guides the intuition that β_1 should be narrowest for[13] $G(t) = \delta(t)$ such that $\beta_1(t) = H(t) = \Theta(t) e^{-\gamma_1 t/2}$, which is exactly the β_1 we found in the $k \to \infty$ limit above.

[13]The unit weight follows from G preserving the normalization of the wave packet with respect to the convolved function H. To be clear, we are not claiming that any $G(t)$ with this property can be produced; only certain α_1 and hence G are possible.

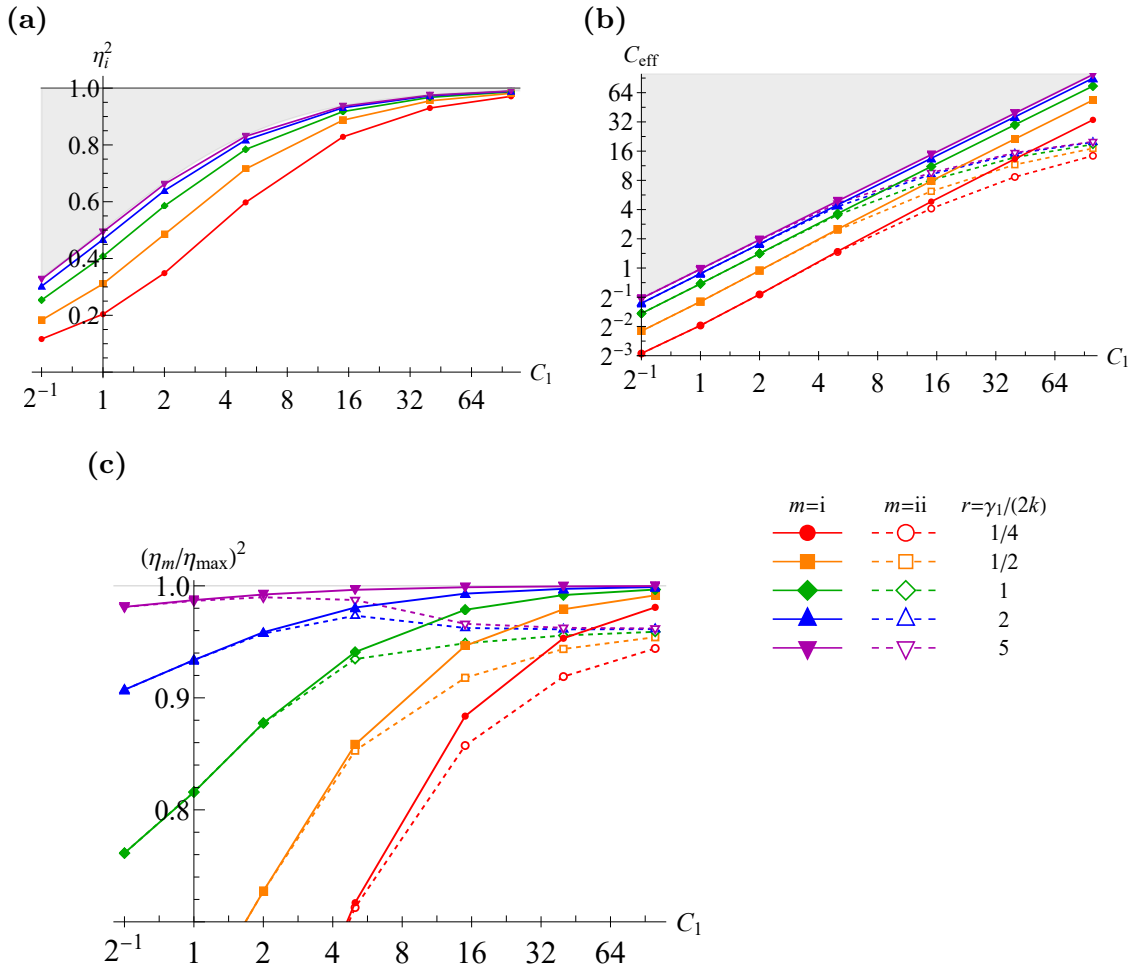

FIGURE A.5. Plots quantifying wave packet subnormalization η_m due to photon loss caused by spontaneous decay during the Raman process for various C_1 and r values under each model m (see the legend). (a) Plot of $\mathcal{P}_{\text{em}} = \eta_{\text{i}}^2$ versus C_1 for several r values. The model ii curves are omitted in this case to reduce visual clutter yet are included in (b) and (c). (b) Plot of the effective cooperativity C_{eff}, which satisfies $\mathcal{P}_{\text{em}} = C_{\text{eff}}/(1 + C_{\text{eff}})$, versus C_1, which shows how fast driving lowers the achieved cooperativity relative to the ideal value. (c) The relative deviations of each η_m^2 from $\eta_{\max}^2 \equiv \mathcal{P}_{\text{em-max}} = C_1/(1 + C_1)$ as a function of C_1. For large r these curves approach the $C_1/(1 + C_1)$ bound, which is indicated via the light gray shading in (a) and (b) and the 1 line in (c). In (b) and (c) we see that under model ii we end up doing significantly worse than model i for large C_1 as the values of C_{eff} and $(\eta_m/\eta_{\max})^2$ seem to converge to constant sub optimal values for each r. Note this does occur and is a result of how we choose the detuning Δ_1. This behavior is ameliorated if one chooses even larger detunings, say scaling as $\sim C_1\gamma_1$ for large C_1.

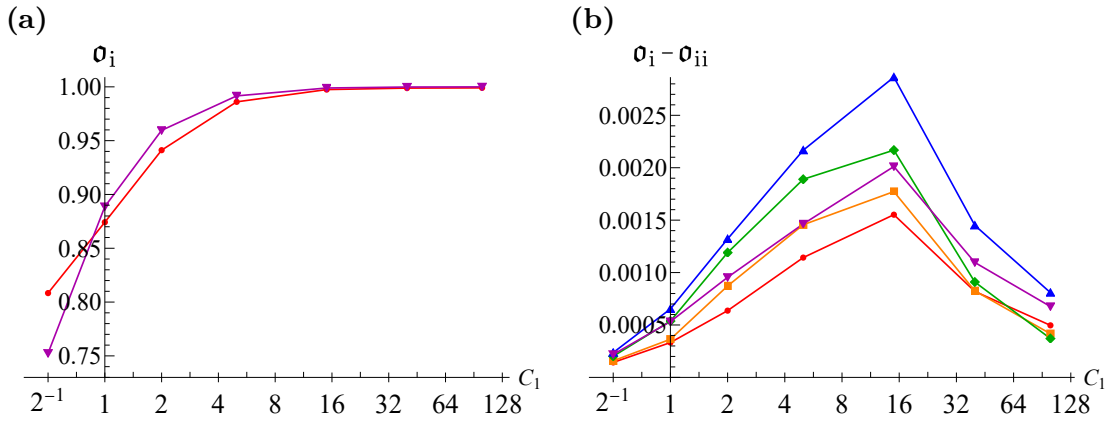

FIGURE A.6. (a) Plot of the overlap $\mathfrak{o}_i$ versus C_1 for $r = 1/4$ (red, circles) and $r = 5$ (purple, triangles), other r values are omitted to reduce visual clutter. (b) Plot of the overlap differences between each model $\mathfrak{o}_i - \mathfrak{o}_{ii}$ versus C_1 for each of the r values considered in Fig. A.5, using the same coloring at point marker scheme. We see that $\mathfrak{o}_i$ quickly approaches 1 as C_1 increases. For instance, for $C_1 = 5$, the smallest overlap $\mathfrak{o}_i$ we find is 98.6% for $r = 1/4$ and the overlap slightly increases as r increase up to 99.2% for $r = 5$. Under model ii the overlaps only shift down slightly by $\sim 0.1\%$ as can be seen in (b).

This was a slight degression, but the point we want to make is that the decay rate γ_1, which is fixed by the cavity-transmission-line interaction, ultimately limits the possible wave packets that can be produced. This is good to know because narrower wave packets are less susceptible to frequency errors. To see this, note that for ideal values of ξ and T, assuming l is large enough to transform the entire wave packet, we have

$$P_{\text{success}} = \left| \int_{-\infty}^{\infty} d\mathcal{T}\; e^{i\frac{\Delta\omega_0}{\gamma_2}\mathcal{T}} \beta_1^2(\mathcal{T}/\gamma_1) \right|^2 = \left| \mathcal{F}\left[\beta_1^2\right]\left(\frac{\Delta\omega_0}{\gamma_2}\right) \right|^2, \tag{A.43}$$

where $\mathcal{T} = \gamma_2(T^* - t)$ is a dimensionless time variable with Fourier conjugate frequency variable $\Delta\omega_0/\gamma_2$ with $\mathcal{F}[\cdot]$ denoting the Fourier transform. Thus, if the oscillations in the phase $e^{i\frac{\Delta\omega_0}{\gamma_2}\mathcal{T}}$ occur over short time scales relative to the temporal duration of β_1, then the integrand will tend to average out to zero. We can protect against this by reducing β_1's temporal duration (broadening $\mathcal{F}\left[\beta_1^2\right]$) as then the phase will

be more stable in the window where β_1 is appreciable, leading to a larger probability of success. As an example of this, in the limit of a impulse response laser pulse G_1, i.e., as $k \to \infty$ in the logistic α_1 case, we have that β_1 is given by Eq. (A.33) and hence

$$P_{\text{success}} = \left| \int_0^\infty d\mathcal{T} \; e^{i\frac{\Delta\omega_0}{\gamma_2}\mathcal{T}} e^{-\mathcal{T}} \right|^2 = \frac{1}{1 + (\Delta\omega_0/\gamma_2)^2}, \tag{A.44}$$

which is Lorentzian function of $\Delta\omega_0$ with peak value of unity and FWHM of $2\gamma_2$ [which is wider than the FWHM of $1.4\gamma_2$ for the $k = 2\gamma_2$ case shown in Fig. 4.2 as $\beta_1(t)$ is narrower here].

This can be contrasted against the case where no unitary transformation is implemented. Using the same pulses G_j,

$$P_{\text{success}} = \left| \int_{-\infty}^{\infty} dt' \; \Phi^*(t')\Psi(t') \right|^2 = \gamma_1\gamma_2 \left| \int_{-\infty}^{\infty} dt' \; e^{i\omega_{0i}t'} \beta_1(\xi_i(T_i - t'))\beta_1(t') \right|^2, \tag{A.45}$$

which will clearly tend to average out to zero due to fast-oscillating phase $e^{i\omega_{0i}t}$ unless both $|\Psi(t)|$ and $|\Phi(t)|$ are narrowly peaked around the same time. We can evaluate this integral exactly in the $k \to \infty$ limit considered above, where $\beta_1(t) = \Theta(t)e^{-\gamma_1 t/2}$ so with $g = (\gamma_1 - \gamma_2)/2$ as intermediate shorthand

$$P_{\text{success}}(T_i > 0) = \gamma_1\gamma_2 e^{-\gamma_2 T_i} \left| \frac{e^{(i\omega_{0i} - g)T_i} - 1}{i\omega_{0i} - g} \right|^2 \leq \frac{4\gamma_1\gamma_2 e^{-\gamma_2 T_i}}{\omega_{0i}^2 + g^2} \leq \frac{4\gamma_1\gamma_2}{\omega_{0i}^2} \tag{A.46}$$

while $P_{\text{success}}(T_i \leq 0) = 0$. This rightmost bound in Eq. (A.46) is clearly relavent for large $|\omega_{0i}|$, in which case it naturally takes on a form similar to Eq. (A.44) in the case of large $|\Delta\omega_0|$. Clearly we see that without a unitary transformation, P_{success} rapidly decreases as $|\omega_{0i}|$ gets large relative to $\gamma_{1,2}$ (as one would expect).

A.2.5 Producible wave packets

Similar to how we specified G_1 in terms of α_1 in Eq. (A.27), we can alternatively specify G_1 in terms of β_1. Thus, just as we limited possible α_1 in §A.2.2, here we will show that not all β_1 can be produced (and hence that system 1 cannot produce wave packets with entirely arbitrary temporal shapes). From the EOMs for system 1, Eqs. (A.23a-b), only can derive that

$$G_1^2(t) = \frac{e^{2i\theta_0(t)}\left[\dot{\beta}_1(t) + (id_1 + \gamma_1/2)\,\beta_1(t)\right]^2}{\alpha_1^2(t_p)e^{2i\theta_0(t_p)} - 2\int_{t_p}^{t} dt' e^{2i\theta_0(t')}\left[\dot{\beta}_1(t') + (id_1 + \gamma_1/2)\,\beta_1(t')\right]\beta_1(t')}, \quad \text{(A.47)}$$

which is valid for different choices of laser frequency and phase determined by the parameters $\dot{\theta}_0 := \dot{\phi}_1 + \delta\omega_1 = \dot{\theta}_1|_{d_1=0}$ and $d_1 = g_1^2/\Delta_1 - \delta_1$ as defined above. As $G_1(t)$ is the laser pulse magnitude, which we picked to be positive without loss of generality by factoring out the phase $e^{i\phi_1(t)}$ in Eq. (A.21), as a consistency condition we must choose $\phi_1(t)$ or equivalently $\theta_0(t)$ to cancel off the phase induced by the β_1 terms in the other parts of the expression. In principle we could work with the condition that the whole expression for $G_1[\beta_1]$ must be real in order to determine the possible functions $\theta_0(t)$ and hence $\phi(t)$. However, doing so leads to a self-referential condition on $\theta_0(t)$ that is unwieldy. Hence one should solve these EOMs numerically in general, and when doing so it can be useful to work with the complex laser pulses $G_j e^{i\phi_j}$ directly instead of their polar decomposition. Note that Ref. 88 get very similar EOMs for their complex control parameter $g(t)$ as compared to our $G_j e^{i\phi_j}$, see their supplemental Eq. (10). However, we can still make progress analytically by considering a subset of all possible β_1, namely those with either a certain 'nice' phase or those that are slowly varying in senses that we will make precise.

$\boldsymbol{\beta_1}$ with simple phase. One way to guarantee that we satisfy the consistency condition that G_1 is real is to set the numerator and denominator of Eq. (A.47) to be real independently. Doing so and using the decomposition $\beta_1(t) = B(t)e^{ib(t)}$ such that $\dot{\beta}_1(t) = \left[\dot{B}(t) + i\dot{b}(t)B(t)\right] e^{ib(t)}$ we have from the numerator that

$$\begin{aligned} & e^{2i(\theta_0+b)} \left[\dot{B} + \frac{1}{2}\gamma_1 B + i\left(\dot{b} + d_1\right) B\right]^2 \in \mathbb{R} \\ \implies & 2(\theta_0 + b) + 2\arctan\left(\frac{\dot{b} + d_1}{\dot{B}/B + \gamma_1/2}\right) \equiv 0 \mod 2\pi. \end{aligned} \tag{A.48}$$

Note the denominator must be real for all $t \geq t_p$ so at $t = t_p$ we have that $\alpha_1^2(t_p)e^{2i\theta_0(t_p)} \in \mathbb{R}$, where $|\alpha_1(t_p)|$ should be 1 for an appropriate preparation time so we consider the phases to be such that $\alpha_1^2(t_p)e^{2i\theta_0(t_p)} = 1$. Thus, for the denominator to be real at subsequent times the argument of the integral must be real, which along with the above condition from the numerator implies

$$\arctan\left(\frac{\dot{b} + d_1}{\dot{B}/B + \gamma_1/2}\right) \equiv 0 \mod 2\pi \tag{A.49}$$

such that $\dot{b} = -d_1$ and hence $b(t) = b_0 - d_1 t$. Inserting this back into Eq. (A.48) we find that $\theta_0 + b_0 - d_1 t \equiv n\pi$ for n an integer, which then implies that $\theta_0(t) = d_1 t + c_0$ with $c_0 = n\pi - b_0$ some constant. Hence $\dot{\phi}_1(t) = d_1 - \delta\omega_1(t)$ for which the d_1 shift acts as a base frequency for ϕ_1, see Eq. (A.21). With these simplifications we have

$$G_1(t) = \frac{\dot{B}(t) + \frac{1}{2}\gamma_1 B(t)}{\sqrt{1 - 2\int_{t_p}^{t} dt' \left[\dot{B}(t') + \frac{1}{2}\gamma_1 B(t')\right] B(t')}}, \tag{A.50}$$

which is the same pulse we obtain in the case where the 'nice' laser pulse are phase are used such that α_1 and β_1 have a constant phase, so we can take them to be real.

Hence we have a closed form (integral) expression for G_1 in terms of the class of wave packets with $\beta_1(t) = B(t)e^{-id_1 t}$ (dropping the constant phase b_0) for which the amplitude $B(t)$, which specifies the wave packet shape, satisfies the relation

$$2\int_{t_p}^{t} dt' \left(\dot{B} + \frac{\gamma_1}{2}B\right) B \leq 1 \quad \forall\ t > t_p. \tag{A.51}$$

Note that this condition is more easily violated than the one for α_1. For instance, there is no pulse G_1 that will produce the, seemingly reasonable, normalized Gaussian wave packet corresponding to $B(t) = (\gamma_1\sigma\sqrt{\pi})^{-1/2}\, e^{-t^2/2\sigma^2}$, which violates inequality of Eq. (A.51) for all σ. Gaussian wave packets are of interest, in part, as they are 'minimum uncertainty wave packets' that saturate the Heisenberg uncertainty relation. As demonstrated by Ref. 305, this ultimately leads to them being optimally tolerant to mode-mismatch errors in photonic quantum information processing including for linear optical quantum computing. To demonstrate this impossibility, we consider the inequality of Eq. (A.51) for this Gaussian B taking $t_p \to -\infty$:

$$I_{\text{Gauss}}(t) := 1 - 2\int_{-\infty}^{t} dt' \left(\dot{B} + \frac{\gamma_1}{2}B\right) B = \frac{\text{erfc}(t/\sigma)}{2} - \frac{e^{-t^2/\sigma^2}}{\sqrt{\pi}\gamma_1\sigma} \overset{?}{\geq} 0, \tag{A.52}$$

where

$$\text{erfc}(x) := \frac{2}{\sqrt{\pi}}\int_{x}^{\infty} dy\ e^{-y^2} \tag{A.53}$$

is the complimentary error function. We can compute the extrema of $I_{\text{Gauss}}(t)$ using the dimensionless time $\tau = t/\sigma$ and decay rate $g = \gamma_1\sigma/2$

$$0 = \frac{dI_{\text{Gauss}}}{d\tau} = \frac{d}{d\tau}\left(\frac{\text{erfc}(\tau)}{2} - \frac{e^{-\tau^2}}{\sqrt{\pi}2g}\right) = \frac{1}{\sqrt{\pi}}e^{-\tau^2}\left(\frac{\tau}{g} - 1\right) \implies \tau = g > 0, \tag{A.54}$$

which is a minimum as

$$\left.\frac{d^2 I_{\text{Gauss}}}{d\tau^2}\right|_{\tau=g} = \frac{1}{\sqrt{\pi}} e^{-\tau^2}\left[\frac{1}{g} - 2\tau\left(\frac{\tau}{g} - 1\right)\right]\Bigg|_{\tau=g} = \frac{1}{\sqrt{\pi} g} e^{-g^2} > 0. \tag{A.55}$$

Hence the minimum value is

$$\min\left[I_{\text{Gauss}}(\tau)\right] = I_{\text{Gauss}}(\tau = g) = \frac{1}{2}\left(\text{erfc}(g) - \frac{e^{-g^2}}{\sqrt{\pi} g}\right) < 0 \tag{A.56}$$

as for $x > 0$

$$\text{erfc}(x) < \frac{2}{\sqrt{\pi}} \int_x^\infty dy\ \frac{y}{x} e^{-y^2} = \frac{1}{\sqrt{\pi} x} \int_{x^2}^\infty d(y^2) e^{-y^2} = \frac{1}{\sqrt{\pi} x} e^{-x^2}. \tag{A.57}$$

Hence the inequality of Eq. (A.52) is violated for all g and hence all σ as I_{Gauss} goes negative for some times t, which entails that there is no pulse that will produce Gaussian wave packet with any standard deviation σ. Many other wave packets shapes do not have this drastic behavior that the Gaussian has, where they can never be produced ideally. For instance, the symmetric, normalized $B(t) = (2\gamma_1\sigma)^{-1/2}\,\text{sech}(t/\sigma)$ can be ideally produced for $\sigma \geq 2/\gamma_1$ setting a lower bound for such a photons temporal width. To show this one can consider the inequality of Eq. (A.51) for this B, analogous to our treatment of the Gaussian case in Eq. (A.52):

$$I_{\text{sech}}(t) := 1 - 2\int_{-\infty}^{t} dt' \left(\dot{B} + \frac{\gamma_1}{2} B\right) B = \frac{1}{2}\left(1 - \tanh(t/\sigma) - \frac{\text{sech}^2(t/\sigma)}{\gamma_1 \sigma}\right). \tag{A.58}$$

Then, one can easily show that $I_{\text{sech}}(t)$ goes negative for some t if $\gamma_1\sigma < 2$, whereas it is entirely positive for $\gamma_1\sigma \geq 2$.

Note, however, we can rescale the desired β_1 by a weight $0 < w < 1$ such that we produce a subnormalized wave packet, i.e., a superposition of the vacuum and

the wave packet.[14] Then, modifying the above Gaussian case, we have that if the quantity

$$I^{(w)}_{\text{Gauss}}(\tau) = 1 - w^2 + \frac{w^2}{2}\left(\text{erfc}(\tau) - \frac{e^{-\tau^2}}{\sqrt{\pi}g}\right) \tag{A.59}$$

is positive $\forall\tau$ then the corresponding B can be produced. Using the above analysis this function has a minimum at $\tau = g$ of

$$\min\left[I^{(w)}_{\text{Gauss}}(\tau)\right] = 1 - w^2 + \frac{w^2}{2}\left(\text{erfc}(g) - \frac{e^{-g^2}}{\sqrt{\pi}g}\right) \tag{A.60}$$

and as

$$\frac{-1}{\sqrt{\pi}g} < -x_g \equiv \text{erfc}(g) - \frac{e^{-g^2}}{\sqrt{\pi}g} < 0 \quad \text{for } g > 0 \tag{A.61}$$

it follows that

$$\min\left[I^{(w)}_{\text{Gauss}}(\tau)\right] \geq 0 \quad \text{if} \quad w^2 \leq w^2_{\text{max}} \equiv \frac{1}{1 + x_g/2}. \tag{A.62}$$

Hence, any Gaussian wave packet can be probabilistically produced with a probability of at most

$$P_{\text{Gauss-prod}} = w^2_{\text{max}} = \left[1 + \frac{e^{-(\gamma_1\sigma/2)^2}}{\sqrt{\pi}\gamma_1\sigma} - \frac{1}{2}\text{erfc}(\gamma_1\sigma/2)\right]^{-1} \tag{A.63}$$

depending on the Gaussian's standard deviation σ as plotted in Fig. A.7.

Complimentarily, with probability $1 - P_{\text{Gauss-prod}}$, no photon will be produced and the excitation will remain in atom 1 [so a Υ_2 error would occur in Eq. (4.43)]. To actually produce the desired wave packet one could employ the requisite laser pulse as determined by Eq. (A.50) with an appropriately subnormalized B and herald the

[14] This can be done for any wave packet envelope provided the integral expression on the LHS of the inequality of Eq. (A.51), which we will refer to as $\mathcal{I}(t)$, is finite $\forall\, t$. Then one can simply choose $w^2 \leq 1/\max\{\mathcal{I}(t)\}$ to force the inequality to hold.

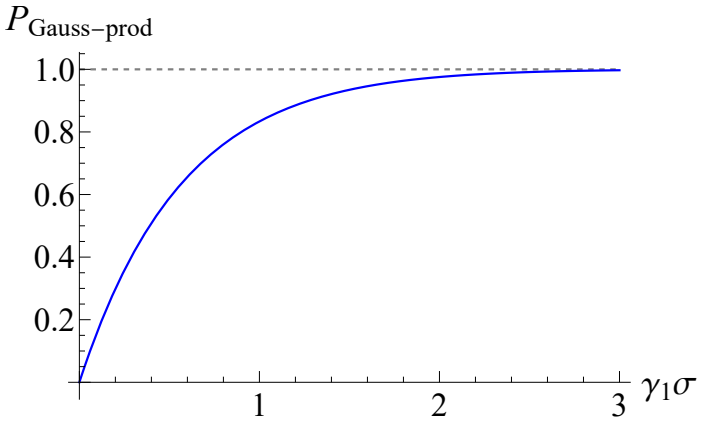

FIGURE A.7. Plot of $P_{\text{Gauss-prod}}$ as a function of $\gamma_1\sigma$ [see the text, including Eq. (A.63), for details].

success of the production by a measurement on atom 1. Specifically, by measuring if atom 1 is in the state $|e_1\rangle$, if so the excitation has remained in atom 1 and no photon has been produced so the atom must be reset and the procedure repeated until atom 1 undergoes the transition $|e_1\rangle \rightarrow |g_1\rangle$ accompanied by the emission of the desired wave packet. Thus, in principal one could produce a very narrow wave packet with $\sigma \ll \gamma_1^{-1}$ provided they are willing to run the protocol enough times to combat the low probability of production. For instance, in the Gaussian case, a given production attempt could obtain $\sigma = 10^{-3}/\gamma_1$ with the dismal probability of $w_{\text{max}}^2 \approx 2 \cdot 10^{-3}$ (up to additional technical errors that would certainly arise). Note, however, that one can obtain a broader wave packet with more modest probability, e.g., $w_{\text{max}}^2 = 0.83$ for $\sigma = \gamma_1^{-1}$ and $w_{\text{max}}^2 = 0.997$ for $\sigma = 3\gamma_1^{-1}$ (see Fig. A.7).

We acknowledge that this ability to probabilistically produce a desired photon wave packet is not very useful in our case here where we want to implement deterministic QST between two nodes whose effective Hamiltonians are equivalent up to parameter differences that can be circumvented using our unitary. However, we still include this discussion as this ability and related questions like 'What photon

wave packets can be produced?' are interesting and not fully explored topics that may be applicable in different contexts. For instance, such probabilistic photon production may be of interest in heralded remote entanglement generation experiments (see §A.1.7), where the ultimate remote entangled state fidelity is largely determined by the spectral overlap of the photons being sent by two separate nodes. In such a case, one can have additional control of the generated photon wave packet, potentially leading to higher quality entanglement generation, at the expense of a decrease in rate due to the probabilistic production.

Moreover, time-reversed analogs of expressions like Eq. (A.50) for the drive that produces a given wave packet, could be leveraged to design drives that facilitate the absorption of a given wave packet, more generally. In terms of probabilistic reception, this comes with a caveat relative to production. Namely, a probabilistically produced wave packet, like the Gaussian example, will not be probabilistically absorbed with same probability it was emitted. Namely, the absorption probability will be lower than w^2 if we initialize node 2 in the ground state $|g_2\rangle$ as usual, $\alpha_2(-\infty) = 0$, as then the absorption process will not simply be the effective time-reversed process to emission (which here would require that $|\alpha_2(-\infty)| = |\alpha_1(+\infty)|$).[15] In principle, such errors could naturally be corrected using the schemes discussed in §4.3.4 and in §A.3, though this would be at the expense of more protocol repetitions that could be avoided by using a deterministically producible wave packet [or an 'effectively producible' wave packet, where $w_{\max}$ is nearly 1 (e.g., a Gaussian wave packet with $\sigma \gg \gamma_1^{-1}$)]. Taking a step back, in our scheme we can already design drives to produce

[15] As a semi-naive alternative, if we know we are only probabilistically producing a photon, and assuming we can calculate the value of α_1 for long times, we could alternatively prepare the state $|\tilde{g}_2\rangle \equiv |e_2\rangle\alpha_1(\infty) + \sqrt{1-\alpha_1^2(\infty)}|g_2\rangle$ in the attempt to improve absorption. However, this leads to other issues, principally, bit-flip errors can occur both ways: $|\tilde{g}_2\rangle \leftrightarrow |\tilde{e}_2\rangle$ (where $|\tilde{e}_2\rangle$ is an orthonormal state to $|\tilde{g}_2\rangle$ in the $\{|g_2\rangle, |e_2\rangle\}$ subspace), which renders this approach not useful as the ECZ error correction methods cannot be used.

and receive wave packets nearly deterministically (up to cooperativity limitations), i.e., using the time-reversal based prescription of Eq. (3.60), so there is no need to study the problem of how to best receive (absorb) an arbitrary photon wave packet.

Slowly varying $\boldsymbol{\beta_1}$ limit. In the different regime where β_1 is slowly varying, i.e., $|\dot{\beta}_1(t)| \ll |\,(id_1 + \gamma_1/2)\,\beta_1(t)|$, we can simplify Eq. (A.47) making the consistency condition of $G_1 \in \mathbb{R}$ tractable. Using the polar decompositions $\beta_1(t) = B(t)e^{i\theta_\beta(t)}$[16] and $id_1+\gamma_1/2 = \sqrt{d_1^2+\gamma_1^2/4}\; e^{i\arctan(2d_1/\gamma_1)} \equiv De^{i\theta_d}$ and assuming we are in the slowly varying limit so that we can neglect $\dot{\beta}_1(t)$ terms we have

$$G_1^2(t) \approx \frac{D^2 e^{2i\left[\theta_0(t)+\theta_\beta(t)+\theta_d\right]} B^2(t)}{c - 2De^{-i\theta_d}\int_{t_p}^t dt' e^{2i\left[\theta_0(t')+\theta_\beta(t')+\theta_d\right]} B^2(t')} \tag{A.64}$$

with $c = \alpha_1^2(t_p)e^{2i\theta_0(t_p)}$. Then by picking θ_0 such that $\theta_0(t) + \theta_\beta(t) + \theta_d = \eta/2 =$ constant we have

$$G_1^2(t) \approx \frac{D^2 B^2(t)}{e^{i(\arg c - \eta)}|c| - 2De^{-i\theta_d}\int_{t_p}^t dt' B^2(t')}, \tag{A.65}$$

which will be real provided $\eta = \arg c$ and $\theta_d = 0 \implies d_1 = 0$[17] such that $\theta_0(t) = \arg c/2 - \theta_\beta(t)$. Thus for early t_p for which $|\alpha_1(t_p)| \to 1$ we have

$$G_1^2(t) \approx \frac{\gamma_1^2 B^2(t)/4}{1 - \gamma_1 \int_{t_p}^t dt' B^2(t')}. \tag{A.66}$$

[16] We use a different symbol to denote the angle here, θ_β, to avoid confusion with the case above with angle b.

[17] Note that although $\theta_d = \pi$ would naively be less restrictive as then the denominator would always be positive, this is not possible in fact $|\theta_d| \leq \pi/2$ as the quantity $\gamma_1/2 + id_1$, which θ_d is the argument of, has positive real component.

Moreover, taking $t_p \to -\infty$, as the contribution from $B(t)$ should be negligible before t_p, we can use the normalization condition on $\Psi(t) = \sqrt{\gamma_1}\beta_1(t)$ of $\int_{t_p}^{\infty} dt' |\Psi(t')|^2 = 1$ to obtain

$$G_1(t) \approx \frac{\gamma_1 B(t)/2}{\sqrt{\gamma_1 \int_t^{\infty} dt' B^2(t')}} = \frac{\sqrt{\gamma_1}}{2} \frac{|\Psi(t)|}{\sqrt{\int_t^{\infty} dt' |\Psi(t')|^2}}, \tag{A.67}$$

This suggests we can pick any phase for the wave packet we like θ_β provided we work in the slowly varying limit $|\dot{\beta}_1(t)| \ll \frac{\gamma_1}{2}|\beta_1(t)|$, tune $d_1 = 0$, and select the laser phase such that $\dot{\phi}_1 = -\dot{\theta}_\beta(t) - \delta\omega_1$. Note that sufficiently fast varying phases, which would correspond to large variations about the photon wave packets central carrier frequency, will ultimately be incompatible with the Markov approximation [128] needed to obtain the amplitude EOMs we started this section with. This issue will be limited by the appropriate selection of wave packets satisfying the slowly varying condition, which for the polar decomposition of β_1 is that $(\dot{B}/B)^2 + (\dot{\theta}_\beta)^2 \ll \gamma_1^2/4$. However, analysis of such deviations from Markovianity is beyond the scope of this dissertation. As an example let us consider the normalized target amplitude

$$\beta_1^{\text{target}}(t) = \sqrt{\frac{k}{2\gamma_1}} \operatorname{sech}(kt) e^{i[\arctan(kt)+\pi/2]} := B(t) e^{i\theta_\beta(t)}, \tag{A.68}$$

which has a nice symmetric envelope and its phase smoothly goes from 0 to π. We can do quite well in generating a wave packet of this form by putting ourselves in the slowly varying condition, which in this case amounts to $k \ll \gamma_1/2$ as illustrated in Figs. A.8 and A.9.

Comparison to Ref. 155. We note that Refs. 155 and subsequently 150 perform similar analysis identifying the requisite pulses to produce certain photon wave packets and both report laser pulses of the same form as Eq. (A.67). Refs. 155 provide further analysis and conditions for when adiabatic elimination of the excited state, $|r\rangle$ in our

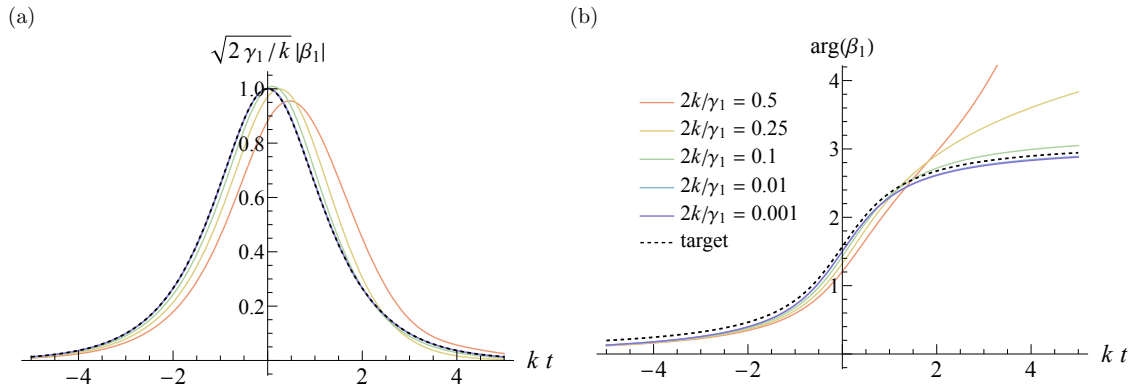

FIGURE A.8. Plots of (a) scaled magnitude and (b) phase of the amplitude β_1 in several instances. For the colored lines corresponding to various k values, β_1 is determined by solving the amplitude EOMs of Eq. (A.23) directly for the laser pulse magnitude and phase specified by Eq. (A.67) and $\theta_0 = -\theta_\beta$, respectively, when trying to obtain the target amplitude $\beta_1^{\text{target}}(t)$ (dashed black lines). This plot shows that as $2k/\gamma_1$ (which is equal to r^{-1} from previous subsections) decreases the slowly varying solution quite accurately matches the target amplitude (and hence wave packet shape). Note there appears to be a small residual phase offset for small k though this will not affect the overlap $\mathcal{I}(k)$ in Fig. A.9 below.

notation, is possible in a three-level Λ-type atom (beyond just the large detuning case we consider in this work). They analyze the single photons that can be produced by an atomic ensemble of N such atoms in a cavity. Ref. 150 extend aspects of the work of Ref. 155 by accounting for the impact of additional atomic structure including higher excited states for the case of a single Λ-type atom in a cavity. We emphasize that their reported complex Rabi frequencies will only produce the intended wave packet if it is sufficiently broad wave in time in both magnitude and phase (i.e., is slowly varying), as is the case for Eq. (A.67). They both mention such limitations in their work, though we think it is appropriate to reiterate that these results are limited in that not any single photon shape can be produced.

We will now explicitly demonstrate the correspondence of the Rabi frequency determined by Ref. 155 and that which we determine. Specifically, we start with

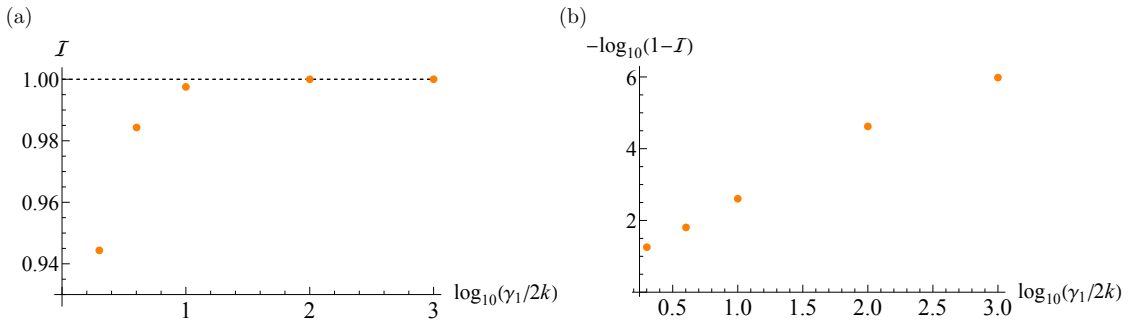

FIGURE A.9. Plot of the overlap $\mathcal{I}(k) \equiv \left| \int_{-t_m}^{t_m} dt\ \gamma_1 \beta_1^{\text{target}}(t) \beta_1^*(t;k) \right|$ versus $\gamma_1/2k$ on (a) linear-log and (b) log-log scale. In $\mathcal{I}(k)$ the function $\beta_1(t;k)$ corresponds to the colored line in Fig. A.8 with the corresponding value of k. See the Fig. A.8 caption for how these $\beta_1(t;k)$ are calculated. An overlap of one entails that the emitted wave packet $\sqrt{\gamma_1}\beta_1$ has the target shape and phase. We see that this overlap monotonically increases approaching 1 as k/γ_1 decreases, this serves to demonstrate the validity of the slowly varying approximation. Here we take the integration bounds to be $\pm t_m = \pm 15/k$ for our numerics.

Eq. (21) of Ref. 155, which gives the necessary complex (slowly-varying) Rabi frequency to emit a wave packet $e(t)$ (in their notation) to be

$$\Omega(t) = -\frac{\gamma(1+C)+i\Delta}{\sqrt{2\gamma(1+C)}} \frac{e(t)}{\sqrt{\int_t^\infty dt' |e(t')|^2}} e^{\frac{i\Delta}{2\gamma(1+C)} \ln\left(1-\int_0^t dt' |e(t')|^2\right)}, \tag{A.69}$$

where they have the cooperativity $C = g^2 N/\kappa\gamma$. In their notation γ is the decay rate of the optical coherence of the upper level (our $|r\rangle$), 2κ is the cavity decay rate (our γ_j for node $j = 1, 2$), and as in our case g is coupling of an atom to the cavity mode, and Δ is the laser detuning though they use the opposite sign convention from us. To make this case align with ours we work with special cases of both results. Note that their result, summarized in Eq. (A.69), accounts for the impact of cavity and atomic parameters on photon production (as quantified by the cooperativity C relative to the detuning Δ/γ) more carefully than our work does (as they have different scopes). The special case of our work with a slowly varying β_1, as given in Eq. (A.67), should

align with the special case of their result with $N = 1$ atom (per cavity), a large cooperativity $C \gg 1$, and a far off-resonant Raman scheme $|\Delta| \gg \gamma C$. In this case their result, Eq. (A.69), becomes

$$\Omega(t) = -i\Delta\sqrt{\frac{\kappa}{2g^2}}\frac{e(t)}{\sqrt{\int_t^\infty dt'|e(t')|^2}}e^{\frac{i\Delta\kappa}{2g^2}\ln\left(\int_t^\infty dt'|e(t')|^2\right)}, \tag{A.70}$$

as they work with the starting time $t_p = 0$. Note that formally this large C limit could be determined by taking $\gamma \to 0$, noting that $\gamma C = g^2/\kappa$ is independent of γ, though one needs to be careful with the corresponding interpretation.[18]

Translating to our notation via appropriate relabelings of $\kappa \to \gamma_1/2$ (for node 1), $\Delta \to -\Delta_1$, and $e(t) = \Psi(t) = \sqrt{\gamma_1}\beta_1(t)$ (taken to be a normalized wave packet) we have

$$\Omega(t) = \frac{i\sqrt{\gamma_1}\Delta_1}{2g_1}\frac{\beta_1(t)}{\sqrt{\int_t^\infty dt'|\beta_1(t')|^2}}e^{\frac{-i\Delta_1\gamma_1}{4g_1^2}\ln\left(\gamma_1\int_t^\infty dt'|\beta_1(t')|^2\right)}. \tag{A.71}$$

However, their Ω is defined as half the traditional Rabi frequency, which is $\Omega_1 e^{-i\phi_1}$ in our notation, hence we have the following correspondence to our Rabi frequency

[18] One may be tempted to think that as 'spontaneous emission from the upper level can be suppressed by using an off-resonant Raman scheme' (as is often stated, e.g., see Ref. 1, 154), one should be able to achieve $\gamma = \Gamma_{sd}/2 \to 0$ 'simply' by using a large detuning Δ. However, this is not the case: the effects of spontaneous decay cannot be eliminated nor does $\Gamma_{sd}/2$ approach 0 for large detuning (it is a constant). Accordingly, statements such as the one above should be made with caution to avoid giving a misleading impression. This idea comes from the fact that the *effective* spontaneous decay rate of the upper level, Γ_{eff}, is suppressed in a Raman process that is far detuned relative to the drive strength Ω as $\Gamma_{\text{eff}}(t) = \Gamma_{sd}[\Omega(t)/2\Delta]^2$, as shown in Eq. (A.38) [154]. However, the atom-cavity coupling is similarly modified (suppressed for large detuning) in this effective picture, i.e., $g \to G(t) = g\Omega(t)/2\Delta$ and these two effects balance out so the cooperativity is left unchanged: $C_{\text{eff}} = \frac{2G^2(t)}{\kappa\Gamma_{\text{eff}}(t)} = \frac{2g^2}{\kappa\Gamma_{sd}} = C$. In other words, the probability of spontaneous emission per unit time can indeed be strongly inhibited in a far off-resonant high-Q cavity, yet in this regime the effective coupling $G(t) \propto 1/\Delta$ is likewise inhibited so one must drive for a comparably longer time. A large detuning is indeed vital in the adiabatic elimination of the upper level in the Raman process and for effectively eliminating the factor Γ_r in Eq. (A.37). Nevertheless, the impact of cooperativity in Eq. (A.38) remains even for large Δ and ultimately, as seen in §A.2.3, gives rise to an upper bound for the efficiency $P_{\text{em-max}} = C/(1+C)$, which is independent of detuning [154, 155]. Note that if multiple excited state levels are included that couple to the intended Raman process this bound does acquire a frequency dependence [150].

magnitude

$$\Omega_1(t) \leftrightarrow 2|\Omega(t)| \approx \frac{\sqrt{\gamma_1}|\Delta_1|}{g_1} \frac{|\beta_1(t)|}{\sqrt{\int_t^\infty dt' |\beta_1(t')|^2}}. \tag{A.72}$$

Meanwhile using definition of G_1 in terms Ω_1,[19] and using the slowly varying pulse Eq. (A.67) we have

$$\Omega_1(t) = \frac{2|\Delta_1|}{g_1} G_1(t) \approx \frac{\sqrt{\gamma_1}|\Delta_1|}{g_1} \frac{|\beta_1(t)|}{\sqrt{\int_t^\infty dt' |\beta_1(t')|^2}}, \tag{A.73}$$

which precisely matches the result of Ref. 155 in the appropriate limit, i.e., the $2|\Omega(t)|$ above. For completeness we must also compare the phases, we should have the following phase correspondence:

$$-\phi_1(t) \leftrightarrow \arg \Omega(t). \tag{A.74}$$

Note the minus sign on ϕ_1 in the equation above, which is due to our phases ϕ_j corresponding to a lowering operator, $|e_j\rangle\langle r_j|$, in the original node Hamiltonian, whereas their complex Ω corresponding to a raising operator. We analyze this by first considering the $\delta\omega_1(t) = \Omega_1^2(t)/(4\Delta_1)$ integral term in ϕ_1 with Ω_1 given by Eq. (A.73):

$$\int dt\ \delta\omega_1(t) = \frac{\gamma_1\Delta_1}{4g_1^2} \int dt\ \frac{\gamma_1|\beta_1(t)|^2}{\gamma_1 \int_t^\infty dt'\ |\beta_1(t')|^2} = -\frac{\gamma_1\Delta_1}{4g_1^2} \ln\left(\gamma_1 \int_t^\infty dt'\ |\beta_1(t')|^2\right) \tag{A.75}$$

[19]Note the Δ_1 in the proportionality constant between Ω_1 and G_1 should technically have a modulus on it in order for Ω_1 to be a magnitude, with $G_1 > 0$. This can be adapted by including the sign of Δ_1 into the phase ϕ_1 via the argument of Δ_1 (either 0 or π), which contributes a constant that can be lumped into the constant of Eq. (A.77).

(the γ_1 is included in the logarithm so that it has appropriate dimensions). Meanwhile from Eq. (A.71) we have

$$\arg\Omega(t) = -\frac{\pi}{2} + \theta_\beta(t) - \frac{\gamma_1\Delta_1}{4g_1^2}\ln\left(\gamma_1\int_t^\infty dt'\ |\beta_1(t')|^2\right), \tag{A.76}$$

where we are again using the notation $\theta_\beta = \arg\beta_1$. Thus, we see that by integrating the condition $\dot{\phi}_1 = -\dot{\theta}_\beta(t) - \delta\omega_1$ we have

$$-\phi_1(t) = \theta_\beta(t) - \frac{\gamma_1\Delta_1}{4g_1^2}\ln\left(\gamma_1\int_t^\infty dt'\ |\beta_1(t')|^2\right) + \text{constant}, \tag{A.77}$$

which is specified up to a constant encoding the initial condition. We indeed find that $-\phi_1(t) = \arg\Omega(t)$ (up to the unphysical constant) so both the phase and magnitude of our Rabi frequency match that of Ref. 155 in the appropriate limit.

A.3 Error analysis and correction

As discussed in §4.4, the practical utility and potential versatility of a QST scheme like ours comes in consonance with the use of error correction protocols. Our scheme is designed to minimize the presence of errors, so that the relatively costly error correction protocols are subject to less overhead. Here we will elaborate on the simplifying strategies and their corresponding standard errors considered in §4.2.5 (§A.3.1). Then, we will further analyze the independence of unitary transformation errors via the index of separability (§A.3.2). Finally, we will further analyze the ECZ protocols highlighted in §4.3.4, which are two error correction protocols that are well suited to our hybrid QST scheme (§A.3.3–§A.3.5) [2, 164].

A.3.1 Accounting for standard errors

Here we elaborate on how the losses we set aside in our simplified treatment of §4.2.5 can be incorporated into the analysis. For clarity of exposition we will focus on our 'exemplar case' in which each node consists of a Λ-type atom (or ion) in an optical cavity and they are coupled via optical fiber. In Table A.1 we list the attained values, across multiple such experiments, of several parameters that are used to quantify the atom- (or ion-) cavity and cavity-channel losses of strategies 1) and 2), respectively. (Similar ideas should apply to other node and channel implementations though the formulas used will not necessarily be of the same form.) We refer the reader to other works (via citations) for a more thorough treatment of these issues, chiefly see Refs. 154, 155, and 150.

Strategy 1). We distinguish strategy 1) from 2) as even if we consider an ideal cavity [strategy 2)], the maximum efficiency of emission into (or absorption out of) a specific cavity mode is limited by the atomic structure. For instance, the spontaneous decay rate Γ_{sd} of the Λ system's upper level (relative to parameters of the driving laser and cavity) limits the probability of being able to produce the desired photon in the Raman transition. Refs. 155, 150, and 154 show this – that the optimal emission and absorption efficiencies are bounded above – in contexts similar to our exemplar case, finding an upper bound for $\mathcal{P}_{\rm em}$ based on the emitter cooperativity parameter $C_{\rm em}$ as

$$\mathcal{P}_{\rm em} = \frac{C_{\rm em}}{1 + C_{\rm em}} \quad \text{with} \quad C_{\rm em} \equiv \frac{4g^2}{\gamma\Gamma_{sd}} \tag{A.78}$$

TABLE A.1. Extended version of Table 4.1, characterizing couplings of atoms or ions in optical cavities. The table is split into two panels with consistent row ordering and includes the additional parameters couplings g, γ, Γ_{sd}, all reported over 2π in MHz, for atomic decay (Panel A) and $\mathcal{T}_i, \mathcal{T}_o, \mathcal{L}$ for cavity loss (Panel B). Some references report a combined undesired coupling rate $\mathcal{T}_o + \mathcal{L}$, shown as a centered value under the two corresponding columns. The values of $\mathcal{T}_i, \mathcal{T}_o, \mathcal{L}$ are reported in parts per million unless otherwise noted using the $\propto$ symbol. In these other cases, the respective values reported are the 'correct' and 'lossy' cavity decay rates κ_c and κ_l divided by 2π in MHz, which satisfy $\gamma = 2(\kappa_c + \kappa_l)$ [$= 2\kappa$ in many references]. Importantly, $\kappa_c \propto \mathcal{T}_i$ and $\kappa_l \propto \mathcal{T}_o + \mathcal{L}$ with the same proportionality constant (which depends on the speed of light and length of the cavity) [150, 154] and thus $C_{\text{cav}} = \kappa_c/\kappa_l$. These parameter values were found in the accompanying reference(s), translated to our notation (see footnote 20), reported to the accuracies given in their respective original work(s), and then used to calculate the cooperativities and probabilities via Eqs. (A.78) and (A.79). Each of the neutral atom experiments reported uses a single ^{87}Rb atom in a cavity (accordingly they share the same Γ_{sd} value). The reported trapped ion experiments use various emitter(s) (in a cavity in each case): Ref. 175 uses a single $^{174}\text{Yb}^+$ atom, Ref. 174 use up to 5 $^{40}\text{Ca}^+$ ions, and the others use a single $^{40}\text{Ca}^+$ ion. The combined probability of the full emission process at node 1 and symmetrically of absorption at node 2, assuming identical nodes, is $P_{\text{tot}} = (\mathcal{P}_{\text{em}}\mathcal{P}_{\text{cav}})^2$. [We do not consider nor propagate the errors for these values, the cooperativities are shown to two decimal places and the probabilities $(\mathcal{P}_{\text{em}}, \mathcal{P}_{\text{cav}}, P_{\text{tot}})$ are shown to the nearest 0.1% (or the leading nonzero digit)].

Panel A

Emitter type	Reference	Emitter (atomic) decay				
		$g/2\pi$	$\gamma/2\pi$	$\Gamma_{sd}/2\pi$	C_{em}	$\mathcal{P}_{\text{em}}$ (%)
Neutral atom	[34]	5	6	6	2.78	73.5†
	[176, 177]	6.7	5	6	5.99	85.7
	[178]	20‡	4	6	66.67	98.5
	[150]	4.9	5.4	6.06	2.93	74.6
	[179] A	7.6	5	6	7.70	88.5
	[179] B	7.6	5.6	6	6.88	87.3
	[306]	2.7	1.06	6	4.58	82.1
Ion	[156]	0.92	2.4	1.69	0.83	45.5
	[175]	1.6	50	4.22	0.05	4.6
	[174]	0.9	0.47	22.3	0.31	23.6
	[166] A	0.77	0.137	21.48	0.81	44.7
	[166] B	1.2	0.14	21.48	1.92	65.7
	[173]	12.3	8.2	23.0	3.21	76.2

TABLE A.1. (continued).

Panel B

...	Cavity loss					Combined loss
	$\mathcal{T}_i$	$\mathcal{T}_o$	$\mathcal{L}$	C_{cav}	$\mathcal{P}_{\text{cav}}$ (%)	P_{tot} (%)
	100	6	5.1*	9.00*	90.0*	43.8
	95	8		11.88	92.2	62.5
	17.8	2.5	11	1.32	56.9	31.4
...	$\propto 2.4$	$\propto 0.3$		8.00	88.9	44.0
	$\propto 2.3$	$\propto 0.2$		11.50	92.0	66.3
	$\propto 2.4$	$\propto 0.4$		6.00	85.7	56.0
	-	-	-	-	-	-
	600	6	NR	NR	NR	<20.3
	100	10	200	0.48	32.3	0.02
	100	5	9.9*	6.69*	87.0*§	4.2
...	13	1.3	50.7*	0.25*	20.0*	0.8
	90	2.9	22.5*	3.55*	78.0*	26.3
	25	25	75	0.25	20.0¶	2.3

†: Ref. 34 reports an analog of $\mathcal{P}_{\text{em}}$, their 'photon production efficiency,' to be 60%, which is lower than our calculated value, potentially due to their reported g value being a maximum, parameter uncertainties, or other degradations. Using this value for $\mathcal{P}_{\text{em}}$ results in $P_{\text{tot}} = 29.2\%$.

‡: We note that Ref. 178 is able to obtain a large coupling g yet in a different context than our work of cavity electromagnetically induced transparency (not single photon emission and absorption). Similar emitter values are reported in subsequent work from this group, e.g., Ref. 307 have the same emitter decay parameters (though $g/2\pi$ drops slightly due to cavity driving).

*: In some references, no value of $\mathcal{L}$ is given (nor the combined $\mathcal{T}_o + \mathcal{L}$), yet a quantity analogous to $\mathcal{P}_{\text{cav}}$ is reported. In these cases we infer the values of C_{cav} and $\mathcal{L}$ by backtracking.

-: Dashes are used for Ref. 306's cavity parameters as their setup is used for cavity enhanced measurement of one of two optical-tweezer-trapped atoms rather than controlled photon production out an asymmetric cavity.

NR: Not reported values of $\mathcal{L}$ nor $\mathcal{P}_{\text{cav}}$, in which case we take $\mathcal{L} = 0$ in the ensuing overestimation of $\mathcal{P}_{\text{cav}}$ (indicated via <). References and table values with - and NR qualifications are omitted in the abridged Table 4.1.

§: This value of $\mathcal{P}_{\text{cav}}$ is reported in Table I of Ref. 154.

¶: The fiber-cavity setup of Ref. 173 is used to achieve a state-of-the-art strong coupling g and large C_{cav} (for ion-cavity-QED experiments). Their setup is not designed for single-photon production preferentially out of one of the mirrors so the corresponding C_{cav} and $\mathcal{P}_{\text{cav}}$ reported here are strong lower bounds for the achievable values in an asymmetric cavity setup (e.g., for QST or remote entanglement generation).

as seen in §A.2.3. This cooperativity is written in our notation[20] with the nodal subscripts omitted. We do not expect such a bound to significantly limit us here as we are chiefly concerned with nodes in the strong-coupling of cavity QED limit with large atom-cavity couplings compared to the cavity linewidth and spontaneous emission rate, i.e., $2g \gtrsim \gamma, \Gamma_{sd}$. Note that this cooperativity based bound *cannot* be surpassed by 'simply' using a far off-resonant Raman process (see footnote 18). However, significant coupling to other excited states could change this, and indeed understanding the impact of the multilevel structure of realistic atoms in cavity quantum electrodynamics (QED) is an active area of research, wherein optical pumping offers a potential means of controlling decay channels to other states thereby potentially still achieving controlled interactions of single-photons with material qubits [150, 275, 308]. This entails that, within our model, certain wave packets can be emitted (or absorbed) with efficiency $\mathcal{P}_{\mathrm{em}}$, which is near unity for large C_{em}. Notably, not all wave packet shapes can be produced (even up to a scaling factor). The class of wave packets that can be produced at or near this efficiency is determined by the control drives $G_j(t)$ and the cavity linewidths γ_j (see §A.2).

Strategy 2). In terms of cavity loss, we note that although the probability of loss per single reflection from the cavity can be very low (parts per million), the number of round-trips the photon makes is comparably large for a high-Q cavity so cavity loss

[20] See footnote 4. Additionally, our use of Γ_{sd} to denote the spontaneous decay rate of an emitter was chosen to avoid ambiguity with the node-transmission-line couplings γ_j and with the Green's function Γ introduced in §4.3.1. In particular, note that the full cavity and atomic linewidths of γ and Γ_{sd} in our notation are often reported as 2κ and $2\gamma^{(\mathrm{atom})}$ [the superscript is used here to distinguish this parameter from our γ] in other work, respectively. In such other works, the corresponding half-linewidths κ and $\gamma^{(\mathrm{atom})}$ are typically referred to as the cavity field decay rate (or photon exit rate) and the atomic polarization decay rate, respectively (e.g., see Refs. 155 and 154). For instance, our emitter cooperativity C_{em} is equal to $4\mathcal{C} = \frac{2g^2}{\Gamma\kappa}$ in the notation of Ref. 154 and corresponds to $\frac{g^2}{\gamma\kappa}$ in the notation of Ref. 155 (in which the parameter $\gamma = \gamma_e/2 + \gamma_{\mathrm{deph}}$ accounts for the possibility of an additional dephasing mechanism on top of spontaneous emission of the upper state). See §A.1.2 and the comparison to Ref. 155 in §A.2.5 for some additional discussion.

becomes significant. In our exemplar case an asymmetric cavity is employed, which uses mirrors with different transmissivities to preferentially couple the cavity output to the transmission line. We denote the cavity mirror coupled to the transmission line as the inner one and the ideally perfectly reflecting mirror as the outer one (the light and dark gray mirrors in Fig. 1.5, respectively). Thus, we can calculate the probability of cavity light being emitted in the correct mode given the mirrors' respective transmissivities $\mathcal{T}_i$ and $\mathcal{T}_o$ as

$$\mathcal{P}_{\text{cav}} = \frac{\mathcal{T}_i}{\mathcal{T}_i + \mathcal{T}_o + \mathcal{L}} = \frac{C_{\text{cav}}}{1 + C_{\text{cav}}} \quad \text{with} \quad C_{\text{cav}} \equiv \frac{\mathcal{T}_i}{\mathcal{T}_o + \mathcal{L}}, \tag{A.79}$$

where $\mathcal{L}$ accounts for any additional coupling of the cavity to wrong output modes, e.g., due to absorption and scattering loss and in the second equality we put the equation in terms of a 'cavity cooperativity'[21] C_{cav}. Symmetrically, such a degradation of the overall success probability also occurs due to loss during absorption at cavity 2.

In general, there will be additional mode-matching losses between the cavities and transmission line. We do not explicitly treat these losses, yet they could easily be included via a less than unity prefactor for $\mathcal{P}_{\text{cav}}$. In particular, one would have 'mode-mismatch' factors, similar to $\eta_\perp$ of Eq. (A.9), for each cavity, when accounting for its coupling to the transverse modes of the transmission line.

Strategy 3). Generally, photon loss in a transmission line, e.g., fiber, occurs exponentially with length. That is, the probability that an initial photon will have

[21]The probability of an excitation transfer (be it atom to cavity, cavity to transmission line, vice versa, etc.) can be expressed schematically as $\mathcal{P}$ = (desired rate)/(total rate), where total rate = desired rate + undesired rate. Thereby, one can naturally define a corresponding cooperativity parameter C = (desired rate)/(undesired rate), which quantifies how well something (e.g., an emitter or cavity) couples to a desired output mode, such that $\mathcal{P} = C/(1 + C)$.

not been absorbed after propagating a distance x in the transmission line is

$$P_3(x) = e^{-x/x_{\mathrm{tl}}}, \tag{A.80}$$

where x_{tl} is a (frequency dependent) attenuation distance in a particular transmission line (e.g., see the quantum repeater references mentioned in §4.1.1). We simply state these standard results here and refer the reader to Ref. 154 for further discussion and analysis of such fiber and cavity losses in deterministic QST schemes. Note that the probability of photon loss due to the unitary transformation itself, e.g., due to absorption or scattering at U or if U is intrinsically probabilistic, is implicitly accounted for by the potential subnormalization of Ψ. For a given setup this can be made more explicit if an underlying transformation device efficiency $0 \leq \eta_U \leq 1$ can be characterized, then one can simply map $P_3 \to \eta_U P_3$.

Note that the applicability of this simple post hoc photon attenuation model relies on us leveraging the quantum trajectory formalism and the ECZ protocols. This is because on a single attempt, photon loss will undoubtedly lead to uncontrolled entanglement with other systems (e.g., the transmission line and its surroundings) and hence decoherence. However, by leveraging the carefully constructed redundancy of the ECZ protocols that makes it possible to detect when quantum jumps occur (see §A.3.4), we can effectively herald on the successful, smooth evolution transmissions.

Strategy 4). The strength and phase of the drives [laser pulses $G_j(t)$ in our case] used to control the systems can only themselves be controlled up to some precision set by their implementation. However, they can typically be controlled on short enough timescales relative to the cavity decay rate, e.g., a pulse duration on the order of $\gamma^{-1} \sim 1$ μs is typical in optical systems. Thus, good drive control is typically a modest assumption, yet we reiterate that the relative timing of the drives on sub γ^{-1}

time scales is also crucial. See Ref. 150 for an example of the precision with which such drives can be controlled on sub-μs time scales. There they report a photon production fidelity $\mathcal{F}$, given by the norm squared temporal overlap of the actual and target temporal modes, of 90%, which they suspect could be increased to 98% by suitably tuning the frequency of the local oscillator used. This indicates that errors in the drives of order $1 - \mathcal{F} \lesssim 1\%$, in terms of producing a photon wave packet with a particular desired shape and realizable duration (based on cavity and system parameters), should be achievable in a well-engineered setup, at least for atom in a cavity type nodes. Ref. 156 demonstrated a similar ability to generate single photons of $\sim 1 - 5$ μs widths with controllable envelope shape (on a sub μs timescale) using a trapped ion in a cavity yet they did not report target-actual state fidelities.

Strategy 5). Dispersion in the channel leads to a change in the shape and phase of the photon wave packet $\Psi(t)$, its impact can thus be accounted for by Eq. (4.2). Additionally, the wave packet will experience a group time delay due to its propagation in the transmission line which we assume is accounted for in the relative timing of U and of the drives $G_j(t)$. Material dispersion in the transmission line occurs due to the different frequency components of a wave packet traveling at different speeds due to a frequency dependent index of refraction $n_{\text{tl}}(\omega)$. Hence, its impact can be lessened by using photon wave packets with small frequency bandwidths compared to the frequency scale over which $n_{\text{tl}}(\omega)$ is approximately linear (relative to a given central frequency) (see §A.2.1). Accordingly, strategy 5), like 4), is less appropriate in cases where fast varying drives are desired (as we have alluded to this is an interested regime for achieving faster rates yet it comes with a multitude of complications).

If the dispersion is known and systematic (say by characterizing the channel) it can be (at least partially) compensated for by adjusting U. For instance, the stretching parameter ξ can be used to mitigate wave packet broadening issues due to dispersion (see §A.1.4). For a given implementation, accounting for the impacts of dispersion is crucial for matching the actual (dispersed) wave packet $\Psi(t)$ to the target shape $\Phi(t)$, as is necessary to obtain P_{success} near 1. However, such analysis is beyond the scope of this dissertation and we therefore recommend its further consideration by the community, both generally (e.g., see Ref. 128) as well as in particular implementations.

Summary. Thus, P_{success} of Ch. IV, which accounts for the impact of the unitary transformation, can be modified to account for the impacts of strategies 1)–3) through the post hoc multiplication of their respective survival probabilities as given by Eq. (4.14). In cases where strategies 4) and 5) are not appropriate, the actual wave packet Ψ will be intimately effected and the corresponding impacts must be accounted for in P_{success} itself, similar to how we analyzed errors in U. A full analysis accounting for the impact of additional structure (energy levels) of the emitter in strategy 1), laser errors in strategy 4), and channel induced distortion in strategy 5) would require additional model details about the nodes being used and the drives used to control them and so is not considered here. Moreover, there may be additional degradation factors depending on the precise setup (e.g., $\eta_\perp$ and η_U, as we alluded to).

A.3.2 Index of separability

To quantify the extent to which unitary transformation parameter errors depend on each other, we used the index of separability, $\mathcal{S}$. Here we elaborate on our methods for computing $\mathcal{S}$ for various two-variable joint probability distributions as defined in Eq. (4.39); this includes stability analysis accomplished by changing the input values

used. For each of the error variable pairs, we compute the separability index on evenly spaced n by n grids over the scaled versions of the regions illustrated in Fig. 4.5, which we will collectively refer to as $R = \{T, \xi, \omega_0 : |\gamma_2 \Delta T| \leq 7.5, |\Delta \ell_\xi| \leq 6, |\Delta \omega_0/\gamma_2| \leq 3\}$, picked based on widths of the single error variable P_{success} distributions. We refer to the region with each parameters domain scaled up by s as R_s. In Table A.2 we report $\mathcal{S}$ values for different regions and different matrix sizes (corresponding to different spacings). We consider $\mathcal{S}$ values computed using the singular values of the original matrices, A, as well as their zero-mean counterparts, $A^{(0)}$, defined for an $m \times n$ matrix A as $A^{(0)}_{ij} \equiv A_{ij} - \frac{1}{nm} \sum_{k=1}^{m} \sum_{l=1}^{n} A_{kl}$. We see that the original (nonzero mean) values are relatively stable (at least within a given region). The values reported in Eqs. (4.40)–(4.42) are given in the first row (in the nonzero-mean case). The intuition behind being able to change the region size is that these functions decay to zero for large errors and padding a matrix with zeros does not changes its nonzero singular values.

We will now explain why additionally considering $\mathcal{S}$ for the zero-mean counterpart of A, $A^{(0)}$, is valuable. If the original matrix under consideration A has nonzero-mean element μ, it is a mean-zero perturbation of the rank 1 matrix whose entries are all μ and hence there should be a corresponding singular value that is close to $|\mu|$. For appreciable $|\mu|$, relative to variations in the matrix elements, this singular value will be quite large (it can be the maximum) and will skew the separability $\mathcal{S}$ towards large values (closer to 1). For instance, one can show that for a large $n \times n$ matrix U with i.i.d. elements from a uniform distribution on $[0, 1]$, the expectation value of $\mathcal{S}(U^{(0)})$ tends to 0 as $n \to \infty$, whereas without shifting to a zero-mean matrix $\mathcal{S}(U)$ would tend to 3/4 as $n \to \infty$. (This can easily be checked numerically or more carefully using random matrix theory.) In the 61×61 case (to align with the values computed

TABLE A.2. Index of separability, $\mathcal{S}$, for each possible pairs of errors in the parameters ω_0, ξ, and T with the same parameter values used in the main text plots ($k = 2$, $\omega_{0i} = 50$, $\xi_i = 1/2$, and in units where $\gamma_2 = 1$). Here we vary i) whether we work with the original matrix (A) or its zero-mean counterpart ($A^{(0)}$) indicated by the presence of a (0) superscript, ii) what region the value is computed using, and iii) what matrix size is used for sampling over the region (in each case we chose the grid spacing to obtain a square $n \times n$ matrix). We include enough digits to show differences between the values. Calculation methods are discussed at the start of this section, which includes the region sizes considered. In each case, we effectively take l to be infinite, i.e., we consider the entire transformed wave packet. This does not significantly change the results, for instance changing to $l = 10c/\gamma_2$ (assuming $t_f = t_s + t_l/\xi_i$ still) in the case shown in the top row gives no change in the computed values to the reported precision. Note that $S_{\omega_0,T}$ is more stable than $S_{T,\xi}$ and $S_{\omega_0,\xi}$ because it goes to zero more quickly over the considered regions.

Case description		Indices of separability					
Region	n	$S_{T,\xi}$	$S_{\omega_0,\xi}$	$S_{\omega_0,T}$	$S^{(0)}_{T,\xi}$	$S^{(0)}_{\omega_0,\xi}$	$S^{(0)}_{\omega_0,T}$
R_2	121	0.869	0.870	0.9976548	0.800	0.804	0.969
R_2	61	0.869	0.869	0.9976548	0.801	0.805	0.970
R_2	41	0.868	0.869	0.9976547	0.801	0.805	0.970
$R_{4/3}$	81	0.886	0.886	0.9976548	0.765	0.770	0.942
$R_{4/3}$	41	0.886	0.885	0.9976548	0.767	0.771	0.943
R	61	0.902	0.901	0.9976551	0.726	0.732	0.908
R	31	0.901	0.900	0.9976550	0.729	0.735	0.910

in Table A.2), such a matrix has mean 0.758 with standard deviation 0.004. Hence the given nonzero-mean $\mathcal{S}$ values should be compared to ~ 0.75 for a random matrix instead of their global minimum of $1/n \sim 0$.[22] Accordingly, we report both the zero and nonzero-mean cases as we want to show that the ordering of the separability indices is not determined by the means and because the zero-mean matrices are less stable under changes to the region size,[23] respectively. Moreover, (in light of the phenomena discussed in footnotes 22 and 23) the original and zero-mean matrix separability indices, S and $S^{(0)}$, are upper and lower bounds for the separability index approached for large grid sizes, as can be seen in Fig. A.10 below. (We do not go to larger s values here to avoid additional complications with numerical integration of sharply localized and highly oscillatory functions.)

The perceptive reader may have noticed that $S_{T,\xi} \approx S_{\omega_0,\xi}$ in each of the above cases and wondered if this is a coincidence or due to some underlying structure. The answer is partially both, in that this behavior does not hold as closely for other emitted wave packets and corresponding amplitudes β_1 yet often these values will be close to one another. To gain some intuition behind this, we note that Eq. (4.30) can be expressed in terms of the dimensionless error variables $x = \Delta\omega_0/\gamma_2$, $y = \Delta\ell_\xi$, and

[22]Comparing against this 0.75 value specifically, which comes from a $\mu = 1/2$ case, is of course a drastic simplification. It is somewhat reasonable for the sizes of matrices we consider which have appreciable means (on the order of 0.5). However, this effect will become less and less of an issue as we consider P_{success} matrices over larger regions as they decay to zero away from their peaks and hence their means will approach zero. Accordingly, S tends to decrease as a function of s (in the region size R_s).

[23]For an original matrix A the edge of the considered regions (for which the errors are large) will be nearly zero, yet after subtracting the mean this value will be take on a values around $-\mu$ (which will go to zero for large grids but much slower than the original case). Padding by the necessary nonzero values will change the singular values of $A^{(0)}$ under increases to the region size, quantified by s. Specifically, the maximum singular value (relative to the others) will tend to increase as a function of s and hence $S^{(0)}$ will as well. For instance, for small s, P_{success} should be approximately constant so each of the zero-mean matrix approximations will be close to the constant matrix with all zero entries for which $S^{(0)} = 0$. As s increases and more structure is revealed a dominant singular value will thus emerge.

$z = \gamma_2 \Delta T$ (see footnote 6), in the $l \to \infty$ case where no matter what unitary errors occur all of the wave packet is transformed, as

$$P_{\text{success}}(x,y,z) = \left| \int_{-\infty}^{\infty} dt \underbrace{\sqrt{\gamma_2} e^{-i\omega_{0i}(T_i - t)} \beta_1^* \left(\xi_i (T_i - t)\right)}_{\Phi^*(t)} \underbrace{\sqrt{\gamma_1 \xi} e^{i\omega_0 (T-t)} \beta_1 \left(\xi (T-t)\right)}_{\Psi(t)} \right|^2$$
$$= 2^y \left| \int_{-\infty}^{\infty} d\tau \; e^{ix\tau} \beta_{\gamma 1}^* (\tau) \, \beta_{\gamma 1} \left(2^y (\tau + z)\right) \right|^2, \tag{A.81}$$

where in the last line we changed to the dimensionless time variable $\tau = \gamma_2 (T_i - t)$ and defined $\beta_{\gamma 1}(\tau) := \beta_1 (\tau / \gamma_1)$. Note this clearly shows that for a given shape of the emitted (not transformed) wave packet, which is proportional to the amplitude $\beta_{\gamma 1}$, the maximum value of P_{success} (which will be reduced due to other errors including those caused by finite l) is determined by the three errors parameters x, y, and z. For instance, regardless of what wave packet is emitted from node 1, a stretching error is always determined by the parameter $y = \Delta \ell_\xi = \log_2 (\xi / \xi_i)$. Thus if we consider a different implementation of node 2, called node $2'$, with larger coupling $\gamma_2' = 100 \gamma_2$ such that $\xi_i' = 100 \xi_i$ (for fixed γ_1), then to achieve the same stretching error we would need $\xi' = 100 \xi$ (the exact factor does not matter). Thus, the results for given parameter values, e.g., $\zeta = \omega_{0i}$ and γ_2, can clearly be generalized to different values via scaling. This entails that plots like Figs. 4.1-4.5, which do assume a certain emitted wave packet shape, can be applied to a node 2 with any parameter values [assuming it can be modeled by an effective Hamiltonian of the form discussed in §A.1.2 and given by Eq. (4.4)].

Now, noting that Fig. 4.5 (a) looks quite similar to Fig. 4.5 (b) after the mapping $y \to -y$, we compute $P_{z,y} \equiv P_{\text{success}}(0, y, z)$ and $P_{x,-y} \equiv P_{\text{success}}(x, -y, 0)$ so we can compare them. Defining ϖ to be the Fourier conjugate variable to τ with $\beta_{\gamma 1}(\tau) =$

$\int_{-\infty}^{\infty} \frac{d\varpi}{2\pi} e^{-i\varpi\tau} \tilde{\beta}_{\gamma 1}(\varpi)$, we have that (with all integrals taken from $-\infty$ to ∞)

$$P_{z,y} = 2^y \left| \int d\tau \ \beta^*_{\gamma 1}(\tau)\, \beta_{\gamma 1}\left(2^y(\tau + z)\right) \right|^2 = 2^y \left| \int d\tau \int \frac{d\varpi}{2\pi} \beta^*_{\gamma 1}(\tau) \tilde{\beta}_{\gamma 1}(\varpi) e^{-i2^y(z+\tau)\varpi} \right|^2 \tag{A.82}$$

and using $\tau' = 2^{-y}\tau$ in an intermediate step

$$\begin{aligned} P_{x,-y} &= 2^{-y} \left| \int d\tau \ e^{ix\tau} \beta^*_{\gamma 1}(\tau) \beta_{\gamma 1}\left(2^{-y}\tau\right) \right|^2 = 2^y \left| \int d\tau' \ e^{-ix2^y\tau'} \beta^*_{\gamma 1}(\tau')\, \beta_{\gamma 1}(2^y\tau') \right|^2 \\ &= 2^y \left| \int d\tau \int \frac{d\varpi}{2\pi} \beta^*_{\gamma 1}(\tau)\, \tilde{\beta}_{\gamma 1}(\varpi) e^{-i2^y(x+\varpi)\tau} \right|^2, \end{aligned} \tag{A.83}$$

which evidently takes on a similar form except for differences in the phase. Namely, the phases are equal under the exchanges $x \leftrightarrow z$ and $\varpi \leftrightarrow \tau$. Thus, if $\beta^*_{\gamma 1}(v) \approx \tilde{\beta}_{\gamma 1}(v)$ as functions, then $P_{z,y} \approx P_{x,-y}$ and it would follow that $S_{T,\xi} \approx S_{\omega_0,\xi}$. We can now confirm whether this intuition is valid in our case here, where $\beta_1(t)$ is given by Eq. (A.30). More precisely, from Fig. 4.5 we seem to have the scaling $2.5x \leftrightarrow z$ so we actually anticipate $P_{z=2.5x,y} \approx P_{x,-y}$ which would imply that

$$\int dv dv' \beta^*_{\gamma 1}(2.5v) \tilde{\beta}_{\gamma 1}(v'/2.5) e^{-i2^y(x+v)v'} \approx \int dv' dv \beta^*_{\gamma 1}(v') \tilde{\beta}_{\gamma 1}(v) e^{-i2^y(x+v)v'}, \tag{A.84}$$

which clearly has $\beta^*_{\gamma 1}(2.5v) = \tilde{\beta}_{\gamma 1}(v)$ as an exact solution (in which case the approximation would become an equality). This argument could clearly be applied to scalings other than the 2.5 value considered. We can quantify the degree to which the approximation $\beta^*_{\gamma 1}(2.5v) \approx \tilde{\beta}_{\gamma 1}(v)$ holds by computing the magnitude of the inner product of the two functions. Doing so numerically in our case with $\beta_1(t)$ given by Eq. (A.30), we find

$$\left| \int dv \ \hat{\beta}_{\gamma 1}(2.5v) \hat{\tilde{\beta}}_{\gamma 1}(v) \right| = 0.96, \tag{A.85}$$

where a function with a hat indicates that it is unit normalized as

$$\hat{f}(v) = \frac{f(v)}{\sqrt{\int dv' |f(v')|^2}}. \tag{A.86}$$

This inner product magnitude will be 1 if the functions are the same (up to a proportionality constant) so this large value of 0.96 indicates the approximation $\beta^*_{\gamma 1}(2.5v) \approx \tilde{\beta}_{\gamma 1}(v)$ is quite good, from which it follows that $S_{T,\xi} \approx S_{\omega_0,\xi}$ as we found.

Note that this is not always the case. A simple example illustrating this is the $r \to 0$ limit given in Eq. (A.33), for which $\beta_{\gamma 1}(\tau) = \Theta(\tau) e^{-\tau/2}$ and from Eq. (A.81) it directly follows that

$$P^{r\to 0}_{\text{success}}(x, y, z) = \frac{2^{y+2}}{(1+2^y)^2 + (2x)^2} \times \begin{cases} e^z, & z \leq 0 \\ e^{-2^y z}, & z > 0 \end{cases}. \tag{A.87}$$

In this case, because we have an easy to work with analytical formula for P_{success}, we can plot how the separability indices change for significantly larger regions, see Fig. A.10. We again consider scaling the bounds of the rectangular base region R by s in each direction (ω_0, ξ, and T) yielding the region R_s. We see that for each parameter pair the $\mathcal{S}$ values of both the original and zero-mean matrices converge to the same value, namely, $S_{\omega_0,T} = 1.00 > S_{\omega_0,\xi} = 0.85 > S_{T,\xi} = 0.78$ (with uncertainties of at most 0.01 in each case). Note that for $y = 0$ the function $P^{r\to 0}_{\text{success}}(x, 0, z) = e^{-|z|}/(1 + x^2)$ is evidently separable (it is a product of a function of x alone and a function of z alone) so an index of separability of $S_{\omega_0,T} = 1$ is fitting, in fact, requisite. We note that the ordering of the separability indices remains consistent for large grids

and $S_{T,\xi} \not\approx S_{\omega_0,\xi}$ here.[24] This aligns with our main point here, that ω_0 and T errors are nearly separable while the other errors pairs are less so.

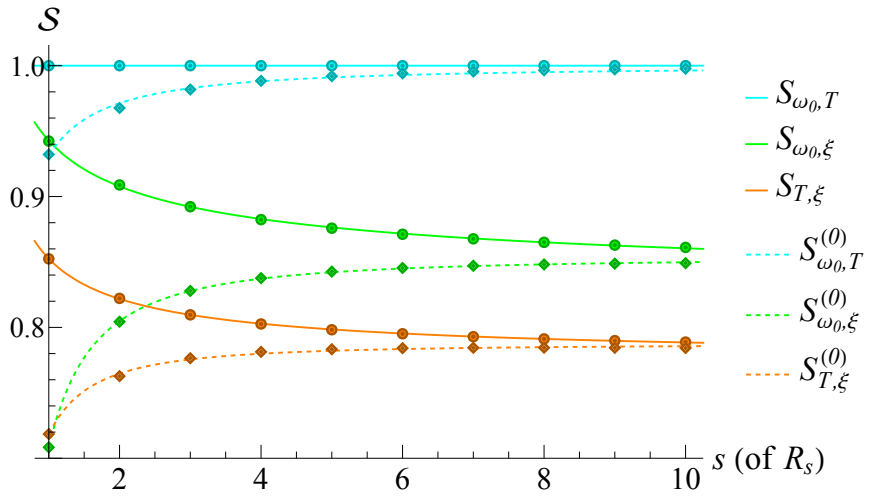

FIGURE A.10. Plots of the indices of separability, $\mathcal{S}$, for each error parameter pair as a function of region size as quantified by the scaling s corresponding to region R_s. This is done for both the original nonzero-mean matrices (solid lines) and their zero-mean counterparts (dashed lines), which serves as upper and lower bounds for the corresponding $\mathcal{S}$ value, respectively. These bounds approach one another as s increases and so $\mathcal{S}$ closes in to a fixed value (as reported above). Thus, although either matrix (original or zero mean) can itself be used for a separability estimate, they are best used in concert. The shown (circular and kite shaped) points are calculated for integer values of s from 1 to 10 with by evaluating Eq. (A.87) on a matrix (original and zero-mean counterpart) evaluated over the corresponding region R_s, where the spacing are kept constant for each error variable at the original region dimensions of R (from end to end) divided by 100. The underlaid curves are a power-law fit to the corresponding data points.

As mentioned in Ch. IV, we do not account for implementation specific dependencies of the parameters of U (and hence of the corresponding errors). However, we will now give a brief example of the role such additional dependencies play in analyzing multiple errors. In the sum frequency generation based implementation proposed by Ref. 37, the unitary parameter ω_0 would generically not

[24]This is intuitive here as the exponentially decaying $\beta_{\gamma 1}(\tau)$ is quite different than its Fourier transform, whose modulus squared is a Lorentzian.

be experimentally correlated with the parameters ξ and T. However, ξ and T may be correlated depending on the linear dispersion of the material used to implement the transformation. In this implementation, a frequency error could occur due to inaccurate characterization of or the inability to produce the frequencies of the pump pulse driving the transformation as well as the Raman lasers driving both systems. Furthermore, we have assumed these lasers to be monochromatic, where in reality they will have some natural linewidth leading to ω_0 errors. A stretching error would occur due to an incorrect group slowness (inverse group velocity), β'_j, in one of the bands $j \in \{1, 2, p\}$ as $\xi = \frac{\beta'_p - \beta'_2}{\beta'_1 - \beta'_p} > 0$. Note that $\beta_j(\omega)$ describes the linear dispersion of the medium so such an error could occur due to incorrect characterization of or defects in the material. Furthermore, higher-order dispersion, which Ref. 37 assumed to be negligible, could lead to an effective broadening of ξ that would induce errors. Here the timing T and corresponding errors are determined by the pump lasers timing relative to the wave packet emitted by system 1. Similar to ξ errors, this would also be affected by incorrect group slownesses, β'_j. Accordingly, ξ and T errors would also correspond to changes in the realized value of l for a given nonlinear medium length L (see App. A.1.5) due to changes in the linear dispersion of the medium.

A.3.3 Overview of ECZ protocols

As discussed in §A.1.6, the hybridization of QST, including the implementation of U, is simpler in the mode occupation number encoding. However, one ostensible drawback of this encoding is that a logical zero (e.g., no photon, $|0\rangle$) is not distinguishable from a photon loss error $|1\rangle \to |0\rangle$. Indeed, in our basic scheme, such loss is tantamount to an amplitude damping noise channel on the receiving qubit, which, if appreciable, would be ruinous for a single hybrid QST trial. Propitiously,

our scheme can naturally be extended to correct such errors by leveraging the ECZ error correction protocols of Refs. 2 and 164, which use auxiliary atoms (or other emitters) at each node to serve as a form of redundancy in the case of such a photon loss error. Then photon loss and phase errors can be detected and if an error occurs, the state of an auxiliary atom at the sending node will be projected onto the desired state to be transferred (at least after an appropriate local quantum computation) and an attempt of transferring the state can be repeated. One necessary condition for these protocols, as mentioned in §4.3.4, is that we are in a regime where no relevant photon production can occur (and that input field is in the vacuum state), i.e., the mapping $|0\rangle \rightarrow |1\rangle$ is not possible. This condition allows the ECZ protocols to be relatively simple and typically have less overhead as compared to other standard error correction schemes, which have to be able to correct for both $|1\rangle \rightarrow |0\rangle$ and $|0\rangle \rightarrow |1\rangle$ logical errors.

We will primarily focus on the earlier ECZ protocol [2] for concreteness and consistency with the exemplar atom in cavity systems we consider (though these protocols apply for other types of nodes provided the various steps can be implemented), mentioning differences in the later protocol [164] when applicable. Their basic setup is similar to our work except there are two atoms in each cavity to act as a form of redundancy and each atom has slightly different level structure due to one additional ground state (see Fig. A.11). One technical complication of using multiple atoms in a cavity is in accounting for the impact of the spatial dependence of the atom cavity coupling $g_j(\vec{x})$. Such position dependence is also present in the single atom case, though the interaction of the multiple atoms (or emitters more generally), especially as local operations are performed on the atoms, will increase the variation of $g_j(\vec{x})$. This will lead to some errors due to the chosen Raman pulses G_j being

slightly incompatible with the actual values of the couplings $g_j(\vec{x})$. Both our scheme and their protocol use states named $|g\rangle$ and $|e\rangle$ to encode the qubit. However, in our scheme these are the only two (long-lived) levels and they are joined by a Raman transition. Whereas in this ECZ protocol the 'excited' qubit state $|e\rangle$ is linked via a Raman transition to an auxiliary level $|r\rangle$, not to be confused with our upper level of the same name. In this case, ECZ's nominal ground state $|g\rangle$ is isolated in terms of transitions to the other levels during the Raman process, though it could possibly amplitude damp or phase shift due to interacting with the environment [e.g., due to photon absorption or spontaneous emission (to another level outside the levels considered)]. Despite these differences, our protocol can easily be mapped to their level structure with the EOMs we derive for our $|e\rangle \leftrightarrow |g\rangle$ Raman transition simply corresponding to $|e\rangle \leftrightarrow |r\rangle$ for ECZ.

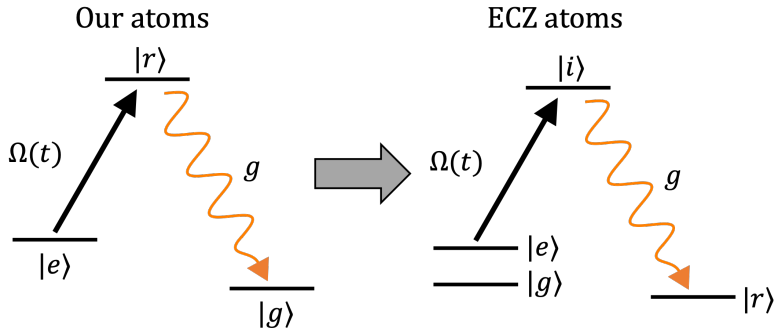

FIGURE A.11. Comparison of atomic configurations in our scheme (left) versus that used in the earlier ECZ error correction protocol (right) [2].

A.3.4 First ECZ protocol summary

We will now summarize the earlier ECZ protocol [2]. We include this for reference and so that we can analyze the expected number of repetitions of a primitive of the protocol, $E[n]$, necessary for successful QST. This is accomplished by explicitly

tracking the normalization factors. To our knowledge, this calculation of $E[n]$ and our commentary is novel, though we want to emphasize that the protocol itself is fully credited to Ref. 2. We use their labeling for the atoms, cavity 1 contains two atoms 1 and b (for *backup*) while cavity 2 contains two atoms 2 and a (for *auxiliary*). The cavities are coupled to a transmission line in a unidirectional manner analogous to our scheme that allows a photon emitted by system 1 to propagate to and potentially be absorbed by system 2. Their protocol consist of five steps:

(i) "Local redundant encoding." The state we want to transfer is initially encoded in atom 1 as $|\psi_1\rangle = c_0|g_1\rangle + c_1|e_1\rangle$ with atom b in $|g_b\rangle$ and the system 2 atoms both in the auxiliary level, $|r_2\rangle|r_a\rangle$, such that the total state is $|\psi_{\text{tot}}\rangle = |g_b\rangle|\psi_1\rangle|r_2\rangle|r_a\rangle$. Then we perform an entangling operation $U_{b1} = \text{CNOT}_{b1}(H_b \otimes X_1)$ (with b acting as the control qubit for the CNOT, as depicted in Fig. A.12) on the system 1 qubits, where H and X are the Hadamard and not gates. This yields the state

$$|\psi_{\text{tot}}\rangle \xrightarrow{U_{b1}} \frac{1}{\sqrt{2}}\left(|\overline{\psi}_b\rangle|g_1\rangle + |\psi_b\rangle|e_1\rangle\right)|r_2\rangle|r_a\rangle = \frac{1}{\sqrt{2}}\left(|\overline{\psi}_b\rangle|\Phi_i\rangle + |\psi_b\rangle|\Psi_i\rangle\right) \tag{A.88}$$

with $|\overline{\psi}_j\rangle = X|\psi_j\rangle = c_1|g_j\rangle + c_0|e_j\rangle$ for j one of the atom labels, $|\Phi_i\rangle = |g_1\rangle|r_2\rangle|r_a\rangle$, and $|\Psi_i\rangle = |e_1\rangle|r_2\rangle|r_a\rangle$ with i denoting the step of the protocol. We will track how these states $|\Psi\rangle$ and $|\Phi\rangle$ (not to be confused with our actual and ideal wave packets), evolve over the steps of the protocol, notably they will stay orthogonal $\langle\Psi|\Phi\rangle = 0$ for each step (denoted in their subscript). Here atom b at system 1 acts as a form of redundancy in case an error occurs, it does not explicitly participate in the transmissions.

(ii) "Transmission from atom 1 to 2." We now implement our QST scheme between atom 1 and atom 2. The possibility of photon loss and spontaneous emission to other atomic levels during the transfer leads to dissipative dynamics which can be described

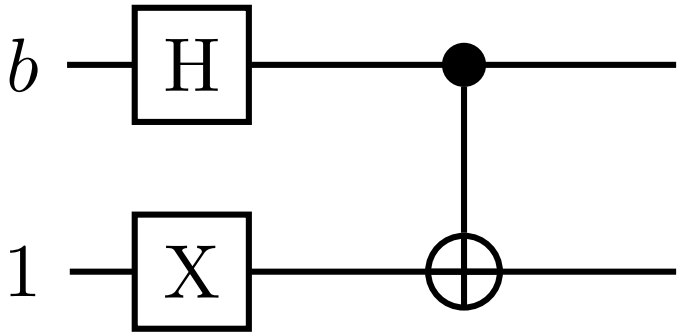

FIGURE A.12. The gate U_{b1} as a circuit diagram.

in the quantum trajectory formalism [122, 140, 141]. In this description, for long times the system will either undergo a dissipative quantum jump due to loss, causing the state of the atoms to leave the desired subspace, with probability P_{jump} or it will undergo smooth evolution (no quantum jump occurs) with probability $1 - P_{\text{jump}}$. If a quantum jump does not occur, the states evolve according to an effective Hamiltonian H_{eff} for large times according to Eq. (4.43), which can be restated in the language of ECZ yielding their Eq. (3) [2]

$$\begin{array}{ll} |g_1\rangle|r_2\rangle & \\ |e_1\rangle|r_2\rangle & \end{array} \xrightarrow{H_{\text{eff}}} \begin{array}{c} \alpha|g_1\rangle|r_2\rangle \\ \beta|r_1\rangle|e_2\rangle + \Upsilon_1|r_1\rangle|r_2\rangle + \Upsilon_2|e_1\rangle|r_2\rangle \end{array} . \tag{A.89}$$

(Here we try to use Ref. 2's notation including state labels, except we use $\Upsilon_{1,2}$ instead of $\gamma_{1,2}$ to avoid confusion with our node-channel couplings γ_j).

The amplitudes α and β are ideally 1, their departure from unity corresponds to amplitude damping and phase errors. An error in α would typically be a phase error in the ground states $|g\rangle$ and $|r\rangle$. This could be a (likely small) phase error due to expected imperfections in accounting for the phases imparted to these states by the ac Stark shifts during the Raman process or due to magnetic field noise (e.g., in a

Zeeman or hyperfine qubit). Additionally, (typically with much lower probability) α errors could occur as a result of more dramatic effects such as transition to a state out of the qubit manifold or auxiliary state $\{|g\rangle, |e\rangle, |r\rangle\}$, e.g., by spontaneous emission, followed by repumping to $|g_1\rangle|r_2\rangle$ [164]. Thus, α will typically be a pure phase though its value depends strongly on which states are used to encode the material qubit. The amplitude β accounts for an excitation being successfully transferred. An error in β could occur due to loss of the intermediate photon or an error in the local oscillators used to track the phase. Meanwhile, Υ_2 corresponds to an error where the excitation to be transferred undesirably remains at system 1, say due to an incorrect first Raman pulse that does not induce the transition $|e_1\rangle \rightarrow |g_1\rangle$.[25] Finally, Υ_1 corresponds to photon loss during the transmission (photon absorption, leaking out of cavity 2, spontaneous emission during the first Raman process, an incorrect second Raman pulse that does not induce the transition $|r_2\rangle \rightarrow |e_2\rangle$, etc.).

For this transmission attempt we will have $|\beta|^2 + |\Upsilon_1|^2 + |\Upsilon_2|^2 = 1$, where we assume that we either stay in the single-excitation subspace (β and Υ_2 terms) or atom 1 undergoes the Raman transition from $|e_1\rangle$ to $|r_1\rangle$ yet the photon is lost so atom 2 stays in $|r_2\rangle$ (Υ_1 term), which corresponds to a quantum jump mechanism. Note that $|\alpha| \leq 1$ due to spontaneous emission to other levels (α is treated differently than β and $\Upsilon_{1,2}$ as said other levels are outside the subspace we have considered so we do not write their amplitudes explicitly). In this case where no quantum jump occurs, we need to renormalize the entire state by dividing by $\mathcal{N}_{ii} = \sqrt{(1 + |\alpha|^2)/2}$.

[25]Note that Υ_2 errors can be mapped onto Υ_1 errors by performing the local operation $|e_1\rangle \rightarrow |r_1\rangle$ after the transmission, say via optically pumping, then we obtain a map of the same form as equation (3) of Ref. 164.

Thus, under the above map for a transmission attempt, the states become

$$|\Phi_{ii}\rangle = \alpha'|g_1\rangle|r_2\rangle|r_a\rangle \tag{A.90}$$

and

$$|\Psi_{ii}\rangle = \left(\beta'|r_1\rangle|e_2\rangle + \Upsilon_1'|r_1\rangle|r_2\rangle + \Upsilon_2'|e_1\rangle|r_2\rangle\right)|r_a\rangle \tag{A.91}$$

where we define the primed amplitudes as their original counterparts renormalized, e.g., $\alpha' = \alpha/\mathcal{N}_{ii}$ and likewise for β', Υ_1', and Υ_2', such that $|\alpha'|^2+|\beta'|^2+|\Upsilon_1'|^2+|\Upsilon_2'|^2 = 2$ [with the normalization due to the convention of Eq. (A.88)].

Alternatively, a quantum jump can occur due to either the loss of an excitation with probability[26] $P_{\text{jump}}^{(1)} = 1 - (|\beta|^2 + |\Upsilon_2|^2) = |\Upsilon_1|^2$ or due to amplitude damping of the ground states with probability $P_{\text{jump}}^{(0)} = 1 - |\alpha|^2$. Due to original amplitudes of the initial state in Eq. (A.88), where effectively $|c_e| = |c_g| = 1/\sqrt{2}$ in our notation, we have that

$$P_{\text{jump}} = \frac{1}{2}\left(P_{\text{jump}}^{(0)} + P_{\text{jump}}^{(1)}\right) = \frac{1}{2}\left(1 - |\alpha|^2 + |\Upsilon_1|^2\right). \tag{A.92}$$

As noted by Ref. 2, such a quantum jump is a special case of Eq. (A.89) with $\alpha = \beta = \Upsilon_2 = 0$, the corresponding error can be detected in step (iv) (detailed below) [2]. Importantly, the protocol still works if a quantum jump occurs during one transmission but not the other; this is notable because the amplitudes will be different in this case yet the error can still be detected.

[26]Mapping this to our earlier notation $|\beta| \to |\alpha_2(t_e)|$ and $|\Upsilon_2| \to |\alpha_1(t_e)|$, we see that this is the same jump probability one would obtain from Eq. (3.65), when accounting for the possibility that atom 1 stays excited, which contributes to an error (via Υ_2) but not an jump.

Next after the transmission attempt, we measure whether atom 1 is in state $|e_1\rangle$. If yes, an error has occurred where no photon has been emitted, and the state collapses to

$$|\psi_{\rm tot}\rangle \to |\psi_b\rangle|e_1\rangle|r_2\rangle|r_a\rangle. \tag{A.93}$$

In this case, the backup atom b has recovered the original state so, after resetting the other atoms, steps (i-ii) can then be repeated (with the roles of atoms 1 and b switched) until no Υ_2 error occurs. The probability of having to stop and repeat the protocol at step (ii) is

$$P_{ii} = \frac{|\Upsilon_2'|^2}{2} = \frac{|\Upsilon_2|^2}{1+|\alpha|^2}, \tag{A.94}$$

which should be very small (under appropriate driving, G_1). Otherwise, if atom 1 is not found to be in $|e_1\rangle$, then the corresponding term in Eq. (A.91) is projected out and the state is renormalized, e.g., $\alpha' \to \alpha'' = \alpha'/\sqrt{1-\frac{1}{2}|\Upsilon_2'|^2}$ with β'' and Υ_1'' defined similarly.

(iii) "Symmetrization." Perform a local operation on atom 1 that maps $|r_1\rangle \to |g_1\rangle$ and $|g_1\rangle \to |e_1\rangle$, such that

$$|\Phi_{iii}\rangle = \alpha''|e_1\rangle|r_2\rangle|r_a\rangle \tag{A.95}$$

and

$$|\Psi_{iii}\rangle = |g_1\rangle\left(\beta''|e_2\rangle + \Upsilon_1''|r_2\rangle\right)|r_a\rangle. \tag{A.96}$$

(iv) "Transmission from atom 1 to a." The states evolve according to the map above, Eq. (A.89), with $2 \to a$, with potentially different amplitudes (denoted by tildes). If no quantum jump occurs, with probability $1-\tilde{P}_{\rm jump}$, this yields the

renormalized states

$$|\Phi_{iv}\rangle = \alpha'' \left(\tilde{\beta}' |r_1\rangle|e_a\rangle + \tilde{\Upsilon}'_1 |r_1\rangle|r_a\rangle + \tilde{\Upsilon}'_2 |e_1\rangle|r_a\rangle \right) |r_2\rangle \tag{A.97}$$

and

$$|\Psi_{iv}\rangle = \tilde{\alpha}' |\Psi_{iii}\rangle, \tag{A.98}$$

where, as in step (ii), we define the normalized amplitudes by dividing the original tilded ones by

$$\mathcal{N}_{iv} = \sqrt{\frac{|\alpha|^2 + |\tilde{\alpha}|^2 \left(1 - |\Upsilon_2|^2\right)}{1 + |\alpha|^2 - |\Upsilon_2|^2}}, \tag{A.99}$$

e.g., $\tilde{\beta}' = \tilde{\beta}/\mathcal{N}_{iv}$. Alternatively, a jump will occur with a probability analogous to Eq. (A.92) with $\tilde{P}^{(1)}_{\text{jump}} = |\tilde{\Upsilon}_1|^2 |\alpha''|^2$ and $\tilde{P}^{(0)}_{\text{jump}} = \left(1 - |\tilde{\alpha}|^2\right) \left(|\beta''|^2 + |\Upsilon''_1|^2\right)$ (which take on their previous form multiplied by the relative probability of actually being in that state) so that

$$\tilde{P}_{\text{jump}} = \frac{1}{2} \left[\left(1 - |\tilde{\alpha}|^2\right) \left(|\beta''|^2 + |\Upsilon''_1|^2\right) + |\tilde{\Upsilon}_1|^2 |\alpha''|^2 \right]. \tag{A.100}$$

Then we measure if the atoms at node 2 are in the state $|r_2\rangle|r_a\rangle$.[27] If yes, the states are (up to a common normalization factor)

$$|\Phi_{iv}\rangle \to \alpha \left(\tilde{\Upsilon}_1 |r_1\rangle + \tilde{\Upsilon}_2 |e_1\rangle \right) |r_2\rangle|r_a\rangle \tag{A.101}$$

and

$$|\Psi_{iv}\rangle \to \tilde{\alpha} \Upsilon_1 |g_1\rangle|r_2\rangle|r_a\rangle \tag{A.102}$$

[27]Note Ref. 2 says to measure if atom 1 is in $|e_1\rangle$ before this, though we do not need to as the same error can be detected by this measurement.

and an error has occurred and we measure the state of atom 1. If $|g_1\rangle$ is measured, atom b is in the state $|\psi_b\rangle$, otherwise if we measure $|r_1\rangle$ or $|e_1\rangle$, then atom b is in the state $|\overline{\psi}_b\rangle$ and a NOT gate, X, should be performed. Either way, atom b ends in the state to be transferred $|\psi_b\rangle$, and the process should be repeated (after resetting the other atoms). Similar to step (ii), the probability having to stop and repeat the protocol here is

$$P_{iv} = \frac{1}{2}\left[|\alpha''|^2(|\tilde{\Upsilon}'_1|^2 + |\tilde{\Upsilon}'_2|^2) + |\tilde{\alpha}'|^2|\Upsilon''_1|^2\right]. \tag{A.103}$$

If we do not measure $|r_2\rangle|r_a\rangle$, the states are

$$|\Phi_{iv}\rangle \to \alpha\tilde{\beta}|r_1\rangle|r_2\rangle|e_a\rangle \tag{A.104}$$

and

$$|\Psi_{iv}\rangle \to \tilde{\alpha}\beta|g_1\rangle|e_2\rangle|r_a\rangle \tag{A.105}$$

(up to a common normalization factor). Hence under the assumption that the α and β errors are systematic and hence the same for both transmissions, i.e., $\alpha = \tilde{\alpha}$ and $\beta = \tilde{\beta}$, we have (accounting for the normalization)

$$|\psi_{\text{tot}}\rangle = \frac{e^{i\arg(\alpha\beta)}}{\sqrt{2}}\left(|\overline{\psi}_b\rangle|r_1\rangle|r_2\rangle|e_a\rangle + |\psi_b\rangle|g_1\rangle|e_2\rangle|r_a\rangle\right), \tag{A.106}$$

where we can neglect the phase as it is global.

(v) "Teleportation." We first perform a local operation that takes $|r_2\rangle \to |g_2\rangle$. Then we make several measurements of the state of: (a) atom b in the standard basis, (b) atom 1 in the $|\pm_1\rangle = (|g_1\rangle \pm |r_1\rangle)/\sqrt{2}$ basis, and (c) atom a in the $|\pm_a\rangle = (|e_a\rangle \pm |r_a\rangle)/\sqrt{2}$ basis. We summarize the results in a piecewise function, where in each

line the right-most part, after the comma, summarizes the measurement outcomes

$$|\psi_{\rm tot}\rangle \rightarrow \begin{cases} c_1|g_2\rangle + c_0|e_2\rangle, & |g_b\rangle|+_1\rangle|+_a\rangle \\ c_1|g_2\rangle - c_0|e_2\rangle, & |g_b\rangle|+_1\rangle|-_a\rangle \\ -c_1|g_2\rangle + c_0|e_2\rangle, & |g_b\rangle|-_1\rangle|+_a\rangle \\ -c_1|g_2\rangle - c_0|e_2\rangle, & |g_b\rangle|-_1\rangle|-_a\rangle \\ c_0|g_2\rangle + c_1|e_2\rangle, & |e_b\rangle|+_1\rangle|+_a\rangle \\ c_0|g_2\rangle - c_1|e_2\rangle, & |e_b\rangle|+_1\rangle|-_a\rangle \\ -c_0|g_2\rangle + c_1|e_2\rangle, & |e_b\rangle|-_1\rangle|+_a\rangle \\ -c_0|g_2\rangle - c_1|e_2\rangle, & |e_b\rangle|-_1\rangle|-_a\rangle \end{cases} . \tag{A.107}$$

These resulting states of atom 2 can clearly all be changed to the desired state $|\psi_2\rangle = c_0|g_2\rangle + c_1|e_2\rangle$ using standard local operations. Hence, we have effectively teleported the state from atom 1 to 2, even in the presence of errors and noise.

A.3.5 Scope of ECZ protocols

This protocol [2] can lead to ideal QST after an appropriate number of process repetitions (trials), assuming the errors in the transmission are systematic within a given trial and the system channel interaction is described by a Markovian process. Specifically, it is assumed that the parameters α and β, which account for phase shift and amplitude damping of the atomic qubit encoding, are the same in both transmissions in a given trial, e.g., steps (ii) and (iv). If these parameters are not systemic and hence vary in a given trial, the fidelity of the resulting tilded state $|\tilde{\psi}_{\rm tot}\rangle$ [with $\alpha \neq \tilde{\alpha}$ and $\beta \neq \tilde{\beta}$ in Eqs. (A.104) and (A.105) yet accounting for normalization]

with the target state $|\psi_{\rm tot}\rangle$ of Eq. (A.106) is

$$\mathcal{F}_{\rm tot} = \left|\langle\psi_{\rm tot}|\tilde{\psi}_{\rm tot}\rangle\right|^2 = \frac{\left|\alpha\tilde{\beta} + \tilde{\alpha}\beta\right|^2}{2(|\tilde{\alpha}|^2|\beta|^2 + |\alpha|^2|\tilde{\beta}|^2)}. \tag{A.108}$$

This total state fidelity limits the ultimate fidelity of the state transferred in step (v). To quantify the discrepancy we define $\tilde{\alpha} = r_a e^{i\delta_a}\alpha$, $\tilde{\beta} = r_b e^{i\delta_b}\beta$, and $\delta_{ab} \equiv \delta_a - \delta_b$ such that

$$\mathcal{F}_{\rm tot} = \frac{\left|r_b + r_a e^{i\delta_{ab}}\right|^2}{2(r_a^2 + r_b^2)} = \frac{1}{2} + \frac{r_a r_b}{r_a^2 + r_b^2}\cos(\delta_{ab}), \tag{A.109}$$

which oscillates about $1/2$ as a function of δ_{ab} with amplitude $0 \leq r_a r_b/(r_a^2+r_b^2) \leq 1/2$ with the maximum amplitude occurring at $r_a = r_b$ (note $r_a \approx 1$ typically). This clearly emphasizes the need to suppress phase errors as, no matter what r_a and r_b are, this fidelity is maximum for $\delta_{ab} = 0$ and averages to the futile value of $1/2$ over all phase errors $0 \leq \delta_{ab} < 2\pi$. Importantly, one only needs δ_{ab} to be small over subsequent transmissions in a given trial, not necessarily between trials. Thus, in cases where systematic errors are dominant $\mathcal{F}_{\rm tot} \approx 1$ and this protocol is appropriate.

Note that the later ECZ protocol [164] extends the former by being able to correct for more general random errors, namely $\alpha \neq \tilde{\alpha}$ or $\beta \neq \tilde{\beta}$, in a noisy channel with potentially non-Markovian decoherence. To make this possible, one has to repeat certain 'purification' process that causes the joint state of one qubit at node 1 and one at node 2 to iteratively approach a target entangled state (e.g., a Bell state) with a fidelity that should exponentially approach 1. Then quantum state teleportation can be used to implement QST between the nodes [83, 309]. Note that both of the ECZ protocols assume that local operations can be performed perfectly on the ground states of a single atom (emitter more generally), including the auxiliary ground state for Ref. 2, and for entanglement operations on two atoms in a given node. This

condition of error-free local gates could of course be approached using quantum error correction schemes at the nodes themselves. However, this would be at the cost of a large overhead in physical qubits with long coherence times that are acted on by high fidelity gates (i.e., in the fault-tolerant limit), which even if possible would likely make interfacing with the communication channel more difficult. Hence, as discussed in the §4.4, a compromise needs to be made between the potential benefit of an error correction protocol and the additional overhead and errors that will accompany it.

Now that we have kept track of the probabilities of having to restart the earlier ECZ protocol [2] due to a quantum jump occurring or after detecting an error in the measurements of steps (ii) and (iv), we can compute the expected number of trials of the protocol $E[n]$. The probability that an entire trial is successful is

$$P_s = (1 - P_{\text{jump}})(1 - P_{ii})(1 - \tilde{P}_{\text{jump}})(1 - P_{iv}) \tag{A.110}$$

and the corresponding probability of a given trial failing (having to be stopped and repeated) is $P_f = 1 - P_s$. Thus the expected number of trials (repetitions of the protocol) until success is the standard

$$E[n] = P_s \sum_{n=1}^{\infty} n P_f^{n-1} = \frac{P_s}{(1 - P_f)^2} = \frac{1}{P_s}. \tag{A.111}$$

[In the language of statistics, the probability distribution underlying such a process is called the geometric distribution (assuming independent trials with the same P_s) and its properties are well known, e.g., its standard deviation is $\sqrt{1 - P_s}/P_s = E[n]\sqrt{1 - 1/E[n]}$.] Now our task is to carefully compute P_s; to do so we must keep track of the scaling of the renormalized variables. Doing so, using Eq. (A.92), (A.94), (A.100), and (A.103), and proceeding under the assumption that all the errors are

systematic and hence the same for both transmissions (including the $\Upsilon_{1,2}$ ones for simplicity, though this is not strictly necessary), we have

$$\begin{aligned} P_s &= \frac{1}{2}\left(1+|\alpha|^2-|\Upsilon_1|^2\right)\left(1-\frac{|\Upsilon_2|^2}{1+|\alpha|^2}\right) \\ &\quad\times\left(1-\frac{1-|\beta|^2|\alpha|^2-|\Upsilon_2|^2}{1+|\alpha|^2-|\Upsilon_2|^2}\right)\left(1-\frac{2|\Upsilon_1|^2+|\Upsilon_2|^2}{2-|\Upsilon_2|^2}\right) \\ &= \frac{|\alpha|^2|\beta|^2(1+|\beta|^2)(1+|\alpha|^2-|\Upsilon_1|^2)}{(1+|\alpha|^2)(2-|\Upsilon_2|^2)}, \end{aligned} \tag{A.112}$$

where we used the relation $|\beta|^2+|\Upsilon_1|^2+|\Upsilon_2|^2=1$. Hence, in this systematic case

$$E[n]=\frac{1}{P_s}=\frac{(1+|\alpha|^2)(2-|\Upsilon_2|^2)}{|\alpha|^2|\beta|^2(1+|\beta|^2)(1+|\alpha|^2-|\Upsilon_1|^2)}. \tag{A.113}$$

If we take $|\alpha|=1$, as was the case in the main text, we find

$$P_s=\frac{|\beta|^2\left(1+|\beta|^2\right)\left(2-|\Upsilon_1|^2\right)}{2\left(2-|\Upsilon_2|^2\right)}, \tag{A.114}$$

which is clearly zero only if $\beta=0$ as one may expect. Moreover, if we assume that a photon is already created at node 1, i.e., there are no errors in the first Raman pulse, then $\Upsilon_2=0$ so the above expression simplifies to

$$P_s=\frac{|\beta|^2\left(1+|\beta|^2\right)^2}{4}. \tag{A.115}$$

Although we expect to be dominated Υ_1 errors with $|\alpha|\approx 1$ and $\Upsilon_2\approx 0$, suppose that each variable suffers an order ε error. Specifically, we take $|\Upsilon_1|^2=x\varepsilon$ and $|\Upsilon_2|^2=(1-x)\varepsilon$ with $0\leq x\leq 1$ such that $|\beta|^2=1-\varepsilon$ and for simplicity we also take $|\alpha|^2=1-\varepsilon$ as an effectively worst case scenario (as generically β errors will be much more significant than those in α). In this model, the lowest values of P_s all occur for

$x = 1$ and in that worst case we obtain

$$E[n] = \frac{1}{(1-\varepsilon)^3}, \tag{A.116}$$

which is small (near 1) for ε near 0 yet diverges toward $+\infty$ as $\varepsilon \to 1$. This divergence is similar to the case considered in Ch. IV with $|\alpha| = 1$, see Eq. (4.44), yet occurs more rapidly (as one would expect, as we are considering a case with both α and β amplitude damping errors).

APPENDIX B

INTERFERENCE OF INTERFERENCE EFFECTS

We encourage readers to actively engage with the ideas presented in this work. To facilitate this, here we provide several "do-it-yourself"-type exercises that are intended to beget further open-ended exploration of our setup. These exercises are intended to be solved through a combination of pen-and-paper calculations and simulation work using the Virtual Lab (VL) developed by Quantum Flytrap (QF).[1] Accordingly, each exercise is tagged with at least one of the categories: analytical (A) or Quantum Flytrap (QF). Solutions are provided in App. B.2 and extend beyond what we expect a typical reader would find (e.g., in Exercise 2, we present a general class of solutions along with several notable subcases, whereas identifying these subcases alone should be sufficient for the reader).

We chose to frame the appendices as exercises and solutions because we find the solutions interesting, yet we also think that many readers should be well equipped to solve (at least some of) the exercises. Moreover, the exercises and overall content of this paper are well suited for students to explore in an advanced undergraduate or early graduate course in quantum mechanics, quantum optics, or quantum information. Thus, we encourage instructors of such courses to use these exercises or variations thereof in their teaching (with appropriate acknowledgment). This work is the appendiceal content of Ch. V as available in the preprint Ref. 5 (these exercises and their solutions were)

[1]The Virtual Lab is an excellent resource for simulating, exploring, and learning about photonic interference, including our setup. It can be accessed online at lab.quantumflytrap.com/lab, which includes descriptions of how to use it. See Ref. 208 for further details.

B.1 Exercises and simulation tools

1. **Simulate the full setup.** [QF]

   Simulate our full setup (shown in Fig. 5.1) in the QF VL. Suggested workflow:

   (a) Start by exploring QF's preexisting MZi and HOMi setups as well as the different components available in the VL.

   (b) Extend this to the full setup, and run the simulation to see that it is behaving as expected.

   (c) Characterize the probability distribution of two-photon detection events and make a plot analogous to Fig. 5.7. Do so by running the simulation N times (determine a reasonable number and modify as necessary) and analyzing the resulting data using your software of choice (a spreadsheet editor is sufficient).

2. **Can we eliminate or enhance the interference of interference effects?** [A, QF]

   Consider varying the transmission and reflection coefficients of the BSs used in the setup (while preserving left-right symmetry). Assume that none of the path amplitudes are zero so that both MZi and HOMi occur to some extent.

   (a) Can the BS coefficients be altered such that $P_{2,3} = 0$? If so, give an example and discuss whether the semi-naive reasoning is now valid. If not, show why.

   (b) How can these coefficients be altered to maximize $P_{2,3}$, while maintaining both full MZi and HOMi? [*Hint: The respective conditions for these full*

interference effects are $O_S + Z_S = 0$ (for both sides S) and $Z_L Z_R + C_L C_R = 0$; see Sec. 5.3.3.]

Explore your findings in QF's VL.

3. **What if the photons are distinguishable?** [A, QF]

   Consider the setup of Fig. 5.1, except suppose that the photons are fully distinguishable, e.g., they have two different colors or have orthogonal polarizations. How does the two-photon event probability distribution of Fig. 5.7 change? [*Hints: Use the counting method from the main text, but modify it to account for certain outcomes (that were previously indistinguishable) now being distinguishable. As in Exercise 1, use QF's VL to explore (the input photons' colors and/or polarizations can be adjusted). Coincident detection probabilities, such as $P_{2,3}$ and $P_{1,4}$, can be shown in the VL (see Fig. B.1; the VL's "beam" mode can be used to easily show the long-run values of these probabilities).*]

4. **Are single-photon inputs necessary?** [A]

   Rather than using true single-photon inputs, can we see the same "interference of interference " phenomenon using weak coherent states as one or both of the inputs?

   Additional context. To review (or briefly introduce) coherent states, we note that they can be defined by their number state representation (expressed in Dirac notation) as

$$|\alpha\rangle = e^{-|\alpha|^2/2} \sum_{n=0}^{\infty} \frac{\alpha^n}{\sqrt{n!}} |n\rangle, \tag{B.1}$$

where $|n\rangle$ is the state with n photons (in the relevant mode) and α is a complex number that characterizes the full state.[2] Thus, the corresponding probability of measuring n photons is

$$P_n = |\langle n|\alpha\rangle|^2 = e^{-|\alpha|^2}|\alpha|^{2n}/n! \tag{B.2}$$

Accordingly, for small $|\alpha| \ll 1$, i.e., a "weak coherent state," one can reasonably truncate the sum of Eq. (B.1) as higher photon number terms will be suppressed. As we are concerned with two-photon events, we need to keep the terms up to quadratic order ($n = 2$):

$$|\alpha\rangle \approx \frac{|0\rangle + \alpha|1\rangle + \frac{\alpha^2}{\sqrt{2}}|2\rangle}{\sqrt{1 + |\alpha|^2 + |\alpha|^4/2}}. \tag{B.3}$$

For example, when $|\alpha| = 0.1$: $P_0 \approx 99.005\%$, $P_1 \approx 0.990\%$, and $P_{n\geq 2} \approx 0.005\%$. This means that when measuring such a state, roughly 99% of the time there will be no photon, yet during the nearly 1% of the time when at least one photon is present, there is a roughly 99.5% chance it will be a single photon. Naturally, this leads to the question: can weak coherent state sources (e.g., weak lasers, which are widely accessible) be considered as effective single-photon sources with efficiency of P_1?

5. **What if the photons are partially distinguishable?** [A, QF]

   Extend Exercise 3 to the case of partially distinguishable input photons, again determining all possible two-photon detection probabilities. Does $P_{2,3}$ change?

[2] In particular, coherent states are subject to Poissonian statistics with the average photon number and variance being equal and given by $\langle a^\dagger a\rangle = \mathrm{Var}(a^\dagger a) = |\alpha|^2$ (see any standard quantum optics textbook for further details [310, 311]).

What does this suggest about the "interference of interference" phenomenon we discussed? [*Disclaimer: this is more difficult than the previous exercises. Hints: Introduce a parameter quantifying how distinguishable the input photons are (think carefully about how this should be done). If exploring in QF's VL, use a polarization encoding so that distinguishability of the two photons can be nearly continuously varied. Additionally, polarizing BSs can then be used to sort the outputs based on polarization.*]

B.2 Exercise solutions

Here we outline potential solutions to the above exercises.

1. **Full setup simulation.**

Here we show the results of simulating our setup for $N = 1000$ trials in QF's VL. In Fig. B.1 we show a screenshot of our setup simulated in VL. By analyzing the experimental outcomes of the simulation, we obtain the two-photon event probability distribution shown in Fig. B.2, which yields results very similar to what we predicted (see Fig. 5.7).

2. **Altering interference of interference.**

(a) We will extend our setup by letting the BS transmission and reflection coefficients (t and $r = \sqrt{1-t^2}$, respectively) vary from the all 50:50 case considered in the main text, while maintaining a left-right symmetric setup. In particular, we denote the transmission coefficients of the first, center most, outer middle, and final BSs (in terms of the order of interaction) as t_0, t_c, t_m, and t_f, respectively. Then the relevant path amplitudes are $O = it_0 r_m t_f$, $Z = i^3 r_0 r_c r_f$, and $C = i^2 r_0 t_c r_f$ (we omit the side

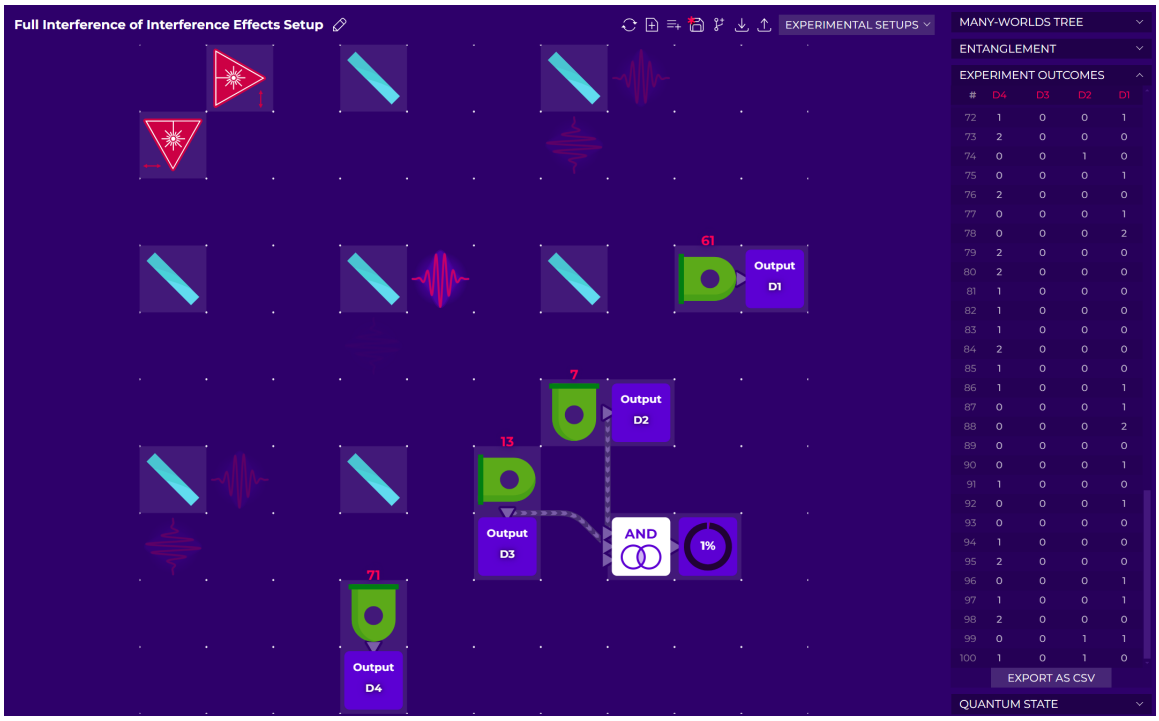

FIGURE B.1. Screenshot of our setup in QF's VL after 100 experimental trials have been completed (see footnote 1). We see that $P_{2,3} \neq 0$ as $1/100 = 1\%$ of the trials have resulted in a D_2D_3 coincidence (shown using VL's AND logic gate and output "stat counter").

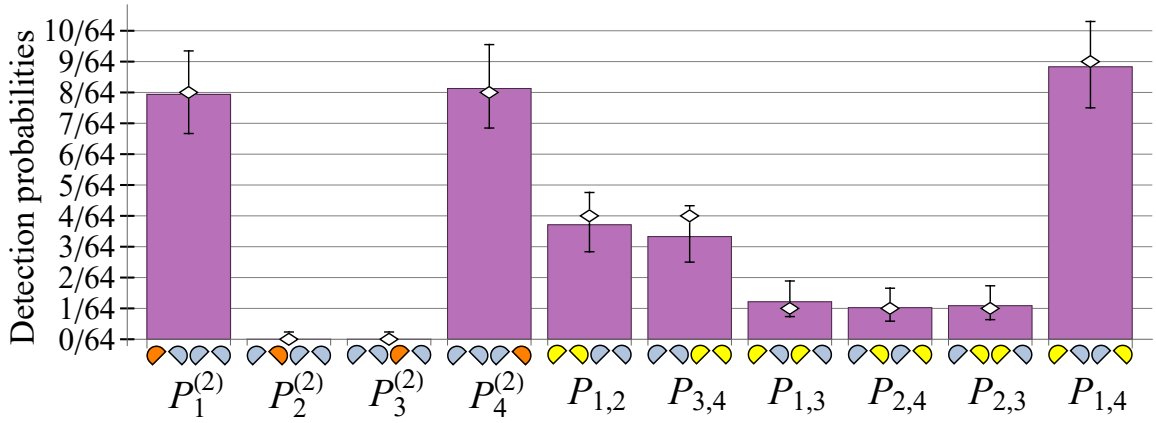

FIGURE B.2. Two-photon event probabilities simulated in VL over $N = 1000$ trials. Error bars indicate the Clopper–Pearson binomial confidence interval with a 95% confidence level, all of which contain the calculated values of Fig. 5.7 (shown as diamonds). (Refer to Fig. 5.7 for variable and color descriptions.)

S labels as the setup is left-right symmetric). To obtain $P_{2,3} = 0$, we need $\mathcal{A}_{2,3} = 0$, which necessitates that $(O + Z)^2$ cancels C^2 by Eq. (5.10). It follows that

$$t_0 r_m t_f - r_0 r_c r_f = \pm r_0 t_c r_f, \tag{B.4}$$

which can be expressed entirely in terms of the reflectivities $R_j \equiv r_j^2 = 1 - t_j^2$ as

$$2R^* \equiv \frac{R_m(1 - R_0)(1 - R_f)}{R_0 R_f} = 1 \pm 2\sqrt{R_c(1 - R_c)} \tag{B.5}$$

corresponding to an entire class of setups for which $P_{2,3} = 0$. [Note that these solutions are constrained to a circle in the (R^*, R_c) plane of radius $1/2$ centered at $(1/2, 1/2)$.]

To restrict this further, suppose that we want to maintain HOMi in the sense that $Z^2 + C^2 = 0$. Along with the problem assumptions (that $O, Z, C \neq 0$), this constraint corresponds to the $R^* = 1$ case of Eq. (B.5) such that $r_c = t_c = 1/\sqrt{2}$ and $\mathcal{A}_{2,3} = O(O + 2Z) = 0$. It follows that $O = -2Z$, so Z must be suppressed and O enhanced relative to the all 50:50 case wherein $O = -Z$. Several corresponding solutions are highlighted in Table B.1. Thus, in order to properly attain the semi-naive value of $P_{2,3} = 0$, one must relinquish either MZi, HOMi, or a combination thereof, altering how the interference effects interfere. Accordingly, the semi-naive reasoning is still not valid; here it wrongly predicts $P_{2,3} > 0$.

TABLE B.1. Several reflectivity triplets that satisfy Eq. (B.5) with $(R^*, R_c) = (1, 1/2)$ for which $P_{2,3} = 0$.

	R_m	R_0	R_f
Case 1	$1/2$	$1/3$	$1/3$
Case 2	1	$\sqrt{2} - 1$	$\sqrt{2} - 1$
Case 3	1	$1/2$	$1/3$

(b) Now, contrary to (a), we want to maximize $P_{2,3}$ by tuning the t and r coefficients of the various BSs. Maintaining both full MZi and HOMi necessitates the relations

$$0 = O + Z = i(t_0 r_m t_f - r_0 r_c r_f) \tag{B.6}$$

and

$$0 = Z^2 + C^2 = R_0 R_f (T_c - R_c), \tag{B.7}$$

respectively, where we used the amplitudes defined in (a) along with $R_j \equiv r_j^2$ and $T_j \equiv t_j^2$.

Equation (B.7) implies $T_c = R_c = 1/2$, which we can use along with Eqs. (B.7) and (B.6) to express $\mathcal{A}_{2,3}$ in two ways [e.g., see the reductions of Eqs. (5.10)–(5.12)]:

$$\mathcal{A}_{2,3} = C^2 = -Z^2 = \frac{1}{2} R_0 R_f \tag{B.8a}$$

$$= -O^2 = R_m T_0 T_f. \tag{B.8b}$$

These expressions for $\mathcal{A}_{2,3}$ constrain the relationship between R_0 and R_f which can self-consistently be used to eliminate R_f (or equivalently R_0) as

$$\mathcal{A}_{2,3} = \frac{R_0(1 - R_0)}{R_0/R_m + 2(1 - R_0)}. \tag{B.9}$$

We want to maximize $P_{2,3}$ but, as $\mathcal{A}_{2,3}$ is real in this case, we can simply maximize it. Using elementary calculus, we find that a maximum of $P_{2,3}^{(\max)} = 17 - 12\sqrt{2} \approx 2.94\%$ occurs for $R_m = 1$ and $R_0 = R_f = 2 - \sqrt{2}$.

This value is roughly 88% larger than the raw value of $P_{2,3} = 1/64 \approx 1.56\%$ in our setup. We note that in Ref. 258, Hardy considers a version of this setup with

$R_c = R_0 = 1/2$, $R_m = 1$, and $R_f = 2/3$ that nearly saturates the upper bound, achieving $P_{2,3} = 1/36 \approx 2.78\%$ (which is identical to value we would obtain when postselecting on cases where neither photon is lost; see Fig. 5.7). Part of the intrigue of maximizing this probability is that it makes demonstrating Bell's Theorem (see Sec. 5.3.4) potentially easier [259].

3. **Distinguishability impact.**

As a concrete example, we take the left and right input photons to be red and blue, respectively, though any other orthogonal modes could be used. The corresponding analysis is simplified for distinguishable inputs (relative to the main text) as identical two-photons effects like Bose enhancement and HOMi will not come into play, and we can talk about which photon does what. In particular, the quantities

$$P_{L\to i\&R\to j} = |\mathcal{A}_{L\to i}\mathcal{A}_{R\to j}|^2 \quad (i,j \in \{1,2,3,4\}) \tag{B.10}$$

are now well-defined and correspond to the probabilities of the red (left input) and blue (right input) photons reaching detectors i and j, respectively. (The amplitudes $\mathcal{A}_{S\to j}$ were introduced in Sec. 5.3.3.) Moreover, the line of reasoning that was semi-naive for identical photons [see Eq. (5.14)] is now valid. In particular, as we are not measuring the output colors, the coincident detection probabilities are given by a classical-like sum of the corresponding distinguishable outcome probabilities:

$$P_{i,j}^{(\mathrm{dist})} = P_{L\to i\&R\to j} + P_{L\to j\&R\to i} \quad (i \neq j). \tag{B.11}$$

[One could explicitly determine the individual probabilities, $P_{L\to i\&R\to j}$, by measuring the colors of the output photons, e.g., using dichroic BSs before detection. By not

measuring the output colors, we forgo knowledge of the specific values of $P_{L\to i\&R\to j}$ and $P_{L\to j\&R\to i}$, yet their measured sum is nevertheless determined by Eq. (B.11) as distinguishable processes do not interfere [234].]

Comparing this to the case of identical photons considered in Sec. 5.3.4, wherein $P_{i,j}^{(\mathrm{id})} = |\mathcal{A}_{i,j}|^2$ with $\mathcal{A}_{i,j}$ given by Eq. (5.15), one finds

$$P_{i,j}^{(\mathrm{id})} = P_{i,j}^{(\mathrm{dist})} + 2\,\mathrm{Re}\left(\mathcal{A}_{L\to i}\mathcal{A}_{R\to j}\mathcal{A}_{L\to j}^{*}\mathcal{A}_{R\to i}^{*}\right) \tag{B.12}$$

(for $i \neq j$). That is, compared to the distinguishable case, $P_{i,j}^{(\mathrm{id})}$ includes cross terms, which are the signatures of quantum interference. Meanwhile, the joint detection probabilities ($i = j$) are

$$P_{i,i} = P_{L\to i\&R\to i}, \tag{B.13}$$

which may look unchanged but are no longer Bose enhanced (see footnote 6 in §5.3).

To evaluate the 16 probabilities, $P_{L\to i\&R\to j}$, we start by using the counting method to determine all the relevant single-photons amplitudes:

$$\mathcal{A}_{L\to 1} = \mathcal{A}_{R\to 4} = i^2/\sqrt{2}, \tag{B.14a}$$

$$\mathcal{A}_{L\to 2} = \mathcal{A}_{R\to 3} = 0, \tag{B.14b}$$

$$\mathcal{A}_{L\to 3} = \mathcal{A}_{R\to 2} = i^2/\sqrt{2^3}, \tag{B.14c}$$

$$\mathcal{A}_{L\to 4} = \mathcal{A}_{R\to 1} = i/\sqrt{2^3}. \tag{B.14d}$$

Then the probabilities are given by Eq. (B.10), as summarized in Table B.2, from which one can read off the ten color-insensitive two-photon-detection probabilities using Eq. (B.11). We see that due to a lack of Bose enhancement here, $P_1^{(2)}$ and $P_4^{(2)}$ decrease from their values of 1/8 in the indistinguishable case to 1/16. Meanwhile, $P_{1,4}$

increases to 17/64 from its previous value of 9/64, as the alternatives ($\mathcal{A}_{L\to 1}\mathcal{A}_{R\to 4}$ and $\mathcal{A}_{L\to 4}\mathcal{A}_{R1}$) no longer destructively interfere; rather, their corresponding probabilities add. Meanwhile, the other seven two-photon detection probabilities (those involving detectors D_2 or D_3) are unchanged relative to the main text (see Fig. 5.7). This is because the amplitude contribution of paths where a photon reaches the inner detector on its own side always vanishes due to MZi ($O + Z = 0$). See the solution to Exercise 5 for a generalization of these results to partially distinguishable photons and for a discussion of the impact of distinguishability on the interference of interference effects phenomenon.

TABLE B.2. All 16 outcome probabilities $P_{L,i\&R,j}$ for distinguishable photons (see text for description).

	$L,1$	$L,2$	$L,3$	$L,4$
$R,1$	1/16	0	1/64	1/64
$R,2$	1/16	0	1/64	1/64
$R,3$	0	0	0	0
$R,4$	1/4	0	1/16	1/16

4. **Single photon versus weak coherent state inputs.**

We consider two cases: (1) one weak coherent state input is used and the other input is a genuine single-photon or (2) two weak coherent state inputs are used. In case (1), one will most likely get only a single detector click due to the single-photon input and the dominant $n = 0$ contribution of the weak coherent state. The next most likely result is the desired one, wherein one obtains a two photon detection event where either two separate detectors click or one detector registers two incident photons (assuming photon-number-resolving detectors for simplicity here). This suggests that our setup (and the predicted interference effects) should work in this case with little modification except for an overall drop in efficiency to about $P_1 \approx |\alpha|^2$ for small α.

Note, however, that the precise event statistics and corresponding error analysis will change.

In case (2), the two sources, which we will call A and B, each emit a weak coherent state $|\alpha\rangle$ and $|\beta\rangle$, respectively. We will assume that they have similar mean photon numbers $|\alpha|^2 \approx |\beta|^2$. The issue is that a two photon detection event could be caused by multiple channels: (i) the desired one where both sources contribute a single photon with probability $P_{11} = P_1^{(A)} P_1^{(B)} = e^{-|\alpha|^2-|\beta|^2}|\alpha\beta|^2$,[3] or (ii) the two photons each come from the same arm (which is undesired in that it will lead to a different process and hence different interference than the setup we have considered). Note that (ii) can occur in two ways: either two photons from A and none from B contribute, with probability $P_{20} = P_2^{(A)} P_0^{(B)} = e^{-|\alpha|^2-|\beta|^2}|\alpha|^4/2$, or vice versa (none from A and two from B), with probability $P_{02} = P_0^{(A)} P_2^{(B)} = e^{-|\alpha|^2-|\beta|^2}|\beta|^4/2$. For identical sources, $|\alpha| = |\beta|$,

$$P_{20} = P_{02} = \frac{1}{2} e^{-2|\alpha|^2} |\alpha|^4 = \frac{1}{2} P_{11}, \tag{B.15}$$

so one is equally likely to get one of the undesired outcomes, $P_{20} + P_{02}$, as the desired one, P_{11}. [Moreover, one cannot do better by using weak coherent states with different average photon numbers. That is, selecting $|\alpha| = |\beta|$ is the best one can do (in terms of maximizing P_{11} relative to $P_{20} + P_{02}$).] Thus, although one could indeed use two weak coherent states as the input states to our optical setup, the resulting interference and detection statistics will be very different than case (1) and the case of two single photon inputs (e.g., the output state will not be entangled).

[3]Here we are using the notation $P_{ij} := P_i^{(A)} P_j^{(B)}$ corresponding the probability of a contribution with i photons from source A and j from B (we avoid commas in the subscript here to distinguish these probabilities from those considered in the main text).

5. **Partial distinguishability.**

Method background. This exercise can be solved purely in terms of amplitudes by combining the counting method introduced in the main text with its adaptation in Exercise 3 (see footnote 5 below). However, we will instead use this as an opportunity to establish an explicit connection between our approach and the standard second-quantized formalism. The key mathematical tools we will need from this formalism are the so-called creation and annihilation operators $a^\dagger$ and a, respectively. For a given photonic mode, these operators can be defined by their action on photon number states (introduced in Exercise 4): $a^\dagger|n\rangle = \sqrt{n+1}|n+1\rangle$ and $a|n\rangle = \sqrt{n}|n-1\rangle$ ($n = 0, 1, 2, ...$). That is, $a^\dagger$ creates a photon, while a removes (or "annihilates") a photon (hence their names). For a more thorough introduction to these operators and the underlying formalism, see standard quantum optics textbooks [133, 310, 311].

Solution. Now consider a case of partially distinguishable input photons described by two orthogonal modes H and V with respective creation operators $h^\dagger$ and $v^\dagger$. We take these modes to represent horizontal (H) and vertical (V) photon polarizations (with the other degrees of freedom of the photons assumed to be fixed and identical). Other orthogonal modes can be considered similarly, e.g., it is common to introduce partial distinguishability via the relative time delay between the two photons [242, 250]. In particular, suppose the initial two-photon state is $|\psi_0\rangle = h_L^\dagger d_R^\dagger|\text{vac}\rangle \equiv |H_L D_R\rangle$, corresponding to left input photon being in the H mode and the right being a "diagonal" mode (D) defined by

$$d^\dagger \equiv \mathcal{C}h^\dagger + \sqrt{1-|\mathcal{C}|^2}v^\dagger. \tag{B.16}$$

Note that here D corresponds to a general superposition of the H and V modes, not necessarily an equal superposition with 45° polarization. (In the quantum computing nomenclature, one would say that $|D\rangle = d^\dagger|\text{vac}\rangle$ represents a photonic qubit in the polarization encoding.) The parameter $0 \leq |\mathcal{C}| \leq 1$ characterizes how distinguishable the two photons are[4] and $|\text{vac}\rangle$ is the vacuum state (corresponding to all modes being in the unoccupied $n = 0$ state). (Operator subscripts of the form $S \in \{L, R\}$ denote the starting side of an input photon and subscripts of $\{1, 2, 3, 4\}$ are later used to denote the final detector reached.)

To translate amplitude-path diagrams (e.g., as used in Fig. 5.6) into a state, we need to account for these distinguishable modes. As in Eq. (5.9), we can split the $\mathrm{D}_i\mathrm{D}_j$ coincident detection outcome into two processes corresponding to paths, where photon L reaches D_i and photon R reaches D_j or vice versa. Crucially, these processes are now partially distinguishable, which must be accounted for in their final state contribution, so for $i \neq j$

$$\begin{aligned} |\psi_{i,j}\rangle &= \left(\mathcal{A}_{L\to i}\mathcal{A}_{R\to j}h_i^\dagger d_j^\dagger + \mathcal{A}_{L\to j}\mathcal{A}_{R\to i}h_j^\dagger d_i^\dagger\right)|\text{vac}\rangle \\ &= \mathcal{C}\left(\mathcal{A}_{L\to i}\mathcal{A}_{R\to j} + \mathcal{A}_{L\to j}\mathcal{A}_{R\to i}\right)|H_iH_j\rangle \\ &\quad + \sqrt{1-|\mathcal{C}|^2}\left(\mathcal{A}_{L\to i}\mathcal{A}_{R\to j}|H_iV_j\rangle + \mathcal{A}_{L\to j}\mathcal{A}_{R\to i}|V_iH_j\rangle\right). \end{aligned} \tag{B.17}$$

We see that for $|\mathcal{C}| \neq 1$, $h_i^\dagger d_j^\dagger \neq h_j^\dagger d_i^\dagger$, so we cannot factor out a total amplitude as was implicitly done in the main text. Rather, there is an amplitude for each

[4]In particular, the distinguishability parameter $\mathcal{C}$ is equivalent to the state vector overlap of the two (pure) photons, which here is $\mathcal{C} = \langle H|D\rangle$ (see Ch. VI). One can imagine varying $\mathcal{C}$ intentionally to see the impact on interference, e.g., using polarization rotators here (as can be explored in QFs VL). However, in practice, the two photons will be partially distinguishable due to experimental imperfections including relative timing errors, mode misalignments, and variability in the photon sources. Moreover, for mixed states, the overlap, $\mathcal{C}$, is given by the trace of the products of the photons' density matrices [253].

distinguishable outcome $|H_iH_j\rangle$, $|H_iV_j\rangle$, and $|V_iH_j\rangle$. (Note that these amplitudes can be determined by counting, as in the main text, without the need to ever explicitly use creation operators or write down quantum states.) As in Exercise 3, $P_{i,j}$ is a classical-like sum of the probabilities of these distinguishable outcomes, except now the $|H_iH_j\rangle$ outcome is present and admits two-photon interference. In particular, as $|\mathcal{C}|$ decreases from 1 to 0 (i.e., the photons are made more distinguishable), it is necessary to gradually shift from adding quantum amplitudes to adding probabilities.[5]

That is, distinguishability destroys interference (see Sec. 5.3.5). For $i = j$

$$|\psi_{i,i}\rangle = \mathcal{A}_{L\to i}\mathcal{A}_{R\to i}h_i^\dagger d_i^\dagger|\text{vac}\rangle \tag{B.18}$$

with

$$h_i^\dagger d_i^\dagger|\text{vac}\rangle = \mathcal{C}\sqrt{2}|2H_i\rangle + \sqrt{1-|\mathcal{C}|^2}|H_iV_i\rangle, \tag{B.19}$$

wherein Bose enhancement accounts for the $\sqrt{2}$ factor in the first term, yet is not manifest in the second term. The corresponding single-photon amplitudes can be determined using the counting method and are given in Eq. (B.14).

We see that for outcomes involving the inner detectors (D_2 or D_3), one term in the first line of Eq. (B.17) will vanish due to MZi (e.g., as $\mathcal{A}_{L\to 2} = \mathcal{A}_{R\to 3} = 0$) and similarly Eq. (B.18) will vanish. For instance, for a D_2D_3 detection,

$$\boxed{|\psi_{2,3}\rangle = \left[(O+Z)^2 h_2^\dagger d_3^\dagger + C^2 d_2^\dagger h_3^\dagger\right]|\text{vac}\rangle,} \tag{B.20}$$

[5] The probability of each detection event, $\mathcal{E}$, is given by a weighted sum of its values in the fully distinguishable and indistinguishable cases, denoted here as P_{dist} and P_{indist}, respectively. In particular, after introducing a mode-overlap parameter $\mathcal{C}$ [as in Eq. (B.16), whose squared modulus $|\mathcal{C}|^2$ is the probability that the two inputs will be in the same mode], we have $P_{\mathcal{E}}(\mathcal{C}) = |\mathcal{C}|^2 P_{\text{indist}} + (1-|\mathcal{C}|^2)P_{\text{dist}}$, as can be confirmed using Eqs. (B.17)–(B.19). Note, however, that systems of more than two particles exhibit rich collective interference with a more intricate dependence on indistinguishability, e.g., which underlies boson sampling [242].

where the $h_2^\dagger d_3^\dagger$ contribution vanishes due to MZi ($O + Z = 0$) so only the $d_2^\dagger h_3^\dagger$ term contributes and $P_{2,3} = |C|^4 = 1/64$ remains unchanged. Similarly, $P_2^{(2)}, P_3^{(2)}, P_{1,2}, P_{3,4}, P_{1,3}$ and $P_{2,4}$ remain unchanged relative to Fig. 5.7. As seen when solving Exercise 3, only the other three probabilities ($P_1^{(2)}$, $P_4^{(2)}$, and $P_{1,4}$) change. In particular, $P_1^{(2)} = P_4^{(2)} = \frac{1}{16}(1 + |\mathcal{C}|^2)$, so each of these values are reduced by $\frac{1}{16}(1 - |\mathcal{C}|^2) \equiv \delta P$ relative to the indistinguishable case due to a suppression of Bose enhancement. Correspondingly, $P_{1,4}$ is enhanced by $\frac{1}{8}(1 - |\mathcal{C}|^2) = 2\delta P$ to a value of $P_{1,4} = \frac{1}{64}[17 - 8|\mathcal{C}|^2]$ as distinguishability diminishes interference. Note that non-destructive measurements [312] before the final BSs will similarly diminish interference (as they distinguish different processes and hence provide 'which-path' information).

Interpretation. From Eq. (B.20), it is easy to see that the coincident inner detection probability $P_{2,3}$ does not depend on whether the photons are identical or not so long as MZi ($O + Z = 0$) occurs. Someone who does not know about the HOM effect will likely not be surprised by this result: for distinguishable input photons (e.g., one H, one V), the photons can be reasoned about separately and, as discussed in Solution 3, the semi-naive reasoning correctly predicts the value of $P_{2,3} = |C_L C_R|^2 = 1/64$ [as premises (i) and (ii) hold, while HOMi no longer seems to preclude a crossing in premise (iii)]. Without knowing the HOM effect, this probability need not necessarily vary with photon distinguishability. However, if one does know of the effect, they might (semi-naively) expect that continuously changing the polarization of the V photon to H should make it necessary to take HOMi into account. Then, one explanation for why the HOM effect does not seem to work in this setup, i.e., that $P_{2,3}(\mathcal{C})$ is constant, is in terms of interference of interference.

One might be tempted to interpret $P_{2,3}(\mathcal{C})$ being constant as an indication that HOMi does not play a role in the processes leading to a D_2D_3 coincident detection. However, if the final BSs are omitted [225, 226] or the photons are non-destructively measured before they reach the final BSs, one will indeed see extremely different results depending on how distinguishable the input photons are. For instance, with the final BSs removed, identical photons will never exit opposite ports of the central BS (due to HOMi), whereas distinguishable photons indeed can. In particular, even though 7/10 of the considered two-photon detection probabilities do not depend on $\mathcal{C}$, the entanglement structure of the final photonic state does, which has important implications regarding the potential to demonstrate Bell's theorem in a setup [259] (e.g, such a demonstration could not be done with distinguishable photons, $\mathcal{C} = 0$).

APPENDIX C

LIGHT-MATTER INTERACTION

Here we discuss the 'origins' and motivations for the Hamiltonian of Eq. (2.2) (§C.2), which—as discussed in Ch. 2.2—serves as an appropriate starting point for our work. Then we consider a unitarily equivalent multipolar representation of this Hamiltonian, which is a generalization of Eq. (2.19), that naturally prefaces input-output theory (§C.3). Note that these treatments largely following the treatment of Ref. 22, which is a great textbook for understanding the interaction of light and matter, from more thorough discussions of the fundamentals presented in this appendix to more advanced topics.

C.1 Mathematical preliminaries

Throughout this dissertation, though especially in this appendix, it will be helpful to consider the spatial Fourier transform of various quantities such as electromagnetic fields. We will use the symmetric convention,

$$F(\boldsymbol{r}) = \frac{1}{(2\pi)^{3/2}} \int d^3k \; \mathcal{F}(\boldsymbol{k}) e^{i\boldsymbol{k}\cdot\boldsymbol{r}} \tag{C.1}$$

and

$$\mathcal{F}(\boldsymbol{k}) = \frac{1}{(2\pi)^{3/2}} \int d^3r \; F(\boldsymbol{r}) e^{-i\boldsymbol{k}\cdot\boldsymbol{r}}, \tag{C.2}$$

as then there are no lingering factors of 2π in the Parseval–Plancherel identity:

$$\int d^3r \; F^*(\boldsymbol{r}) G(\boldsymbol{r}) = \int d^3k \; \mathcal{F}^*(\boldsymbol{k}) \mathcal{G}(\boldsymbol{k}). \tag{C.3}$$

We will often use script letters to indicate to denote the spatial Fourier transforms of real space functions, though this should also be made evident by the function's argument ($\boldsymbol{r}$ versus $\boldsymbol{k}$). For temporal Fourier transforms between time, t, and angular frequency, ω, we use the similar convention

$$F(t) = \frac{1}{\sqrt{2\pi}} \int d\omega \; \mathcal{F}(\omega) e^{-i\omega t} \tag{C.4}$$

and

$$\mathcal{F}(\omega) = \frac{1}{\sqrt{2\pi}} \int dt \; F(t) e^{i\omega t}, \tag{C.5}$$

where one should heed the swap of the signs in the exponentials (which is done in accordance with standard wave theory).

C.2 The standard Lagrangian of electrodynamics

The classical dynamics of a system of particles and electromagnetic fields with which they interact can be derived from the Lagrangian

$$L = \sum_n \frac{1}{2} m_n \dot{r}_n^2 + \frac{\varepsilon_0}{2} \int d^3 r \left[E^2(\boldsymbol{r}) - c^2 B^2(\boldsymbol{r}) \right] + \sum_n q_n \left[\dot{\boldsymbol{r}}_n \cdot \boldsymbol{A}(\boldsymbol{r}_n) - U(\boldsymbol{r}_n) \right]. \tag{C.6}$$

The electric and magnetic fields can be expressed in terms of the scalar potential U and vector potential $\boldsymbol{A}$ as

$$\boldsymbol{E} = -\partial_t \boldsymbol{A} - \boldsymbol{\nabla} U \tag{C.7}$$

and

$$\boldsymbol{B} = \boldsymbol{\nabla} \times \boldsymbol{A}, \tag{C.8}$$

respectively (see Table 2.1 for a glossary of the symbols used). In particular, as one can easily show (see §C.2.1), the corresponding Euler–Lagrange equations of motion (EOMs),

$$\frac{\partial L}{\partial q_i} - \frac{d}{dt}\frac{\partial L}{\partial \dot{q}_i} = 0, \tag{C.9}$$

for the paths of the particles $\boldsymbol{q} \to \boldsymbol{r}_n$ and fields $\boldsymbol{q} \to U, \boldsymbol{A}$, are nothing but the standard Lorentz equation

$$m_n \ddot{\boldsymbol{r}}_n = q_n \left[\boldsymbol{E}(\boldsymbol{r}_n) + \dot{\boldsymbol{r}}_n \times \boldsymbol{B}(\boldsymbol{r}_n) \right], \tag{C.10}$$

Gauss's law

$$\boldsymbol{\nabla} \cdot \boldsymbol{E} = \frac{1}{\varepsilon_0}\rho, \tag{C.11}$$

and Ampère-Maxwell law

$$\boldsymbol{\nabla} \times \boldsymbol{B} = \frac{1}{c^2}\left(\partial_t \boldsymbol{E} + \frac{1}{\varepsilon_0}\boldsymbol{j} \right). \tag{C.12}$$

Here $\rho(\boldsymbol{r}) = \sum_n q_n \delta^3(\boldsymbol{r} - \boldsymbol{r}_n)$ and $\boldsymbol{j}(\boldsymbol{r}) = \sum_n q_n \dot{\boldsymbol{r}}_n \delta^3(\boldsymbol{r} - \boldsymbol{r}_n)$ are the charge density and current, respectively (here we consider a collection of points charge, though this can easily be generalized to continuous charge and current distributions). Equations (C.11) and (C.12) are two of Maxwell's equations, the other two of which immediately follow from Eqs. (C.7) and (C.8):

$$\boldsymbol{\nabla} \cdot \boldsymbol{B} = \boldsymbol{\nabla} \cdot (\boldsymbol{\nabla} \times \boldsymbol{A}) = 0 \tag{C.13}$$

and

$$\boldsymbol{\nabla} \times \boldsymbol{E} = -\partial_t \boldsymbol{\nabla} \times \boldsymbol{A} - \boldsymbol{\nabla} \times (\boldsymbol{\nabla} U) = -\partial_t \boldsymbol{B}, \tag{C.14}$$

assuming $\boldsymbol{A}$ and U are continuously twice differentiable. In the following subsections we will verify the claimed Eqs. (C.10)–(C.12) (§C.2.1), motivate why we work in the Coulomb gauge (§C.2.2), and canonically quantize the theory to arrive at the Hamiltonian of Eq. (2.2) (§C.2.3). See Chapter II of Ref. 22 for a similar[1] justification of this Hamiltonian and further details.

C.2.1 Euler–Lagrange EOMs

We now explicitly verify that Eqs. (C.10)–(C.12) are the claimed Euler–Lagrange equations. For the particles, $\boldsymbol{q} \to \boldsymbol{r}_n$, using $\partial_i = \partial_{r_{n,i}}$ as shorthand (even though more generally this notation is used for continuum variables, like the fields, $\partial_j = \partial_{r_j}$), we have

$$\frac{\partial L}{\partial r_{n,i}} = q_n \left(\dot{\boldsymbol{r}}_n \cdot \partial_i \boldsymbol{A} - \partial_i U \right) \tag{C.15}$$

and

$$\frac{d}{dt} \frac{\partial L}{\partial \dot{r}_{n,i}} = \frac{d}{dt} \left(m_n \dot{r}_{n,i} + q_n A_i \right) = m_n \ddot{r}_{n,i} + q_n \partial_t A_i + q_n \dot{\boldsymbol{r}}_n \cdot \left(\boldsymbol{\nabla} A_i \right) \tag{C.16}$$

such that Eq. (C.9) implies

$$\frac{m_n}{q_n} \ddot{r}_{n,i} = \dot{\boldsymbol{r}}_n \cdot \partial_i \boldsymbol{A} - \partial_i U - \partial_t A_i - \dot{\boldsymbol{r}}_n \cdot \left(\boldsymbol{\nabla} A_i \right) \tag{C.17a}$$

$$= E_i + \dot{r}_{n,j} \left(\partial_i A_j - \partial_j A_i \right) \tag{C.17b}$$

$$= E_i + \left(\dot{\boldsymbol{r}}_n \times \boldsymbol{B} \right)_i , \tag{C.17c}$$

[1] Note that for the fields, Ref. 22 tends to work in reciprocal space (which admittedly is simpler once the corresponding machinery has been set up, e.g., Maxwell's equation are local therein), though we will work in real space in this section to provide an alternative exposition.

which are the components of Eq. (C.10). Note that we are using Einstein's summation convention in Eq. (C.17b) and used the Levi-Civita symbol identity $\epsilon_{ijk}\epsilon_{klm} = \delta_{il}\delta_{jm} - \delta_{im}\delta_{jl}$ to obtain Eq. (C.17c).

For the fields, starting with $q \to U$, we have

$$\frac{d}{dt}\frac{\partial L}{\partial \dot{U}} = 0 \tag{C.18}$$

and hence

$$0 = \frac{\partial L}{\partial U} = \int d^3r \left[\varepsilon_0 E_j \left(\partial_U E_j\right) - \partial_U \sum_n q_n \delta^3(\boldsymbol{r} - \boldsymbol{r}_n) U(\boldsymbol{r}) \right] \tag{C.19a}$$

$$= \int d^3r \left[-\varepsilon_0 E_j \left(\partial_U \partial_j U\right) - \sum_n q_n \delta^3(\boldsymbol{r} - \boldsymbol{r}_n) \right], \tag{C.19b}$$

where integrating the first term by parts (assuming the potentials go to zero at infinity) and recognizing the charge density in the second term, we have

$$0 = \int d^3r \left[\varepsilon_0 (\partial_j E_j) \left(\partial_U U\right) - \rho(\boldsymbol{r}) \right] = \int d^3r \left[\varepsilon_0 \boldsymbol{\nabla} \cdot \boldsymbol{E} - \rho(\boldsymbol{r}) \right], \tag{C.20}$$

which holds for all U so the integrand itself must vanish,[2] implying Eq. (C.11). Using similar methods for $\boldsymbol{q} \to \boldsymbol{A}$, we have

$$\frac{\partial L}{\partial A_i} = \varepsilon_0 \int d^3r \left[E_j(\partial_{A_i} E_j) - c^2 B_j(\partial_{A_i} B_j)\right] + \partial_{A_i} \int d^3r \sum_n q_n \delta^3(\boldsymbol{r} - \boldsymbol{r}_n)\dot{\boldsymbol{r}}_n \cdot \boldsymbol{A}(\boldsymbol{r}) \tag{C.21a}$$

$$= \varepsilon_0 \int d^3r \left[-c^2 B_j(\partial_{A_i}\epsilon_{jkl}\partial_k A_l)\right] + \int d^3r \sum_n q_n \delta^3(\boldsymbol{r} - \boldsymbol{r}_n)\dot{r}_{n,i} \tag{C.21b}$$

$$= \int d^3r \left[\varepsilon_0 c^2(\partial_k B_j)(\epsilon_{jki}) + j_i(\boldsymbol{r})\right] \tag{C.21c}$$

$$= \int d^3r \left[-\varepsilon_0 c^2(\boldsymbol{\nabla} \times \boldsymbol{B})_i + j_i(\boldsymbol{r})\right] \tag{C.21d}$$

and[3]

$$\frac{d}{dt}\frac{\partial L}{\partial \dot{A}_i} = \frac{d}{dt}\varepsilon_0 \int d^3r E_j \left(\partial_{\dot{A}_i} E_j\right) = \int d^3r \left(-\varepsilon_0 \partial_t E_i\right). \tag{C.22}$$

Together with the corresponding Euler–Lagrange equation (which holds for all $\boldsymbol{A}$), these relations imply Eq. (C.12).

C.2.2 Eliminating redundant variables and the choice of gauge

Lagrangians are useful in relativistic contexts (among others), such as in quantum field theories, wherein Lorentz invariance can be made manifest [this can be made the case for Eq. (C.6) if the kinetic energy term is treated relativistically]. However, we want to find a Hamiltonian operator describing the interaction of light with non-relativistic matter, e.g., to use in the Schrödinger or Heisenberg equations. In general,

[2]This type of argument can be avoided by working with the Lagrangian density $\mathcal{L}$, defined via $L = \int d^3r \mathcal{L}$, for the fields instead of L itself.

[3]At a glance, it might seem that we are missing terms when taking the total time derviative in Eq. (C.22), e.g., perhaps $\frac{d}{dt}E_i(\boldsymbol{r},t) = \partial_t E_i + \frac{dr_j}{dt}\partial_j E_i$. However, here—for the fields—r_j is just a parameter so $dr_j/dt = 0$ and there is no issue.

this can be done by identifying the conjugate momentum,

$$p_j = \frac{\partial L}{\partial \dot{q}_j}, \tag{C.23}$$

for each coordinate q_j in the Lagrangian L. Then the corresponding Hamiltonian is

$$H(q_j, p_j) = \dot{q}_j p_j - L, \tag{C.24}$$

which can be made into a quantum operator by promoting the phase-space coordinate pairs $\{q_j, p_j\}$ to canonically conjugate operators satisfying $[x_i, p_j] = i\hbar\delta_{ij}$ (this procedure is known as "second quantization").

With the Lagrangian of Eq. (C.6), for $q \to U$ we have the problem that

$$p_U = \frac{\partial L}{\partial \dot{U}} = 0, \tag{C.25}$$

so $\{U, p_U\}$ cannot itself be canonically quantized and U is not a true dynamic variable . Thus, we will opt to eliminate the redundant variable U from the description by writing it in terms of the other variables: $U = U(\boldsymbol{r}_n, \boldsymbol{A})$.

We note that there is additional redundant DOF in the description, it is the longitudinal part of the vector potential, $\boldsymbol{A}_\parallel$, though the reasoning is not quite as obvious as it having a null conjugate momentum. First we note that any nice[4] vector field can be decomposed as $\boldsymbol{v}(\boldsymbol{r}) = \boldsymbol{v}_\parallel(\boldsymbol{r}) + \boldsymbol{v}_\perp(\boldsymbol{r})$, into a longitudinal part $\boldsymbol{v}_\parallel$, with $\boldsymbol{\nabla} \times \boldsymbol{v}_\parallel(\boldsymbol{r}) = \boldsymbol{0}$, and transverse part $\boldsymbol{v}_\perp$, with $\boldsymbol{\nabla} \cdot \boldsymbol{v}_\perp(\boldsymbol{r}) = 0$. As a hint for why

[4]This is the Helmholtz decomposition and it holds for any continuously twice differentiable functions that decay faster than $1/r$ as $r \to \infty$. We have already assumed that the potentials are such functions. This can easily be understood in reciprocal space as the decomposition of the spatial Fourier transform of $\boldsymbol{v}(\boldsymbol{r})$ as $\boldsymbol{v}(\boldsymbol{k}) = \boldsymbol{v}_\parallel(\boldsymbol{k}) + \boldsymbol{v}_\perp(\boldsymbol{k})$, wherein $\boldsymbol{v}_\parallel(\boldsymbol{k})$ is longitudinal (parallel to $\boldsymbol{k}$, $\boldsymbol{k} \times \boldsymbol{v}_\parallel(\boldsymbol{k}) = \boldsymbol{0}$) and $\boldsymbol{v}_\perp(\boldsymbol{k})$ is transverse (orthogonal to $\boldsymbol{k}$, $\boldsymbol{k} \cdot \boldsymbol{v}_\perp(\boldsymbol{k}) = 0$).

$\boldsymbol{A}_\parallel$ is redundant, note that, as one can easily show using the methods of §C.2.1, the Lagrangian (density) EOM for $\boldsymbol{A}_\parallel$ is

$$\frac{\partial \mathcal{L}}{\partial A_{\parallel,i}} - \frac{d}{dt}\frac{\partial \mathcal{L}}{\partial \dot{A}_{\parallel,i}} = j_i(\boldsymbol{r}) + \varepsilon_0 \partial_t E_i(\boldsymbol{r}) = 0. \tag{C.26}$$

This can be put into a more recognizable term by taking a spatial derivative ∂_i (then contracting over i) and using Gauss's law:

$$\boldsymbol{\nabla} \cdot \boldsymbol{j}(\boldsymbol{r}) = -\varepsilon_0 \partial_t \boldsymbol{\nabla} \cdot \boldsymbol{E}(\boldsymbol{r}) = -\partial_t \rho(\boldsymbol{r}), \tag{C.27}$$

which is nothing but the conservation of charge. This is clearly not an EOM for $\boldsymbol{A}_\parallel$ and hence $\boldsymbol{A}_\parallel$ is not a true dynamic variable, its value can be chosen arbitrarily with no impact on the dynamics of the system. This can also be seen as, under a gauge transformation $\{\boldsymbol{A} \to \boldsymbol{A} + \boldsymbol{\nabla} F, U \to U - \partial_t F\}$, $\boldsymbol{A}_\parallel \to \boldsymbol{A}_\parallel + \boldsymbol{\nabla} F$ while $\boldsymbol{A}_\perp$ is invariant as $\boldsymbol{\nabla} F$ is necessarily longitudinal. More fundamentally, one can show that the $\boldsymbol{A}_\parallel$ terms in L are expressible as a total time derivative, which does not change the physics and hence can be removed [22]. Accordingly, throughout this dissertation we make the simplest choice: $\boldsymbol{A}_\parallel \equiv \boldsymbol{0}$, which is called the *Coulomb gauge*, wherein $\boldsymbol{A} = \boldsymbol{A}_\perp$ so $\boldsymbol{\nabla} \cdot \boldsymbol{A} = 0$. Henceforth, we will often omit the $\perp$ label with it being implied.

Thus, we can eliminate the redundant degrees of freedom ($\boldsymbol{A}_\parallel$ and U) by working in the Coulomb gauge and writing the scalar potential, U, in terms of the dynamic variables $\boldsymbol{A}_\perp$ and $\boldsymbol{r}_n$. To eliminate U, we take the divergence of Eq. (C.7), use Gauss's law, and do some algebra to find $\nabla^2 U = -\frac{1}{\varepsilon_0}\rho$, i.e., U satisfies the Poisson equation with source $-\rho/\varepsilon_0$. One can then solve for U using the Green's function for Poisson's

equation as

$$U(\boldsymbol{r},t)=\frac{1}{4\pi\varepsilon_0}\int d^3r'\frac{\rho(\boldsymbol{r}',t)}{|\boldsymbol{r}-\boldsymbol{r}'|}, \tag{C.28}$$

which is nothing but the Coulomb potential of the charges. Using Eq. (C.7), this can further be used to eliminate

$$\boldsymbol{E}_{\parallel}(\boldsymbol{r},t)=-\boldsymbol{\nabla}U(\boldsymbol{r},t). \tag{C.29}$$

Thus, "the" electric field under consideration will typically be $\boldsymbol{E}_{\perp}=-\dot{\boldsymbol{A}}$ (in the Coulomb gauge). Meanwhile, $\boldsymbol{B}=\boldsymbol{B}_{\perp}=\boldsymbol{\nabla}\times\boldsymbol{A}$ is always transverse.

After doing such eliminations in Eq. (C.6) and doing some integration by parts, one gets the redundancyless Lagrangian

$$L(\boldsymbol{r}_n,\boldsymbol{A})=T_p+\int d^3r\mathcal{L}'_f, \tag{C.30}$$

where the first term is the kinetic energy of the particles,

$$T_p=\sum_n\frac{1}{2}m_n\dot{r}_n^2, \tag{C.31}$$

and the second is everything else written in terms of the Lagrangian density

$$\mathcal{L}'_f=\mathcal{L}_f-\frac{1}{2}\rho(\boldsymbol{r},\boldsymbol{r}_n)U(\boldsymbol{r},\boldsymbol{r}_n) \tag{C.32}$$

with

$$\mathcal{L}_f=\frac{\varepsilon_0}{2}\left\{\dot{A}^2(\boldsymbol{r})-c^2\left[\boldsymbol{\nabla}\times\boldsymbol{A}(\boldsymbol{r})\right]^2\right\}+\boldsymbol{j}(\boldsymbol{r},\boldsymbol{r}_n)\cdot\boldsymbol{A}(\boldsymbol{r}). \tag{C.33}$$

This Lagrangian density, $\mathcal{L}'_f$, characterizes the fields and their interactions with the particles, yet in it we see a term proportional to ρU that curiously only depends on

the particles via $\boldsymbol{r}_n$ and not on the fields $\boldsymbol{A}$. Upon further inspection, we find that this term is the Coulomb energy of the particles:

$$\frac{1}{2}\int d^3r\rho(\boldsymbol{r})U(\boldsymbol{r}) = \frac{1}{8\pi\varepsilon_0}\int d^3r\int d^3r'\frac{\rho(\boldsymbol{r})\rho(\boldsymbol{r}')}{|\boldsymbol{r}-\boldsymbol{r}'|} = \frac{1}{8\pi\varepsilon_0}\sum_{n,m}\frac{q_nq_m}{|\boldsymbol{r}_n-\boldsymbol{r}_m|} \equiv V_{\text{Coul}}. \tag{C.34}$$

(We will return to V_{Coul}, the $n=m$ terms specifically, at the end of §C.2.5.)

C.2.3 Canonical quantization in the Coulomb gauge

Thus, we arrive at the Lagrangian in terms of the coordinates $q \in \{r_{n,i}, A_i\}$:

$$L(\boldsymbol{r}_n, \boldsymbol{A}) = T_p - V_{\text{Coul}} + \int d^3r\mathcal{L}_f, \tag{C.35}$$

from which we can find the corresponding Hamiltonian via the prescription indicated above. The conjugate momenta are

$$p_{n,i} = \frac{\partial L}{\partial \dot{r}_{n,i}} = m_n\dot{r}_{n,i} + q_nA_i(\boldsymbol{r}_n) \tag{C.36}$$

and, up to a subtlety discussed below,

$$\pi_i = \frac{\partial \mathcal{L}_f}{\partial \dot{A}_i} = \varepsilon_0\dot{A}_i. \tag{C.37}$$

(We use π to denote that this is a continuum variable conjugate momenta, i.e., is defined relative to $\mathcal{L}$ rather than L.) From Eq. (C.24) and some algebra, we thus get

the standard electromagnetic interaction Hamiltonian in the Coulomb gauge:

$$H = \sum_n \frac{1}{2m_n} \left[\boldsymbol{p}_n - q_n \boldsymbol{A}(\boldsymbol{r}_n)\right]^2 + V_{\text{Coul}} + \frac{\varepsilon_0}{2} \int d^3r \left[\dot{A}^2 + c^2 \left(\boldsymbol{\nabla} \times \boldsymbol{A}\right)^2\right]. \tag{C.38}$$

This Hamiltonian is nearly ripe for canonical quantization as the particle variables $r_{n,i}$ and $p_{n,i}$ form a conjugate pair, yet $A_i(\boldsymbol{r})$ and $\pi_i(\boldsymbol{r})$ are not true conjugate pairs (this is the subtlety alluded to above). In particular, it was sloppy to call the quantities $\pi_i(\boldsymbol{r})$ given in Eq. (C.37) the conjugate momenta to $A_i(\boldsymbol{r})$. This is because these A_i are not truly independent coordinates, they are constrained by the relation $\partial_i A_i = 0$ in the Coulomb gauge. Thus, one should more properly work in reciprocal space, where $\boldsymbol{\mathcal{A}}(\boldsymbol{k}) = \boldsymbol{\mathcal{A}}_\perp(\boldsymbol{k})$, the Fourier transform of $\boldsymbol{A}(\boldsymbol{r})$, can be broken into two transverse components each aligned with one of the orthonormal polarization vectors, $\boldsymbol{\varepsilon} \in \{\boldsymbol{\varepsilon}_1, \boldsymbol{\varepsilon}_2\}$, spanning the subspace transverse to $\boldsymbol{k}$:

$$\boldsymbol{\mathcal{A}}(\boldsymbol{k}) = \mathcal{A}_{\boldsymbol{\varepsilon}_1}(\boldsymbol{k})\boldsymbol{\varepsilon}_1 + \mathcal{A}_{\boldsymbol{\varepsilon}_2}(\boldsymbol{k})\boldsymbol{\varepsilon}_2 = \sum_{\boldsymbol{\varepsilon}} \mathcal{A}_{\boldsymbol{\varepsilon}}(\boldsymbol{k})\boldsymbol{\varepsilon}. \tag{C.39}$$

[The Coulomb gauge constraint is then trivially satisfied by there not being a third (longitudinal) component.] These two $\mathcal{A}_{\boldsymbol{\varepsilon}}(\boldsymbol{k})$ are then the true independent field coordinates, which each have a proper conjugate momentum $\pi_{\boldsymbol{\varepsilon}}(\boldsymbol{k}) = \varepsilon_0 \dot{\mathcal{A}}_{\boldsymbol{\varepsilon}}(\boldsymbol{k})$. Then $\boldsymbol{\pi}(\boldsymbol{k}) = \sum_{\boldsymbol{\varepsilon}} \pi_{\boldsymbol{\varepsilon}}(\boldsymbol{k})\boldsymbol{\varepsilon} = \varepsilon_0 \dot{\boldsymbol{\mathcal{A}}}(\boldsymbol{k})$ and one nonetheless ends up with $\boldsymbol{\pi}(\boldsymbol{r}) = \varepsilon_0 \dot{\boldsymbol{A}}(\boldsymbol{r})$ as is consistent with Eq. (C.37) [22].

With that clarified, we can use the Parseval–Plancherel identity, Eq. (C.3), to express the last term of Eq. (C.38) in reciprocal space, yielding

$$H = \sum_n \frac{1}{2m_n} \left[\boldsymbol{p}_n - q_n \boldsymbol{A}(\boldsymbol{r}_n)\right]^2 + V_{\text{Coul}}(\{\boldsymbol{r}_n\}) + \frac{\varepsilon_0}{2} \int d^3k \left[\frac{\boldsymbol{\pi}^*(\boldsymbol{k}) \cdot \boldsymbol{\pi}(\boldsymbol{k})}{\varepsilon_0^2} + c^2 k^2 \boldsymbol{\mathcal{A}}^*(\boldsymbol{k}) \cdot \boldsymbol{\mathcal{A}}(\boldsymbol{k})\right], \tag{C.40}$$

which is expressed entirely in terms of canonically conjugate variables—with the understanding that, in the first term, $\boldsymbol{A}(\boldsymbol{r}_n)$ is a function of the particle position, $\boldsymbol{r}_n$, and the field variables, $\mathcal{A}_{\boldsymbol{\varepsilon}}(\boldsymbol{k})$, as later made concrete in Eq. (C.47). This H can thus be quantized simply by replacing the conjugate pairs $\{r_{n,i}, p_{n,i}\}$ and $\{\mathcal{A}_{\boldsymbol{\varepsilon}}(\boldsymbol{k}), \pi_{\boldsymbol{\varepsilon}}(\boldsymbol{k})\}$ with operators satisfying the commutation relations [22]

$$[r_{n,i}, p_{m,j}] = i\hbar\delta_{nm}\delta_{ij} \tag{C.41}$$

and[5]

$$\left[\mathcal{A}_{\boldsymbol{\varepsilon}}(\boldsymbol{k}), \pi^{\dagger}_{\boldsymbol{\varepsilon}'}(\boldsymbol{k}')\right] = i\hbar\delta_{\boldsymbol{\varepsilon}\boldsymbol{\varepsilon}'}\delta^3(\boldsymbol{k}-\boldsymbol{k}'). \tag{C.42}$$

Moreover, these operators commute with themselves (even for different labels, e.g., $[p_{n,i}, p_{m,k}] = 0$, $[A_{\boldsymbol{\varepsilon}}(\boldsymbol{k}), A_{\boldsymbol{\varepsilon}'}(\boldsymbol{k}')] = 0$, etc.) and the particle operators commute with field operators.

Motivated by the normal mode decomposition of the transverse electromagnetic field in reciprocal space, we introduce the operator

$$a_{\boldsymbol{\varepsilon}}(\boldsymbol{k}) = \sqrt{\frac{\varepsilon_0}{2\hbar\omega}}\left[\omega\mathcal{A}_{\boldsymbol{\varepsilon}}(\boldsymbol{k}) + \frac{i}{\varepsilon_0}\pi_{\boldsymbol{\varepsilon}}(\boldsymbol{k})\right], \tag{C.43}$$

with $\omega = \omega_k = ck$, and its adjoint $a^{\dagger}_{\boldsymbol{\varepsilon}}(\boldsymbol{k})$. From the commutator of Eq. (C.42), one finds

$$\left[a_{\boldsymbol{\varepsilon}}(\boldsymbol{k}), a^{\dagger}_{\boldsymbol{\varepsilon}'}(\boldsymbol{k}')\right] = \delta_{\boldsymbol{\varepsilon},\boldsymbol{\varepsilon}'}\delta^3(\boldsymbol{k}-\boldsymbol{k}') \tag{C.44}$$

[5]Note that as we are working with complex fields $\mathcal{A}_{\boldsymbol{\varepsilon}}(\boldsymbol{k})$ that are promoted to operators, their complex conjugates are promoted to the corresponding adjoint (or Hermitian conjugate) operators, $\mathcal{A}^*_{\boldsymbol{\varepsilon}}(\boldsymbol{k}) = \mathcal{A}_{\boldsymbol{\varepsilon}}(-\boldsymbol{k}) \to \mathcal{A}^{\dagger}_{\boldsymbol{\varepsilon}}(\boldsymbol{k})$, and likewise for their conjugate momenta, $\pi^*_{\boldsymbol{\varepsilon}}(\boldsymbol{k}) = \pi_{\boldsymbol{\varepsilon}}(-\boldsymbol{k}) \to \pi^{\dagger}_{\boldsymbol{\varepsilon}}(\boldsymbol{k})$. The correspondence between complex conjugation and flipping the sign of $\boldsymbol{k}$ is inherited from H being real and likewise applies to the adjoints upon quantization.

as well as

$$[a_{\boldsymbol{\varepsilon}}(\boldsymbol{k}), a_{\boldsymbol{\varepsilon}'}(\boldsymbol{k}')] = \left[a^\dagger_{\boldsymbol{\varepsilon}}(\boldsymbol{k}), a^\dagger_{\boldsymbol{\varepsilon}'}(\boldsymbol{k}')\right] = 0. \tag{C.45}$$

These relations demonstrate that $a^\dagger_{\boldsymbol{\varepsilon}}(\boldsymbol{k})$ and $a_{\boldsymbol{\varepsilon}}(\boldsymbol{k})$ are the raising and lowering operators for a harmonic oscillator of frequency $\omega = ck$, respectively. As introduced in §1.4, the action of these operators, $a^\dagger_{\boldsymbol{\varepsilon}}(\boldsymbol{k})$ and $a_{\boldsymbol{\varepsilon}}(\boldsymbol{k})$, on states of the electromagnetic field is to create or annihilate a photon in the mode $\{\boldsymbol{k}, \boldsymbol{\varepsilon}\}$, respectively.

One can invert Eq. (C.43) and its adjoint expression, to find

$$\mathcal{A}_{\boldsymbol{\varepsilon}}(\boldsymbol{k}) = \sqrt{\frac{\hbar}{2\varepsilon_0 \omega}} \left[a_{\boldsymbol{\varepsilon}}(\boldsymbol{k}) + a^\dagger_{\boldsymbol{\varepsilon}}(-\boldsymbol{k})\right] \tag{C.46}$$

as well as a similar expression for $\pi_{\boldsymbol{\varepsilon}}(\boldsymbol{k})$. From Eqs. (C.1), (C.39), and (C.46) one then obtains

$$\boldsymbol{A}(\boldsymbol{r}) = \int \frac{d^3k}{(2\pi)^{3/2}}\, \boldsymbol{\mathcal{A}}(\boldsymbol{k}) e^{i\boldsymbol{k}\cdot\boldsymbol{r}} = \int d^3k \sum_{\boldsymbol{\varepsilon}} \mathcal{A}_k \boldsymbol{\varepsilon} \left[a_{\boldsymbol{\varepsilon}}(\boldsymbol{k}) e^{i\boldsymbol{k}\cdot\boldsymbol{r}} + a^\dagger_{\boldsymbol{\varepsilon}}(\boldsymbol{k}) e^{-i\boldsymbol{k}\cdot\boldsymbol{r}}\right] \tag{C.47}$$

with $\mathcal{A}_k \equiv \left[2(2\pi)^3 \varepsilon_0 \omega_k / \hbar\right]^{-1/2}$ [precisely as claimed in Eq. (2.8) of the main text]. After leveraging these expressions and doing some algebra, one can write the quantized operator version of Eq. (C.40), expressed fully in terms of the particle operators $\{r_{n,i}, p_{n,i}\}$ and field operators $\{a_{\boldsymbol{\varepsilon}}(\boldsymbol{k}), a^\dagger_{\boldsymbol{\varepsilon}}(\boldsymbol{k})\}$, as

$$\begin{aligned} H = &\sum_{n=1}^{N} \frac{1}{2m_n} \left[\boldsymbol{p}_n - q_n \boldsymbol{A}(\boldsymbol{r}_n)\right]^2 + V_{\text{Coul}}(\{\boldsymbol{r}_n\}) \\ &+ \int d^3k \frac{\hbar\omega_k}{2} \sum_{\boldsymbol{\varepsilon}} \left[a^\dagger_{\boldsymbol{\varepsilon}}(\boldsymbol{k}) a_{\boldsymbol{\varepsilon}}(\boldsymbol{k}) + a_{\boldsymbol{\varepsilon}}(\boldsymbol{k}) a^\dagger_{\boldsymbol{\varepsilon}}(\boldsymbol{k})\right], \end{aligned} \tag{C.48}$$

where, in the first term, it is implicit that $\boldsymbol{A}(\boldsymbol{r}_n)$, which is Eq. (C.47) evaluated at $\boldsymbol{r} \to \boldsymbol{r}_n$, is a function of the field operators $\{a_{\boldsymbol{\varepsilon}}(\boldsymbol{k}), a^\dagger_{\boldsymbol{\varepsilon}}(\boldsymbol{k})\}$ as well as $\boldsymbol{r}_n$.

C.2.4 Field expansions

The transverse vector potential $\boldsymbol{A} = \boldsymbol{A}_\perp$ (in the Coulomb gauge) is of fundamental importance in developing this formalism. However, we ultimately care about the (physical) electromagnetic fields. Thus, we note that the transverse fields admit normal-mode field expansions in terms of $a_{\boldsymbol{\varepsilon}}(\boldsymbol{k})$ and $a^\dagger_{\boldsymbol{\varepsilon}}(\boldsymbol{k})$. Namely, following Eq. (C.47),

$$\boldsymbol{E}_\perp(\boldsymbol{r}) = -\dot{\boldsymbol{A}} = -\int d^3k \sum_{\boldsymbol{\varepsilon}} \mathcal{A}_k \boldsymbol{\varepsilon} \left[\dot{a}_{\boldsymbol{\varepsilon}}(\boldsymbol{k}) e^{i\boldsymbol{k}\cdot\boldsymbol{r}} + \dot{a}^\dagger_{\boldsymbol{\varepsilon}}(\boldsymbol{k}) e^{-i\boldsymbol{k}\cdot\boldsymbol{r}}\right] \tag{C.49}$$

and

$$\boldsymbol{B}(\boldsymbol{r}) = \boldsymbol{B}_\perp = \boldsymbol{\nabla}\times\boldsymbol{A} = \int d^3k \sum_{\boldsymbol{\varepsilon}} i\mathcal{A}_k \left(\boldsymbol{k}\times\boldsymbol{\varepsilon}\right) \left[a_{\boldsymbol{\varepsilon}}(\boldsymbol{k}) e^{i\boldsymbol{k}\cdot\boldsymbol{r}} - a^\dagger_{\boldsymbol{\varepsilon}}(\boldsymbol{k})^{-i\boldsymbol{k}\cdot\boldsymbol{r}}\right]. \tag{C.50}$$

This form for $\boldsymbol{E}_\perp$, written in terms of time derivatives of the creation and annihilation operators, is not particularly instructive until we determine $\dot{a}_{\boldsymbol{\varepsilon}}(\boldsymbol{k})$, which can be done leveraging its Heisenberg EOM: $i\hbar\dot{a}_{\boldsymbol{\varepsilon}}(\boldsymbol{k}) = [a_{\boldsymbol{\varepsilon}}(\boldsymbol{k}), H]$, with H given by Eq. (C.48). After some algebra, and the repeated leveraging of the field commutator of Eq. (C.44), one obtains

$$\dot{a}_{\boldsymbol{\varepsilon}}(\boldsymbol{k}) + i\omega_k a_{\boldsymbol{\varepsilon}}(\boldsymbol{k}) = \frac{i}{\sqrt{2\varepsilon_0\hbar\omega_k}} \boldsymbol{\varepsilon}\cdot\boldsymbol{j}(\boldsymbol{k}), \tag{C.51}$$

where $\boldsymbol{j}(\boldsymbol{k})$ is defined as the Fourier transform of the symmetrized current

$$\boldsymbol{j}(\boldsymbol{r}) = \sum_n \frac{q_n}{2}\left[\boldsymbol{v}_n\delta^3(\boldsymbol{r}-\boldsymbol{r}_n) + \delta^3(\boldsymbol{r}-\boldsymbol{r}_n)\boldsymbol{v}_n\right] \tag{C.52}$$

with $\boldsymbol{v}_n \equiv [\boldsymbol{p}_n - q_n \boldsymbol{A}(\boldsymbol{r}_n)]/m_n$. Using Eq. (C.51) to eliminate $\dot{a}_{\boldsymbol{\varepsilon}}(\boldsymbol{k})$ and its adjoint from Eq. (C.49), we have

$$\begin{aligned}
\boldsymbol{E}_\perp(\boldsymbol{r}) &= i \int d^3k \mathcal{A}_k \Bigg(\omega_k \sum_{\boldsymbol{\varepsilon}} \boldsymbol{\varepsilon} \left[a_{\boldsymbol{\varepsilon}}(\boldsymbol{k}) e^{i\boldsymbol{k}\cdot\boldsymbol{r}} - a^\dagger_{\boldsymbol{\varepsilon}}(\boldsymbol{k}) e^{-i\boldsymbol{k}\cdot\boldsymbol{r}} \right] \\
&\qquad - \frac{1}{\sqrt{2\varepsilon_0 \hbar \omega_k}} \left[\boldsymbol{j}(\boldsymbol{k}) e^{i\boldsymbol{k}\cdot\boldsymbol{r}} - \boldsymbol{j}^\dagger(\boldsymbol{k}) e^{-i\boldsymbol{k}\cdot\boldsymbol{r}} \right] \Bigg) \qquad \text{(C.53a)} \\
&= i \int d^3k \; \omega_k \mathcal{A}_k \sum_{\boldsymbol{\varepsilon}} \boldsymbol{\varepsilon} \left[a_{\boldsymbol{\varepsilon}}(\boldsymbol{k}) e^{i\boldsymbol{k}\cdot\boldsymbol{r}} - a^\dagger_{\boldsymbol{\varepsilon}}(\boldsymbol{k}) e^{-i\boldsymbol{k}\cdot\boldsymbol{r}} \right], \qquad \text{(C.53b)}
\end{aligned}$$

which confirms Eq. (2.13) and is a more standard and useful expression for $\boldsymbol{E}_\perp$ in terms of the creation and annihilation operators themselves, rather than their time derivatives. Note that to go from Eq. (C.53a) to Eq. (C.53b), we negated space, $\boldsymbol{k} \to -\boldsymbol{k}$, in the $\boldsymbol{j}^\dagger(\boldsymbol{k}) e^{-i\boldsymbol{k}\cdot\boldsymbol{r}}$ term and leveraged that $\boldsymbol{j}^\dagger(\boldsymbol{k}) = \boldsymbol{j}(-\boldsymbol{k})$ as $\boldsymbol{j}(\boldsymbol{r})$ is real.

It is important to note that although the explicit dependence of $\boldsymbol{E}_\perp$ on the current $\boldsymbol{j}(\boldsymbol{r})$ canceled in the above equation, the current still impacts $\boldsymbol{E}_\perp$ (as well as $\boldsymbol{A}$ and $\boldsymbol{B}$) through $a_{\boldsymbol{\varepsilon}}(\boldsymbol{k})$. In particular, formally solving Eq. (C.51), given an initial condition at time t_0, yields

$$a_{\boldsymbol{\varepsilon}}(\boldsymbol{k}, t) = a_{\boldsymbol{\varepsilon}}(\boldsymbol{k}, t_0) e^{-i\omega(t-t_0)} + i \int_{t_0}^{t} dt' \frac{\boldsymbol{\varepsilon} \cdot \boldsymbol{j}(\boldsymbol{k}, t')}{\sqrt{2\varepsilon_0 \hbar \omega_k}} e^{-i\omega(t-t')}. \qquad \text{(C.54)}$$

Thus, for the free field, $\boldsymbol{j} = \boldsymbol{0}$, has plane wave solutions, i.e., $a_{\boldsymbol{\varepsilon}}(\boldsymbol{k}, t)$ $[a^\dagger_{\boldsymbol{\varepsilon}}(\boldsymbol{k}, t)]$ has time dependence $e^{-i\omega t}$ $[e^{+i\omega t}]$ and annihilates [creates] a monocromatic, plane-wave photon with wavevector $\boldsymbol{k}$, frequency $\omega_k = ck$, and polarization $\boldsymbol{\varepsilon}$ (though one can construct wave packets; see Fig. 1.3). More generally, in the presence of sources, $\boldsymbol{j} \neq \boldsymbol{0}$, the photonic mode solutions will be more complicated, polychromatic wave packets.

C.2.5 UV divergences

When a given operator is expanded in terms of creation and annihilation operators, it is often instructive to put all of the creation operators, $a^\dagger$, to the left and annihilation operators, a, to the right (called normal-ordering) using their commutator, Eq. (C.44). For instance, the operator portion of the last term of H in the Eq. (C.40) can be expressed in normal order as

$$\frac{1}{2}\left[a_{\boldsymbol{\varepsilon}}(\boldsymbol{k})a^\dagger_{\boldsymbol{\varepsilon}}(\boldsymbol{k}) + a^\dagger_{\boldsymbol{\varepsilon}}(\boldsymbol{k})a_{\boldsymbol{\varepsilon}}(\boldsymbol{k})\right] = a^\dagger_{\boldsymbol{\varepsilon}}(\boldsymbol{k})a_{\boldsymbol{\varepsilon}}(\boldsymbol{k}) + \frac{1}{2}\delta^3(\mathbf{0}). \tag{C.55}$$

A normally ordered, non-constant term exhibits the nicety that its vacuum expectation value is always zero, e.g., $\langle \text{vac}| \left(a^\dagger\right)^m a^n |\text{vac}\rangle = 0$ (this is likewise the case for multimode operators), where $|\text{vac}\rangle$ is the state with every field mode in its (harmonic oscillator) ground state, $|0\rangle$. As presented, the non-operator term $\frac{1}{2}\delta^3(\mathbf{0})$ diverges, leading to an infinite vacuum energy in Eq. (C.48) (the sum of the harmonic oscillator ground state energies, $\frac{1}{2}\hbar\omega_k$, over the full continuum of modes). This is just one of the infinities in H, the other is the self-energy terms in V_{Coul} [the $n = m$ terms in Eq. (C.34)]. These so-called ultraviolet (UV) divergences are remnants of our non-relativistic description of the matter, which is not valid for high-frequency modes. In particular, we implicitly included these relativistic modes in our reciprocal (real) space integrals by including large $\boldsymbol{k}$ (small $\boldsymbol{r}$) contributions. Because we are not interested in these high-frequency modes (we are concerned with low-energy quantum systems), we can temper these infinities by introducing a UV cutoff $g(k)$, to be included in k-space integrals, that by fiat suppresses high-frequency contributions, i.e., $g(k)$ would be unity up til some energy scale $\hbar c k_c \sim mc^2$ (for m a typical particle mass), beyond which it decreases to zero. To make this more evident for the self-energy terms, we

express Eq. (C.34) in reciprocal space [see sections I.B.5 a) and II.C.5 d) of Ref. 22]

$$V_{\text{Coul}} = \sum_{n,m} \frac{q_n q_m}{2\varepsilon_0 (2\pi)^3} \int d^3k \frac{e^{-i\boldsymbol{k}\cdot(\boldsymbol{r}_n - \boldsymbol{r}_m)}}{k^2}. \tag{C.56}$$

We can split this into self-energy and interparticle contributions, $V_{\text{Coul}} = V_{\text{self}} + V$, with

$$V_{\text{self}} = \sum_{n} \frac{q_n^2}{2\varepsilon_0 (2\pi)^3} \int d^3k \frac{1}{k^2} \tag{C.57}$$

and

$$V(\{\boldsymbol{r}_n\}) = \sum_{n \neq m} \frac{q_n q_m}{2\varepsilon_0 (2\pi)^3} \int d^3k \frac{e^{-i\boldsymbol{k}\cdot(\boldsymbol{r}_n - \boldsymbol{r}_m)}}{k^2} = \frac{1}{8\pi\varepsilon_0} \sum_{n \neq m} \frac{q_n q_m}{|\boldsymbol{r}_n - \boldsymbol{r}_m|}. \tag{C.58}$$

For the vacuum energy term, we note that it diverges at every point in reciprocal space due to the $\delta^3(\mathbf{0})$ term in Eq. (C.55) (this can be regarded as an infrared divergence). One can temper this by quantizing the theory in a cubical box of side lengths L (that should be taken to ∞ at the end of the calculation), in which case reciprocal space is discretized so integrals therein are replaced by sums, $\int d^3k f(\boldsymbol{k}) \to \sum_{\boldsymbol{k}} \left(\frac{2\pi}{L}\right)^3 f(\boldsymbol{k})$. The ultimate result of such a quantizing in a box procedure is that one can make the effective replacement $\delta^3(\mathbf{0}) \to (L/2\pi)^3$. Ultimately, by introducing a cutoff $g(k)$ and working in a finite volume, L^3, the previous divergences become constants (no operator dependence):

$$H_{\text{UV}} = V_{\text{self}} + E_{\text{vac}} = \int d^3k \; g(k) \left[\frac{(\sum_n q_n^2)}{2\varepsilon_0 (2\pi)^3} \frac{1}{k^2} + \sum_{\boldsymbol{\varepsilon}} \frac{\hbar\omega_k}{2} \left(\frac{L}{2\pi}\right)^3 \right] \tag{C.59a}$$

$$= \frac{(\sum_n q_n^2)\, k_c}{4\pi^2 \varepsilon_0} + \frac{\hbar c L^3}{8\pi^2} k_c^4, \tag{C.59b}$$

where we have treated $g(k)$ as a step function that goes from one to zero at k_c, if $g(k)$ smoothly drops off around k_c, the last equality will only be the leading order approximation. For any finite L and k_c, $H_{\rm UV}$ can be treated as a finite energy offset that is of no physical significance (it will not change resulting EOMs) and hence can be ignored.[6] Then, after these divergences have been effectively removed, one can take the physical limit $L \to \infty$ and arrive at the light-matter Hamiltonian in the Coulomb gauge

$$\boxed{H_{\rm lm} = \sum_n \frac{1}{2m_n}\left[\boldsymbol{p}_n - q_n \boldsymbol{A}(\boldsymbol{r}_n)\right]^2 + V(\{\boldsymbol{r}_n\}) + \int d^3k \sum_{\boldsymbol{\varepsilon}} \hbar\omega_k a^\dagger_{\boldsymbol{\varepsilon}}(\boldsymbol{k}) a_{\boldsymbol{\varepsilon}}(\boldsymbol{k}).} \tag{C.60}$$

To obtain Eq. (2.2), one extends Eq. (C.60) to include the possibility of external fields via an additional vector potential $\boldsymbol{A}_{\rm ext}$ and background potential energy function $V_{\rm ext}$ (see CII of Ref. 22, page 141). Henceforth we allow for these additional fields and, while its not strictly necessary, we find it convenient to also work in the Coulomb gauge for these external fields, e.g., then $\boldsymbol{E}_{\perp,\rm tot} = -\dot{\boldsymbol{A}}_{\rm tot}$. Note that one should in principle include the cutoff function $g(k)$ in the above expression (and subsequent ones), e.g, to indicate that the Coulomb interaction breaks down at very close distances. However, doing so is tantamount to not considering situations in which such high frequency modes are dynamic or relevant, which will be our approach. More complete treatments of such UV divergences using a relativistic description of

[6] We acknowledge that this treatment is rather cavalier, yet we note that the removal of such divergences is both incredibly standard and often justified (as confirmed by experiment). In particular, this cavalier treatment will suffice for our purposes as the looming divergence, e.g., in Eq. (C.48) and subsequent Hamiltonians, can safely be ignored as they will not alter the physics we analyze in Chs. III and IV. Note, however, that there are instances wherein the structure of electromagnetic divergences—such as those in Eq. (C.59a), which we ignored—are important, e.g., in calculating the Lamb shift (which requires relativistic quantum electrodynamics; see section 13.12 of Ref. 133).

the matter, i.e., quantum field theory with renormalization (which also includes the notion of a UV cutoff), are left to other works (e.g., see Ref. 313).

C.3 Multipolar interaction Hamiltonian

As discussed in the main text (§2.2.2), it will be useful to unitarily transform this so-called "minimal coupling" Hamiltonian of Eq. (C.60) into a more convenient and illuminating form for our purposes. Thus, we start with a brief review of such Hamiltonian transformations (§C.3.1). We will then show how the Power–Zienau–Woolley (PZW) transformation takes us from interaction terms of the form $\frac{q}{m}\boldsymbol{p}\cdot\boldsymbol{A}$ to dipole-interaction terms, $\boldsymbol{d}\cdot\boldsymbol{E}$, in the long-wavelength approximation (§C.3.2).

C.3.1 Quantum representations under unitarily equivalent Hamiltonians

We start by reviewing how unitarily equivalent Hamiltonians can be used to ease calculations and provide physical insights. Under a unitary transformation, which may depend on the dynamic variables of a theory and time, $U(t)$, one can define a correspondence between the states and operators in two descriptions, labeled 1 and 2, respectively as

$$|\psi_2(t)\rangle = U(t)|\psi_1(t)\rangle \tag{C.61}$$

and

$$\mathcal{O}_2(t) = U(t)\mathcal{O}_1(t)U^\dagger(t). \tag{C.62}$$

One then clearly sees that expectation values are identical in the two representations:

$$\langle\mathcal{O}\rangle = \langle\psi_2|\mathcal{O}_2|\psi_2\rangle = \langle\psi_1|U^\dagger U\mathcal{O}_1U^\dagger U|\psi_1\rangle = \langle\psi_1|\mathcal{O}_1|\psi_1\rangle \tag{C.63}$$

(all at time t), where $U^\dagger U = I$ as U is unitary. One can further show that transition amplitudes are also identical in the two representations.

Note, however, that the Hamiltonian is special and transforms in a different manner to a generic operator $\mathcal{O}$. To see this, consider the Schrödinger equation in the two representations: $i\hbar\frac{d}{dt}|\psi_j(t)\rangle = H_j(t)|\psi_j(t)\rangle$ for $j = 1, 2$. To see the relation between these Hamiltonians we multiply Eq. (C.61) by $i\hbar$, then take a time derivative:

$$i\hbar\frac{d}{dt}|\psi_2(t)\rangle = \left[U(t)H_1(t) + i\hbar\frac{dU(t)}{dt}\right]|\psi_1(t)\rangle = \left[U(t)H_1(t) + i\hbar\frac{dU(t)}{dt}\right]U^\dagger(t)|\psi_2(t)\rangle, \tag{C.64}$$

where the product rule and the $j = 1$ Schrödinger equation were used to establish the first equality, and the second equality follows from inverting Eq. (C.61). For consistency with the $j = 2$ Schrödinger equation, we thus identify

$$H_2(t) = U(t)H_1(t)U^\dagger(t) + i\hbar\dot{U}(t)U^\dagger(t), \tag{C.65}$$

so, relative to Eq. (C.62), the transformed Hamiltonian acquires an additional term for time-dependent unitaries, $U(t)$. Some important examples of this transformation are going from the Schrödinger picture to the Heisenberg picture [see Eq. (1.8)] or interaction picture (see §2.2.4).

C.3.2 Power–Zienau–Woolley transformation

In Eq. (2.16), we expressed the PZW transformation in real space. However, to make the connection to and subsequently employ the LWA it will be helpful to work in reciprocal space. Thus, we use the Parseval–Plancherel identity to express the

PZW unitary transformation as

$$U(t) = \exp\left[\frac{-i}{\hbar}\int d^3k\ \boldsymbol{\mathcal{P}}^*(\boldsymbol{k})\cdot\boldsymbol{\mathcal{A}}_{\rm tot}(\boldsymbol{k},t)\right], \tag{C.66}$$

where $\boldsymbol{\mathcal{A}}_{\rm tot}(\boldsymbol{k},t)$ and $\boldsymbol{\mathcal{P}}(\boldsymbol{k})$ are the Fourier transforms of the total vector potential $\boldsymbol{A}_{\rm tot}(\boldsymbol{r},t)$ and polarization distribution $\boldsymbol{P}(\boldsymbol{r})$, respectively. From Eqs. (C.39) and (C.46), we find

$$\boldsymbol{\mathcal{A}}_{\rm tot}(\boldsymbol{k},t) = \sqrt{\frac{\hbar}{2\varepsilon_0\omega}}\sum_{\boldsymbol{\varepsilon}}\boldsymbol{\varepsilon}\left[a_{\boldsymbol{\varepsilon}}(\boldsymbol{k}) + a^\dagger_{\boldsymbol{\varepsilon}}(-\boldsymbol{k})\right] + \boldsymbol{\mathcal{A}}_{\rm ext}(\boldsymbol{k},t) \tag{C.67a}$$

$$= \int\frac{d^3r}{(2\pi)^{3/2}}\boldsymbol{A}_{\rm tot}(\boldsymbol{r},t)e^{-i\boldsymbol{k}\cdot\boldsymbol{r}}, \tag{C.67b}$$

where we added the term $\boldsymbol{\mathcal{A}}_{\rm ext}(\boldsymbol{k},t)$ to allow external fields to be included in the description, as is consistent with Eq. (2.5). The Fourier transform of $\boldsymbol{P}(\boldsymbol{r})$, as given by Eq. (2.17), is

$$\boldsymbol{\mathcal{P}}(\boldsymbol{k}) = \sum_n\int_0^1 du\frac{q_n\boldsymbol{r}_n}{(2\pi)^{3/2}}e^{-iu(\boldsymbol{k}\cdot\boldsymbol{r}_n)}. \tag{C.68}$$

As noted in §2.2.2, one can calculate the full PZW transformed Hamiltonian as is done by Refs. 22 and 133. However, this is seldom necessary in quantum-information processing because the material quantum systems used, e.g., to encode qubits, are typically very small compared to wavelength, λ, of light interacting with them.

Accordingly, it is standard[7] to use the long-wavelength approximation introduced in §1.3.5 and focus on dominant interactions. Under this approximation, one expands $\boldsymbol{\mathcal{P}}(\boldsymbol{k})$ for long-wavelength modes, $\boldsymbol{k}\cdot\boldsymbol{r}_n \ll 1$, using $e^{-iu(\boldsymbol{k}\cdot\boldsymbol{r}_n)} = 1 - iu(\boldsymbol{k}\cdot\boldsymbol{r}_n) + \mathcal{O}(\boldsymbol{k}\cdot\boldsymbol{r}_n)^2$.

[7]Indeed, even after deriving the full PZW transformed Hamiltonian, the aforementioned Refs. 22 and 133 often employ the long-wavelength approximation.

Truncating this expansion to next to leading order, we will work with

$$\mathcal{P}_j(\boldsymbol{k}) = \sum_n \frac{q_n r_{n,j}}{(2\pi)^{3/2}} \left[1 - \frac{i}{2}(\boldsymbol{k}\cdot\boldsymbol{r}_n)\right] = \frac{1}{(2\pi)^{3/2}}\left(d_j - ik_i Q_{ij}\right) \tag{C.69}$$

with

$$\boldsymbol{d} = \sum_n \boldsymbol{d}_n \equiv \sum_n q_n \boldsymbol{r}_n \tag{C.70}$$

the dipole moment operator and

$$Q_{ij} = \frac{1}{2}\sum_n q_n r_{n,i} r_{n,j} \tag{C.71}$$

the (nontraceless) quadrupole moment tensor operator. One can, of course, account for more intricate variations in the field via higher-order terms in the its Taylor expansion, which correspond to higher-order multipolar interactions.

We can now transform the Hamiltonian of Eq. (2.2), which is Eq. (C.60) with external fields, via U. Using Eq. (C.65)

$$H'(t) = U(t)H_{\rm lm}(t)U^\dagger(t) + i\hbar\dot{U}(t)U^\dagger(t) \tag{C.72}$$

with the unitary

$$U(t) = \exp\left[\frac{-i}{\hbar}\int \frac{d^3k}{(2\pi)^{3/2}}\left(d_j + ik_i Q_{ij}\right)\mathcal{A}_{{\rm tot},j}(\boldsymbol{k},t)\right]. \tag{C.73}$$

To determine H' we will first determine how the dynamical variables transform. The simplest case is

$$\boldsymbol{r}_n \to \boldsymbol{r}'_n = U\boldsymbol{r}_n U^\dagger = \boldsymbol{r}_n \tag{C.74}$$

as $U(t)$ does not depend on $\boldsymbol{p}_n$ and hence commutes with $\boldsymbol{r}_n$. Similarly, functions of $\boldsymbol{r}_n$, including $\boldsymbol{A}_{\rm tot}(\boldsymbol{r}_n,t)$ and $V_{\rm tot}(\boldsymbol{r}_n,t)$, are unchanged. To evaluate the other (less trivial) variable transformations, we will employ the Baker–Campbell–Hausdorff lemma

$$e^X Y e^{-X} = \sum_{n=0}^{\infty} \frac{1}{n!}[X^n_{,}Y] \tag{C.75}$$

using the shorthand

$$[X^n_{,}Y] \equiv [\underbrace{X,\cdots[X,[X}_{n\text{ times}},Y]]\cdots] \tag{C.76}$$

with $[X^0_{,}Y] \equiv Y$. In the special case where $[X,[X,Y]] = 0$ one finds $e^X Y e^{-X} = Y + [X,Y]$.

Thus, the conjugate particle momentum components transform as

$$p_{n,k} \to p'_{n,k} = U p_{n,k} U^\dagger = \sum_{m=0}^{\infty} \frac{1}{m!}[\ln(U)^m_{,}p_{n,k}]. \tag{C.77}$$

We first consider

$$[\ln(U), p_{n,k}] = \left[\frac{-i}{\hbar}\int d^3k \frac{1}{(2\pi)^{3/2}}\left(d_j + ik_i Q_{ij}\right)\mathcal{A}_{{\rm tot},j}(\boldsymbol{k},t), p_{n,k}\right] \tag{C.78a}$$

$$= \frac{-i}{\hbar}\int d^3k \frac{1}{(2\pi)^{3/2}}\left[d_j + ik_i Q_{ij}, p_{n,k}\right]\mathcal{A}_{{\rm tot},j}(\boldsymbol{k},t) \tag{C.78b}$$

for which it is helpful to note that Eq. (2.3) can be extended to

$$[f(\boldsymbol{r}_n), p_{m,j}] = i\hbar\delta_{nm}\partial_{r_{m,j}} f(\boldsymbol{r}_n) \tag{C.79}$$

such that

$$[d_j, p_{n,k}] = \sum_m q_m [r_{m,j}, p_{n,k}] = i\hbar q_n \delta_{jk} \tag{C.80}$$

and

$$[Q_{ij}, p_{n,k}] = \frac{1}{2}\sum_m q_m[r_{m,i}r_{m,j}, p_{n,k}] = \frac{i}{2}\hbar q_n \left(r_{n,i}\delta_{jk} + \delta_{ik}r_{n,j}\right). \tag{C.81}$$

It follows that

$$\frac{1}{q_n}[\ln(U), p_{n,k}] = \int \frac{d^3k}{(2\pi)^{3/2}} \left[\delta_{jk} + \frac{i}{2}k_i \left(r_{n,i}\delta_{jk} + \delta_{ik}r_{n,j}\right)\right] \mathcal{A}_{\mathrm{tot},j}(\boldsymbol{k}, t), \tag{C.82a}$$

$$= A_{\mathrm{tot},k}(\boldsymbol{r} = \boldsymbol{0}, t) + \frac{1}{2}\left(r_{n,i}\delta_{jk} + \delta_{ik}r_{n,j}\right)\left[\partial_i A_{\mathrm{tot},j}(\boldsymbol{r}', t)\right]_{\boldsymbol{r}'\to\boldsymbol{0}} \tag{C.82b}$$

$$= A_{\mathrm{tot},k}(\boldsymbol{0}, t) + \frac{1}{2}r_{n,j}\left[\partial_j A_{\mathrm{tot},k}(\boldsymbol{r}', t) + \partial_k A_{\mathrm{tot},j}(\boldsymbol{r}', t)\right]_{\boldsymbol{r}'\to\boldsymbol{0}} \tag{C.82c}$$

$$= A_{\mathrm{tot},k}(\boldsymbol{0}, t) + \frac{1}{2}\left[\boldsymbol{r}_n \times \boldsymbol{B}_{\mathrm{tot}}(\boldsymbol{0}, t)\right]_k + (\boldsymbol{r}_n \cdot \boldsymbol{\nabla})A_{\mathrm{tot},k}(\boldsymbol{0}, t), \tag{C.82d}$$

where we used the Fourier relation of Eq. (C.67b) and the identity

$$\int \frac{d^3k}{(2\pi)^3}k_i e^{-i\boldsymbol{k}\cdot\boldsymbol{r}} = i\partial_i \int \frac{d^3k}{(2\pi)^3}e^{-ik_j r_j} = i\partial_i \delta^3(\boldsymbol{r}), \tag{C.83}$$

followed by integration by parts to go from Eq. (C.82a) to Eq. (C.82b).Then we used

$$\left(\boldsymbol{r}_n \times \boldsymbol{B}\right)_k = \left[\boldsymbol{r}_n \times (\boldsymbol{\nabla} \times \boldsymbol{A})\right]_k = r_{n,j}\left(\partial_k A_j - \partial_j A_k\right) \tag{C.84}$$

for the total fields to go from Eq. (C.82c) to Eq. (C.82d). We now see that the series terminates as $[\ln(U)^2_{;}\, p_{n,k}] = 0$, i.e., $[\ln(U), p_{n,k}]$ commutes with $\ln(U)$ as both are functions of $\boldsymbol{r}_n$ and $\boldsymbol{\mathcal{A}}_{\mathrm{tot}}$, such that

$$\begin{aligned}\boldsymbol{p}'_n &= p_{n,k} + [\ln(U), p_{n,k}] \\ &= \boldsymbol{p}_n + q_n\left[\frac{1}{2}\boldsymbol{r}_n \times \boldsymbol{B}_{\mathrm{tot}}(\boldsymbol{r}, t) + (1 + \boldsymbol{r}_n \cdot \boldsymbol{\nabla})\boldsymbol{A}_{\mathrm{tot}}(\boldsymbol{r}, t)\right]_{\boldsymbol{r}\to\boldsymbol{0}}.\end{aligned} \tag{C.85}$$

Next we consider the transformation of the field variables, $a_{\boldsymbol{\varepsilon}}(\boldsymbol{k})$. Starting with

$$[\ln(U), a_{\boldsymbol{\varepsilon}}(\boldsymbol{k})] = \frac{-i}{\hbar}\int d^3k' \sqrt{\frac{\hbar}{2\varepsilon_0\omega'}}\mathcal{P}_j^*(\boldsymbol{k}')\sum_{\boldsymbol{\varepsilon}'}\boldsymbol{\varepsilon}_j'\left[a_{\boldsymbol{\varepsilon}'}(\boldsymbol{k}') + a_{\boldsymbol{\varepsilon}'}^\dagger(-\boldsymbol{k}'), a_{\boldsymbol{\varepsilon}}(\boldsymbol{k})\right] \tag{C.86a}$$

$$= \frac{i}{\hbar}\int d^3k' \sqrt{\frac{\hbar}{2\varepsilon_0\omega'}}\mathcal{P}_j^*(\boldsymbol{k}')\sum_{\boldsymbol{\varepsilon}'}\boldsymbol{\varepsilon}_j'\delta_{\boldsymbol{\varepsilon},\boldsymbol{\varepsilon}'}\delta^3(\boldsymbol{k}+\boldsymbol{k}') \tag{C.86b}$$

$$= \frac{i}{\hbar}\sqrt{\frac{\hbar}{2\varepsilon_0\omega}}\mathcal{P}_j^*(-\boldsymbol{k})\boldsymbol{\varepsilon}_j \tag{C.86c}$$

we see that higher order commutators clearly vanish, $[\ln(U)^2_{,}\, a_{\boldsymbol{\varepsilon}}(\boldsymbol{k})] = 0$, leaving us with

$$a_{\boldsymbol{\varepsilon}}'(\boldsymbol{k}) = a_{\boldsymbol{\varepsilon}}(\boldsymbol{k}) + \frac{i}{\sqrt{2\varepsilon_0\hbar\omega}}\boldsymbol{\varepsilon}\cdot\boldsymbol{\mathcal{P}}^*(-\boldsymbol{k}). \tag{C.87}$$

With these transformations, we can now rewrite Eq. (C.72) as

$$\begin{aligned} H'(t) = &\sum_n \frac{1}{2m_n}\left[\boldsymbol{p}_n' - q_n\boldsymbol{A}_{\text{tot}}(\boldsymbol{r}_n,t)\right]^2 + V_{\text{tot}}(\boldsymbol{r}_n,t) \\ &+ \int d^3k \sum_{\boldsymbol{\varepsilon}} \hbar\omega_k a_{\boldsymbol{\varepsilon}}'^\dagger(\boldsymbol{k})a_{\boldsymbol{\varepsilon}}'(\boldsymbol{k}) + \int d^3k \boldsymbol{\mathcal{P}}^*(\boldsymbol{k})\cdot\dot{\boldsymbol{\mathcal{A}}}_e(\boldsymbol{k},t), \end{aligned} \tag{C.88}$$

where the last term was evaluated noting that $\boldsymbol{\mathcal{A}}_e$ carries all the time dependence in $\boldsymbol{\mathcal{A}}_{\text{tot}}$. This transformation is exact as written—even though we truncated $\boldsymbol{\mathcal{P}}$ in Eq. (C.69)—because $U(t)$ is a unitary frame change. In this exact form, in the first term of H' we have the expression

$$\begin{aligned} \boldsymbol{p}_n' - q_n\boldsymbol{A}_{\text{tot}}(\boldsymbol{r}_n,t) = \boldsymbol{p}_n &+ \frac{1}{2}\boldsymbol{d}_n\times\boldsymbol{B}_{\text{tot}}(\boldsymbol{0},t) \\ &+ q_n\underbrace{\left[(1+\boldsymbol{r}_n\cdot\boldsymbol{\nabla})\boldsymbol{A}_{\text{tot}}(\boldsymbol{r},t) - \boldsymbol{A}_{\text{tot}}(\boldsymbol{r}_n,t)\right]_{\boldsymbol{r}\to\boldsymbol{0}}}_{\mathcal{O}(kr_n)^2 \overset{\text{LWA}}{\longrightarrow} 0}. \end{aligned} \tag{C.89}$$

Then, to actually leverage the LWA, we expand the vector potential itself, consistently to next to leading order, as

$$\boldsymbol{A}_{\rm tot}(\boldsymbol{r}_n,t) \approx \int \frac{d^3k}{(2\pi)^{3/2}} \boldsymbol{\mathcal{A}}_{\rm tot}(\boldsymbol{k},t)\,(1+i\boldsymbol{k}\cdot\boldsymbol{r}_n) = \left[(1+\boldsymbol{r}_n\cdot\boldsymbol{\nabla})\boldsymbol{A}_{\rm tot}(\boldsymbol{r},t)\right]_{\boldsymbol{r}\to\boldsymbol{0}} \quad \text{(C.90)}$$

such that the last term in Eq. (C.89) can be regarded as zero under the LWA as indicated via the underbrace. Note that dropping this term is the only time the LWA is used in this section, the other zero argument fields are obtained directly from the exact transformation, which singles-out the low frequency, $\boldsymbol{r}\to\boldsymbol{0}$, modes. With this approximation, after doing some algebra and organizing the various contributions, we obtain the (truncated) multipolar interaction Hamiltonian

$$H'(t) \approx H_{\rm sys} + H_B + H_{E\text{-dip}} + H_{E\text{-quad}} + H_{B\text{-dip}} + H_{\rm diamag} + H^{(\rm self)}_{E\text{-dip}} + H^{(\rm self)}_{E\text{-quad}} \quad \text{(C.91)}$$

with

$$H_{\rm sys} = V_{\rm tot}(\boldsymbol{r}_n,t) + \sum_n \frac{p_n^2}{2m_n}, \quad \text{(C.92a)}$$

$$H_B = \int d^3k \sum_{\boldsymbol{\varepsilon}} \hbar\omega_k a^\dagger_{\boldsymbol{\varepsilon}}(\boldsymbol{k}) a_{\boldsymbol{\varepsilon}}(\boldsymbol{k}), \quad \text{(C.92b)}$$

$$H_{E\text{-dip}} = -\boldsymbol{d}\cdot\boldsymbol{E}_{\perp,\rm tot}(\boldsymbol{0},t), \quad \text{(C.92c)}$$

$$H_{E\text{-quad}} = -Q_{ij}\left[\partial_i E_{\perp,{\rm tot},j}(\boldsymbol{r},t)\right]_{\boldsymbol{r}\to\boldsymbol{0}}, \quad \text{(C.92d)}$$

$$H_{B\text{-dip}} = -\boldsymbol{m}\cdot\boldsymbol{B}_{\rm tot}(\boldsymbol{0},t), \quad \text{(C.92e)}$$

$$H_{\rm diamag} = \sum_n \frac{1}{8m_n}\left[\boldsymbol{d}_n\times\boldsymbol{B}_{\rm tot}(\boldsymbol{0},t)\right]^2, \quad \text{(C.92f)}$$

$$H^{(\rm self)}_{E\text{-dip}} = \frac{1}{2\varepsilon_0}\int \frac{d^3k}{(2\pi)^3}\sum_{\boldsymbol{\varepsilon}} (\boldsymbol{\varepsilon}\cdot\boldsymbol{d})^2, \quad \text{(C.92g)}$$

$$H^{(\text{self})}_{E\text{-quad}} = \frac{1}{2\varepsilon_0}\int \frac{d^3k}{(2\pi)^3}\sum_{\boldsymbol{\varepsilon}}(\varepsilon_j k_i Q_{ij})^2, \tag{C.92h}$$

which we dissect in the following subsection. With its origin being the classical Lagrangian of Eq. (C.6), this Hamiltonian is "spin free," in that it does not account for interactions with spin. Such intrinsically quantum interactions are briefly alluded to in the main text (e.g., see §1.3.4) and can be added post hoc as necessary.

C.3.3 Parsing the multipolar interaction Hamiltonian

Now we will address each of the terms in the multipolar interaction Hamiltonian in turn, from Eq. (C.92a) to Eq. (C.92h). Equation (C.92a) is the Hamiltonian for the system of particles themselves, H_{sys}, which consists of their kinetic energy and the potential energy landscape they are subject to via their mutual Coulomb interaction as well as any external fields. Equation (C.92b) is the Hamiltonian of the fields themselves, which, evidently, is the Hamiltonian for a collection of harmonic oscillators for a continuum of modes (for every point in $\boldsymbol{k}$ space with two polarizations) and thus may be regarded as an electromagnetic reservoir or photonic bath (hence the B subscript).

The next four terms are all types of light-matter interactions. The first two of which, Eqs. (C.92c) and (C.92d), are the electric dipole and quadrupole interactions, which characterize the dominant interactions of electric fields with charged matter. We leveraged $\dot{\boldsymbol{A}}_{\text{tot}} = -\boldsymbol{E}_{\perp,\text{tot}}$ (as is valid in the Coulomb gauge) to express them as they are. Note that, more properly, we should be working in terms of the transverse displacement field in this representation, with $\boldsymbol{E}_\perp \to \boldsymbol{D}_\perp/\varepsilon_0$ (see Ref. 22 IV.C.4 and A_{IV}.2). However, the ultimate expansions in terms of the photonic modes (a and $a^\dagger$) will not be changed, so we will not be concerned with this subtlety. The next two

interactions, of Eqs. (C.92e) and (C.92f), are the magnetic dipole and diamagnetic interactions, which characterize the dominant interactions of magnetic and charged material with magnetic fields. In the magnetic dipole interaction

$$\boldsymbol{m} = \frac{1}{2}\sum_n \boldsymbol{d}_n \times \frac{\boldsymbol{p}_n}{m_n} \tag{C.93}$$

is the magnetic dipole moment operator, with $\boldsymbol{d}_n = q_n \boldsymbol{r}_n$, which we made manifest using the identity

$$\boldsymbol{p} \cdot (\boldsymbol{r} \times \boldsymbol{B}_{\text{tot}}) = -(\boldsymbol{r} \times \boldsymbol{p}) \cdot \boldsymbol{B}_{\text{tot}}. \tag{C.94}$$

Nominally, Eq. (C.92e) should be symmetrized, e.g., of the form $-\frac{1}{2}(\boldsymbol{m} \cdot \boldsymbol{B} + \boldsymbol{B} \cdot \boldsymbol{m})$, however the magnetic field is evaluated at $\boldsymbol{r} = \boldsymbol{0}$ [see Eq. (C.85)] and hence is a function of the field variables alone and thus commutes with $\boldsymbol{m}$. Finally, we note that the last two terms in Eq. (C.91) are self energies of the dipole and quadrupole interaction, respectively. They can be handled similarly to the Coulomb self-energy considered in §C.2.5, i.e., by introducing a UV cutoff, $g(k)$, these two terms are constant energy offsets and can thus be dropped (see footnote 6).

C.3.3.1 Typical orders of magnitude of various electromagnetic interactions.

Here we consider the strengths of the various electromagnetic interactions terms in Eq. (C.91). To estimate the orders of magnitude of these interactions we identify the typical scales of the relevant variables. The field quantities are $B \sim E/c$ and $\partial_i \sim k$ (we leave E as a free parameter). Next, we identify the characteristic particle mass, charge, and size as $m_n \sim m_s$, $q_n \sim q$, and $r_n \sim r_s$, respectively; for typical AMO experiments these correspond to the electron mass, electron charge, and atomic radius (of order the Bohr radius). Thus, $d \sim q r_s$, $Q \sim q r_s^2$, and $p_n \sim m_s c k r_s$ (which

can be understood as $p \approx m_s \Delta r/\Delta t$ with $\Delta r \sim r_s$ and $\Delta t \sim 1/\omega = 1/ck$). Using these characteristic values in the interaction Hamiltonians of Eqs. (C.92c)–(C.92f), we have

$$H_{\text{int}} \equiv \underbrace{H_{E\text{-dip}}}_{\mathcal{O}(qr_sE)} + \underbrace{H_{B\text{-dip}}}_{\mathcal{O}(kr_s \cdot qr_sE)} + \underbrace{H_{E\text{-quad}}}_{\mathcal{O}(kr_s \cdot qr_sE)} + \underbrace{H_{\text{diamag}}}_{\mathcal{O}\left(\frac{qr_sE}{m_sc^2} \cdot qr_sE\right)}. \tag{C.95}$$

Recall that for the systems we consider, and quite generally in quantum information processing, $kr_s \ll 1$, which underlies the LWA (see §1.3.5). Thus, the magnetic-dipole and electric-quadrupole interactions are suppressed by a factor of kr_s relative to the electric-dipole interaction, and higher order multipolar interactions are further suppressed by powers of kr_s. Accordingly, under the LWA one often drops higher order interactions, including $H_{B\text{-dip}}$ and $H_{E\text{-quad}}$ (see Eq. (2.46), for a consideration of their inclusion).

Meanwhile, the strength of diamagnetic interaction relative to the other interaction terms depends on the field strength, E. It is instructive to consider when the diamagnetic term is comparable to the magnetic-dipole and electric-quadrupole interactions, using Eq. (C.95) we see that this occurs for $qr_sE/(m_sc^2) \sim kr_s$. Thus, for corresponding field strengths, $E \sim m_sc^2k/q \equiv E_{\text{triad}}$, this triad of interactions share the same energy scale $\mathcal{O}\left[m_ec^2(kr_s)^2\right]$ and the electric-dipole interaction has energy $\mathcal{O}\left[m_ec^2(kr_s)\right]$, which is clearly quite relativistic. To further indicate this, we consider an electron interacting with $\lambda = 780$ nm light (e.g., the D_2 transition in ^{87}Rb), for which the corresponding field strength is $E_{\text{triad}} = 4 \cdot 10^{12}$ V/m (which will only get larger for smaller λ). Such a field is incredibly strong, though achievable with high-powered lasers, it would ionize the atom itself and thus goes beyond the low-energy systems and interactions we are concerned with. Accordingly, the diamagnetic interaction is typically weak compared to the other interactions (for the more modest

fields used in quantum information processing) and can indeed be neglected for the systems we consider. Thus, we are left with the electric-dipole interaction as our primary interaction of interest:

$$\boxed{H_{\text{int}} \approx H_{E\text{-dip}} = -\boldsymbol{d} \cdot \boldsymbol{E}_{\perp,\text{tot}}(\boldsymbol{0}, t)} \tag{C.96}$$

as was presented in Eq. (2.22). However, more generally, one should focus on the dominant interaction term, which depends on the interaction and context (e.g., transitions can be dipole-forbidden and hence require higher-order interactions). Moreover, the phenomenological model we are working towards (see §2.3) is relatively impartial to the precise interaction(s) used.

REFERENCES CITED

[1] J. I. Cirac, P. Zoller, H. J. Kimble, and H. Mabuchi. Quantum state transfer and entanglement distribution among distant nodes in a quantum network. *Physical Review Letters*, 78(16):3221, 1997.

[2] S. J. van Enk, Juan I Cirac, and Peter Zoller. Ideal quantum communication over noisy channels: a quantum optical implementation. *Physical Review Letters*, 78(22):4293, 1997.

[3] Kevin Randles and S. J. van Enk. Quantum state transfer and input-output theory with time reversal. *Physical Review A*, 108(1):012421, 2023.

[4] Kevin Randles and S. J. van Enk. Success probabilities in time-reversal-based hybrid quantum state transfer. *Physical Review A*, 110(1):012415, 2024.

[5] Kevin J Randles and S. J. van Enk. Interference of interference effects. *arXiv preprint arXiv:2501.03505*, 2025 (a condensed version of this article has been accepted by the American Journal of Physics).

[6] Jonathan P Dowling and Gerard J Milburn. Quantum technology: the second quantum revolution. *Philosophical Transactions of the Royal Society of London. Series A: Mathematical, Physical and Engineering Sciences*, 361(1809):1655–1674, 2003.

[7] Michael A Nielsen and Isaac L Chuang. *Quantum computation and quantum information*. Cambridge University Press, 2010.

[8] Christian L Degen, Friedemann Reinhard, and Paola Cappellaro. Quantum sensing. *Reviews of modern physics*, 89(3):035002, 2017.

[9] D Ganapathy, W Jia, M Nakano, V Xu, N Aritomi, T Cullen, N Kijbunchoo, SE Dwyer, A Mullavey, L McCuller, et al. Broadband quantum enhancement of the LIGO detectors with frequency-dependent squeezing. *Physical Review X*, 13(4):041021, 2023.

[10] Nicolas Gisin and Rob Thew. Quantum communication. *Nature photonics*, 1(3):165–171, 2007.

[11] Stefano Pirandola, Ulrik L Andersen, Leonardo Banchi, Mario Berta, Darius Bunandar, Roger Colbeck, Dirk Englund, Tobias Gehring, Cosmo Lupo, Carlo Ottaviani, et al. Advances in quantum cryptography. *Advances in optics and photonics*, 12(4):1012–1236, 2020.

[12] John Preskill. Quantum computing 40 years later. In *Feynman lectures on computation*, pages 193–244. CRC Press, 2023.

[13] Peter W Shor. Algorithms for quantum computation: discrete logarithms and factoring. In *Proceedings 35th annual symposium on foundations of computer science*, pages 124–134. Ieee, 1994.

[14] Chris Monroe, David M Meekhof, Barry E King, Wayne M Itano, and David J Wineland. Demonstration of a fundamental quantum logic gate. *Physical Review Letters*, 75(25):4714, 1995.

[15] Jonathan A Jones and Michele Mosca. Implementation of a quantum algorithm on a nuclear magnetic resonance quantum computer. *The Journal of chemical physics*, 109(5):1648–1653, 1998.

[16] NIST Standard Reference Database 69: NIST Chemistry WebBook. Silicon. Available online at webbook.nist.gov, 2025.

[17] Daniel Gottesman. An introduction to quantum error correction. In *Proceedings of Symposia in Applied Mathematics*, volume 58, pages 221–236, 2002.

[18] SJ van Enk. Atoms, dipole waves, and strongly focused light beams. *Physical Review A*, 69(4):043813, 2004.

[19] Jun John Sakurai and Jim Napolitano. *Modern quantum mechanics*. Cambridge University Press, 2020.

[20] Daniel A Steck. *Quantum Mechanics*. Available online at steck.us/teaching, 2024.

[21] SJ van Enk and Daniel A Steck. All Hilbert spaces are the same: consequences for generalized coordinates and momenta. *arXiv preprint arXiv:2502.08494*, 2025.

[22] Claude Cohen-Tannoudji, Jacques Dupont-Roc, and Gilbert Grynberg. *Photons and atoms: introduction to quantum electrodynamics*. John Wiley & Sons, 1989.

[23] Philippe Blanchard and Erwin Brüning. *Mathematical methods in Physics: Distributions, Hilbert space operators, variational methods, and applications in quantum physics*, volume 69. Birkhäuser, 2015.

[24] Kurt Jacobs. *Quantum measurement theory and its applications*. Cambridge University Press, 2014.

[25] Marco Frasca. A modern review of the two-level approximation. *Annals of Physics*, 306(2):193–208, 2003.

[26] Colin D Bruzewicz, John Chiaverini, Robert McConnell, and Jeremy M Sage. Trapped-ion quantum computing: Progress and challenges. *Applied physics reviews*, 6(2), 2019.

[27] Karen Wintersperger, Florian Dommert, Thomas Ehmer, Andrey Hoursanov, Johannes Klepsch, Wolfgang Mauerer, Georg Reuber, Thomas Strohm, Ming Yin, and Sebastian Luber. Neutral atom quantum computing hardware: performance and end-user perspective. *EPJ Quantum Technology*, 10(1):32, 2023.

[28] Dolev Bluvstein, Harry Levine, Giulia Semeghini, Tout T Wang, Sepehr Ebadi, Marcin Kalinowski, Alexander Keesling, Nishad Maskara, Hannes Pichler, Markus Greiner, et al. A quantum processor based on coherent transport of entangled atom arrays. *Nature*, 604(7906):451–456, 2022.

[29] Alexandre Blais, Jay Gambetta, Andreas Wallraff, David I Schuster, Steven M Girvin, Michel H Devoret, and Robert J Schoelkopf. Quantum-information processing with circuit quantum electrodynamics. *Physical Review A*, 75(3):032329, 2007.

[30] Abhinandan Antony, Martin V Gustafsson, Guilhem J Ribeill, Matthew Ware, Anjaly Rajendran, Luke CG Govia, Thomas A Ohki, Takashi Taniguchi, Kenji Watanabe, James Hone, et al. Miniaturizing transmon qubits using van der waals materials. *Nano letters*, 21(23):10122–10126, 2021.

[31] Brian J Smith and MG Raymer. Photon wave functions, wave-packet quantization of light, and coherence theory. *New Journal of Physics*, 9(11):414, 2007.

[32] Michael G Raymer and Ian A Walmsley. Temporal modes in quantum optics: then and now. *Physica Scripta*, 95(6):064002, 2020.

[33] H Jeff Kimble. The quantum internet. *Nature*, 453(7198):1023–1030, 2008.

[34] Stephan Ritter, Christian Nölleke, Carolin Hahn, Andreas Reiserer, Andreas Neuzner, Manuel Uphoff, Martin Mücke, Eden Figueroa, Joerg Bochmann, and Gerhard Rempe. An elementary quantum network of single atoms in optical cavities. *Nature*, 484(7393):195–200, 2012.

[35] Philipp Kurpiers, Paul Magnard, Theo Walter, Baptiste Royer, Marek Pechal, Johannes Heinsoo, Yves Salathé, Abdulkadir Akin, Simon Storz, J-C Besse, et al. Deterministic quantum state transfer and remote entanglement using microwave photons. *Nature*, 558(7709):264–267, 2018.

[36] Magdalena Stobińska, Gernot Alber, and Gerd Leuchs. Perfect excitation of a matter qubit by a single photon in free space. *EPL (Europhysics Letters)*, 86(1):14007, 2009.

[37] Michael G Raymer, Dileep V Reddy, Steven J van Enk, and Colin J McKinstrie. Time reversal of arbitrary photonic temporal modes via nonlinear optical frequency conversion. *New Journal of Physics*, 20(5):053027, 2018.

[38] Matthias Bock, Pascal Eich, Stephan Kucera, Matthias Kreis, Andreas Lenhard, Christoph Becher, and Jürgen Eschner. High-fidelity entanglement between a trapped ion and a telecom photon via quantum frequency conversion. *Nature communications*, 9(1):1–7, 2018.

[39] Xu Han, Wei Fu, Chang-Ling Zou, Liang Jiang, and Hong X Tang. Microwave-optical quantum frequency conversion. *Optica*, 8(8):1050–1064, 2021.

[40] Michał Karpiński, Michał Jachura, Laura J Wright, and Brian J Smith. Bandwidth manipulation of quantum light by an electro-optic time lens. *Nature Photonics*, 11(1):53–57, 2017.

[41] Matthew R Brown, Markus Allgaier, Valérian Thiel, John D Monnier, Michael G Raymer, and Brian J Smith. Interferometric imaging using shared quantum entanglement. *Physical Review Letters*, 131(21):210801, 2023.

[42] Stephanie Wehner, David Elkouss, and Ronald Hanson. Quantum internet: A vision for the road ahead. *Science*, 362(6412):eaam9288, 2018.

[43] Abhishek Sadhu, Meghana Ayyala Somayajula, Karol Horodecki, and Siddhartha Das. Practical limitations on robustness and scalability of quantum internet. *arXiv preprint arXiv:2308.12739*, 2023.

[44] Lov K Grover. Quantum telecomputation. *arXiv preprint quant-ph/9704012*, 1997.

[45] J Ignacio Cirac, AK Ekert, Susana F Huelga, and Chiara Macchiavello. Distributed quantum computation over noisy channels. *Physical Review A*, 59(6):4249, 1999.

[46] Alessio Serafini, Stefano Mancini, and Sougato Bose. Distributed quantum computation via optical fibers. *Physical Review Letters*, 96(1):010503, 2006.

[47] Liang Jiang, Jacob M Taylor, Anders S Sørensen, and Mikhail D Lukin. Distributed quantum computation based on small quantum registers. *Physical Review A*, 76(6):062323, 2007.

[48] Christopher Monroe and Jungsang Kim. Scaling the ion trap quantum processor. *Science*, 339(6124):1164–1169, 2013.

[49] Robert Beals, Stephen Brierley, Oliver Gray, Aram W Harrow, Samuel Kutin, Noah Linden, Dan Shepherd, and Mark Stather. Efficient distributed quantum computing. *Proceedings of the Royal Society A: Mathematical, Physical and Engineering Sciences*, 469(2153):20120686, 2013.

[50] Rodney Van Meter and Simon J Devitt. The path to scalable distributed quantum computing. *Computer*, 49(9):31–42, 2016.

[51] D Main, P Drmota, DP Nadlinger, EM Ainley, A Agrawal, BC Nichol, R Srinivas, G Araneda, and DM Lucas. Distributed quantum computing across an optical network link. *Nature*, pages 1–6, 2025.

[52] Shlomi Kotler, Raymond W Simmonds, Dietrich Leibfried, and David J Wineland. Hybrid quantum systems with trapped charged particles. *Physical Review A*, 95(2):022327, 2017.

[53] Dany Lachance-Quirion, Yutaka Tabuchi, Arnaud Gloppe, Koji Usami, and Yasunobu Nakamura. Hybrid quantum systems based on magnonics. *Applied Physics Express*, 12(7):070101, 2019.

[54] Yiwen Chu and Simon Gröblacher. A perspective on hybrid quantum opto-and electromechanical systems. *Applied Physics Letters*, 117(15):150503, 2020.

[55] Yiwen Chu, Jonathan D Pritchard, Hailin Wang, and Martin Weides. Hybrid quantum devices: Guest editorial. *Applied Physics Letters*, 118(24):240401, 2021.

[56] Angela Sara Cacciapuoti, Marcello Caleffi, Francesco Tafuri, Francesco Saverio Cataliotti, Stefano Gherardini, and Giuseppe Bianchi. Quantum internet: networking challenges in distributed quantum computing. *IEEE Network*, 34(1):137–143, 2019.

[57] David Awschalom, Karl K Berggren, Hannes Bernien, Sunil Bhave, Lincoln D Carr, Paul Davids, Sophia E Economou, Dirk Englund, Andrei Faraon, Martin Fejer, et al. Development of quantum interconnects (quics) for next-generation information technologies. *PRX Quantum*, 2(1):017002, 2021.

[58] CB Young, A Safari, P Huft, J Zhang, E Oh, R Chinnarasu, and M Saffman. An architecture for quantum networking of neutral atom processors. *Applied Physics B*, 128(8):151, 2022.

[59] Jacob P Covey, Harald Weinfurter, and Hannes Bernien. Quantum networks with neutral atom processing nodes. *npj Quantum Information*, 9(1):90, 2023.

[60] Ramil Nigmatullin, Christopher J Ballance, Niel De Beaudrap, and Simon C Benjamin. Minimally complex ion traps as modules for quantum communication and computing. *New Journal of Physics*, 18(10):103028, 2016.

[61] Ismail Volkan Inlek, Clayton Crocker, Martin Lichtman, Ksenia Sosnova, and Christopher Monroe. Multispecies trapped-ion node for quantum networking. *Physical Review Letters*, 118(25):250502, 2017.

[62] Andreas Reiserer, Norbert Kalb, Machiel S Blok, Koen JM van Bemmelen, Tim H Taminiau, Ronald Hanson, Daniel J Twitchen, and Matthew Markham. Robust quantum-network memory using decoherence-protected subspaces of nuclear spins. *Physical Review X*, 6(2):021040, 2016.

[63] P-J Stas, Yan Qi Huan, Bartholomeus Machielse, Erik N Knall, Aziza Suleymanzade, Benjamin Pingault, Madison Sutula, Sophie W Ding, Can M Knaut, Daniel R Assumpcao, et al. Robust multi-qubit quantum network node with integrated error detection. *Science*, 378(6619):557–560, 2022.

[64] Göran Wendin. Quantum information processing with superconducting circuits: a review. *Reports on Progress in Physics*, 80(10):106001, 2017.

[65] Frank Arute, Kunal Arya, Ryan Babbush, Dave Bacon, Joseph C Bardin, Rami Barends, Rupak Biswas, Sergio Boixo, Fernando GSL Brandao, David A Buell, et al. Quantum supremacy using a programmable superconducting processor. *Nature*, 574(7779):505–510, 2019.

[66] Xiao Xue, Maximilian Russ, Nodar Samkharadze, Brennan Undseth, Amir Sammak, Giordano Scappucci, and Lieven MK Vandersypen. Quantum logic with spin qubits crossing the surface code threshold. *Nature*, 601(7893):343–347, 2022.

[67] Guido Burkard, Thaddeus D Ladd, Andrew Pan, John M Nichol, and Jason R Petta. Semiconductor spin qubits. *Reviews of Modern Physics*, 95(2):025003, 2023.

[68] Pengfei Wang, Chun-Yang Luan, Mu Qiao, Mark Um, Junhua Zhang, Ye Wang, Xiao Yuan, Mile Gu, Jingning Zhang, and Kihwan Kim. Single ion qubit with estimated coherence time exceeding one hour. *Nature communications*, 12(1):233, 2021.

[69] Kenneth R Brown, Jungsang Kim, and Christopher Monroe. Co-designing a scalable quantum computer with trapped atomic ions. *npj Quantum Information*, 2(1):1–10, 2016.

[70] M Morgado and S Whitlock. Quantum simulation and computing with Rydberg-interacting qubits. *AVS Quantum Science*, 3(2), 2021.

[71] Thaddeus D Ladd, Fedor Jelezko, Raymond Laflamme, Yasunobu Nakamura, Christopher Monroe, and Jeremy Lloyd O'Brien. Quantum computers. *nature*, 464(7285):45–53, 2010.

[72] H M Meyer, R Stockill, M Steiner, C Le Gall, Clemens Matthiesen, E Clarke, A Ludwig, J Reichel, M Atatüre, and M Köhl. Direct photonic coupling of a semiconductor quantum dot and a trapped ion. *Physical Review Letters*, 114(12):123001, 2015.

[73] Norbert M Linke, Dmitri Maslov, Martin Roetteler, Shantanu Debnath, Caroline Figgatt, Kevin A Landsman, Kenneth Wright, and Christopher Monroe. Experimental comparison of two quantum computing architectures. *Proceedings of the National Academy of Sciences*, 114(13):3305–3310, 2017.

[74] P Rabl, D DeMille, John M Doyle, Mikhail D Lukin, RJ Schoelkopf, and P Zoller. Hybrid quantum processors: molecular ensembles as quantum memory for solid state circuits. *Physical Review Letters*, 97(3):033003, 2006.

[75] Margareta Wallquist, Klemens Hammerer, Peter Rabl, Mikhail Lukin, and Peter Zoller. Hybrid quantum devices and quantum engineering. *Physica Scripta*, 2009(T137):014001, 2009.

[76] Ze-Liang Xiang, Sahel Ashhab, JQ You, and Franco Nori. Hybrid quantum circuits: Superconducting circuits interacting with other quantum systems. *Reviews of Modern Physics*, 85(2):623, 2013.

[77] Gershon Kurizki, Patrice Bertet, Yuimaru Kubo, Klaus Mølmer, David Petrosyan, Peter Rabl, and Jörg Schmiedmayer. Quantum technologies with hybrid systems. *Proceedings of the National Academy of Sciences*, 112(13):3866–3873, 2015.

[78] Nicolas Maring, Pau Farrera, Kutlu Kutluer, Margherita Mazzera, Georg Heinze, and Hugues de Riedmatten. Photonic quantum state transfer between a cold atomic gas and a crystal. *Nature*, 551(7681):485–488, 2017.

[79] Pasquale Scarlino, David J Van Woerkom, Udson C Mendes, Jonne V Koski, Andreas J Landig, Christian Kraglund Andersen, Simone Gasparinetti, Christian Reichl, Werner Wegscheider, Klaus Ensslin, et al. Coherent microwave-photon-mediated coupling between a semiconductor and a superconducting qubit. *Nature communications*, 10(1):3011, 2019.

[80] AA Clerk, KW Lehnert, P Bertet, JR Petta, and Y Nakamura. Hybrid quantum systems with circuit quantum electrodynamics. *Nature Physics*, 16(3):257–267, 2020.

[81] Nikolai Lauk, Neil Sinclair, Shabir Barzanjeh, Jacob P Covey, Mark Saffman, Maria Spiropulu, and Christoph Simon. Perspectives on quantum transduction. *Quantum Science and Technology*, 5(2):020501, 2020.

[82] Aishwarya Kumar, Aziza Suleymanzade, Mark Stone, Lavanya Taneja, Alexander Anferov, David I Schuster, and Jonathan Simon. Quantum-enabled millimetre wave to optical transduction using neutral atoms. *Nature*, 615(7953):614–619, 2023.

[83] Charles H Bennett, Gilles Brassard, Claude Crépeau, Richard Jozsa, Asher Peres, and William K Wootters. Teleporting an unknown quantum state via dual classical and Einstein-Podolsky-Rosen channels. *Physical Review Letters*, 70(13):1895, 1993.

[84] Raju Valivarthi, Marcel li Grimau Puigibert, Qiang Zhou, Gabriel H Aguilar, Varun B Verma, Francesco Marsili, Matthew D Shaw, Sae Woo Nam, Daniel Oblak, and Wolfgang Tittel. Quantum teleportation across a metropolitan fibre network. *Nature Photonics*, 10(10):676–680, 2016.

[85] Christian Weedbrook, Stefano Pirandola, Raúl García-Patrón, Nicolas J Cerf, Timothy C Ralph, Jeffrey H Shapiro, and Seth Lloyd. Gaussian quantum information. *Reviews of Modern Physics*, 84(2):621, 2012.

[86] Marco Lucamarini, Zhiliang L Yuan, James F Dynes, and Andrew J Shields. Overcoming the rate–distance limit of quantum key distribution without quantum repeaters. *Nature*, 557(7705):400–403, 2018.

[87] Mirko Pittaluga, Mariella Minder, Marco Lucamarini, Mirko Sanzaro, Robert I Woodward, Ming-Jun Li, Zhiliang Yuan, and Andrew J Shields. 600-km repeater-like quantum communications with dual-band stabilization. *Nature Photonics*, 15(7):530–535, 2021.

[88] Christopher J Axline, Luke D Burkhart, Wolfgang Pfaff, Mengzhen Zhang, Kevin Chou, Philippe Campagne-Ibarcq, Philip Reinhold, Luigi Frunzio, SM Girvin, Liang Jiang, et al. On-demand quantum state transfer and entanglement between remote microwave cavity memories. *Nature Physics*, 14(7):705–710, 2018.

[89] P Campagne-Ibarcq, E Zalys-Geller, A Narla, S Shankar, P Reinhold, L Burkhart, C Axline, W Pfaff, L Frunzio, RJ Schoelkopf, et al. Deterministic remote entanglement of superconducting circuits through microwave two-photon transitions. *Physical Review Letters*, 120(20):200501, 2018.

[90] N Leung, Y Lu, S Chakram, RK Naik, N Earnest, R Ma, K Jacobs, AN Cleland, and DI Schuster. Deterministic bidirectional communication and remote entanglement generation between superconducting qubits. *npj quantum information*, 5(1):18, 2019.

[91] H-S Chang, YP Zhong, Audrey Bienfait, M-H Chou, Christopher R Conner, Étienne Dumur, Joel Grebel, Gregory A Peairs, Rhys G Povey, Kevin J Satzinger, et al. Remote entanglement via adiabatic passage using a tunably dissipative quantum communication system. *Physical Review Letters*, 124(24):240502, 2020.

[92] Youpeng Zhong, Hung-Shen Chang, Audrey Bienfait, Étienne Dumur, Ming-Han Chou, Christopher R Conner, Joel Grebel, Rhys G Povey, Haoxiong Yan, David I Schuster, et al. Deterministic multi-qubit entanglement in a quantum network. *Nature*, 590(7847):571–575, 2021.

[93] Luke D Burkhart, James D Teoh, Yaxing Zhang, Christopher J Axline, Luigi Frunzio, Michel H Devoret, Liang Jiang, Steven M Girvin, and Robert J Schoelkopf. Error-detected state transfer and entanglement in a superconducting quantum network. *PRX Quantum*, 2(3):030321, 2021.

[94] Mateo Casariego, Emmanuel Zambrini Cruzeiro, Stefano Gherardini, Tasio Gonzalez-Raya, Rui André, Gonçalo Frazão, Giacomo Catto, Mikko Möttönen, Debopam Datta, Klaara Viisanen, et al. Propagating quantum microwaves: towards applications in communication and sensing. *Quantum Science and Technology*, 8(2):023001, 2023.

[95] Giuseppe Vallone, Davide Bacco, Daniele Dequal, Simone Gaiarin, Vincenza Luceri, Giuseppe Bianco, and Paolo Villoresi. Experimental satellite quantum communications. *Physical Review Letters*, 115(4):040502, 2015.

[96] Juan Yin, Yuan Cao, Yu-Huai Li, Sheng-Kai Liao, Liang Zhang, Ji-Gang Ren, Wen-Qi Cai, Wei-Yue Liu, Bo Li, Hui Dai, et al. Satellite-based entanglement distribution over 1200 kilometers. *Science*, 356(6343):1140–1144, 2017.

[97] Yu-Ao Chen, Qiang Zhang, Teng-Yun Chen, Wen-Qi Cai, Sheng-Kai Liao, Jun Zhang, Kai Chen, Juan Yin, Ji-Gang Ren, Zhu Chen, et al. An integrated space-to-ground quantum communication network over 4,600 kilometres. *Nature*, 589(7841):214–219, 2021.

[98] Laurent de Forges de Parny, Olivier Alibart, Julien Debaud, Sacha Gressani, Alek Lagarrigue, Anthony Martin, Alexandre Metrat, Matteo Schiavon, Tess Troisi, Eleni Diamanti, et al. Satellite-based quantum information networks: use cases, architecture, and roadmap. *Communications Physics*, 6(1):12, 2023.

[99] Tasio Gonzalez-Raya, Mateo Casariego, Florian Fesquet, Michael Renger, Vahid Salari, Mikko Möttönen, Yasser Omar, Frank Deppe, Kirill G Fedorov, and Mikel Sanz. Open-air microwave entanglement distribution for quantum teleportation. *Physical Review Applied*, 18(4):044002, 2022.

[100] AG Radnaev, YO Dudin, R Zhao, HH Jen, SD Jenkins, A Kuzmich, and TAB Kennedy. A quantum memory with telecom-wavelength conversion. *Nature Physics*, 6(11):894–899, 2010.

[101] Khabat Heshami, Duncan G England, Peter C Humphreys, Philip J Bustard, Victor M Acosta, Joshua Nunn, and Benjamin J Sussman. Quantum memories: emerging applications and recent advances. *Journal of modern optics*, 63(20):2005–2028, 2016.

[102] Andreas Wallucks, Igor Marinković, Bas Hensen, Robert Stockill, and Simon Gröblacher. A quantum memory at telecom wavelengths. *Nature Physics*, 16(7):772–777, 2020.

[103] Elena Arenskötter, Tobias Bauer, Stephan Kucera, Matthias Bock, Jürgen Eschner, and Christoph Becher. Telecom quantum photonic interface for a $^{40}Ca^{+}$ single-ion quantum memory. *npj Quantum Information*, 9(1):34, 2023.

[104] H-J Briegel, Wolfgang Dür, Juan I Cirac, and Peter Zoller. Quantum repeaters: the role of imperfect local operations in quantum communication. *Physical Review Letters*, 81(26):5932, 1998.

[105] L-M Duan, Mikhail D Lukin, J Ignacio Cirac, and Peter Zoller. Long-distance quantum communication with atomic ensembles and linear optics. *Nature*, 414(6862):413–418, 2001.

[106] William J Munro, Koji Azuma, Kiyoshi Tamaki, and Kae Nemoto. Inside quantum repeaters. *IEEE Journal of Selected Topics in Quantum Electronics*, 21(3):78–90, 2015.

[107] Koji Azuma, Sophia E Economou, David Elkouss, Paul Hilaire, Liang Jiang, Hoi-Kwong Lo, and Ilan Tzitrin. Quantum repeaters: From quantum networks to the quantum internet. *Reviews of Modern Physics*, 95(4):045006, 2023.

[108] Crispin W Gardiner and Matthew J Collett. Input and output in damped quantum systems: Quantum stochastic differential equations and the master equation. *Physical Review A*, 31(6):3761, 1985.

[109] K Stannigel, Peter Komar, SJM Habraken, SD Bennett, Mikhail D Lukin, P Zoller, and P Rabl. Optomechanical quantum information processing with photons and phonons. *Physical Review Letters*, 109(1):013603, 2012.

[110] Wentao Jiang, Christopher J Sarabalis, Yanni D Dahmani, Rishi N Patel, Felix M Mayor, Timothy P McKenna, Raphaël Van Laer, and Amir H Safavi-Naeini. Efficient bidirectional piezo-optomechanical transduction between microwave and optical frequency. *Nature communications*, 11(1):1166, 2020.

[111] Amirparsa Zivari, Niccolò Fiaschi, Roel Burgwal, Ewold Verhagen, Robert Stockill, and Simon Gröblacher. On-chip distribution of quantum information using traveling phonons. *Science Advances*, 8(46):eadd2811, 2022.

[112] Audrey Bienfait, Kevin J Satzinger, YP Zhong, H-S Chang, M-H Chou, Chris R Conner, É Dumur, Joel Grebel, Gregory A Peairs, Rhys G Povey, et al. Phonon-mediated quantum state transfer and remote qubit entanglement. *Science*, 364(6438):368–371, 2019.

[113] Tomáš Neuman, Matt Eichenfield, Matthew E Trusheim, Lisa Hackett, Prineha Narang, and Dirk Englund. A phononic interface between a superconducting quantum processor and quantum networked spin memories. *npj Quantum Information*, 7(1):121, 2021.

[114] Jie Zhao, Yulong Liu, Longhao Wu, Chang-Kui Duan, Yu-xi Liu, and Jiangfeng Du. Observation of anti-pt-symmetry phase transition in the magnon-cavity-magnon coupled system. *Physical Review Applied*, 13(1):014053, 2020.

[115] BR Mollow. Power spectrum of light scattered by two-level systems. *Physical Review*, 188(5):1969, 1969.

[116] BR Mollow. Pure-state analysis of resonant light scattering: Radiative damping, saturation, and multiphoton effects. *Physical Review A*, 12(5):1919, 1975.

[117] G Milburn and DF Walls. Production of squeezed states in a degenerate parametric amplifier. *Optics Communications*, 39(6):401–404, 1981.

[118] D. F. Walls and Gerard J. Milburn. *Quantum Optics*. Springer, second edition, 2008.

[119] MJ Collett and CW Gardiner. Squeezing of intracavity and traveling-wave light fields produced in parametric amplification. *Physical Review A*, 30(3):1386, 1984.

[120] CW Gardiner. Inhibition of atomic phase decays by squeezed light: A direct effect of squeezing. *Physical Review Letters*, 56(18):1917, 1986.

[121] H Ritsch and P Zoller. Systems driven by colored squeezed noise: The atomic absorption spectrum. *Physical Review A*, 38(9):4657, 1988.

[122] Crispin W Gardiner, A Scott Parkins, and Peter Zoller. Wave-function quantum stochastic differential equations and quantum-jump simulation methods. *Physical Review A*, 46(7):4363, 1992.

[123] H J Carmichael. Quantum trajectory theory for cascaded open systems. *Physical Review Letters*, 70(15):2273, 1993.

[124] C W Gardiner. Driving a quantum system with the output field from another driven quantum system. *Physical Review Letters*, 70(15):2269, 1993.

[125] Vittorio Giovannetti and David Vitali. Phase-noise measurement in a cavity with a movable mirror undergoing quantum brownian motion. *Physical Review A*, 63(2):023812, 2001.

[126] Lajos Diósi. Non-markovian open quantum systems: Input-output fields, memory, and monitoring. *Physical Review A*, 85(3):034101, 2012.

[127] Jing Zhang, Yu-xi Liu, Re-Bing Wu, Kurt Jacobs, and Franco Nori. Non-markovian quantum input-output networks. *Physical Review A*, 87(3):032117, 2013.

[128] Guillermo F Peñas, Ricardo Puebla, and Juan José García-Ripoll. Improving quantum state transfer: correcting non-markovian and distortion effects. *Quantum Science and Technology*, 8(4):045026, 2023.

[129] Joshua Combes, Joseph Kerckhoff, and Mohan Sarovar. The SLH framework for modeling quantum input-output networks. *Advances in Physics: X*, 2(3):784–888, 2017.

[130] J Dalibard, J Dupont-Roc, and C Cohen-Tannoudji. Vacuum fluctuations and radiation reaction: identification of their respective contributions. *Journal de Physique*, 43(11):1617–1638, 1982.

[131] Edwin Albert Power and Sigurd Zienau. Coulomb gauge in non-relativistic quantum electro-dynamics and the shape of spectral lines. *Philosophical Transactions of the Royal Society of London. Series A, Mathematical and Physical Sciences*, 251(999):427–454, 1959.

[132] R Gr Woolley. Molecular quantum electrodynamics. *Proceedings of the Royal Society of London. A. Mathematical and Physical Sciences*, 321(1547):557–572, 1971.

[133] Daniel A Steck. *Quantum and Atom Optics*. Available online at steck.us/teaching, 2012.

[134] TE Northup and R Blatt. Quantum information transfer using photons. *Nature photonics*, 8(5):356–363, 2014.

[135] Chris Fleming, NI Cummings, Charis Anastopoulos, and Bei-Lok Hu. The rotating-wave approximation: consistency and applicability from an open quantum system analysis. *Journal of Physics A: Mathematical and Theoretical*, 43(40):405304, 2010.

[136] Daniel Braak. Integrability of the Rabi model. *Physical Review Letters*, 107(10):100401, 2011.

[137] Matthew T Rakher, Lijun Ma, Oliver Slattery, Xiao Tang, and Kartik Srinivasan. Quantum transduction of telecommunications-band single photons from a quantum dot by frequency upconversion. *Nature Photonics*, 4(11):786–791, 2010.

[138] Nikolai Lauk, Neil Sinclair, Shabir Barzanjeh, Jacob P Covey, Mark Saffman, Maria Spiropulu, and Christoph Simon. Perspectives on quantum transduction. *Quantum Science and Technology*, 5(2):020501, 2020.

[139] Bharath Srivathsan, Gurpreet Kaur Gulati, Alessandro Cere, Brenda Chng, and Christian Kurtsiefer. Reversing the temporal envelope of a heralded single photon using a cavity. *Physical Review Letters*, 113(16):163601, 2014.

[140] Jean Dalibard, Yvan Castin, and Klaus Mølmer. Wave-function approach to dissipative processes in quantum optics. *Physical Review Letters*, 68(5):580, 1992.

[141] Klaus Mølmer, Yvan Castin, and Jean Dalibard. Monte Carlo wave-function method in quantum optics. *JOSA B*, 10(3):524–538, 1993.

[142] A David Boozer, Andreea Boca, Russell Miller, Tracy E Northup, and H Jeffrey Kimble. Reversible state transfer between light and a single trapped atom. *Physical Review Letters*, 98(19):193601, 2007.

[143] Søren Gammelmark, Brian Julsgaard, and Klaus Mølmer. Past quantum states of a monitored system. *Physical Review Letters*, 111(16):160401, 2013.

[144] Chaitali Joshi, Ben M Sparkes, Alessandro Farsi, Thomas Gerrits, Varun Verma, Sven Ramelow, Sae Woo Nam, and Alexander L Gaeta. Picosecond-resolution single-photon time lens for temporal mode quantum processing. *Optica*, 9(4):364–373, 2022.

[145] Philipp Müller, Tristan Tentrup, Marc Bienert, Giovanna Morigi, and Jürgen Eschner. Spectral properties of single photons from quantum emitters. *Physical Review A*, 96(2):023861, 2017.

[146] Gerd Leuchs and Markus Sondermann. Time-reversal symmetry in optics. *Physica Scripta*, 85(5):058101, 2012.

[147] Markus Allgaier, Vahid Ansari, Linda Sansoni, Christof Eigner, Viktor Quiring, Raimund Ricken, Georg Harder, Benjamin Brecht, and Christine Silberhorn. Highly efficient frequency conversion with bandwidth compression of quantum light. *Nature communications*, 8(1):14288, 2017.

[148] Dave Kielpinski, Joel F Corney, and Howard M Wiseman. Quantum optical waveform conversion. *Physical Review Letters*, 106(13):130501, 2011.

[149] RW Andrews, AP Reed, K Cicak, JD Teufel, and KW Lehnert. Quantum-enabled temporal and spectral mode conversion of microwave signals. *Nature communications*, 6(1):10021, 2015.

[150] Olivier Morin, Matthias Körber, Stefan Langenfeld, and Gerhard Rempe. Deterministic shaping and reshaping of single-photon temporal wave functions. *Physical Review Letters*, 123(13):133602, 2019.

[151] Etienne Brion, Line Hjortshøj Pedersen, and Klaus Mølmer. Adiabatic elimination in a lambda system. *Journal of Physics A: Mathematical and Theoretical*, 40(5):1033, 2007.

[152] Howard M Wiseman. Defending continuous variable teleportation: why a laser is a clock, not a quantum channel. *Journal of Optics B: Quantum and Semiclassical Optics*, 6(8):S849, 2004.

[153] Harrison Ball, William D Oliver, and Michael J Biercuk. The role of master clock stability in quantum information processing. *npj Quantum Information*, 2(1):1–8, 2016.

[154] B Vogell, B Vermersch, TE Northup, BP Lanyon, and CA Muschik. Deterministic quantum state transfer between remote qubits in cavities. *Quantum Science and Technology*, 2(4):045003, 2017.

[155] Alexey V Gorshkov, Axel André, Mikhail D Lukin, and Anders S Sørensen. Photon storage in Λ-type optically dense atomic media. I. Cavity model. *Physical Review A*, 76(3):033804, 2007.

[156] Matthias Keller, Birgit Lange, Kazuhiro Hayasaka, Wolfgang Lange, and Herbert Walther. Continuous generation of single photons with controlled waveform in an ion-trap cavity system. *Nature*, 431(7012):1075–1078, 2004.

[157] Alexey V Gorshkov, Axel André, Michael Fleischhauer, Anders S Sørensen, and Mikhail D Lukin. Universal approach to optimal photon storage in atomic media. *Physical Review Letters*, 98(12):123601, 2007.

[158] Luigi Giannelli, Tom Schmit, Tommaso Calarco, Christiane P Koch, Stephan Ritter, and Giovanna Morigi. Optimal storage of a single photon by a single intra-cavity atom. *New Journal of Physics*, 20(10):105009, 2018.

[159] Saumya Biswas and SJ van Enk. Detecting two photons with one molecule. *Physical Review A*, 104(4):043703, 2021.

[160] Thomas Pellizzari. Quantum networking with optical fibres. *Physical Review Letters*, 79(26):5242, 1997.

[161] SJ van Enk, HJ Kimble, JI Cirac, and Peter Zoller. Quantum communication with dark photons. *Physical Review A*, 59(4):2659, 1999.

[162] David J Wineland, Christopher Monroe, Wayne M Itano, Dietrich Leibfried, Brian E King, and Dawn M Meekhof. Experimental issues in coherent quantum-state manipulation of trapped atomic ions. *Journal of research of the National Institute of Standards and Technology*, 103(3):259, 1998.

[163] H Jeff Kimble. Strong interactions of single atoms and photons in cavity QED. *Physica Scripta*, 1998(T76):127, 1998.

[164] SJ van Enk, JI Cirac, and P Zoller. Photonic channels for quantum communication. *Science*, 279(5348):205–208, 1998.

[165] Crispin Gardiner and Peter Zoller. *Quantum noise: a handbook of Markovian and non-Markovian quantum stochastic methods with applications to quantum optics*. Springer Science & Business Media, 2004.

[166] V Krutyanskiy, M Galli, V Krcmarsky, S Baier, DA Fioretto, Y Pu, A Mazloom, P Sekatski, M Canteri, M Teller, et al. Entanglement of trapped-ion qubits separated by 230 meters. *Physical Review Letters*, 130(5):050803, 2023.

[167] Victor Krutyanskiy, Marco Canteri, Martin Meraner, James Bate, Vojtech Krcmarsky, Josef Schupp, Nicolas Sangouard, and Ben P Lanyon. Telecom-wavelength quantum repeater node based on a trapped-ion processor. *Physical Review Letters*, 130(21):213601, 2023.

[168] Peter C Humphreys, Norbert Kalb, Jaco PJ Morits, Raymond N Schouten, Raymond FL Vermeulen, Daniel J Twitchen, Matthew Markham, and Ronald Hanson. Deterministic delivery of remote entanglement on a quantum network. *Nature*, 558(7709):268–273, 2018.

[169] Robert Stockill, MJ Stanley, Lukas Huthmacher, Edmund Clarke, Maxim Hugues, AJ Miller, Clemens Matthiesen, Claire Le Gall, and Mete Atatüre. Phase-tuned entangled state generation between distant spin qubits. *Physical Review Letters*, 119(1):010503, 2017.

[170] Andreas Reiserer and Gerhard Rempe. Cavity-based quantum networks with single atoms and optical photons. *Reviews of Modern Physics*, 87(4):1379, 2015.

[171] Paul Magnard, Simon Storz, Philipp Kurpiers, Josua Schär, Fabian Marxer, Janis Lütolf, Theo Walter, J-C Besse, Mihai Gabureac, Kevin Reuer, et al. Microwave quantum link between superconducting circuits housed in spatially separated cryogenic systems. *Physical Review Letters*, 125(26):260502, 2020.

[172] AS Parkins, P Marte, P Zoller, and HJ Kimble. Synthesis of arbitrary quantum states via adiabatic transfer of zeeman coherence. *Physical Review Letters*, 71(19):3095, 1993.

[173] Hiroki Takahashi, Ezra Kassa, Costas Christoforou, and Matthias Keller. Strong coupling of a single ion to an optical cavity. *Physical Review Letters*, 124(1):013602, 2020.

[174] Stephen Begley, Markus Vogt, Gurpreet Kaur Gulati, Hiroki Takahashi, and Matthias Keller. Optimized multi-ion cavity coupling. *Physical Review Letters*, 116(22):223001, 2016.

[175] M Steiner, HM Meyer, J Reichel, and M Köhl. Photon emission and absorption of a single ion coupled to an optical-fiber cavity. *Physical Review Letters*, 113(26):263003, 2014.

[176] Andreas Reiserer, Stephan Ritter, and Gerhard Rempe. Nondestructive detection of an optical photon. *Science*, 342(6164):1349–1351, 2013.

[177] Andreas Reiserer, Norbert Kalb, Gerhard Rempe, and Stephan Ritter. A quantum gate between a flying optical photon and a single trapped atom. *Nature*, 508(7495):237–240, 2014.

[178] Haytham Chibani. *Photon blockade with memory and slow light using a single atom in an optical cavity*. PhD thesis, Technische Universität München, 2016.

[179] Severin Daiss, Stefan Langenfeld, Stephan Welte, Emanuele Distante, Philip Thomas, Lukas Hartung, Olivier Morin, and Gerhard Rempe. A quantum-logic gate between distant quantum-network modules. *Science*, 371(6529):614–617, 2021.

[180] Xu Han, Wei Fu, Chang-Ling Zou, Liang Jiang, and Hong X Tang. Microwave-optical quantum frequency conversion. *Optica*, 8(8):1050–1064, 2021.

[181] Jeff S Lundeen, Alvaro Feito, Hendrik Coldenstrodt-Ronge, Kenny L Pregnell, Ch Silberhorn, Timothy C Ralph, Jens Eisert, Martin B Plenio, and Ian A Walmsley. Tomography of quantum detectors. *Nature Physics*, 5(1):27–30, 2009.

[182] Hendrik B Coldenstrodt-Ronge, Jeff S Lundeen, Kenny L Pregnell, Alvaro Feito, Brian J Smith, Wolfgang Mauerer, Christine Silberhorn, Jens Eisert, Martin B Plenio, and Ian A Walmsley. A proposed testbed for detector tomography. *Journal of Modern Optics*, 56(2-3):432–441, 2009.

[183] Chandra M Natarajan, Lijian Zhang, Hendrik Coldenstrodt-Ronge, Gaia Donati, Sander N Dorenbos, Val Zwiller, Ian A Walmsley, and Robert H Hadfield. Quantum detector tomography of a time-multiplexed superconducting nanowire single-photon detector at telecom wavelengths. *Optics express*, 21(1):893–902, 2013.

[184] Steven J van Enk. Photodetector figures of merit in terms of POVMs. *Journal of Physics Communications*, 1(4):045001, 2017.

[185] Steve M Young, Mohan Sarovar, and François Léonard. General modeling framework for quantum photodetectors. *Physical Review A*, 98(6):063835, 2018.

[186] Tzula B Propp and SJ van Enk. Quantum networks for single photon detection. *Physical Review A*, 100(3):033836, 2019.

[187] Karl Kraus, Arno Böhm, John D Dollard, and WH Wootters. *States, Effects, and Operations Fundamental Notions of Quantum Theory: Lectures in Mathematical Physics at the University of Texas at Austin*. Springer, 1983.

[188] Kurt Jacobs and Daniel A Steck. A straightforward introduction to continuous quantum measurement. *Contemporary Physics*, 47(5):279–303, 2006.

[189] Jonathan Lavoie, John M Donohue, Logan G Wright, Alessandro Fedrizzi, and Kevin J Resch. Spectral compression of single photons. *Nature Photonics*, 7(5):363–366, 2013.

[190] Sze-Chun Chan and Jia-Ming Liu. Tunable narrow-linewidth photonic microwave generation using semiconductor laser dynamics. *IEEE Journal of selected topics in quantum electronics*, 10(5):1025–1032, 2004.

[191] Steven W Brown, George P Eppeldauer, and Keith R Lykke. Facility for spectral irradiance and radiance responsivity calibrations using uniform sources. *Applied optics*, 45(32):8218–8237, 2006.

[192] Minh A Tran, Duanni Huang, Joel Guo, Tin Komljenovic, Paul A Morton, and John E Bowers. Ring-resonator based widely-tunable narrow-linewidth si/inp integrated lasers. *IEEE Journal of Selected Topics in Quantum Electronics*, 26(2):1–14, 2019.

[193] Mateus Corato-Zanarella, Andres Gil-Molina, Xingchen Ji, Min Chul Shin, Aseema Mohanty, and Michal Lipson. Widely tunable and narrow-linewidth chip-scale lasers from near-ultraviolet to near-infrared wavelengths. *Nature Photonics*, 17(2):157–164, 2023.

[194] Weidong Chen, Julien Cousin, Emmanuelle Poullet, Jean Burie, Daniel Boucher, Xiaoming Gao, Markus W Sigrist, and Frank K Tittel. Continuous-wave mid-infrared laser sources based on difference frequency generation. *Comptes Rendus Physique*, 8(10):1129–1150, 2007.

[195] Mikhail A Belkin, Federico Capasso, Alexey Belyanin, Deborah L Sivco, Alfred Y Cho, Douglas C Oakley, Christopher J Vineis, and George W Turner. Terahertz quantum-cascade-laser source based on intracavity difference-frequency generation. *Nature Photonics*, 1(5):288–292, 2007.

[196] Didier A Depireux, Jonathan Z Simon, David J Klein, and Shihab A Shamma. Spectro-temporal response field characterization with dynamic ripples in ferret primary auditory cortex. *Journal of neurophysiology*, 85(3):1220–1234, 2001.

[197] Carl Eckart and Gale Young. The approximation of one matrix by another of lower rank. *Psychometrika*, 1(3):211–218, 1936.

[198] Gilbert Strang. *Linear algebra and learning from data*. SIAM, 2019.

[199] Kevin Zielnicki, Karina Garay-Palmett, Daniel Cruz-Delgado, Hector Cruz-Ramirez, Michael F O'Boyle, Bin Fang, Virginia O Lorenz, Alfred B U'Ren, and Paul G Kwiat. Joint spectral characterization of photon-pair sources. *Journal of Modern Optics*, 65(10):1141–1160, 2018.

[200] Marios H Michael, Matti Silveri, RT Brierley, Victor V Albert, Juha Salmilehto, Liang Jiang, and Steven M Girvin. New class of quantum error-correcting codes for a bosonic mode. *Physical Review X*, 6(3):031006, 2016.

[201] Netanel H Lindner and Terry Rudolph. Proposal for pulsed on-demand sources of photonic cluster state strings. *Physical Review Letters*, 103(11):113602, 2009.

[202] Yuan Zhan and Shuo Sun. Deterministic generation of loss-tolerant photonic cluster states with a single quantum emitter. *Physical Review Letters*, 125(22):223601, 2020.

[203] Philip Thomas, Leonardo Ruscio, Olivier Morin, and Gerhard Rempe. Efficient generation of entangled multiphoton graph states from a single atom. *Nature*, 608(7924):677–681, 2022.

[204] John Preskill. Quantum computing in the NISQ era and beyond. *Quantum*, 2:79, 2018.

[205] AN Craddock, J Hannegan, DP Ornelas-Huerta, JD Siverns, AJ Hachtel, EA Goldschmidt, James V Porto, Q Quraishi, and SL Rolston. Quantum interference between photons from an atomic ensemble and a remote atomic ion. *Physical Review Letters*, 123(21):213601, 2019.

[206] AM Dyckovsky and S Olmschenk. Analysis of photon-mediated entanglement between distinguishable matter qubits. *Physical Review A*, 85(5):052322, 2012.

[207] Matteo Pompili, Sophie LN Hermans, Simon Baier, Hans KC Beukers, Peter C Humphreys, Raymond N Schouten, Raymond FL Vermeulen, Marijn J Tiggelman, Laura dos Santos Martins, Bas Dirkse, et al. Realization of a multinode quantum network of remote solid-state qubits. *Science*, 372(6539):259–264, 2021.

[208] Piotr Migdał, Klementyna Jankiewicz, Paweł Grabarz, Chiara Decaroli, and Philippe Cochin. Visualizing quantum mechanics in an interactive simulation–Virtual Lab by Quantum Flytrap. *Optical Engineering*, 61(8):081808, 2022.

[209] CH Holbrow, Enrique Galvez, and ME Parks. Photon quantum mechanics and beam splitters. *American Journal of Physics*, 70(3):260–265, 2002.

[210] Enrique J Galvez, Charles H Holbrow, MJ Pysher, JW Martin, N Courtemanche, L Heilig, and J Spencer. Interference with correlated photons: Five quantum mechanics experiments for undergraduates. *American Journal of Physics*, 73(2):127–140, 2005.

[211] Nicholas S DiBrita and Enrique J Galvez. An easier-to-align Hong–Ou–Mandel interference demonstration. *American Journal of Physics*, 91(4):307–315, 2023.

[212] Bill J Luo, Leia Francis, Valeria Rodríguez-Fajardo, Enrique J Galvez, and Farbod Khoshnoud. Young's double-slit interference demonstration with single photons. *American Journal of Physics*, 92(4):308–316, 2024.

[213] Emily Marshman and Chandralekha Singh. Investigating and improving student understanding of quantum mechanics in the context of single photon interference. *Physical Review Physics Education Research*, 13(1):010117, 2017.

[214] Emily Marshman and Chandralekha Singh. Interactive tutorial to improve student understanding of single photon experiments involving a Mach–Zehnder interferometer. *European Journal of Physics*, 37(2):024001, 2016.

[215] Alexandru Maries, Ryan Sayer, and Chandralekha Singh. Can students apply the concept of "which-path" information learned in the context of Mach–Zehnder interferometer to the double-slit experiment? *American Journal of Physics*, 88(7):542–550, 2020.

[216] Moritz Waitzmann, Kim-Alessandro Weber, Susanne Wessnigk, and Ruediger Scholz. Key experiment and quantum reasoning. *Physics*, 4(4):1202–1229, 2022.

[217] Emanuel Knill, Raymond Laflamme, and Gerald J Milburn. A scheme for efficient quantum computation with linear optics. *Nature*, 409(6816):46–52, 2001.

[218] Jacques Carolan, Christopher Harrold, Chris Sparrow, Enrique Martín-López, Nicholas J Russell, Joshua W Silverstone, Peter J Shadbolt, Nobuyuki Matsuda, Manabu Oguma, Mikitaka Itoh, et al. Universal linear optics. *Science*, 349(6249):711–716, 2015.

[219] Pieter Kok, William J Munro, Kae Nemoto, Timothy C Ralph, Jonathan P Dowling, and Gerard J Milburn. Linear optical quantum computing with photonic qubits. *Reviews of modern physics*, 79(1):135–174, 2007.

[220] Sergei Slussarenko and Geoff J Pryde. Photonic quantum information processing: A concise review. *Applied Physics Reviews*, 6(4), 2019.

[221] Sara Bartolucci, Patrick Birchall, Hector Bombin, Hugo Cable, Chris Dawson, Mercedes Gimeno-Segovia, Eric Johnston, Konrad Kieling, Naomi Nickerson, Mihir Pant, et al. Fusion-based quantum computation. *Nature Communications*, 14(1):912, 2023.

[222] Scott Aaronson and Alex Arkhipov. The computational complexity of linear optics. In *Proceedings of the forty-third annual ACM symposium on Theory of computing*, pages 333–342, 2011.

[223] Han-Sen Zhong, Hui Wang, Yu-Hao Deng, Ming-Cheng Chen, Li-Chao Peng, Yi-Han Luo, Jian Qin, Dian Wu, Xing Ding, Yi Hu, et al. Quantum computational advantage using photons. *Science*, 370(6523):1460–1463, 2020.

[224] Scott Aaronson. *Quantum computing since Democritus*. Cambridge University Press, 2013.

[225] Lucien Hardy. Quantum mechanics, local realistic theories, and Lorentz-invariant realistic theories. *Physical Review Letters*, 68(20):2981, 1992.

[226] William TM Irvine, Juan F Hodelin, Christoph Simon, and Dirk Bouwmeester. Realization of Hardy's thought experiment with photons. *Physical Review Letters*, 95(3):030401, 2005.

[227] Jeff S Lundeen and Aephraim M Steinberg. Experimental joint weak measurement on a photon pair as a probe of Hardy's paradox. *Physical Review Letters*, 102(2):020404, 2009.

[228] Peter DD Schwindt, Paul G Kwiat, and Berthold-Georg Englert. Quantitative wave-particle duality and nonerasing quantum erasure. *Physical Review A*, 60(6):4285, 1999.

[229] Berthold-Georg Englert and János A Bergou. Quantitative quantum erasure. *Optics communications*, 179(1-6):337–355, 2000.

[230] Matthias Jakob and Janos A Bergou. Complementarity and entanglement in bipartite qudit systems. *Physical Review A*, 76(5):052107, 2007.

[231] Jian-Wei Pan, Zeng-Bing Chen, Chao-Yang Lu, Harald Weinfurter, Anton Zeilinger, and Marek Żukowski. Multiphoton entanglement and interferometry. *Reviews of Modern Physics*, 84(2):777–838, 2012.

[232] Adeline Orieux and Eleni Diamanti. Recent advances on integrated quantum communications. *Journal of Optics*, 18(8):083002, 2016.

[233] Stefano Pirandola, B Roy Bardhan, Tobias Gehring, Christian Weedbrook, and Seth Lloyd. Advances in photonic quantum sensing. *Nature Photonics*, 12(12):724–733, 2018.

[234] Richard P Feynman, Robert B Leighton, and Matthew Sands. *The Feynman lectures on physics, Vol. III*. Addison-Wesley, 1965.

[235] Richard Phillips Feynman. Space-time approach to non-relativistic quantum mechanics. *Reviews of Modern Physics*, 20(2):367, 1948.

[236] Thomas Young. I. The Bakerian Lecture. Experiments and calculations relative to physical optics. *Philosophical transactions of the Royal Society of London*, (94):1–16, 1804.

[237] Reuben S Aspden, Miles J Padgett, and Gabriel C Spalding. Video recording true single-photon double-slit interference. *American Journal of Physics*, 84(9):671–677, 2016.

[238] Philippe Grangier, Gerard Roger, and Alain Aspect. Experimental evidence for a photon anticorrelation effect on a beam splitter: a new light on single-photon interferences. *Europhysics Letters*, 1(4):173, 1986.

[239] Roger Bach, Damian Pope, Sy-Hwang Liou, and Herman Batelaan. Controlled double-slit electron diffraction. *New Journal of Physics*, 15(3):033018, 2013.

[240] Yang Ji, Yunchul Chung, D Sprinzak, Moty Heiblum, Diana Mahalu, and Hadas Shtrikman. An electronic Mach–Zehnder interferometer. *Nature*, 422(6930):415–418, 2003.

[241] M. W. Hamilton. Phase shifts in multilayer dielectric beam splitters. *American Journal of Physics*, 68(2):186–191, 2000.

[242] Malte C Tichy. Interference of identical particles from entanglement to boson-sampling. *Journal of Physics B: Atomic, Molecular and Optical Physics*, 47(10):103001, 2014.

[243] Richard A Campos, Bahaa EA Saleh, and Malvin C Teich. Quantum-mechanical lossless beam splitter: SU(2) symmetry and photon statistics. *Physical Review A*, 40(3):1371, 1989.

[244] Johannes Skaar, Juan Carlos García Escartín, and Harald Landro. Quantum mechanical description of linear optics. *American Journal of Physics*, 72(11):1385–1391, 2004.

[245] Masud Mansuripur and Ewan M Wright. Fundamental properties of beamsplitters in classical and quantum optics. *American Journal of Physics*, 91(4):298–306, 2023.

[246] Avshalom C Elitzur and Lev Vaidman. Quantum mechanical interaction-free measurements. *Foundations of Physics*, 23:987–997, 1993.

[247] Paul Busch and Christopher Shilladay. Complementarity and uncertainty in Mach–Zehnder interferometry and beyond. *Physics Reports*, 435(1):1–31, 2006.

[248] L Pezzé, A Smerzi, G Khoury, JF Hodelin, and D Bouwmeester. Phase detection at the quantum limit with multiphoton Mach–Zehnder interferometry. *Physical Review Letters*, 99(22):223602, 2007.

[249] KP Zetie, SF Adams, and RM Tocknell. How does a Mach–Zehnder interferometer work? *Physics Education*, 35(1):46, 2000.

[250] Chong-Ki Hong, Zhe-Yu Ou, and Leonard Mandel. Measurement of subpicosecond time intervals between two photons by interference. *Physical Review Letters*, 59(18):2044, 1987.

[251] Peter P Rohde and Timothy C Ralph. Error models for mode mismatch in linear optics quantum computing. *Physical Review A*, 73(6):062312, 2006.

[252] Nijil Lal, Sarika Mishra, and RP Singh. Indistinguishable photons. *AVS Quantum Science*, 4(2), 2022.

[253] Alex E Jones, Shreya Kumar, Simone D'Aurelio, Matthias Bayerbach, Adrian J Menssen, and Stefanie Barz. Distinguishability and mixedness in quantum interference. *Physical Review A*, 108(5):053701, 2023.

[254] Jun OS Yin and SJ Van Enk. Entanglement and purity of one-and two-photon states. *Physical Review A—Atomic, Molecular, and Optical Physics*, 77(6):062333, 2008.

[255] Dietrich Dehlinger and MW Mitchell. Entangled photons, nonlocality, and Bell inequalities in the undergraduate laboratory. *American Journal of Physics*, 70(9):903–910, 2002.

[256] JA Carlson, MD Olmstead, and Mark Beck. Quantum mysteries tested: An experiment implementing Hardy's test of local realism. *American Journal of Physics*, 74(3):180–186, 2006.

[257] Pascale Senellart, Glenn Solomon, and Andrew White. High-performance semiconductor quantum-dot single-photon sources. *Nature nanotechnology*, 12(11):1026–1039, 2017.

[258] Lucien Hardy. A quantum optical experiment to test local realism. *Physics Letters A*, 167(1):17–23, 1992.

[259] Lucien Hardy. Nonlocality for two particles without inequalities for almost all entangled states. *Physical Review Letters*, 71(11):1665, 1993.

[260] Ryszard Horodecki, Paweł Horodecki, Michał Horodecki, and Karol Horodecki. Quantum entanglement. *Reviews of modern physics*, 81(2):865–942, 2009.

[261] John S Bell. On the Einstein Podolsky Rosen paradox. *Physics Physique Fizika*, 1(3):195, 1964.

[262] Albert Einstein, Boris Podolsky, and Nathan Rosen. Can quantum-mechanical description of physical reality be considered complete? *Physical Review*, 47(10):777, 1935.

[263] Margaret D Reid, PD Drummond, WP Bowen, Eric Gama Cavalcanti, Ping Koy Lam, HA Bachor, Ulrik Lund Andersen, and G Leuchs. Colloquium: the Einstein-Podolsky-Rosen paradox: from concepts to applications. *Reviews of Modern Physics*, 81(4):1727–1751, 2009.

[264] Maximilian Schlosshauer. *Elegance and enigma: The quantum interviews*. Springer, 2011.

[265] Adrian J Menssen, Alex E Jones, Benjamin J Metcalf, Malte C Tichy, Stefanie Barz, W Steven Kolthammer, and Ian A Walmsley. Distinguishability and many-particle interference. *Physical Review Letters*, 118(15):153603, 2017.

[266] Rosario Lo Franco and Giuseppe Compagno. Quantum entanglement of identical particles by standard information-theoretic notions. *Scientific reports*, 6(1):1–10, 2016.

[267] Marlan O Scully and Kai Drühl. Quantum eraser: A proposed photon correlation experiment concerning observation and "delayed choice" in quantum mechanics. *Physical Review A*, 25(4):2208, 1982.

[268] CA Schrama, G Nienhuis, HA Dijkerman, C Steijsiger, and HGM Heideman. Destructive interference between opposite time orders of photon emission. *Physical Review Letters*, 67(18):2443, 1991.

[269] MG Raymer, SJ Van Enk, CJ McKinstrie, and HJ McGuinness. Interference of two photons of different color. *Optics Communications*, 283(5):747–752, 2010.

[270] Tzula B Propp and Steven J van Enk. How to project onto an arbitrary single-photon wave packet. *Physical Review A*, 102(5):053707, 2020.

[271] Edwin T Jaynes and Frederick W Cummings. Comparison of quantum and semiclassical radiation theories with application to the beam maser. *Proceedings of the IEEE*, 51(1):89–109, 1963.

[272] D Meschede, Herbert Walther, and G Müller. One-atom maser. *Physical Review Letters*, 54(6):551, 1985.

[273] Andreas Reiserer. Colloquium: Cavity-enhanced quantum network nodes. *Reviews of Modern Physics*, 94(4):041003, 2022.

[274] Stephan Welte, Bastian Hacker, Severin Daiss, Stephan Ritter, and Gerhard Rempe. Photon-mediated quantum gate between two neutral atoms in an optical cavity. *Physical Review X*, 8(1):011018, 2018.

[275] Polnop Samutpraphoot, Tamara Đorđević, Paloma L Ocola, Hannes Bernien, Crystal Senko, Vladan Vuletić, and Mikhail D Lukin. Strong coupling of two individually controlled atoms via a nanophotonic cavity. *Physical Review Letters*, 124(6):063602, 2020.

[276] A Stute, B Casabone, B Brandstätter, K Friebe, TE Northup, and R Blatt. Quantum-state transfer from an ion to a photon. *Nature photonics*, 7(3):219–222, 2013.

[277] LJ Stephenson, DP Nadlinger, BC Nichol, S An, P Drmota, TG Ballance, K Thirumalai, JF Goodwin, DM Lucas, and CJ Ballance. High-rate, high-fidelity entanglement of qubits across an elementary quantum network. *Physical Review Letters*, 124(11):110501, 2020.

[278] J Schupp, V Krcmarsky, V Krutyanskiy, M Meraner, TE Northup, and BP Lanyon. Interface between trapped-ion qubits and traveling photons with close-to-optimal efficiency. *PRX quantum*, 2(2):020331, 2021.

[279] Klemens Hammerer, Anders S Sørensen, and Eugene S Polzik. Quantum interface between light and atomic ensembles. *Reviews of Modern Physics*, 82(2):1041, 2010.

[280] Marek Pechal, Lukas Huthmacher, Christopher Eichler, Sina Zeytinoğlu, AA Abdumalikov Jr, Simon Berger, Andreas Wallraff, and Stefan Filipp. Microwave-controlled generation of shaped single photons in circuit quantum electrodynamics. *Physical Review X*, 4(4):041010, 2014.

[281] Jonas Larson and Themistoklis Mavrogordatos. *The Jaynes–Cummings Model and its Descendants*. IOP Publishing, second edition, 2024.

[282] Kevin Reuer, Jean-Claude Besse, Lucien Wernli, Paul Magnard, Philipp Kurpiers, Graham J Norris, Andreas Wallraff, and Christopher Eichler. Realization of a universal quantum gate set for itinerant microwave photons. *Physical Review X*, 12(1):011008, 2022.

[283] M Khanbekyan and D-G Welsch. Cavity-assisted spontaneous emission of a single Λ-type emitter as a source of single-photon packets with controlled shape. *Physical Review A*, 95(1):013803, 2017.

[284] Kent AG Fisher, Duncan G England, Jean-Philippe W MacLean, Philip J Bustard, Kevin J Resch, and Benjamin J Sussman. Frequency and bandwidth conversion of single photons in a room-temperature diamond quantum memory. *Nature communications*, 7(1):11200, 2016.

[285] Rubayet Al Maruf, Sreesh Venuturumilli, Divya Bharadwaj, Paul Anderson, Jiawei Qiu, Yujia Yuan, Mohd Zeeshan, Behrooz Semnani, Philip J Poole, Dan Dalacu, et al. Widely tunable solid-state source of single-photons matching an atomic transition. *arXiv preprint arXiv:2309.06734*, 2023.

[286] William Huie, Shankar G Menon, Hannes Bernien, and Jacob P Covey. Multiplexed telecommunication-band quantum networking with atom arrays in optical cavities. *Physical Review Research*, 3(4):043154, 2021.

[287] V Krutyanskiy, M Meraner, J Schupp, and BP Lanyon. Polarisation-preserving photon frequency conversion from a trapped-ion-compatible wavelength to the telecom c-band. *Applied Physics B*, 123(9):228, 2017.

[288] Rikizo Ikuta, Toshiki Kobayashi, Tetsuo Kawakami, Shigehito Miki, Masahiro Yabuno, Taro Yamashita, Hirotaka Terai, Masato Koashi, Tetsuya Mukai, Takashi Yamamoto, et al. Polarization insensitive frequency conversion for an atom-photon entanglement distribution via a telecom network. *Nature communications*, 9(1):1997, 2018.

[289] Matthias Bock, Pascal Eich, Stephan Kucera, Matthias Kreis, Andreas Lenhard, Christoph Becher, and Jürgen Eschner. High-fidelity entanglement between a trapped ion and a telecom photon via quantum frequency conversion. *Nature communications*, 9(1):1998, 2018.

[290] Florian Kaiser, Panagiotis Vergyris, Anthony Martin, Djeylan Aktas, Marc P De Micheli, Olivier Alibart, and Sébastien Tanzilli. Quantum optical frequency up-conversion for polarisation entangled qubits: towards interconnected quantum information devices. *Optics Express*, 27(18):25603–25610, 2019.

[291] Pol Forn-Diaz, CW Warren, CWS Chang, AM Vadiraj, and CM Wilson. On-demand microwave generator of shaped single photons. *Physical Review Applied*, 8(5):054015, 2017.

[292] Rishabh Sahu, William Hease, Alfredo Rueda, Georg Arnold, Liu Qiu, and Johannes M Fink. Quantum-enabled operation of a microwave-optical interface. *Nature communications*, 13(1):1276, 2022.

[293] Changqing Wang, Ivan Gonin, Anna Grassellino, Sergey Kazakov, Alexander Romanenko, Vyacheslav P Yakovlev, and Silvia Zorzetti. High-efficiency microwave-optical quantum transduction based on a cavity electro-optic superconducting system with long coherence time. *npj Quantum Information*, 8(1):149, 2022.

[294] Thibault Vogt, Christian Gross, Jingshan Han, Sambit B Pal, Mark Lam, Martin Kiffner, and Wenhui Li. Efficient microwave-to-optical conversion using Rydberg atoms. *Physical Review A*, 99(2):023832, 2019.

[295] Reed W Andrews, Robert W Peterson, Tom P Purdy, Katarina Cicak, Raymond W Simmonds, Cindy A Regal, and Konrad W Lehnert. Bidirectional and efficient conversion between microwave and optical light. *Nature physics*, 10(4):321–326, 2014.

[296] Mohammad Mirhosseini, Alp Sipahigil, Mahmoud Kalaee, and Oskar Painter. Superconducting qubit to optical photon transduction. *Nature*, 588(7839):599–603, 2020.

[297] RD Delaney, MD Urmey, S Mittal, BM Brubaker, JM Kindem, PS Burns, CA Regal, and KW Lehnert. Superconducting-qubit readout via low-backaction electro-optic transduction. *Nature*, 606(7914):489–493, 2022.

[298] Akira Kyle, Curtis L Rau, William D Warfield, Alex Kwiatkowski, John D Teufel, Konrad W Lehnert, and Tasshi Dennis. Optically distributing remote two-node microwave entanglement using doubly parametric quantum transducers. *Physical Review Applied*, 20(1):014005, 2023.

[299] Sagnik Saha, Mikhail Shalaev, Jameson O'Reilly, Isabella Goetting, George Toh, Ashish Kalakuntla, Yichao Yu, and Christopher Monroe. High-fidelity remote entanglement of trapped atoms mediated by time-bin photons. *Nature Communications*, 16(1):2533, 2025.

[300] Boris B Blinov, David L Moehring, L-M Duan, and Chris Monroe. Observation of entanglement between a single trapped atom and a single photon. *Nature*, 428(6979):153–157, 2004.

[301] Benjamin Brecht, Dileep V Reddy, Christine Silberhorn, and Michael G Raymer. Photon temporal modes: a complete framework for quantum information science. *Physical Review X*, 5(4):041017, 2015.

[302] Marek Zukowski, Anton Zeilinger, M Horne, and Artur Ekert. "Event-ready-detectors" Bell experiment via entanglement swapping. *Physical Review Letters*, 71(26), 1993.

[303] Holger P Specht, Jörg Bochmann, Martin Mücke, Bernhard Weber, Eden Figueroa, David L Moehring, and Gerhard Rempe. Phase shaping of single-photon wave packets. *Nature Photonics*, 3(8):469–472, 2009.

[304] Chelo Ferreira and José L López. Asymptotic expansions of the Hurwitz–Lerch zeta function. *Journal of Mathematical Analysis and Applications*, 298(1):210–224, 2004.

[305] Peter P Rohde, Timothy C Ralph, and Michael A Nielsen. Optimal photons for quantum-information processing. *Physical Review A*, 72(5):052332, 2005.

[306] Emma Deist, Yue-Hui Lu, Jacquelyn Ho, Mary Kate Pasha, Johannes Zeiher, Zhenjie Yan, and Dan M Stamper-Kurn. Mid-circuit cavity measurement in a neutral atom array. *Physical Review Letters*, 129(20):203602, 2022.

[307] Christoph Hamsen, Karl Nicolas Tolazzi, Tatjana Wilk, and Gerhard Rempe. Two-photon blockade in an atom-driven cavity QED system. *Physical Review Letters*, 118(13):133604, 2017.

[308] Elmer Suarez, Federico Carollo, Igor Lesanovsky, Beatriz Olmos, Philippe W Courteille, and Sebastian Slama. Collective atom-cavity coupling and nonlinear dynamics with atoms with multilevel ground states. *Physical Review A*, 107(2):023714, 2023.

[309] Charles H Bennett, Gilles Brassard, Sandu Popescu, Benjamin Schumacher, John A Smolin, and William K Wootters. Purification of noisy entanglement and faithful teleportation via noisy channels. *Physical Review Letters*, 76(5):722, 1996.

[310] Rodney Loudon. *The quantum theory of light*. OUP Oxford, 2000.

[311] Christopher C Gerry and Peter L Knight. *Introductory quantum optics*. Cambridge University Press, 2023.

[312] Christine Guerlin, Julien Bernu, Samuel Deleglise, Clement Sayrin, Sebastien Gleyzes, Stefan Kuhr, Michel Brune, Jean-Michel Raimond, and Serge Haroche. Progressive field-state collapse and quantum non-demolition photon counting. *Nature*, 448(7156):889–893, 2007.

[313] Peter W Milonni. *The quantum vacuum: an introduction to quantum electrodynamics*. Academic press, 1993.